Chitosan-Bioglass and chitosan-apatite-wollastonite composites for bone tissue engineering

by

Djurdja Vukajlovic

Supervisors: Dr Katarina Novakovic

Dr Oana Bretcanu

School of Engineering

Newcastle University, UK

The dissertation is submitted for the degree of

Doctor of Philosophy

August 2020

Acknowledgement

Abstract

Synthetic inorganic-organic composites are of interest for bone tissue engineering as an alternative to natural grafts since they resemble the structure of the natural bone and degrade over time, enabling the new bone to grow. In this study, two types of composite materials- chitosan hydrogels with Bioglass 45S5 (BG) particles, and BG and apatite-wollastonite (AW) scaffolds coated with the chitosan hydrogel- have been investigated. Ceramics have been used for high mechanical strength, while chitosan was added to increase flexibility of the composites. Genipin was used as a low toxicity cross-linker, in order to improve stability of the chitosan hydrogels. The aim of this PhD research was to assess the properties of the chitosan- BG and AW composites and aid their advancement to *in vitro* and *in vivo* studies.

The composites were analysed using scanning electron microscopy (SEM), FTIR spectroscopy, fluorescence intensity (FI) measurement and compression test. The BG-hydrogels and the hydrogel coated BG and AW scaffolds were immersed in the simulated body fluid (SBF) for up to 2 weeks and their structure and mechanical properties were examined.

Results showed that BG addition to the chitosan hydrogels improved the mechanical properties both before and after immersion in SBF, but affected the FI measurement. Before coating both BG and AW scaffolds had a porous structure (pores 100-300 µm), while the treatment before SEM imaging affected the porosity of the coated scaffolds. Some apatite deposition was observed on the uncoated BG scaffolds after immersion in SBF for 2 weeks. AW scaffolds were mechanically stronger than BG scaffolds, independent of the coating or testing conditions (before or after SBF), with compressive stress up to 5.68 MPa for AW scaffolds compared to 1.20 MPa for BG scaffolds, reaching the lower limit of the cancellous bone. However, the coating did not improve the mechanical properties of the scaffolds. Nevertheless, after immersion in SBF (for up to 2 weeks), hydrogel coated BG scaffolds had higher compressive stress (~ 0.95 MPa) than uncoated BG scaffolds (~ 0.65 MPa).

List of publications

- Vukajlovic Dj, Parker J, Bretcanu O, Novakovic K. *Chitosan based polymer/bioglass composites for tissue engineering applications*. Materials Science and Engineering: C 2019, 96, 955-967.

- Vukajlovic Dj, Bretcanu O, Novakovic K. *Comparison between chitosan coated Bioglass 45S5 and apatite-wollastonite scaffolds for tissue engineering applications*. In: Workshop for Young Researchers in Ceramics and Glasses for Medical Applications (you-CGMed). 2019, Madrid, Spain: Sociedad Española de Cerámica y Vidrio.

- Vukajlovic Dj, Parker J, Bretcanu O, Novakovic K. *Hydrogel/Bioglass composites for tissue regeneration*. In: NEPIC Technology Showcase Event. 2019, Middlesbrough, UK.

- Vukajlovic Dj, Parker J, Bretcanu O, Novakovic K. *Bioglass scaffolds coated with chitosan-based hydrogels for tissue engineering applications*. In: Chem Eng Day UK 2019. 2019, Edinburgh, UK.

- Stanojevic A, Vukajlovic Dj, Parker J, Novakovic K. *Synthesis and characterization of genipin-crosslinked chitosan hydrogels*. In: Seventeenth Young Researchers' Conference - Materials Science and Engineering. 2018, Belgrade, Serbia: Institute of Technical Sciences of SASA.

- Vukajlovic D, Bretcanu O, Parker J, Novakovic K. *Fluorescence, mechanical and swelling properties of chitosan-genipin and chitosan-genipin-PVP hydrogels*. In: 4th International Conference on Biomedical Polymers and Polymeric Biomaterials (ISBPPB 2018). 2018, Krakow, Poland: International Society for Biomedical Polymers and Polymeric Biomaterials.

- Vukajlovic Dj, Parker J, Bretcanu O, Novakovic K. *Chitosan-based/Bioglass composites for regenerative medicine applications-fluorescence, mechanical properties and volume change*. In: 2018 Chemical Engineering Postgraduate Student Research Conference. 2018, Newcastle, UK.

- Vukajlovic Dj, Parker J, Bretcanu O, Novakovic K. *Chitosan-bioglass composites for applications in regenerative medicine.* In: 2017 Chemical Engineering Postgraduate Student Research Conference. 2017, Newcastle, UK.

Table of content

List of Figures

List of Tables

Abbreviation list

APS	3-aminopropyltriethoxysilane
ATR	Attenuated total reflectance
AW	Apatite-wollastonite glass-ceramic
BE	Backscattered electrons
BG	Bioglass 45S5
Bg	General term for bioactive glasses
CaP	Calcium phosphate
Cht	Chitosan
CL	Cathodoluminescence
DTA	Differential thermal analysis
DTGS	Deuterated triglycine sulfate
ECM	Collagenous extracellular matrix
EDS	Energy dispersive X-ray spectroscopy
FEG	Field-emission gun
FI	Fluorescence intensity
GA	Glutardexyde
GAG	Glycosaminoglycans
Gen	Genipin
GP	Glycerol phosphate disodium salt
GPTMS	Glycidoxypropyltrimethoxysilane
HA	Hydroxyapatite
HACC	Hydroxypropyltrimethyl ammonium chloride chitosan
HCA	Hydroxycarbonate apatite
HMDI	Hexamethylene diisocyanate
HM	Heating microscopy
NMA-HACC	O-acrylamidomethyl-HACC
OPD	Optical path difference
PCA	Polycyanoacrylate
PCL	Poly(ε-caprolactone)
PE	Polyethylene

PGA	Poly(glycolic acid)
PHB	Polyhydroxybutyrate
PLGA	Poly(lactide-co-glycolic acid)
PLLA	Poly(L-lactic acid)
PMT	Photomultiplier tube
PTHF	Poly(tetrahydrofuran)
PU	Polyurethane
PVA	Polyvinyl alcohol
SBF	Simulated body fluid
SE	Secondary electrons
SEM	Scanning electron microscopy
TCP	Tricalcium phosphate
TEM	Transmission electron microscopy
TEOS	Tetraethyl orthosilicate
TRIS	Tris(hydroxymethyl)aminomethane
UV-VIS	Ultraviolet-visible
XRD	X-ray diffraction
ZPD	Zero path difference

Chapter 1 Introduction - The need for synthetic bone grafts

Tissue engineering is a promising field of research which aims to replace and repair damaged or diseased tissues and organs with substitutes made of synthetic or natural compounds. It involves prostheses and parts with the ability to regenerate tissues, as well as vehicles for the delivery of drugs, cells or biomolecules, and the coating of non-biological apparatus (e.g. stents) with materials to enable interaction with cells [1]. According to data from 2020 the biomaterial market was estimated to grow to $215 billion by 2025 from $96 billion in 2019 [2]. Due to injury, disease, surgical procedures, increasing life span and a rising population, orthopaedic implants are in particular demand [3].

After blood, bone transplantation is the second most common tissue transplantation with over 2 million bone graft operations taking place every year worldwide [4, 5]. Autografts (grafting tissue from the same donor from one bone tissue to another), continue to be the gold standard. They are used in about 58 % of all bone graft procedures due to their ability to promote bone formation and induce bone tissue growth without causing an immune response [5]. Other options include allografts (tissue from the same species but not genetically identical), used in about 34 % of bone graft procedures, and xenografts (when the donor is another specie) [5]. However, certain issues associated with these natural materials can arise: a lack of supply of suitable tissue for large defects when using autografts; donor site complications (most commonly persistent pain) and a negative immune response of the patient that can occur when using allografts or xenografts [3, 5, 6]. For these reasons, synthetic materials have been widely investigated as alternatives, currently used in around 8 % of all bone graft procedures [1, 3, 6].

There is evidence of the use of biomaterials as far back as in ancient Egypt. Artificial eyes, teeth and noses were found in the mummies [7]. A xenograft was used in a skull defect in a soldier in 1968, which is recorded as the first bone graft [8]. The term tissue engineering was officially introduced in 1987 [9]. Since its beginning, tissue engineering has developed greatly and there are numerous commercially available synthetic bone graft substitutes [5, 10-15]. In order to replace natural tissue, synthetic materials need to have similar properties to native tissue [16]. Therefore, the structure of the human bone will be illustrated first, followed by the list of properties that are required for the synthetic bone scaffolds. Different

materials and designs for scaffolds will be described, with a focus on composites of bioglasses and bioglass-ceramics and polymers, including chitosan. The main issue related to inorganic-organic composite scaffolds for bone tissue engineering remain the low mechanical properties which make them unsuitable for high load-bearing applications.

The aim of this project is to synthesize composite scaffolds consisting of inorganic and organic phases, which are suitable for bone tissue regeneration as they mimic the structure of a natural bone and degrade over time giving space for the new tissue to grow. The inorganic phases selected for the study are BG 45S5 and AW glass-ceramics, while chitosan is chosen as the organic phase. Both BG and AW are well-known for their ability to induce new bone formation. Although it is the second most abundant natural polymer after cellulose, chitosan is currently a waste material in the food industry, while the research attempts to use its desirable properties suitable for applications in bioengineering, such as biocompatibility and a structure resemblance with glycosaminoglycan which is a part of extracellular matrix, ECM. In this work, chitosan is used as an alternative to commonly employed collagen. Furthermore, genipin, an alternative to other toxic cross-linking agents, is used to form chitosan hydrogels. Two types of composite materials will be developed:

1) genipin cross-linked chitosan hydrogel with the addition of BG particles;
2) BG and AW scaffolds coated with chitosan-genipin hydrogels.

The novelty of this work is that, even though they are all widely recognized in bioengineering, these materials have not been used in a combination suggested here and/or mechanical properties were not described in the literature. One of the main problems of these materials are inadequate mechanical properties. Since these materials have not been used with patients yet, more research is needed to bring them closer to clinical trials. Work reported in this thesis explores the combination of BG and AW with chitosan using genipin as a cross-linker in order to obtain suitable materials for potential applications in bone tissue engineering and investigate their properties upon immersion in the SBF, including mechanical measurements.

The ultimate goal is to evaluate the properties of the composites and investigate the effect of addition of Bioglass powder in chitosan hydrogels and the chitosan coating on the BG and AW scaffolds.

Genipin has been rarely used in the literature and the aim is to investigate if addition of genipin could significantly improve mechanical properties of the chitosan hydrogels. Addition of BG powder to chitosan-based hydrogel is expected to serve as a reinforcement and to improve mechanical properties. The aim is to show if the improvement of mechanical properties is substantial which could make the hydrogels with BG suitable for bone tissue applications.

Behavior of the composites upon immersion in SBF is important in order to predict their properties in the future *in vitro* and *in vivo* experiments. The hydrogels exhibit volume changes in different pH environment and the goal was to investigate the effect of BG powder on the volume of the gels, and consequently on mechanical properties.

AW glass-ceramic is reported to be stronger than BG, which is the reason that both BG and AW scaffolds will be synthesized in this project and their properties will be compared. It is expected that AW scaffolds will have higher compressive strength than BG scaffolds. Chitosan should act as a glue and reinforce the struts of bioglass-ceramic scaffolds and subsequently improve compressive strength. One of the goals was to further investigate mechanical properties and bioactivity upon immersion in SBF, which is important for the application in bone regeneration. Also, chitosan hydrogel coating could slow down the dissolution of the BG and AW scaffolds in SBF and maintain mechanical properties of the composites for longer.

In summary, research hypotheses of this thesis are:

1) Addition of BG powder to chitosan-genipin hydrogels improves mechanical properties of the hydrogels, both before and after immersion in SBF

2) Hydrogel coating of the BG and AW scaffolds improves mechanical properties of the scaffolds before and after immersion in SBF as the coating hinders the dissolution of the glass-ceramic scaffolds in SBF

3) As AW scaffolds are reported to be stronger than BG composite scaffolds, hydrogel coated AW scaffolds will be stronger than hydrogel coated BG scaffolds

4) Chitosan-genipin-BG-powder composites, as well as composites made by coating BG and AW scaffolds with chitosan-genipin hydrogel, will have

3

improved mechanical properties, reaching the values within the range of those of the bone tissue

In order to achieve the abovementioned goals and evaluate the hypotheses, following objectives will be addressed:

1) Synthesis and characterisation of hydrogels with and without BG powder, including evaluation of mechanical properties
2) Investigation of hydrogels behaviour upon immersion in SBF
3) Synthesis of BG and AW scaffolds with and without chitosan-genipin hydrogel coating
4) Investigation of bioactivity and mechanical properties of the hydrogel coated BG and AW scaffolds after immersion in SBF

The structure of the thesis is briefly explained below.

Chapter 2 presents the structure of the human bone, the requirements for the synthetic scaffolds for bone tissue applications and a short literature review of different materials that have been used as scaffolds. Furthermore, commercially available inorganic-organic composites have been described, as well as the next generation of composites-hybrid materials. The structure and properties of Bioglass, apatite-wollastonite and other glass-ceramics, chitosan and chitosan-based materials, have been described in detail. These materials will be further used for the preparation of inorganic-organic composites.

Chapter 3 shows two methods of synthesis of inorganic-organic composites: 1) hydrogels with Bioglass, and 2) Bioglass and apatite-wollastonite scaffolds coated with the hydrogel. Also, a short description of the methods for materials characterization is given here, together with the parameters used for analysis.

Results and discussion have been structured in four chapters. Composites made of chitosan-genipin hydrogels and BG and/or AW glass and glass-ceramic will be synthesized using two methods. Firstly, BG powder will be added to chitosan hydrogels cross-linked with genipin and the composites will be characterized. The effect of BG on microstructure, cross-linking and mechanical properties of the hydrogels will be examined. Furthermore, experiments in the SBF will be conducted in order to investigate how BG affects the shrinkage

4

and mechanical properties of the hydrogels. In the second method, BG and AW glass-ceramic scaffolds synthesized by sponge replication method will be coated with the chitosan hydrogel. The influence of the coating on the mechanical properties and microstructure of these composite scaffolds will be examined, as well as their behaviour, in terms of bioactivity and strength, after immersion in SBF for 2 weeks.

Therefore, Chapter 4 presents the characterization of BG powder. Characterization of hydrogels with BG powder is shown in Chapter 5. Chapter 6 and 7 present the characterization of BG scaffolds and AW scaffolds, respectively, coated with the hydrogels. Chapter 8 shows the results of the mechanical measurements and studies in SBF of BG and AW scaffolds coated with the hydrogel. Chapter 9 highlights the most important conclusions, together with the final recommendations and the future work.

Chapter 2 Literature review

2.1 Structure of the human bone

Human bones is comprised of 10-20 wt% collagen type I, 60-70 wt% bone mineral, 9-20 wt% water and a small amount of other organics (proteins, polysaccharides and lipids) [3, 17, 18]. Bone mineral is based on hydroxyapatite, HA ($Ca_{10}(PO_4)_6(OH)_2$). HA is substituted mainly with CO_3^2, and traces of ions such as Mg^{2+}, Na^+ and Fe^{2+} and it is often referred to as hydroxycarbonate apatite, HCA. On a macroscale, human long bone is composed of cortical bone, cancellous bone, periosteum, endosteum and articular cartilage [3]. While cortical bone is compact, cancellous (trabecular) bone possesses spongy structure. Therefore, cortical bone is stronger than the cancellous bone. Periosteum is the outer layer of the bone, made of fibrous connective tissue containing cells and it is important for bone formation. Endosteum is the inner layer surrounding the marrow cavity, which is important for bone remodelling. Cartilage is based on collagenous matrix exhibiting toughness and flexibility. Cortical bone is made of small units-osteons, which consist of concentric layers called lamellae. Collagen fibres (Figure 2.1) form these lamellae and each fibre contains collagen molecules which are organized in fibrils. HCA crystals occur at sites between collagen molecules, while as a whole HCA is a continuous phase in the bone [3]. Cancellous bone has flat lamellae in form of sheets instead of the cylindrical osteons in cortical bone [19]. Collagen matrix and mineral phase make the bone a two-phase material, flexible organic phase and strong inorganic phase, suitable to resist mechanical stress [20].

Articular cartilage
Cancellous bone
Cortical bone
Osteon
Lamella
Haversian canal
Collagen fiber
Collagen fibril
Collagen molecule
Bone Crystals

10-500 μm
3-7 μm
0.5 μm
1 nm

(a)   (b)   (c)   (d)   (e)

Macrostructure   Microstructure   Nanostructure
    Sub-microstructure   Sub-nanostructure
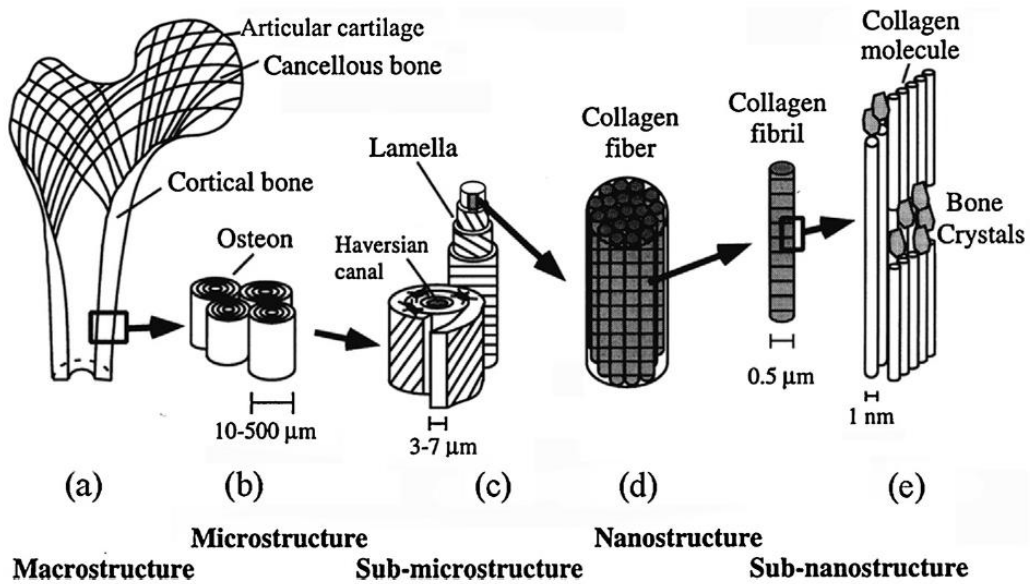
Figure 2.1: *Structure of the bone a) with cortical and cancellous bone, and cartilage on the macrolevel, b) osteon, c) lamella, d) collagen fibre made of fibrils and e) collagen molecules and the mineral phase [3]*

Epiphysis is the end part of the long bone made of cancellous bone which is covered with a thin layer of cortical bone (Figure 2.2) [21]. The space in the spongy bone is filled with red marrow. Diaphysis is the midsection of a long bone surrounding the medullary cavity [21]. While diaphysis has walls composed of cortical bone, the walls of the medullary cavity are made of the cancellous bone. Figure 2.2 also shows organisation of the osteons and blood vessels and nerves in the bone. In the centre of each osteon is the Haversian canal that contains blood vessels and nerves [22].

7
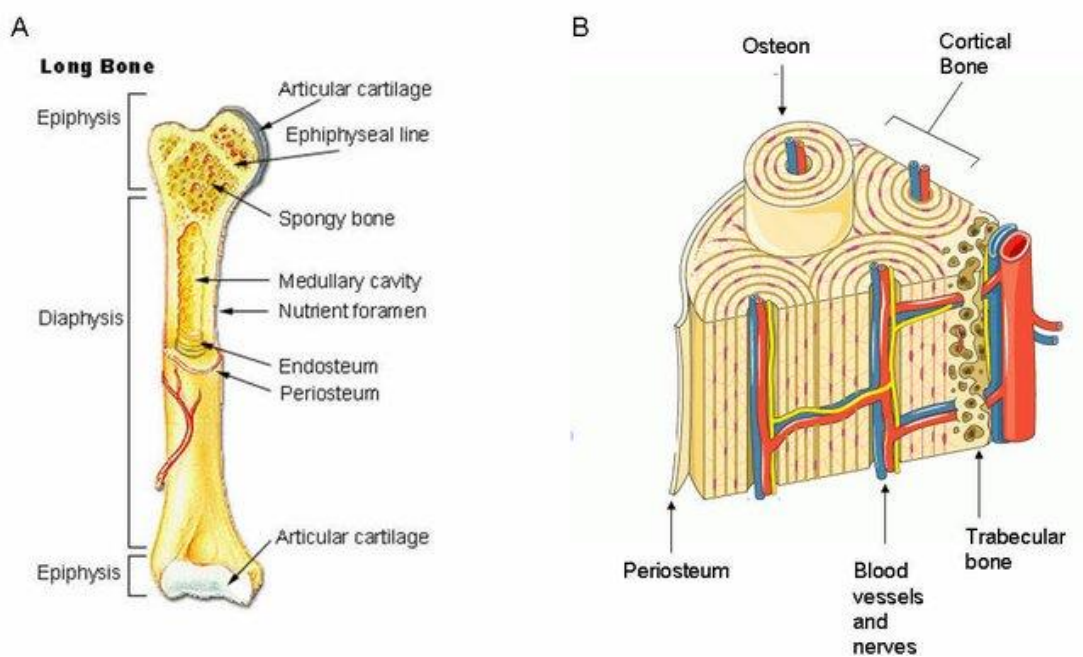
Figure 2.2 Long bone (A) and composition of the bone (B) [22]

There are four types of bone cells: osteoblasts (form the bone matrix), osteocytes (maintain the bone tissue), osteogenic cells (stem cells) and osteoclasts (resorb the bone) [21]. Osteogenic cells are stem cells that differentiate into osteoblasts. Osteoblasts form the bone matrix and secrete the collagen matrix, which then mineralizes. When the cells become incorporated into the bone matrix, they are called osteocytes, which are the most common type of bone cells. Osteoclasts are important for bone resorption. Bone is constantly formed by osteoblasts and the old bone is resorbed by osteoclasts-this process is called remodelling of the bone as a response to external stimuli such as stress and physiological influences.

Most common bone diseases are fracture (loss of bone continuity caused by excess of stress), osteoporosis (weak bones caused by loss of bone minerals), osteogenesis imperfecta (brittle bones caused by defects in collagenous matrix), osteomalacia (soft bones due to deficiency of vitamin D), cancer (causes progressive damage of the bone) and osteomyelitis (infection caused by bacteria) [23].

2.2 Scaffolds and their properties

One way to employ synthetic materials is to design them into scaffolds. Bone scaffold materials are porous and degradable structures that should provide mechanical support to bone defects, and allow cells to proliferate and differentiate [24, 25]. Because of the

aforementioned bone diseases, synthetic bone scaffolds have been developed in order to assist bone healing. The advantage of using scaffolds is that they have a porous structure similar to natural bone tissue and they support bone growth while degrading over time. In order to be successful, bone scaffolds must fulfil numerous requirements:

1) Biocompatibility – this essential property for biomaterials is defined as the ability of a material to support normal cellular activity without causing local or systemic damage to the surrounding living tissue [24]. Ideally, the scaffold should also be osteoconductive (allow bone growth on its surface and in the pores) and osteoinductive (stimulate non-differentiated cells to develop into bone-forming cells) [4, 5, 24, 26]. The porous structure of the scaffolds should allow formation of new blood vessels [4, 24].

2) Bioactivity – this represents the ability of the scaffold's surface to form an apatite layer (bone-like layer of hydroxyapatite) through which the scaffold will bond to the native bone tissue when implanted into the body. A test method first developed by Kokubo for bioactive glass ceramics employs a simulated body fluid (SBF) which has a composition similar to human blood plasma [27]. This test can be used to detect apatite formation on the surface of a material and predict apatite formation *in vivo* (ISO 23317:2014). The mechanism of hydroxyapatite formation and formation of the bone tissue will be further explained in Section 2.4.1.

3) Mechanical properties – it is important that the mechanical properties of the synthetic material match those of the surrounding tissue, along with the load transfer between the implant and the tissue [4, 5, 24]. Properties of cancellous and cortical bone are given in Table 2.1. Load-bearing materials should have mechanical properties within the range of properties of cortical bone (low load-bearing materials exhibit mechanical properties near the lower limit of cortical bone and high load-bearing materials close to the upper limit of the cortical bone range) [28].

Table 2.1: Mechanical properties of cancellous and cortical bone and synthetic scaffolds [5, 24, 29-32]

Property	Cancellous bone	Cortical bone	PLGA/45S5 Bioglass[1] scaffold	Chitosan/ bioglass 58S[2] scaffold	Chitosan/ AW[3] scaffold
Compressive strength	2-20 MPa	100-200 MPa	0.42 MPa	7.68 MPa	3.11 MPa
Compressive modulus	0.1-2 GPa	15-20 GPa	51 MPa	0.46 GPa	Not reported
Tensile strength	10-20 MPa	90-130 MPa	Not reported	3.11 MPa	Not reported
Young's modulus	0.1-4.5 GPa	17-24 GPa	Not reported	0.196 GPa	Not reported
Fracture toughness	0.1-0.8 MPa m$^{1/2}$	2-12 MPa m$^{1/2}$	Not reported	0.24 MPa m$^{1/2}$	Not reported

[1] see Section 2.4.1 for composition of Bioglass 45S5
[2] bioglass 58S (58 SiO_2, 33 CaO and 9 P_2O_5 in wt%)
[3] apatite-wollastonite

So far, synthetic scaffolds are not yet achieving the higher end of the desired properties, which is why their applications have been limited to low load-bearing conditions such as bone fillers and maxillofacial reconstructive procedures [5].

4) Porosity and pore size - scaffolds with pore sizes of 20-1500 µm have been reported for bone tissue engineering [33]. According to *in vitro* and *in vivo* studies, scaffolds are required to possess open interconnected pores with at least 100 µm in diameter in order to enable successful transport of food and oxygen for the cells and to allow removal of waste products [5, 24, 33-35]. *In vivo* studies showed that only pores larger than 100 µm enable healthy mineralized bone formation, while smaller size pores (75-100 µm) lead to the formation of unmineralized bone tissue which causes disease and disorders (e.g. pain, muscle weakness and fracturing of the bone) [35]. At the same time, when the pores had diameters in the region of 10-75 µm, formation of fibrous (scar) tissue, was reported [35]. Fibrous tissue only connects with the surrounding tissue but does not possess mechanical and other characteristics of bone tissue, which can lead to pain, deformity and fracture. Furthermore, several reports suggest that the

optimum pore size is 200-350 μm, and that both micro- and macro-porosity is needed to enhance bone ingrowth [24, 33, 35]. Although high porosity is beneficial for cells to proliferate and differentiate, it reduces the mechanical strength of the scaffold [35]. It is worth noting that healthy cancellous bone has a porosity of 50-90 % with pore sizes of 300-600 μm, and cortical bone has a porosity of 3-12 % with pore sizes of 10-50 μm in diameter [19, 35]. These values, as well as the strength and modulus of the bone, vary depending on race, age and sex [5, 19, 35, 36]. Vitoss™ (Orthovita), a collagen I/β-tricalcium phosphate composite scaffold used clinically, has 90 % porosity with pores ranging from 1 to 900 μm which encompasses the range of healthy cancellous bone [14].

Despite the necessity for macro-porosity, it has been demonstrated that micropores also play an important role for osteogenesis [37]. The apatite layer, which forms on the surface of bioactive implants after immersion in a simulated environment or *in vivo,* is important for bone growth because it initiates cell adhesion, proliferation and differentiation [38]. This apatite layer can also serve as a conductor for bone growth [38]. Since micropores (<20 μm) enlarge the specific surface area, it is easier for the apatite layer to be formed (due to faster ion exchange), and it is easier for proteins to attach to the surface of the material, leading to enhanced cell activity [34, 37]. It is worth reiterating that macro-porosity has a bigger role in affecting the mechanical properties of scaffolds than microporosity [34]. The reason for this is that structures with large pores are only connected via necks/bridges which offer weaker support than denser structures. For example, in 45S5 Bioglass scaffolds with 60 % porosity, reducing the pore size from 700 μm to 400 μm increased compressive strength from 3.5 to 6.7 MPa [39].

The geometry of the pores present in the scaffold is shown to dictate the pattern of bone formation: discontinuous pattern of bone ingrowth with formation of bone islands throughout the scaffold was found in scaffolds containing controlled, network-structured pores, while continuous pattern of bone growth from the margins of the defect was seen in scaffolds with randomly distributed pores. It was concluded that discontinuous bone ingrowth tends to result in faster filling of the scaffold when compared to continuous growth; however, the overall amount of bone formation remained unaffected [40]. Furthermore, when the

samples contained microporous walls, as well as a systematic, organized architecture, both types of bone ingrowth were detected (continuous and discontinuous). These findings suggest that by controlling the pore size of scaffolds, and most importantly pore architecture, it is possible to direct the pattern, discontinuous or continuous, as well as time of bone growth [40].

5) Biodegradability - scaffolds are expected to degrade over time to make room for the new tissue to grow. After implantation, scaffolds should have a similar strength to the host tissue and degrade over time with a controlled rate, depending on the application [4, 5, 24]. Reported degradation times vary from 3 to 6 months for scaffolds used in cranio-maxillofacial (skull, face, jaws, mouth) procedures to approximately 9 months or more for those used in spinal fusion [24]. For example, RegenOss® (JRI Orthopaedics), a clinically used collagen I/hydroxyapatite scaffold, degrades between 6 and 12 months after implantation [14]. Ideally, products formed by degradation of the implanted material should be non-toxic.

6) Porosity and degradation rate interplay – these two factors need to be tuned, that is if the degradation rate of the material is high, initial porosity needs to be low otherwise the scaffold resorbs too fast disabling the mechanical support and affecting the growth of the new tissue [35]. Conversely, materials that degrade at a low rate can be highly porous to bring the degradation rate to an optimal level [35]. Additionally, higher specific surface area accelerates the degradation rate. The general consensus regarding the porosity needed for scaffold application is that high porosity (over 80 %) and bigger pores (>300 μm) favour new bone ingrowth, while mechanical strength dictates the limits of porosity and pore size [35, 41].

2.3 Materials for creating scaffolds

Scaffolds made of metals, ceramics, polymers and combinations of these materials have been studied, and some have been used for clinical applications, such as blood vessels, drug and biomolecules delivery, cartilage, bone, and dental regeneration [5, 8, 10, 13-16, 24, 25, 42-52].

2.3.1 Metallic scaffolds

Most commonly clinically used metallic scaffolds for bone tissue regeneration are titanium (ASTM F67) and titanium alloys Ti-6Al-4V (ASTM F136), stainless steel 316L (ASTM F138) and cobalt-based alloys (ASTM F75 and ASTM F799) [53]. Metallic scaffolds made of tantalum, titanium and titanium alloys, magnesium and nickel-titanium alloy have been widely employed in preclinical and clinical bone tissue applications. Some of them have been used for maxillofacial surgeries (nickel-titanium alloy, Nitinol), joint implants (titanium-aluminium-vanadium alloys) and spine fusion surgeries (titanium) for years. Although metallic scaffolds are suggested to have mechanical properties, such as strength and ductility, suitable for high load-bearing applications, traditional scaffolds such as stainless steel and titanium and titanium alloys lack of biocompatibility, bioactivity, biodegradability and integration with the bone, and the resorption of the tissue around the implant occurs [7, 53, 54]. It should be noted that even though ideal scaffolds are considered as porous materials that degrade over time while having desirable mechanical properties and bioactivity, as mentioned earlier in this section, it is difficult to achieve all the requirements for ideal scaffolds. For example, metallic scaffolds exhibit good mechanical properties but lack of biodegradability, while ceramic and polymer scaffolds are degradable but have low mechanical properties, as it will be later discussed. For these reasons, biodegradable metals (pure and their alloys) have been studied, such as iron, magnesium and zinc [55-57]. Iron and iron-based scaffolds have been reported to have a degradation rate too slow for applications in degradable implants [58]. Another problem with metallic scaffolds is leaching of toxic ions due to corrosion or wear, which causes inflammation or allergic reactions, as in case of magnesium scaffolds, limiting them to preclinical studies [53]. Furthermore, magnesium scaffolds corrode too quickly failing to offer mechanical support to the bone to grow [58, 59]. In order to tackle these problems, the surface modification can be performed using polymers (such as collagen), growth factors and cells [53]. Titanium scaffolds in combination with ceramics (hydroxyapatite, tricalcium phosphate, TCP and calcium phosphate, CaP), polymers (collagen), cells and bone grafts have been under clinical studies [53]. Magnesium-based alloy, Mg-22Zn-2Gd, have been developed in order to control degradation and enhance biocompatibility [59]. The advantage of using the magnesium-based alloy is slower and controlled degradation rate, which is important in order to avoid rapid loss of mechanical properties leading to implant failure and toxicity.

2.3.2 Ceramic and polymer scaffolds, and their combination to fabricate composite scaffolds

Ceramic scaffolds applied in clinics for small bone defects are mostly based on hydroxyapatite and calcium phosphate [60]. Some of the widely used products include ProOsteon® (HA and calcium carbonate), Neobone® (HA), Ceraform® (β-TCP and HA) [61]. They exhibit high compression strength, biocompatibility, bioactivity and biodegradability but also brittleness, which is why their application is limited to non- and low-load bearing defects. Commercially available polymer scaffolds are mostly made of poly(L-lactic acid) (PLLA), poly(lactide-co-glycolic acid) (PLGA), polycyanoacrylate (PCA), lysine diisocyanate-based polyurethane, polyanhydride and collagen, but they have only been used for applications such as soft tissue, drug delivery and wound healing [62]. Polymeric scaffolds can be biocompatible, biodegradable and ductile, however, their mechanical properties are mostly too weak, limiting their use in bone tissue engineering. Also, upon degradation they can leach toxic by-products and sterilization that is required prior to *in vivo* use can affect their properties [7]. Sterilization methods, such as autoclaving and gamma irradiation, can affect the structure of polymers or in some cases, such as UV irradiation, are not efficient enough [63]. Although having many desirable properties, ceramic scaffolds are strong but brittle, while polymer scaffolds are mostly ductile and mechanically weak [5, 8, 10, 16, 24]. Ceramics and bioglasses, in combination with polymers have been developed with the aim of producing a composite biomaterial which will overcome the drawbacks of the individual materials, while resembling natural bone structure consisting of both inorganic and organic components [4, 5]. Yet, fulfilling all the requirements for an ideal scaffold, including high porosity, biocompatibility, biodegradability and suitable mechanical properties, while maintaining all the other parameters remains a challenge [24].

A number of studies have reported *in vivo* testing of polymer/ceramic composite scaffolds designed for haemostasis (to stop bleeding), blood vessels, the delivery of drugs and biomolecules, and cartilage and bone regeneration applications [5, 13, 51, 52, 64-74]. Some of the materials for osteochondral regeneration with a multi-layered type of structure are commercially available. They consist of a combination of polymers (to mimic cartilage) and ceramics (to mimic bone tissue). ChondroMimetic™ is a composite based on type I collagen, chondroitin-6-sulfate, and calcium phosphate. TruFit™ consists of poly(lactic-co-glycolic acid)

(PLGA) and poly(glycolic acid) (PGA) fibers, and calcium sulphate. MaioRegen® is made of three layers: type I collagen, a mixture of type I collagen and hydroxyapatite (60:40 wt% respectively) and a mixture of type I collagen and hydroxyapatite (30:70 wt% respectively) [13]. The use of the natural polymer collagen (in ChondroMimetic^{TM}) was shown to have advantages over PLGA (in TruFit^{TM}). ChondroMimetic^{TM} had better scores (according to Seller's scoring system for cartilage repair), rapid cell infiltration and bone matrix formation within the implanted materials, while TruFit^{TM} had more bone defects in the form of cysts (bone cavities filled with fluid) [75]. The degradation of natural polymers is enzymatic with peptide and saccharide fragments being the products of degradation of collagen, which do not affect the local pH, as they are naturally found in cartilage. On the other hand, degradation of PLGA leads to formation of acid oligomers (of lactic and glycolic acids) which have a detrimental effect on cells and apatite precipitates leading to bone cysts. This was shown to induce a lack of integrity of the PLGA-materials with native tissue. Clinical reports of the multi-layered type of materials are contradictory and vary according to the study conducted [76-78]. Some studies reported good follow-up and success in patients, as some patients were able to return to sport activities, experiencing a relief of symptoms; magnetic resonance imaging (MRI) showed complete filling of the defect and integration of the graft [77, 78]. For example, an Olympic fencer was able to compete 17 months after the implantation surgery [79]. However, the literature also reports a high rate of failure (formation of fibrous tissue and need for reoperation) when the same materials were used in other patients [76, 77]. The opposing outcomes are dependent on the age and previous activity levels of the patient as well as the different defect sites treated.

Some commercially available composite scaffolds for bone tissue applications shown in Table 2.2 [5, 14, 80]. Lerner et al. [81] reported that Vitoss (Orthovita), a scaffold of β-tricalcium phosphate and type I collagen, has similar results to autografts in scoliosis surgery. Radiographs showed complete and continuous fusion of the bone in both cases, while the 4/20 patients who received autographs suffered from donor site pain. One of the most successful commercially available bone graft products in the USA is Healos (DePuy Orthopaedics) which is a scaffold made of a matrix of cross-linked collagen fibres coated with hydroxyapatite [15]. Healos gives similar clinical results to autographs while avoiding donor site complications and requires less time for preparation, making it a successful implant [82].

One big drawback of most of the commercially available polymer/ceramic composite scaffolds is the use collagen, which can cause allergic reactions with some patients (although not common) and transmit pathogens because the collagen comes mainly from porcine and bovine sources [5, 83].

Table 2.2: Commercially available natural polymer/ceramic composite scaffolds [5, 14, 80]

Product	Composition and structure	Recommended use
Collagraft® (Zimmer)	Collagen I fibres and hydroxyapatite/tricalcium phosphate porous granules	Acute long bone fractures and traumatic osseous defects
Collapat® II (BioMet Inc.)	Collagen I and hydroxyapatite (hydroxyapatite granules dispersed in collagen structure)	Aseptic enclosed metaphyseal bone defects
FormaGraft® (Maxigen Biotech Inc.)	Collagen I and hydroxyapatite/β-tricalcium phosphate granules	Bone void filler
Integra Mozaik™ (Integra OrthoBiologics)	Collagen I and β-tricalcium phosphate	Bone void filler
CopiOs® (Zimmer)	Collagen I and calcium phosphate	Bone void filler
Biostite® (Vebas)	Collagen I/chondroitin-6-sulfate and hydroxyapatite	Filling of periodontal defects, pre-prosthetic osseous reconstruction, maxillo-facial reconstructive surgery
Bio-Oss Collagen® (Geistlich Biomaterials)	Porcine collagen and hydroxyapatite granules	Filling of periodontal defects, alveolar ridge
TricOs T® (Baxter)	Fibrin and hydroxyapatite/β-tricalcium phosphate granules	Bone void filler
RegenOss® (JRI Orthopaedics)	Collagen I fibres and Mg-enriched hydroxyapatite nano-crystals	Long bone fractures, revision hip arthroplasty to fill acetabular defects and spinal fusion
NanOss® Bioactive 3D (Pioneer surgical)	Collagen and nano hydroxyapatite granules	Bone void filler
Vitoss™ (Orthovita)	Collagen I and β-tricalcium phosphate	Spinal and trauma surgery
Healos® (DePuy Orthopaedics)	Matrix of cross-linked collagen fibres coated with hydroxyapatite	Spinal surgery

Even though products such as Healos and Vitoss have shown radiological and clinical results comparable to autografts, there are still some issues to be resolved such as the use of collagen and insufficient mechanical properties for high load-bearing applications [5, 14, 82, 84]. The reason for low mechanical properties of all commercially available composite scaffolds is considered to be a weak bonding between the inorganic and the organic phases leading to insufficient mechanical integrity of the implant limiting them to low load-bearing applications, which will be further discussed in Section 2.6.2.

This chapter will further focus on combination of ceramic and polymer materials to fabricate composite scaffolds intended for bone tissue regeneration, with a closer look of alternative options for ceramic (bioglasses and glass-ceramics) and polymer (including natural polymer chitosan) parts to be used.

2.4 Bioglass 4S5S5 and apatite-wollastonite glass-ceramic as a ceramic part of the composite scaffold

2.4.1 Structure and bioactivity of bioglasses and glass-ceramics

Ceramics, glass-ceramics and bioglasses are of interest for tissue engineering applications on their own but also as a way to improve polymer properties (in particular bioactivity and mechanical strength) via the formation of composites which would suit biomedical applications. The first bioglass (45S5 Bioglass, BG, with the composition: 45.0 SiO_2, 24.5 CaO, 24.5 Na_2O, and 6.0 P_2O_5 in wt%) was discovered by Larry Hench in 1969, and it was the first material which formed a good bond with bone [4]. 45S5 Bioglass has shown excellent biocompatibility and bioactivity *in vivo,* as a layer of hydroxyapatite is formed on its surface [4]. 45S5 Bioglass also stimulates new bone formation with superior osteoinductive properties compared to hydroxyapatite and promotes angiogenesis (formation of blood vessels) [25, 85, 86]. Dense 45S5 Bioglass is reported to have a compressive strength of 500 MPa, tensile strength 42 MPa, Young's modulus 35 GPa and fracture toughness of 0.7-1.1 MPa $m^{1/2}$ [30].

Glasses are defined as non-crystalline (amorphous) solids that exhibit a glass transition upon heating [87]. In silicate glasses, the silicate network consists of SiO_4 tetrahedra which are connected via an oxygen atom (bridging oxygen) on the corners, forming Si-O-Si bonds [87]. The order and linking of the tetrahedra differs in silicate glasses compared to silicate ceramics

18

(Figure 2.3). While the tetrahedra in crystalline ceramics form an ordered structure, the silicate network within the glass is chaotic and has only short-range periodicity.
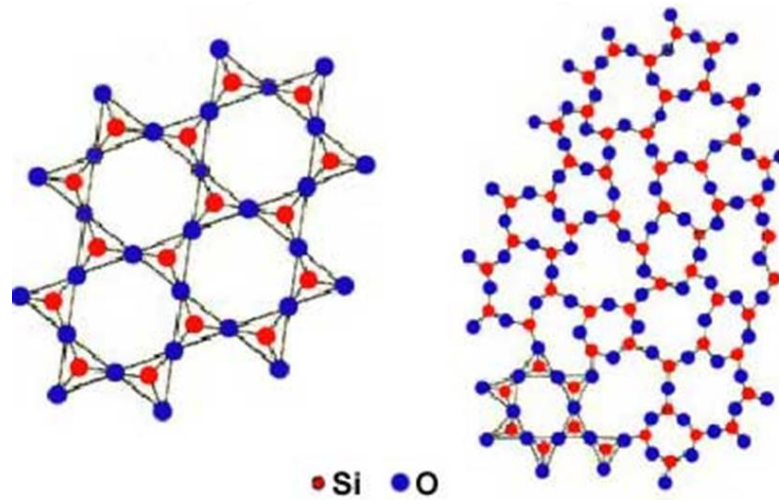
Figure 2.3: Structure of crystalline (left) and amorphous silicate (right) [88]

Addition of ions, such as sodium and calcium in form of their oxides, disrupt the Si-O-Si bonds [87]. Oxygen atoms take the place at the corner of the tetrahedra (non-bridging oxygen), while the cations occupy the interstices (empty space of the network) (Figure 2.4). The cations that modify the silica network are called network modifiers, for example ions such as Na^+, K^+, Ca^{2+}, Ba^{2+}. Cations such as Si^{4+}, B^{3+} and P^{3+}, are called network formers. Intermediate cations, such as Al^{3+}, Mg^{2+} and Zn^{2+}, can help the formation of glass network but also disrupt it as modifiers, and they cannot form the glass network on their own. Therefore, glasses with high content of network modifiers have highly disrupted network with more mobile structural units, which further affects properties such as viscosity, melting point and solubility. On the other hand, ions such as Al^{3+} can take the place of Si^{4+} and increase connectivity of the network.
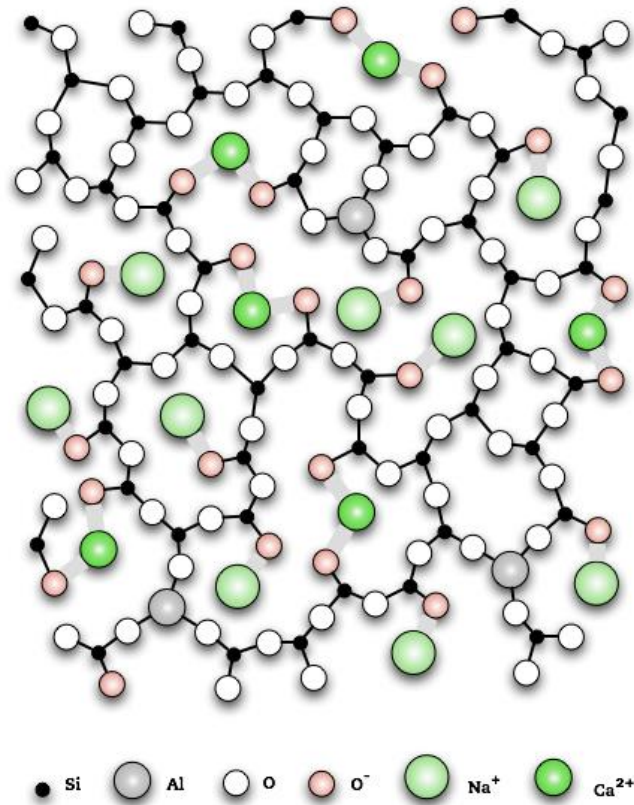
Figure 2.4: Silicate glass structure [89]

In the laboratory glasses can be mainly synthesised by two methods: melt-quenching and sol-gel [4, 87]. Melt-quenching includes mixing and melting the reagents at high temperatures (above 1300 °C) and quenching of the glass mixture in water (obtaining frits) or in metal moulds (obtaining glass monoliths). Sol-gel process involves a precursor, typically thetraethyl orthosilicate (Si(OC$_2$H$_5$), TEOS), which forms a gel at room temperature through hydrolysis (formation of Si-OH) and condensation (to obtain Si-O-Si bonds). The gel comprised of Si-O-Si bonds is further dried at around 600 °C to make a glass. It should be noted that melt-quenched glasses are dense, while sol-gel glasses are porous and have a higher surface area [69]. Furthermore, sol-gel glasses also have a high amount of remaining Si-OH groups in their structure which reduce connectivity [87]. All of these make sol-gel glasses more soluble and bioactive. Therefore, they do not require a high amount of modifiers and can have a high content of silica, up to 90 mol%, and still exhibit bioactivity, while melt-quenched glasses are limited to 60 mol% [4, 87]. However, the disadvantage of sol-gel process is that cracking of the glass occurs due to evaporation of by-products during condensation step and/or shrinkage during drying, making it difficult to obtain glass monoliths [4].

Formation of HCA layer on the bioglass surface *in vivo* or *in vitro* in SBF proceeds in five steps (Figure 2.5) [4, 90-92]:

i. Ion exchange between cations present in the bioglass and H^+ from solution and formation of silanol groups (Si-OH); the pH increases (due to H^+ consumption)

ii. Breaking of Si-O-Si bonds by OH^- and formation of soluble $Si(OH)_4$ (silicic acid) and Si-OH on the surface

iii. Condensation of Si-OH on the surface and formation of a silica gel layer

iv. Migration of Ca^{2+} and PO_4^{2-} from both the glass network through silica layer and from the SBF solution and formation of amorphous calcium phosphate, ACP, layer on the silica layer

v. Incorporation of OH^- and CO_3^{2-} in ACP layer and crystallization to form HCA

The reason that HCA layer forms on bioglasses, and not on regular glasses used for windows and bottles, which have >70 % silica content, is lower content of silica, high CaO/P_2O_5 ratio and high content of Na_2O and CaO (glass modifiers) [90]. There is a relation between connectivity within the silica network and bioactivity. In case of melt-derived bioglasses, low content of silica and addition of network modifiers, such as sodium ions, decrease connectivity and enable dissolution, increasing bioactivity. On the other hand, ions such as Al^{3+} and Ti^{4+} can reduce dissolution and decrease bioactivity. As aforementioned, sol-gel derived bioglasses with high content of silica can be bioactive due to porosity and Si-OH groups which decrease connectivity and increase dissolution and ion release [87].

21
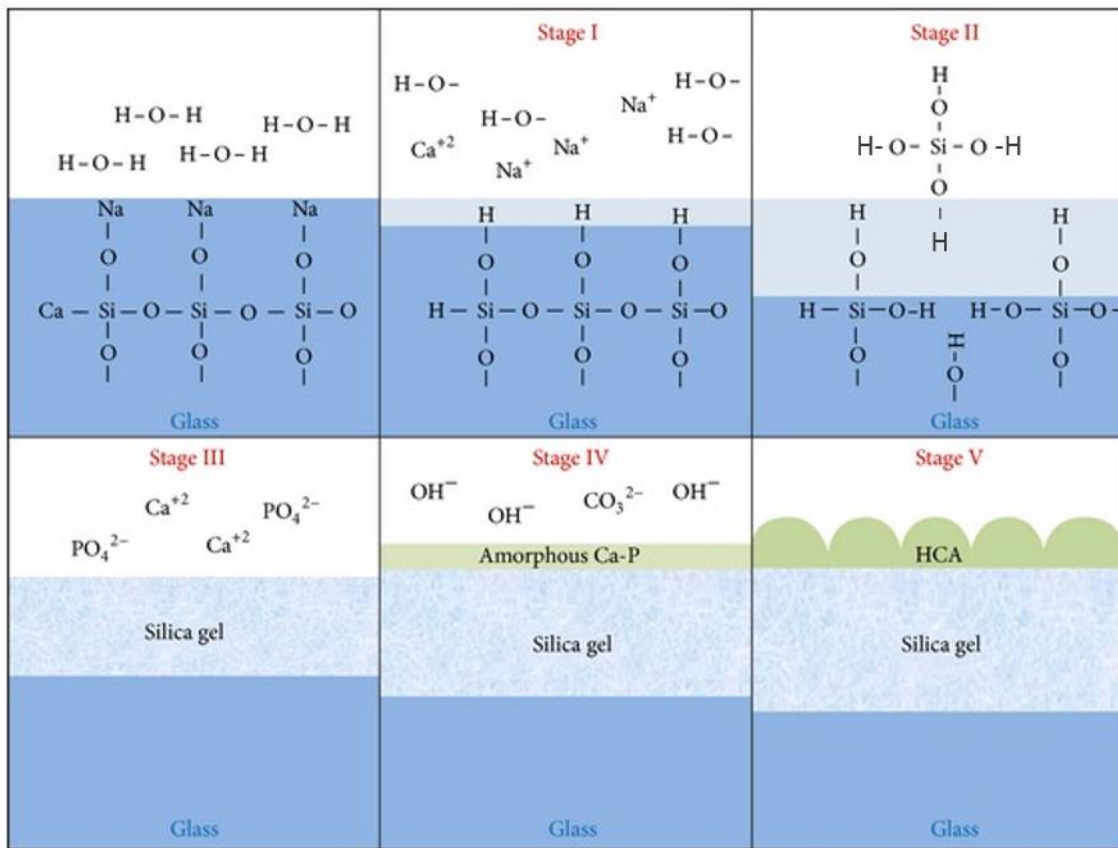
Figure 2.5: Formation of hydroxycarbonate apatite (HCA) layer on the surface of bioglass [93]

In vivo formation of HCA on the surface of bioglass is followed by adsorption of growth factors, and attachment, proliferation and differentiation of osteoprogenitor cells, which form osteoblasts (Figure 2.6) [90, 92]. Osteoblasts (bone-forming cells) secrete the collagenous extracellular matrix (ECM) and control the mineralisation of the organic matrix to form a bone [92]. Bioglass continues to degrade, while the bone tissue grows. It is believed that silicon is released during degradation in the form of silicic acid, $Si(OH)_4$, and excreted out through urine [90].

Bioactive Glass Surface Reaction
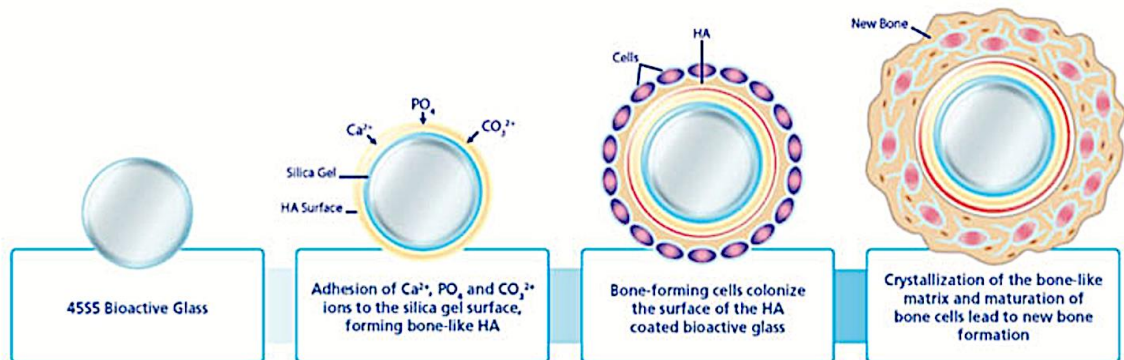
Figure 2.6: Formation of HA layer on the surface of Bioglass 45S5, adhesion of bone-forming cells and mineralisation of collagenous matrix [94]

45S5 Bioglass was then followed by the development of other bioglass and bioglass-ceramic materials, such as 13-93 and apatite-wollastonite (A-W) glass-ceramic (Table 2.3) [4]. All bioglasses and bioglass-ceramics shown in Table 2.3 form a bond with bone, but the length of the bonding process, strength and thickness of the formed bond, as well as the mechanism of bond formation vary among different compositions, which in turn defines their application [95]. By modifying the composition, bioglasses can be designed to degrade at a controlled rate that matches the development of new bone tissue, without any toxic effects [29]. According to M. Pilia et al. [96] commonly used bulk bioglasses have compressive strength of 800-1200 MPa, Young's modulus of 40-140 GPa and fracture toughness of around 2 MPa m$^{1/2}$. Furthermore, because many bioglasses have proven to have considerable antibacterial properties caused by cation leaching and a consequent rise in pH, they are particularly useful in clinical applications [4, 97-101]. For example, 45S5 Bioglass has been shown to kill *Enterococcus Faecalis* which is associated with failed root canal treatment while S53P4 has been shown to kill pathogens associated with enamel caries, root caries and periodontitis [4, 97-101].

Apatite- wollastonite (AW) glass-ceramic developed by Kokubo et al. in 1982 (4.6 MgO, 44.7 CaO, 34.0 SiO$_2$, 16.2 P$_2$O$_5$, 0.5 CaF$_2$ in wt%) is composed of apatite (Ca$_{10}$(PO$_4$)$_6$(O,F$_2$)) and wollastonite (CaSiO$_3$) crystalline phases in a glass matrix (MgO-CaO-SiO$_2$) [102-106]. It is

23

reported that the wollastonite phase makes the AW materials mechanically stronger than other glasses and bioglass-ceramics, including Bioglass 45S5 [107, 108]. Formation of an apatite layer on the surface of AW glass-ceramic, as well as subsequent attachment of cells and bone growth, occur similarly as for bioglasses, described previously [109]. *In vivo* studies showed that AW implants had a good integration with the bone, with bending and compressive strength of 157 MPa and 1 GPa, respectively [105]. One of the most successful bioglass-ceramic implants is Cerabone® (AW), with 50 000 successful bone implants by 2009 [105]. Cerabone® is reported to have tensile strength of 215 MPa, Young's modulus of 120 GPa and toughness of 2 MPa m$^{1/2}$ [105, 110]. One of the issues with AW is lack of biodegradability [105].

2.4.2 Bioglass and glass-ceramic scaffolds

Bioactive glass and glass-ceramic scaffolds can be created by different methods, such as powder sintering, sol-gel process and 3D printing [4]. During the sintering of the particles, templates such as porogens, foaming agents or polyurethane foams are removed leaving a porous structure. Sintering or densification is a process of bonding the particles upon heating and it is driven by the tendency to lower the surface area. The sintering process involves three stages (Figure 2.7) [111]. The first stage starts with formation of 'necks' between the particles. In the intermediate stage, the pore volume decreases while the pores stay interconnected. In this intermediate step, most significant densification occurs. In the final stage the pores become isolated, grains grow and the pores close. Consequently, during sintering, the particles coalesce, the porosity is reduced and the material shrinks.

Loose Powder   Initial Stage   Intermediate Stage   Final Stage
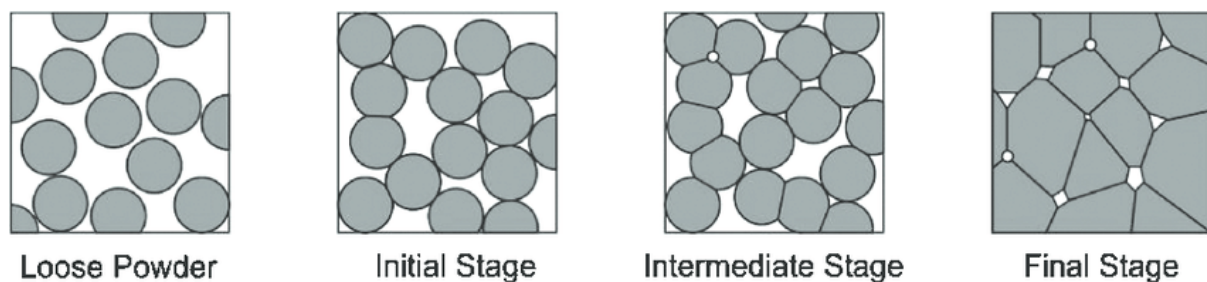
Figure 2.7: Sintering stages [112]

It should be noted that if the sintering temperature is increased above the crystallization point of the glass, the crystallization will occur. Crystallization decreases

solubility and therefore bioactivity, while partial crystallization can compromise the mechanical properties as amorphous parts are preferentially dissolved according to Jones [4]. However, it was also reported that crystallization of scaffolds improves the mechanical properties [113].

Bioactive glass and glass-ceramic scaffolds have a number of excellent properties such as biocompatibility, bioactivity, degradability over time, and interconnected porosity suitable for bone ingrowth [4, 114, 115]. They can also be produced to have similar compressive strength to that of cancellous bone. For example, scaffolds made from 13-93 bioglass have been reported to have a compressive strength of 11 MPa, and an elastic modulus of 3 GPa (85 % porosity with pore size of 100-500 μm) [30]. Generally, the literature shows that the compressive strength for bioglass scaffolds is in the range of 0.2-150 MPa (porosity 30-95 %) and fracture toughness is 0.5-1 MPa m$^{1/2}$ which is low for load-bearing applications [116]. However, these scaffolds are not appropriate for applications that require flexibility or fatigue resistance as they are brittle [4]. Nevertheless, since bioglass has higher mechanical strength than polymers, it has been used in combination with other materials where it serves as reinforcement, improving the properties of polymers [29]. Additionally, according to Jones [4] as well as Tajbakhsh and Hajiali [117], bioglasses can slow down the degradation of some polymers by releasing alkaline ions that reduce the acidic pH produced by polymer degradation thereby acting as a buffer. The degradation rate is dependent on the percentage of bioglass in the composite [4, 117]. Likewise, polymer coatings on BG scaffolds were reported to reduce scaffolds degradation in SBF, maintaining the mechanical properties over time [118]. It has been suggested that the strong, covalent bond between the polymer and bioglass produces simultaneous degradation of both phases of the composite maintaining mechanical integrity of the composite over time (further discussed in Section 2.6.2). However, it should be mentioned that other studies show that bioglass also increases swelling and degradation by making the composite more hydrophilic [4].

Table 2.3: Examples of commercially available bioglass and bioglass-ceramic compositions [95, 119, 120] (composition is given as wt%)

Name	45S5 Bioglass® (NovaBone)	45S5.4F Bioglass®	45B15S5 Bioglass®	52S4.6 Bioglass®	55S4.3 Bioglass®	KGC (Ceravital®)	KGS (Ceravital®)	KGy213 (Ceravital®)	S53P4 (AdminDent1®) (BonAlive®)	A-W Glass-ceramic (Cerabone®)	Ilmaplant-L1® (Biovision GmbH)	Bioverit® (Vitron Spezialwerkstoffe GmbH)	13-93 glass®
SiO_2	45	45	30	52	55	46.2	46	38	53	34	44.3	19-54	54.6
P_2O_5	6	6	6	6	6	/	/	/	4	16.2	11.2	2-10	1.7
CaO	24.5	14.7	24.5	21	19.5	20.2	33	31	20	44.7	31.9	10-34	22.1
$Ca(PO_3)_2$	/	/	/	/	/	25.5	16	13.5	/	/	/	/	/
CAF_2	/	9.8	/	/	/	/	/	/	/	0.5	5	3-23	/
MgO	/	/	/	/	/	2.9	/	/	/	4.6	2.8	2-21	7.7
MgF_2	/	/	/	/	/	/	/	/	/	/	/	/	/
Na_2O	24.5	24.5	24.5	21	19.5	4.8	5	4	23	/	4.6	3-8	6
K_2O	/	/	/	/	/	0.4	/	/	/	/	0.2	/	7.9
Al_2O_3	/	/	/	/	/	/	/	7	/	/	/	8-15	/
B_2O_3	/	/	15	/	/	/	/	/	/	/	/	/	/
Ta_2O_5/TiO_2	/	/	/	/	/	/	/	6.5	/	/	/	/	/
Type	Glass	Glass	Glass	Glass	Glass	Glass-ceramic	Glass-ceramic	Glass-ceramic	Glass	Glass-ceramic	Glass-ceramic	Glass-ceramic	Glass
Application	Middle-ear reconstruction, jaw defects filler	Maxillofacial reconstruction	Middle-ear reconstruction, dental implants	Percutaneous access devices, junction of spinal vertebrae	Dentistry	Middle-ear reconstruction	Middle-ear reconstruction	Middle-ear reconstruction, dental implants	Bony voids and gaps; bone cavity filling, cranio-maxillofacial	Vertebral prosthesis devices	Maxillofacial implants	Orthopaedic surgery (spacers), head and neck surgery (middle-ear implants), stomatology (tooth root and veneer laminates)	Approved for in vivo use (e.g. maxillary alveolar defects)

2.5 Chitosan hydrogel cross-linked with genipin as a polymer part of the composite scaffold

Natural polymers are of interest for tissue engineering as they have superior properties to synthetic polymers, such as enhanced biocompatibility, as their degradation is controlled by enzymes, and ability to stimulate cells [121]. A study showed that BG 45S5 scaffolds coated with natural polymers exhibited higher compressive strength and enhanced bioactivity in comparison to the scaffolds coated with synthetic polymers, while chitosan outperformed other natural polymers in this study in terms of compressive strength and bioactivity [118]. The compressive strength around 13 MPa was reported for chitosan-coated BG 45S5 scaffolds, compared to 2.5 MPa for uncoated BG scaffold. Chitosan possesses a wide range of characteristics, such as non-toxicity, biocompatibility and biodegradability as well as having antibacterial properties while avoiding the problems linked to using collagen [29, 122]. As seen in the Section 2.3.2, collagen is used in most of the commercially available polymer/ceramic scaffolds for bone tissue regeneration but it shows a problem of pathogen transmission as it is derived from natural sources, and possible allergic reactions [5, 14, 123].

2.5.1 Chitosan-structure and properties

Chitosan is a natural linear polysaccharide containing amino and hydroxyl groups (Figure 2.8) [122]. It is derived from chitin (Figure 2.8) by deacetylation, whereas the process is never complete [122, 124]. Chitin, the second most abundant natural polysaccharide after cellulose, can be found in the exoskeleton of insects, shrimps, crabs, lobsters and fungi cell walls [122]. As chitin is a waste material in food industry, production of chitosan is economically achievable and environmentally beneficial [124]. Figure 2.9 shows the process of deacetylation of chitin and production of chitosan [124].
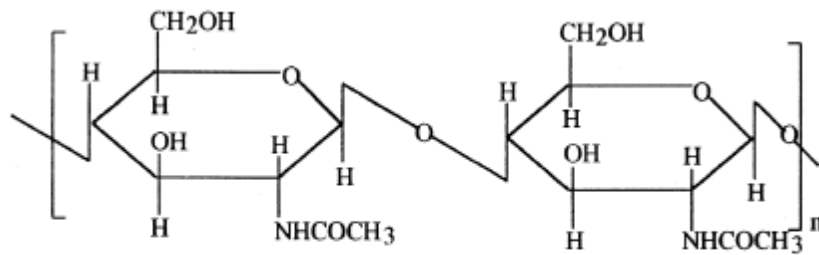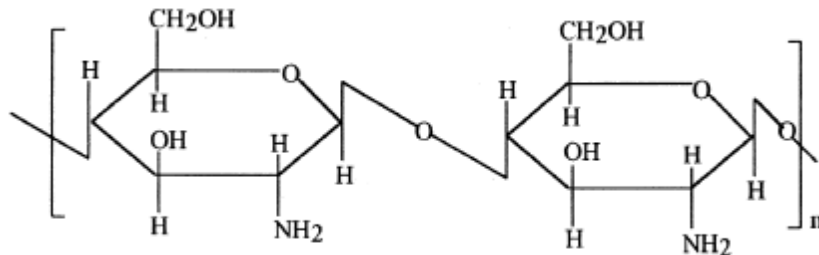
Figure 2.8: Structure of chitin and chitosan [125]
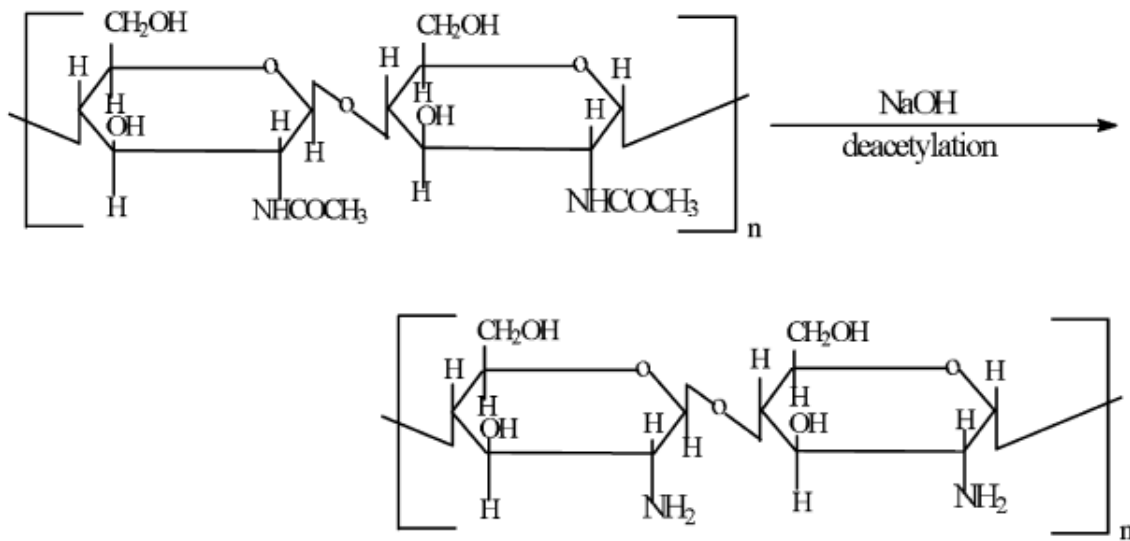
Figure 2.9: Deacetylation of chitin to form chitosan [125]

Chitosan shows a smart behaviour because it shifts from an insoluble to a soluble form depending on pH of the solvent, while the exact pH depends on the level of deacetylation (Figure 2.10) [126-128]. At low pH amino groups get protonated and repulsion between

28

positively charged chains cause solubility and swelling [126, 127]. This property of chitosan can be used in drug delivery applications where drug can be released during swelling due to low pH inside the stomach [126]. On the other hand, at high pH amino groups are deprotonated and chitosan becomes insoluble [126]. Furthermore, its properties are dependent on the level of deacetylation and molecular weight which in turn govern its application [126]. Thus, higher degree of deacetylation makes chitosan more soluble due to the presence of NH_2 group that can shift to NH_3^+ while chitosan with lower degree of deacetylation is more biocompatible [126]. Nevertheless, it should be noted that chitosan can be unsuitable as blood-contacting material as it can cause thrombosis, aggregation of red blood cells and haemolysis [129].
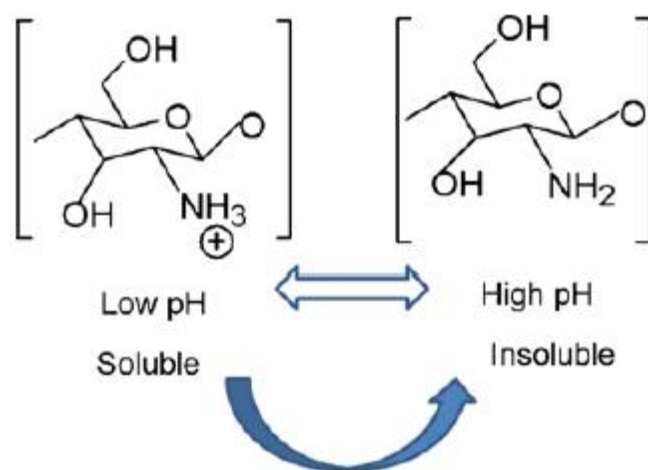
Figure 2.10: Solubility of chitosan [128]

Chitosan is biocompatible with almost all tissues in the body [129]. It can be degraded by enzymes and has a similar structure to that of glycosaminoglycans (GAG), which is a component of extracellular matrix (ECM) that is important for cell adhesion [29, 129]. During degradation, chitosan produces a substance with anti-bacterial properties (chito-oligosaccharides) and the monomeric products (amino sugars) can be metabolized or excreted from the body [129, 130]. Chitosan has also shown osteoconductive ability, as well as the ability to induce neovascularisation but it shows very little osteoinductivity [122, 129].

2.5.2 Chitosan hydrogels

Chitosan can be easily produced in many different forms: films, fibres, scaffolds, beads, particles, gels and solutions [25, 122]. Hydrogels are 3D polymer networks which have affinity for water absorption due to the presence of hydrophilic groups. When in aqueous environment, water infiltrate the hydrogel network and causes swelling, while bonds present in the network stop its dissolution [131-133]. Hydrogels can be composed of natural or synthetic polymeric network [133]. Hydrogels are of an interest in medical application because of their good properties, such as resemblance with human tissue and extracellular matrix. Therefore, they can be applied for tissue repair, as well as drug delivery vehicles [131, 133]. Chitosan hydrogels can be formed with or without the presence of additives. Chitosan NH_3^+ groups can be neutralized using a base, which hinders the repulsion between chitosan chains. It should be noted that additives are added to neutralize the charge but do not participate in the formation of the hydrogel network. Here, hydrogen bonds, hydrophobic interaction and crystalline regions entangle the polymer chains which leads to the formation of the hydrogel (Figure 2.11) [131].

-H bonds
-Hydrophobic interactions
-Crystalline regions
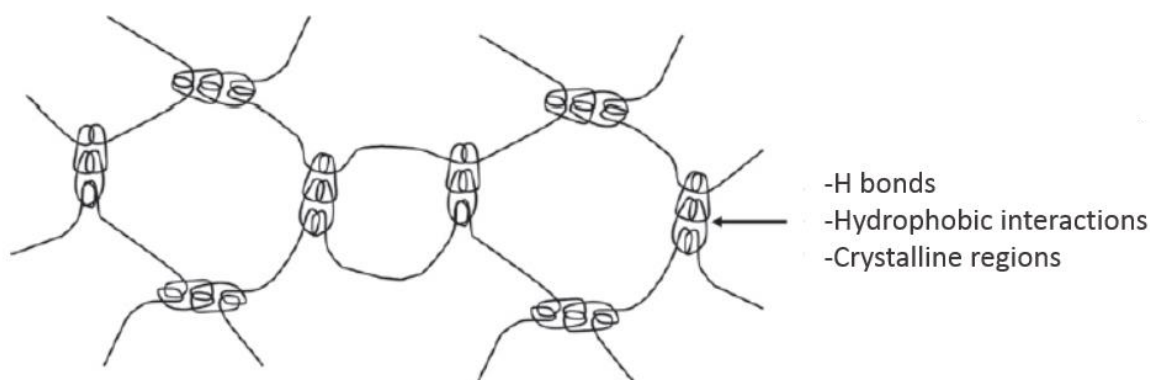
Figure 2.11: Formation of chitosan hydrogel not containing additives [134]

Chitosan hydrogels can form with a presence of additives, when polymer chains are bound via non-covalent, coordination complex and covalent cross-linking (Figure 2.12) [131, 133, 134]. Figure 2.12 a shows that anions, polyanions or anionic polysaccharides form electrostatic bonds with chitosan NH_3^+ groups. In addition to electrostatic bonds, hydrogen bonding, hydrophobic interactions and crystalline regions can occur, although they are weaker than the electrostatic interactions [131]. The addition of another polymer, for example

polyvinyl alcohol (PVA), can form crystalline regions between the chains, which serve as cross-links (similarly as in Figure 2.11) [131, 134]. Another group of non-covalently bound hydrogels are thermosensitive hydrogels, which form a gel from a solution at elevated temperatures caused by hydrophilic-hydrophobic transformation [131, 135]. For example, glycerol phosphate disodium salt (GP) neutralises NH_3^+ groups of chitosan, which hinders repulsion and leads to hydrogen bonds and hydrophobic interactions between chitosan chains at higher temperatures (37 °C). At lower temperatures, hydrogen bonding between polymer and water molecules will lead to hydrophilic interactions and the mixture will stay in a solution. Non-covalently bound hydrogels have the advantage of being clinically safe as no toxic cross-linkers are used [131, 132]. On the other hand, the biggest disadvantages that limits their application are difficulties to control degradation rate and pore sizes, and low mechanical strength [131, 134]. Covalently cross-linked hydrogels can be obtained by using small molecules which form covalent bonds with chitosan (Figure 2.12 c) [131, 134]. Both amino and hydroxyl groups of chitosan can be cross-linked. Covalently cross-linked hydrogels are more stable and the process is irreversible. In conclusion, non-covalent cross-linking methods have the advantage of non-toxicity but the structure of the hydrogel cannot be well controlled, while covalently bounded hydrogels have better mechanical properties; however, cross-linking agents are often toxic.

Non-covalent cross-linking (a)	Coordination complex cross-linking (b)	Covalent cross-linking (c)
Via electrostatic interactions with anions (as phosphates, sulfates and citrates) or polyanions (as proteins (gelatin and collagen…) and anionic polysaccharides (hyaluronic acid…)). Also via H bonds, hydrophobic interactions and crystallization	Via coordination bonds with metal ions (as Pd(II), Pt (II) and Mo(VI)).	Via amide or ester bonds formation (with glyoxal, glutaraldehyde and Genipin…).

Figure 2.12: Formation of chitosan hydrogel with additives through: a) non-covalent, b) coordination complex and c) covalent cross-linking [134]

Factors that can affect properties of hydrogels are molecular weight, degree of crosslinking, and charges within the polymer (cationic or anionic groups). Higher the molecular weight, the more cross-links are formed and thus the stiffness, as well as moduli, are also higher [131]. Also, when exposed to different environmental conditions, such as pH and temperature, they exhibit swelling and de-swelling behaviour [126, 127, 133].

2.5.2.1 Genipin as a cross-linker

While there are a number of cross-linkers used for chitosan hydrogel preparation that react with chitosan's amino groups (glutaraldehyde, formaldehyde, genipin, glyoxal, etc), these agents induce an increase in toxicity. Genipin is a natural compound that is derived from Gardenia jasminoides fruits (Figure 2.13) [136-138]. The advantage of genipin over the other commonly used cross-linkers is significantly lower toxicity (10 000 times less than glutaraldehyde), being nontoxic at concentrations below 0.5 µM. Genipin-cross-linked

materials maintain the same degradation rate and mechanical properties as glutaraldexyde cross-linked materials and, as an added bonus, have an anti-inflammatory effect [127, 131, 138, 139]. Exposure to genipin led to a 5 000 times higher cell proliferation rate compared to glutaraldehyde. Currently, the significant drawback of using genipin is the high cost [137].
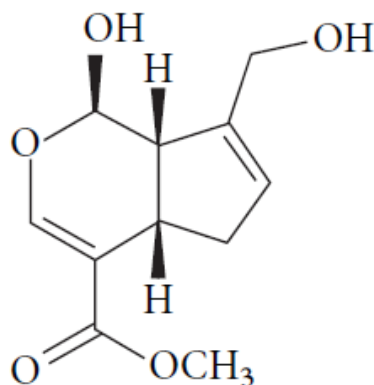
Figure 2.13: Genipin structure

2.5.2.2 Cross-linking of chitosan and genipin

The reaction of genipin with chitosan, producing fluorescent blue-coloured gels, is shown in Figure 2.14 [126, 127, 136, 140, 141]. Genipin can self-polymerise, especially in a higher pH environment, and form oligomers containing up to 88 genipin molecules between chitosan chains (Figure 2.15) [142]. The blue colour is attributed to reaction of genipin with chitosan's amino groups and self-cross-linking between genipin molecules [143-145]. The cross-linked hydrogels have different intensities of blue, depending on the degree of cross-linking [126]. It has been reported that deeper blue colour relates to a mechanically stronger hydrogel [146].

Systems with alternative single and double bonds, called conjugated double bonds, are highly fluorescent [147]. Additionally, a lone pair electrons (non-bonding electrons) can be a part of the system. Red fluorescence emission of the chitosan-genipin hydrogels is attributed to the conjugation path, made of conjugated double bonds and nitrogen atom lone pair electrons, shown in Figure 2.14 (Scheme A and B, circled in blue) [148].

Even though it does not have conjugated double bonds, chitosan can fluoresce due to the presence of $NHCOO^-$ ion which is formed by the reaction of amine and carbon dioxide

(400 nm excitation-470 nm emission peaks) [149]. Genipin absorbs at 240 nm and it has no fluorescent properties [150]. Genipin cross-linked chitosan gels have an excitation peak at around 590 nm and emission peak at 630 nm [136, 140, 151].
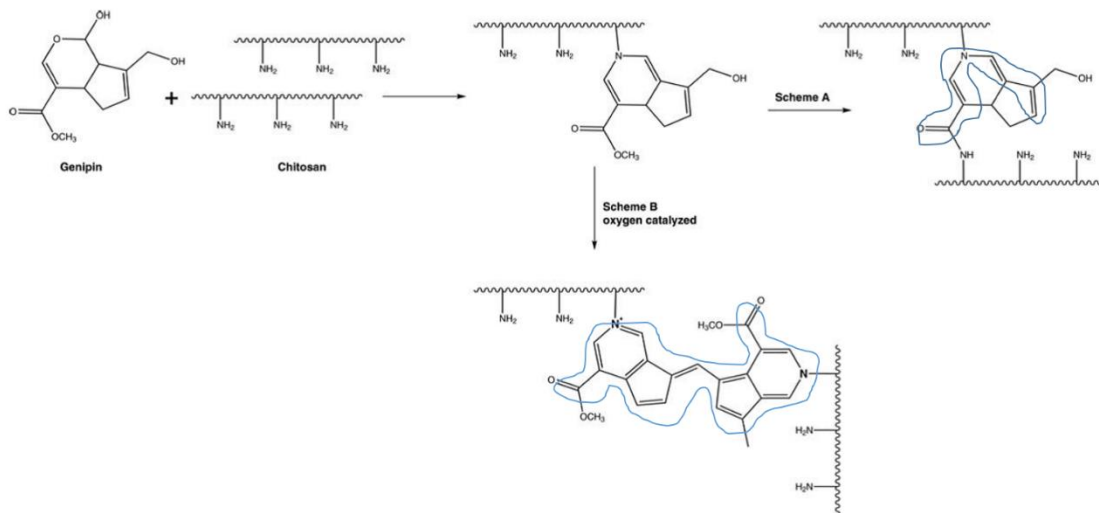
Figure 2.14: Possible genipin/chitosan cross-linking reactions and conjugation path (circled in blue) adapted from [143]
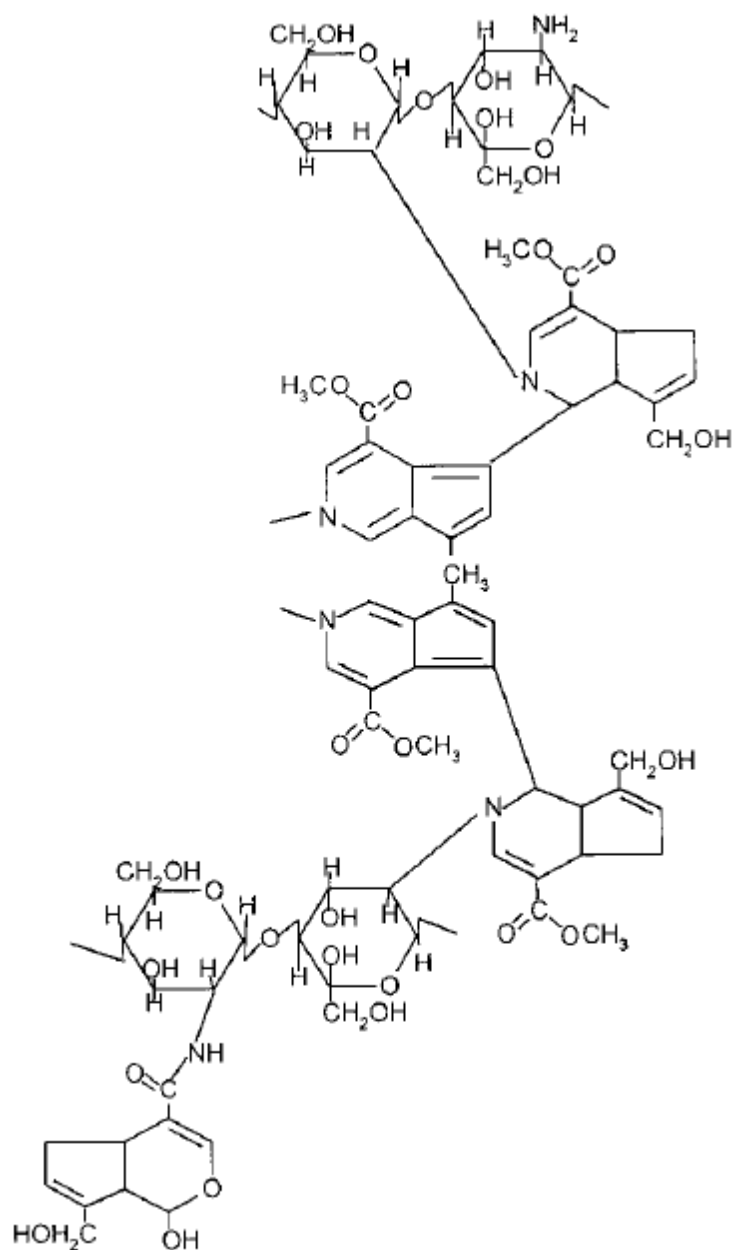
Figure 2.15: Genipin self-polymerization in cross-linked chitosan network [145]

2.5.2.3 Chitosan-genipin hydrogels

As for the effect of genipin concentration to properties of chitosan hydrogels, a study showed that when increasing the amount of genipin from 0.2 % to 0.8 %, hydrogel network changes from being loose and porous, to denser and, finally, compact structure [152]. Pore sizes decreased from being more than 100 μm to around 30 μm, respectively [152]. Similar results were obtained in another study, where chitosan hydrogel with lower concentration of genipin (1.65-3.30 mM) had large interconnected pores, while with higher concentration of

genipin (3.30-5.50 mM), the honey-comb structure with small pores was achieved [138]. Furthermore, it was reported that higher amount of cross-linking leads to mechanically stronger and more fluorescent genipin-cross-linked hydrogels [140].

By varying the reaction conditions, such as temperature or pH, the obtained genipin cross-linked chitosan can express different properties [144]. By increasing the temperature, denser and more cross-linked chitosan networks can be made [153]. Under variable pH conditions, different degrees of cross-linking can be obtained which can influence gel properties such as mechanical properties and the rate of drug release [126, 154, 155]. It was reported that ~ 96 % of the amino groups form cross-linking with genipin at neutral pH (7.4), while only ~ 45 % at pH 9 and ~ 1.4 % at pH 13 due to genipin self-cross-linking at basic pH, which reduces its ability to cross-link with chitosan ultimately decreasing mechanical properties [142]. Additionally, ~ 40 % cross-linking occurred at pH 5, due to protonation of amino groups at acidic pH, which are unable to cross-link with genipin, as only non-protonated amino groups can react. As mentioned previously, it is important to have the capacity to tailor porosity and structure of the material in order to gain desirable properties such as biocompatibility, controlled degradation with a controlled rate and suitable mechanical properties.

2.5.3 Commercially available chitosan materials

Chitosan-based materials have been used in the clinic for wound dressing applications due to its ability to help blood clothing [156]. For example, HemCon® is used as a dressing in dentistry and oral surgery and Axiostat® as a dressing in dental or vascular procedures [157, 158]. Chitohem® in form of chitosan powder is a haemostatic used for oral procedures [158]. Chitosan is also commercially available as a food supplement for digestive health and weight loss [159].

2.6 Polymer/bioglass and polymer/glass-ceramic scaffolds

2.6.1 Types of polymer/bioglass and polymer/glass-ceramic scaffolds

In order to benefit from the advantageous properties of polymers and bioglasses and glass-ceramics, there have been a number of successfully designed polymer/bioglass, and

polymer/glass-ceramic scaffolds. Based on their physical structure (appearance), the composite scaffolds reported so far can be classified in the following groups:

1) **Foam/sponge-like structures (scaffolds)** (Figure 2.16). A variety of methods have been used to develop these scaffolds including freeze-drying, foam replica, phase separation, particle leaching, dip- and slurry-coating and rapid prototyping [160-164]. Also, a large number of different polymers, both synthetic and natural, as well as different compositions of bioglasses and apatite-wollastonite glass ceramic have been used for this type of scaffold in order to obtain different designs [4, 32, 162, 165-178]. In general, scaffolds can be formed in two ways: a) they can consist of a matrix and a coating, where a polymer foam can be coated with a bioglass slurry or a bioglass scaffold can be coated with a polymer solution; or b) they can be formed as a monolith structure from bioglass particles dispersed in polymer solution [29, 161, 163, 164, 179].

500 μm
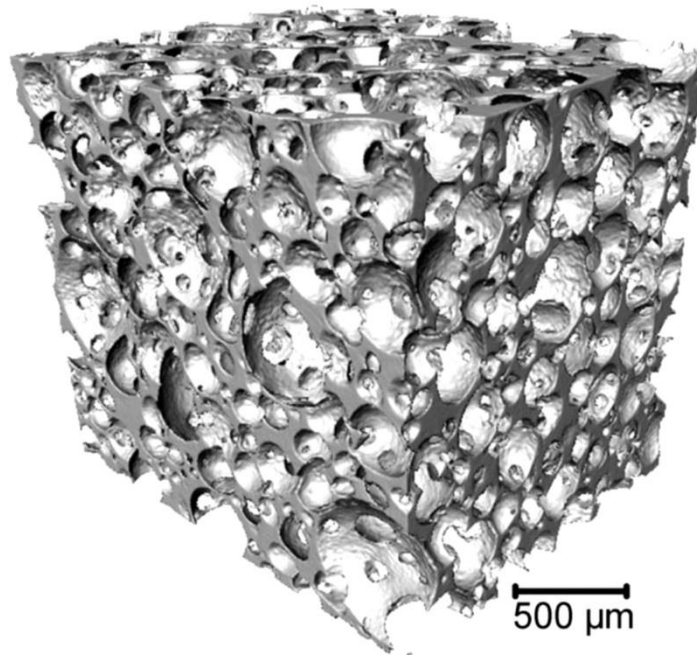
Figure 2.16: Example of a foam-like composite material [180]

2) **Fibre composites** (Figure 2.17). These are most widely synthesised via an electrospinning method, where materials can be mixed together prior to electrospinning or polymer fibres can be immersed in a bioglass slurry to coat the

fibres [68, 69, 181-184]. A high surface area and high porosity make fibre scaffolds attractive for bone tissue applications, although reported mechanical properties are usually low or not stated [68, 183, 185]. Polyhydroxybutyrate (PHB)/poly(ε-caprolactone) (PCL)/58S bioglass (60 SiO_2, 36 CaO, 4 P_2O_5 in mol%) fibre scaffolds designed by Ding et al. exhibited a tensile strength of approximately 2 MPa and Young's modulus in the region of 67-87 MPa [186]. In another study by Foroughi et al, PHB/chitosan/45S5 Bioglass scaffolds showed a tensile strength in the region of 3 MPa and Young's modulus of 0.2 GPa (see Table 2.1 for comparison) [187].
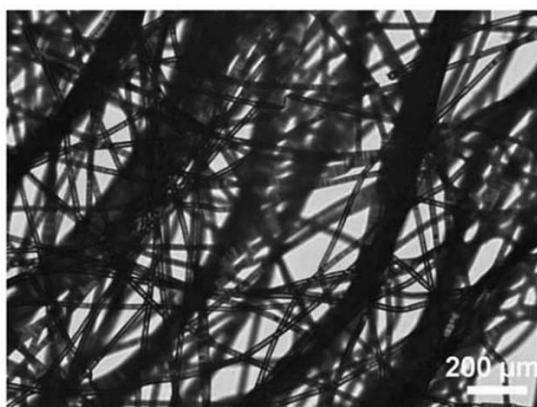
Figure 2.17: Fibre scaffold [183]

3) **Microsphere scaffolds**. Microspheres are mainly composed of polymers, but bioglass or other ceramics can be added to enhance mechanical strength and bioactivity of the materials, and control the degradation of the polymer. Microspheres can be fused together to form a 3D scaffold (Figure 2.18) [188-191]. This can be achieved by heating, using a solvent (e.g. methylene chloride and acetone), which is a milder method compared to heating, or via particle agglomeration techniques. This type of composite scaffold has been used for gene therapy and drug delivery in the antibiotic treatment of infected bone [188, 190]. Prior to fusing, the spheres are loaded with drugs which are released gradually over time. While microspheres offer the ability to encapsulate and release biomolecules and drugs, scaffolds composed of fused microspheres also possess porosity and mechanical support for loading cells, a useful feature for bone regeneration applications. This method of producing scaffolds is reported to give improved mechanical properties similar to cancellous bone [189].
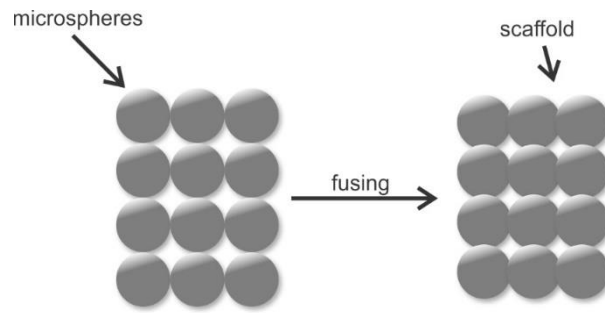
Figure 2.18: Microsphere scaffolds adapted from [189]

4) **Bilayer or multilayer scaffolds.** These scaffolds are designed for osteochondral applications which include both bone and cartilage tissue [13, 192, 193]. They consist of two or more layers; a bone-like layer (calcium phosphate material, polymer coated bioglass scaffold, or bioglass/polymer scaffold) and a cartilage layer (polymer material). The layered structure of the materials follows the natural architecture of a human osteochondral unit, where the bone-like part is used to support bone formation, while the cartilage-like part is used for guiding the formation of cartilage. Some scaffolds have an intermediate layer which serves as a 'glue' between the bioglass and polymer layers, and is usually made from a polymer or a polymer/hydroxyapatite composite (Figure 2.19) [13, 192]. A promising example was developed by Boccaccini et al. in which polyamide short fibres were applied as an external cartilage-like layer, to mimic collagen fibres, on a gelatine coated 45S5 Bioglass scaffold (Figure 2.20) [194].
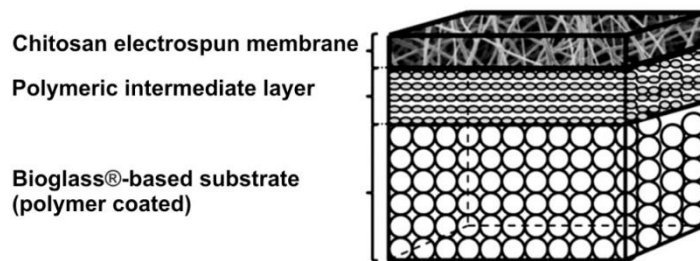
Figure 2.19: Multilayer composite scaffold made of polyvinyl alcohol (PVA) coated bioglass, polymeric (chitosan, alginate, gelatine or sucrose) and chitosan layers [192]. In this case, scaffolds were covered with polymer solution by dipping and the chitosan membrane was fixed manually
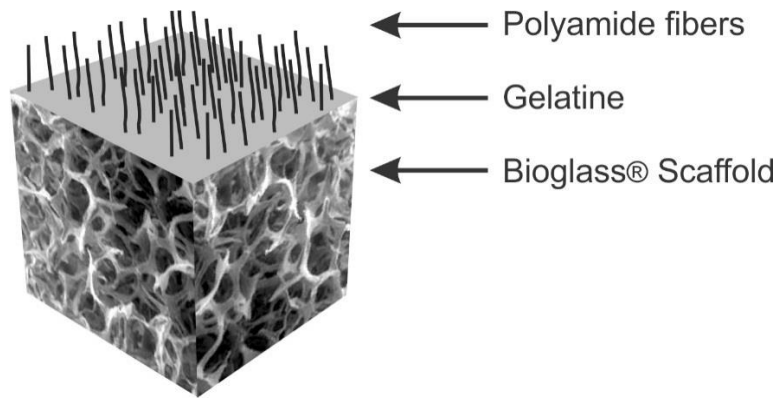
Figure 2.20: Bilayered gelatine coated 45S5 Bioglass scaffold with polyamide short fibres adapted from [194]

5) **Cell-seeded scaffolds**. Here, cells are integrated into the composite scaffolds [52, 195, 196]. The presence of cells in engineered materials is found to improve osteogenesis *in vivo* so these scaffolds can serve as skeletons for cell incorporation and mechanical support [13, 197]. 3D printing or other additive manufacturing methods can be used for scaffold synthesis [195]. Figure 2.21 describes two different approaches for integrating cells into 3D printed materials. In the first approach cells are added to the hydrogel solutions (precursor materials) which are used to print 3D scaffolds. The second approach prints a 3D scaffold and then seeds it with cells [195]. The main issue with the first approach is the difficulty in designing scaffolds with the exact shape and mechanical properties that are required, whereas in the second approach, surface modification is necessary in order for the cells to be attached to the scaffold, which complicates the fabrication process. Cells can also be seeded onto scaffolds fabricated via other routes, such as particulate leaching, thermally induced phase separation (TIPS), and the sponge replica method [52, 64, 196]. Microsphere scaffolds can also be loaded with cells and/or drugs. [191].

While multi-layered scaffolds (group 4) are appropriate for osteochondral regeneration, polymer coated sponge-like bioglass scaffolds (group 1 a) and microsphere scaffolds (group 3) are suggested for use in bone defects as these types of structures give better mechanical properties than fibre scaffolds (group 2) or polymer sponge scaffolds with bioglass particles (group 1 b). Additionally, cell-seeding can improve cell attachment to implanted scaffolds and enhance bone formation.
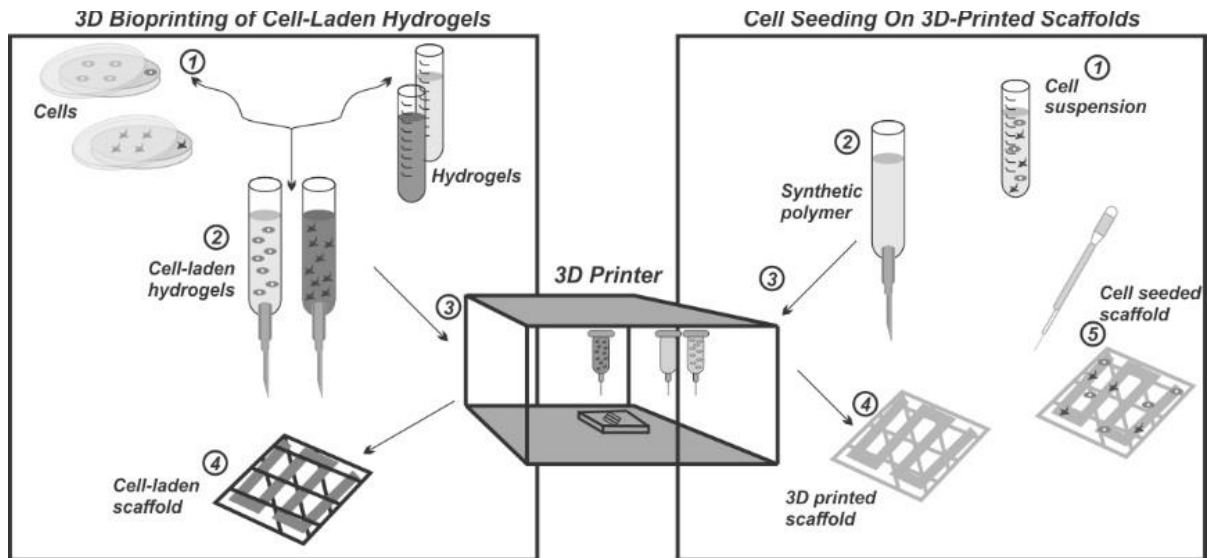
Figure 2.21: Cell-seeded scaffolds adapted from [195]

2.6.2 Development of hybrids with improved bond between the inorganic and organic phases

The lack of high-load bearing applications of the developed polymer/ceramic scaffolds is due to weak bonding between the organic and inorganic phases in the current scaffolds allowing the phases to degrade separately at different rates [4, 5]. This causes insufficient mechanical integrity resulting in inadequate mechanical properties [4]. Ultimately the scaffolds need better interfacial bonding between the polymer and ceramic phases to improve the mechanical properties.

It has been shown that microporosity is needed for good adhesion and linkage between the ceramic and polymer phases, which in turn improves mechanical performance [198]. Good dispersion of the bioglass particles in the polymer matrix is crucial to avoid aggregation and the consequent decrease in strength. Hybrid materials have the potential for a more homogeneous structure as well as the advantage over traditional composites because the constituents are interacting on a molecular level. A hybrid is defined as a composite of an inorganic and an organic material, where properties of the hybrid differ from the individual properties of the two materials because of the interactions between them. Hybrid materials are classed depending on the types of interactions occurring at the interface. *Class I hybrids* have weak bonds such as van der Waals and hydrogen bonds. This can be achieved by sol-gel synthesis, typically by adding the polymer in the sol phase, for example-after hydrolysis of the

precursor TEOS [4, 199]. When covalent bonds between polymer and bioglass are present, the materials are called *Class II hybrids* [4, 200]. These materials have the potential for good bioactivity, improved mechanical properties and controlled and congruent degradation (the composition remains the same during degradation) [4]. For *class II hybrids*, polymer is usually functionalized with a coupling agent prior its addition to the sol phase [4, 201].

Linkage can be achieved by using certain polymers with functional groups or by functionalization of the surface of either the bioglass or polymer before the sol-gel process [4, 202-211]. Silanes (glycidoxypropyltrimethoxysilane (GPTMS) and 3-aminopropyltriethoxysilane (APS)), hexamethylene diisocyanate (HMDI) and polyvinyl alcohol (PVA) are amongst the compounds used for developing *Class I* and *Class II* hybrid materials [202-209]. In a poly (L-lactide) (PLLA)/AW scaffold (with bioglass composition 4.6 MgO, 44.7 CaO, 34.0 SiO_2, 16.2 P_2O_5, 0.5 CaF_2 in wt%), APS was used for functionalisation of the bioglass [206]. APS can bond to both bioglass and polylactide materials due to the presence of silanol groups which react with the bioglass, and amine groups which react with the carboxyl groups of hydrolysed PLLA to form hydrogen bonds. The use of APS to functionalise the bioglass particles improved the bonding between the PLLA and bioglass particles which resulted in better incorporation of the bioglass particles into the PLLA matrix leading to enhanced mechanical properties compared to non-functionalised samples [206]. Improvement of compressive strength was also observed after APS functionalized BG 45S5 scaffolds were coated with collagen [212]. In a different study, gelatine was functionalized with GPTMS and scaffolds with similar compression strength and modulus to cancellous bone were obtained [204]. Another interesting feature of these *Class II hybrid* scaffolds is that the apatite layer forms throughout the scaffold, whereas in pristine bioglass scaffolds (bioglass containing 75 wt% SiO_2 and 25 wt% CaO) it was observed only on the surface [204]. Similarly, carboxylic groups on gelatine can bond to the epoxy group of GPTMS to form a hybrid, where the silanol groups of the GPTMS condense with hydrolysed TEOS, which was used as a precursor [211]. The hybrids exhibited compressive strength up to 60 kPa and Young's modulus up to 1.3 MPa. Hybrid scaffold was composed of polycaprolactone (PCL) and borophosphosilicate glass, where GPTMS was used for functionalization of PCL [210]. Although the hybrid scaffold showed bioactivity *in vitro*, mechanical properties were not reported.

Hexamethylene diisocyanate (HMDI) was used to functionalize PLLA to produce bonded PLLA/bioglass scaffolds (with bioglass composition: 58 CaO, 29 SiO_2, 13 P_2O_5 in wt%) [205]. Even though the Young's moduli of PLLA/bioglass scaffolds with or without HD were similar, higher tensile strength was reported for the scaffold functionalized by diisocyanate [205].

PVA/bioglass hybrid scaffolds (with bioglass composition: 58 SiO_2, 33 CaO, 9 P_2O_5 in wt%) were fabricated by the sol-gel method with the addition of a surfactant followed by ageing and drying [207, 209]. The hydroxyl group of PVA and the hydroxyl group of silanol groups, originating from the hydrolysis of the silicon precursor tetraethyl orthosilicate (TEOS), have been shown to react with each other to form covalent bonds (Figure 2.22) [207]. These PVA/bioglass scaffolds were considered as potential candidates for bone tissue applications, however, so far, no exceptional properties in comparison to other known polymer/bioglass scaffolds have been reported [207, 209].

Tallia et al. have reported a novel hybrid 3D printed scaffold for the applications in cartilage regeneration composed of covalently bonded silica/poly(tetrahydrofuran)/poly(ε-caprolactone) system employing GPTMS to functionalize the organic phase [213]. The hybrid system, which exhibited transparency, flexibility and self-healing properties was used for developing a scaffold. The hybrid scaffold demonstrated compressive strength of 1.2 MPa, which falls in the lower range for human cartilage. Furthermore, the hybrid scaffold stimulates cartilage matrix formation from chondrocytes (cartilage cells) *in vitro*. It was suggested that ingrowth of the new cartilage *in vivo* and improvement of the 3D printing process could enhance the mechanical properties of the hybrid scaffold.
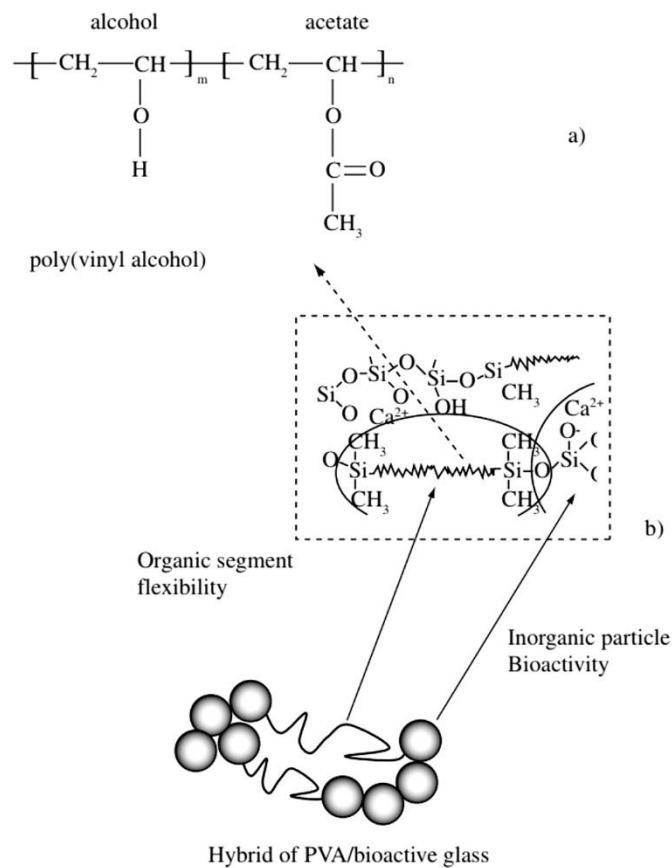
Figure 2.22: a) PVA with a variable hydrolysis degree and b) a hybrid structure [207]

Use of chitosan in hybrid scaffolds has also been reported. Glycidoxypropyltrimethoxysilane (GPTMS) was used for the functionalization of chitosan in order to form covalent bonds with bioglass via sol-gel synthesis with TEOS as a precursor [202]. Compared to chitosan and bioglass composites without GPTMS (*Class I hybrids*), specimens that were covalently bound (*Class II hybrids*) were less brittle. Figure 2.23 shows the functionalization of chitosan with GPTMS and formation of a chitosan/bioglass scaffold through the formation of a glass network, thereby creating the hybrid. GPTMS is used as a cross-linking agent.
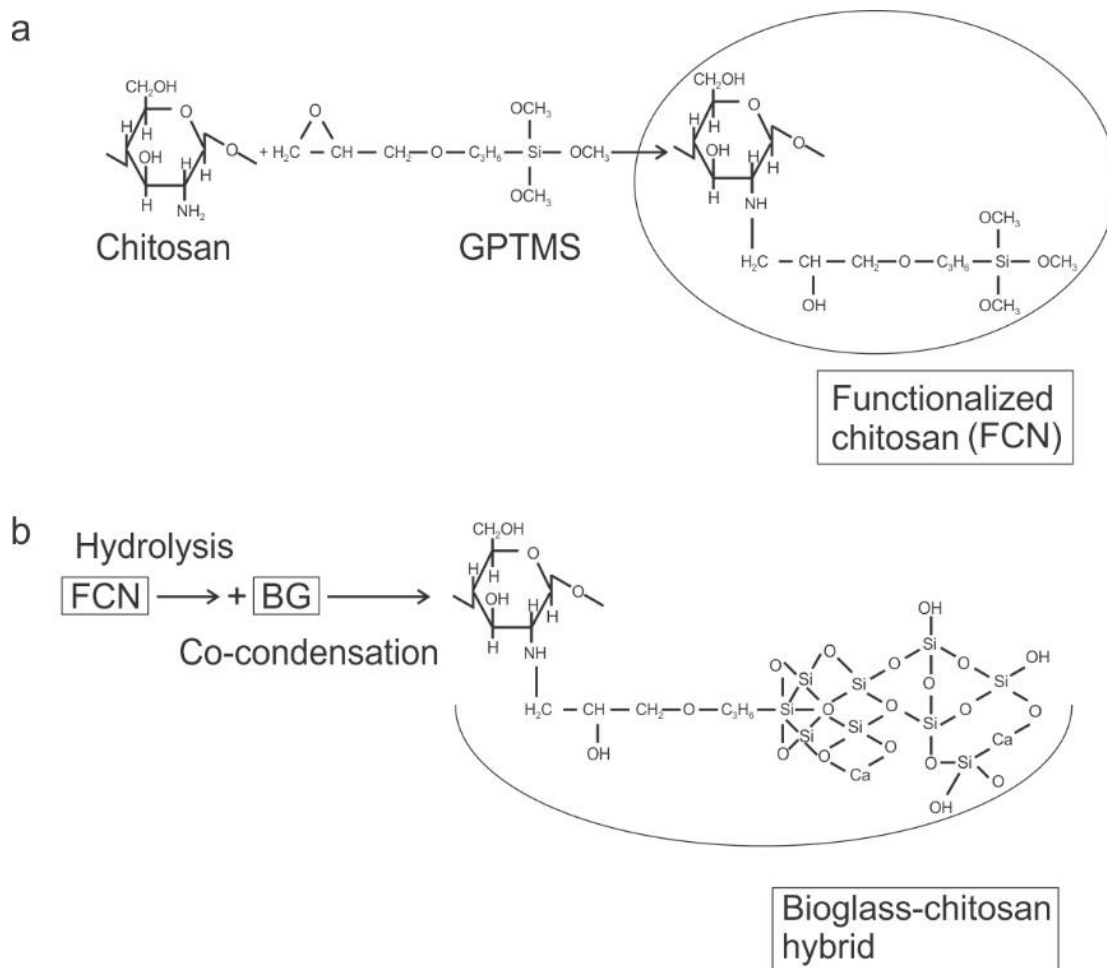
Figure 2.23: a) Functionalization of chitosan with GPTMS and b) formation of chitosan/bioglass hybrid scaffolds adapted from [202]

Another way to form a *Class II hybrid* involving chitosan is using GPTMS while bioglass is not added in this procedure (unlike in the method described in Figure 2.23). The cross-links form by reaction of the epoxy group of GPTMS with the amine group of chitosan. At the same time, the methoxysilane groups undergo hydrolysis to silanol groups which then condense to form a siloxane network [203]. These Si-OH groups bring bioactivity to the polymer.

Literature further describes PVA/chitosan/bioglass 60S (bioglass composition: 60.1 SiO_2, 17.7 Na_2O, 19.6 CaO and 2.6 P_2O_5 in mol%) hybrid scaffolds, fabricated with the addition of glutaraldehyde for cross-linking followed by freeze drying [208]. The untreated scaffolds showed toxicity, but after treatment with phosphate-buffered saline (PBS) cell viability increased. The authors did not clarify whether *Class I* or *Class II* hybrid was developed.

In general, some of the hybrids (APS or HMDI functionalised bioglass/PLLA, GPTMS functionalised chitosan/bioglass, GPTMS functionalised gelatine/bioglass and GPTMS

functionalised silica/poly(tetrahydrofuran)/poly(ε-caprolactone)) showed improved mechanical properties in comparison to composites without functionalisation, but they are still below the high load-bearing region.

2.6.3 Overview of designs of scaffolds made of bioglasses and bioglass-ceramics combined with natural polymers, including chitosan

There has been a number of examples combining bioglasses and glass-ceramics with natural polymers, including chitosan (Cht), for developing scaffolds described in the literature, but the mechanical properties have been reported only in some cases. Table 2.4 summarizes some of the designs found in the literature together with their mechanical properties. Furthermore, in some cases cross-linking agents have been added to the polymers in order to achieve better mechanical stability. It should be noted that only few papers reported the use of genipin (Gen), which has a potential as a natural cross-linking agent, 10 000 less toxic than commonly used glutardexyde (GA). Even though some structures showed enhanced properties after the coating, polymer cross-linking or addition of a cross-linking agent (in case of hybrid scaffolds), the mechanical properties remained low. It could be observed that the mechanical properties reported for different materials vary greatly. The main reasons for this are different methods for the synthesis of composites and diversity of methods for evaluation of mechanical properties. Additionally, while various mechanical requirements need to be fulfilled (Table 2.1), it is often the case that one or two parameters for mechanical properties were measured in order to characterize these materials. Table 2.4 also indicates the main distinctions between the composites from the sources in the literature and this PhD project, where BG and AW in combination with chitosan-genipin hydrogels were used. It should be noted that BG refers only to Bioglass 45S5, while Bg to other compositions of bioglasses. From the Table 2.4 it can be concluded that the best scaffolds for bone tissue engineering is the fiber scaffold made of chitosan fibers coated with the Bg 58S slurry reported by Yang et al. [29] because it not only has best mechanical properties, but it was also tested in both compressive and tensile modes, unlike other reported composite scaffolds. The composite scaffold has only been tested *in vitro*.

According to the Table 2.4, it can be observed that there is a need for standardized mechanical tests in order to be able to directly compare synthesized materials from different

studies. Also, some methods, such as needle punching of polymer fibers, 3D printing of glass-ceramic scaffolds or freeze-drying of polymer mixtures, seem to render better mechanical properties in comparison to other methods, such as sponge replication method or most hybrid compositions. It seems that genipin has not been widely explored in the research as a low-toxicity cross-linker, while the use of AW is also rarely used, even though AW is reported to be stronger than other glasses and glass-ceramics. Therefore, this PhD project combines the properties of BG and AW glass-ceramic scaffolds and chitosan-genipin hydrogels. Two methods for synthesis of inorganic-organic composites are used: 1) addition of BG powder to the chitosan-based hydrogel and 2) chitosan hydrogel coating of the BG and AW scaffolds. While BG and AW scaffolds coated with the hydrogel are expected to have higher mechanical properties, chitosan-genipin hydrogels with BG powder offer the opportunity of injection and *in situ* gelation.

Table 2.4: Mechanical properties of bioglass and bioglass-ceramic/polymer composite scaffolds containing chitosan or other natural polymers (with and without genipin)

Structure	Inorganic	Organic	Coating/mixture/cross-linking agent	Cross-linker for polymer	Compressive strength	Compressive modulus	Tensile strength	Tensile modulus	Distinction	Ref
AW scaffold	AW	Cht	Cht coating	No	3.11 MPa				No cross-linker	[32]
BG scaffold	BG	Gelatine	Gelatine coating	Gen	1.04 MPa				No Cht	[214]
BG scaffold	BG	Separately gelatine and alginate	Polymer coating	Gen for gelatine; $CaCl_2$ for alginate				639 MPa; 734 MPa	No Cht	[215]
BG scaffold	BG	Separately-Cht; gelatine; alginate	Polymer coating	No	13 MPa; 8 MPa; 9 MPa				No cross-linker	[118]
BG scaffold	BG	PCL/Cht	PCL/Cht coating	No	0.2 MPa				No cross-linker	[216]
Bg scaffold	Bg (80 Si, 15 Ca, 5 in mol%)	Cht (modified*)/silk	Polymer coating	No	0.3 MPa				No cross-linker	[217]
Bg scaffold	Bg (80 Si, 15 Ca, 5 in mol%)	Cht (modified**)/zein	Polymer coating	No	0.3 MPa				No cross-linker	[218]
Gelatine scaffold, Bg coating	Bg (75 SiO_2, 25 CaO in wt%)	Gelatine	Bg coating	GA	1 MPa				No Gen	[219]
Bg/Cht/collagen/PVA scaffold	Bg (85 SiO_2, 10 CaO, 5 P_2O_5 in mol%)	Cht/collagen/PVA	Bg particles in polymer mixture	No	11.49 MPa	214 MPa			No cross-linker	[220]
Bg/Cht/gelatine scaffold	Bg 58S	Gelatine/Cht	Bg particles in polymer mixture	GA	2.2 MPa	111 MPa			No Gen	[221]
Bg/Cht/PLGA scaffold	Bg 58S	PLGA/Cht	Bg particles in polymer mixture	GA	2.6 MPa	24 MPa			No Gen	[222]

Structure	Inorganic	Organic	Coating/mixture/cross-linking agent	Cross-linker for polymer	Compressive strength	Compressive modulus	Tensile strength	Tensile modulus	Distinction	Ref
Bg/Cht/gelatine scaffold	Bg (CEL2-45 SiO_2, 3 P_2O_5, 26 CaO, 7 MgO, 15 Na_2O, 4 K_2O in mol%)	Cht/gelatine	Bg particles in polymer mixture	Gen		2.1 MPa			Different Bg;	[171]
Bg/gelllan/xanthan scaffold	Bg (66 Si, 27 Ca, 7 P in mol%)	Gellan/xannthan	Bg particles in polymer mixture	Zinc sulfate ions	1.91 MPa	20.36 MPa			No Gen	[223]
Bg/alginate/PVA scaffold	Bg (unkonown)	Alginate/PVA	Mixing Bg precursor with polymer mixture	No	1.64 MPa	18 MPa			No Cht; no cross-linker	[224]
Bg/alginate scaffold	Bg (80 Si, 15 Ca, 5 in mol%)	Alginate	Bg particles in polymer	$CaCl_2$	1.6 GPa	6 MPa			No Cht	[225]
Silica/Cht/alginate scaffold	Nano Silica	Cht/alginate	Bg particles in polymer mixture	$CaCl_2$	0.59 MPa	8.16 MPa			No Gen	[226]
Bg/Cht scaffold	Bg (50 SiO_2, 45 CaO, 5 P_2O_5 in %)	Cht	Bg particles in polymer	GA	4.69 MPa	120 MPa			No Gen	[227]
Bg/Cht/gelatine scaffold	Bg 58S	Gelatine/Cht	Bg particles in polymer mixture	No		11 MPa			No cross-linker	[228]
Fe-doped BG/Cht scaffold	BG (doped with Fe_2O_3)[#]	Cht	Bg particles in polymer	No	9 MPa				No cross-linker	[229]
Fiber scaffold	BG	PHB/Cht	BG particles in polymer mixture	No			3.42 MPa	210 MPa	No cross-linker	[230]
Fiber scaffold[***]	Bg 58S	Cht	Bg coating	No	7.68 MPa	460 MPa	3.11 MPa	196 MPa	No cross-linker	[29]
Multilayered (bilayered) scaffold	BG	PCL/Cht	1-PCL/Cht coating on BG scaffold; 2-PCL/Cht	No	1 MPa				No cross-linker	[193]

Structure	Inorganic	Organic	Coating/mixture/cross-linking agent	Cross-linker for polymer	Compressive strength	Compressive modulus	Tensile strength	Tensile modulus	Distinction	Ref
Hybrid scaffold	Bg 58S	PVA/Cht	Mixing Bg precursor with polymer mixture	No	0.28 MPa	6.0 MPa			Hybrid, no cross-linker	[209]
Hybrid scaffold	Bg 60S	PVA/Cht	Mixing Bg precursor with polymer mixture	GA	0.26 MPa	2.2 MPa			Hybrid, no Gen	[208]
Hybrid scaffold	Bg (75 SiO_2, 25 CaO in wt%)	Gelatine	Mixing using GPTMS	No	4 MPa	166 MPa			Hybrid	[204]
Hybrid scaffold	/ (from precursor TEOS)	Cht	Mixing using GPTMS	No		0.33 MPa			Hybrid	[202]
Hybrid scaffold	/ (from precursor TEOS)	Cht	Mixing using GPTMS	No	0.2 MPa	8.1 MPa			Hybrid	[231]
Hybrid scaffold	/[##]	Cht	Mixing using GPTMS	No		1.6 GPa			Hybrid	[232]
Hybrid scaffold	/[##]	Cht	Mixing using GPTMS	No			95 MPa	4.8 MPa	Hybrid	[233]
Hybrid scaffolds	BG	Collagen	APS for BG functionalization	No	0.21 MPa				Hybrid	[212]
Hybrid scaffolds	BG	SiO_2/PTHF/PCL	GPTMS	No	1.2 MPa				Hybrid	[213]
Hybrid scaffolds	/ (from precursor TEOS)	Gelatine	GPTMS	No	60 kPa	1.3 MPa			Hybrid	[211]

[*] O-acrylamidomethyl (NMA)-hydroxypropyltrimethyl ammonium chloride chitosan (HACC); [**] HACC; [***]fracture toughness 0.24 MPa m$^{1/2}$;

[#] (1- 45 SiO_2, 22 CaO, 22 Na_2O, 6 P_2O_5 , 5 Fe_2O_3 in wt% and 2- 45 SiO_2, 19.5 CaO, 19.5 Na_2O, 6 P_2O_5 , 10 Fe_2O_3 in wt%);

[##] Glass network produced by hydrolysis and condensation of GPTMS

Chapter 3 Methodology

3.1 Synthesis of Bioglass 45S5, hydrogels and scaffolds

3.1.1 Materials

All chemicals were purchased from Sigma Aldrich. Bioglass 45S5 was made from calcium carbonate (product code 12010), silicon dioxide (product code 84878), sodium carbonate (≥99.5 %, product code 222321) and calcium phosphate (≥96 %, product code 21218). Hydrogels were synthesised from genipin (≥98 %, product code G4796), chitosan (medium molecular weight of 190,000-300,000 $gmol^{-1}$, 80 % deacetylated, product code 448877) and glacial acetic acid (>96 %, product code ARK2183). Poly(vinyl alcohol) (molecular mass 85,000-124,000 $gmol^{-1}$, 99+ % hydrolized, product code 363146, and molecular mass 13,000-23,000 $gmol^{-1}$, 98 % hydrolized, product code 348406) and polyurethane foams (60 ppi, pores per inch from, Recticel, Corby, UK and medium density foam, from Efoam, Bilston, UK) were used for glass-ceramic scaffolds preparation. Simulated body fluid (SBF) was prepared using sodium chloride (≥99.5 %, product code S7653), sodium bicarbonate (product code S5761), potassium chloride (≥99.5 %, product code 60128), potassium phosphate dibasic trihydrate (≥90.0 %, product code P5504), magnesium chloride hexahydrate (product code M2393), calcium chloride (≥ 96.0 %, product code C5670), sodium sulphate (≥90.0%, product code 238597), tris(hydroxymethyl)aminomethane (TRIS) (≥99.8 %, product code 252859) and hydrochloric acid (36.5-38.0 %, product code 258148). All chemicals were used as received. Apatite-wollastonite (AW) powder was received from Glass Technology Service (GTS) Ltd (Sheffield, UK) (100 % <50 μm).

3.1.2 Synthesis of Bioglass 45S5 and apatite-wollastonite glass-ceramic powders

Bioglass 45S5 (BG) (45.0 SiO_2, 24.5 CaO, 24.5 Na_2O, 6.0 P_2O_5 in wt%) was synthesised using the melt quench method [4, 234]. The glass reagents for synthesis of 26 g of Bioglass (Table 3.1) were mixed and shaken for 30 min using a roller mixer (Stuart SRT6). Next, the mixture was transferred into a platinum crucible and heated from room temperature to 1225°C at 10 °C/min (when the lid was removed from the crucible). The temperature was further increased at the same rate to 1400°C and the mixture was kept at that temperature for 30 min. The procedure for preparing Bioglass was previously optimized in Bretcanu's group

to suit the equipment and the material used. The mixture was then quenched in water to make the glass. Carbolite Gero HTF 1800 furnace was used. The glass powder (particle size below 53 μm) was obtained by grinding and sieving. Fritsch Pulverisette 6 was used to grind the glass at 180 rpm for 3 min per cycle. Three cycles were performed to provide adequate grinding of the glass. The powder was subsequently sieved using the Auto sieve shaker (Impact) to obtain particles less than 53 μm. The received AW powder (4.6 MgO, 44.7 CaO, 34.0 SiO_2, 16.2 P_2O_5, 0.5 CaF_2 in wt%) was also sieved to ensure that the particle size is below 53 μm.

Table 3.1: Glass reagents used to synthesise 26 g of BG 45S5

Reagent	Amount (g)
Calcium carbonate	8.12
Sodium carbonate	10.95
Silicon dioxide	11.81
Calcium phosphate	3.55
Overall mixture	34.43

3.1.3 Hydrogel synthesis with and without Bioglass

1.5 % w/v (weight by volume) chitosan solution was prepared by dissolving chitosan powder in 1 % v/v (volume by volume) acetic acid aqueous solution, according to [126, 127, 137]. The solution was stirred with a magnetic stirrer for 24 h in a sealed glass vessel. Genipin solution (0.5 % w/v) was made by dissolving genipin powder in deionized water followed by magnetic stirring until dissolved. In order to synthesise hydrogels, 0.9 ml of chitosan and 0.1 ml of genipin solutions were mixed and magnetically stirred for 5-10 min. Table 3.2 shows hydrogel sample names with the amounts and concentrations of chitosan and genipin solutions (molar ratio was Cht:Gen=1:40, while the ratio between the number of NH_2 groups:Gen molecule was NH_2:Gen=36:1). Different molar ratios of Cht:Gen were tested (1:40 as well as 1:60, 1:80, 1:100, 1:120 and 1:160) and the molar ratio 1:40 was selected because it yielded a stable hydrogel with low amount of the cross-linker. To evaluate the effect addition of BG has on the hydrogel structure, a range of samples was prepared with the different amount of BG powder added: 1 mg, 3 mg and 5 mg BG per 1 ml gel (Table 3.2). In case of gels

with Bioglass, Bioglass powder was added to the chitosan-genipin solution mixture and stirred for approximately 1 h until solution became homogeneous (assessed by the naked eye). Sample mixture was transferred to microplate wells (0.5 ml per well) for fluorescence intensity measurements (Section 3.3) at 37 °C where gelation process was followed *in situ* over 24 h. For all other experiments, gelation was performed in polyethylene (PE) vials. 1 ml of sample mix was transferred to 5 ml PE vials, vials were closed and placed in the oven at 37 °C for 24 h for gelation to take place. Hydrogels formed in vials were stored in a fridge (~ 5 °C) and removed from the vials prior to experiments (Sections 3.2, 3.4-3.7). An example of a synthesised chitosan-genipin hydrogel is shown in Figure 3.1.

Table 3.2: Hydrogels with and without BG powder

Hydrogel	Cht volume (ml)	Cht conc (mol/ml)	Gen volume (ml)	Gen conc (mol/ml)	BG (mg)
Cht-Gen					0
Cht-Gen 1 mg BG	0.9	$5.51 \ 10^{-8}$	0.1	$2.21 \ 10^{-6}$	1
Cht-Gen 3 mg BG					3
Cht-Gen 5 mg BG					5
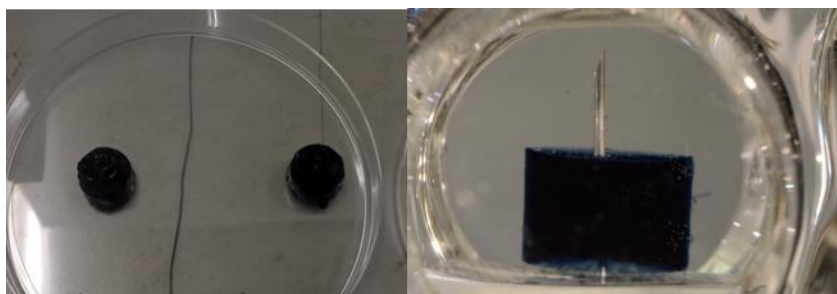
Figure 3.1: Synthesized Cht-Gen hydrogels captured in the Petri dish (left) and in the optical reactor using cameras, setup used as in [235] (right)

3.1.4 Synthesis of Bioglass and apatite-wollastonite scaffolds

BG scaffolds were produced by sponge replica method [167, 214]. Polyurethane (PU) foams (foam 1- 60 ppi, from Recticel and foam 2- medium density foam, from Efoam) were cut in cylindrical shapes with the diameter of 11 mm and height of 13 mm. The foams were coated with a Bioglass slurry. A slurry was made by mixing BG powder (Section 3.1.2), PVA and deionized water (weight ratio BG:PVA:H_2O=30:6:64). PVA added to the slurry was a mixture

of PVA with molar masses 13,000-23,000 $gmol^{-1}$ and 85,000-124,000 $gmol^{-1}$ (weight ratio 1:1). Firstly, 0.6 g of PVA was dissolved in 6.4 g of deionized water and stirred for 1 h at 75 °C. Following, 3 g of BG powder was added and the mixture was further stirred for 15 min. The slurry was used to impregnate the PU foams.

Foam 1 was used with the following impregnation process: after the immersion in the slurry, the excess of the slurry was removed from the foams by gently squeezing in the hands. This process was repeated one more time. Due to aging of the PU foam 1, PU foam 2 was purchased. In case of foam 2, the impregnation procedure slightly differed: immersion in the slurry and squeezing was repeated for 3 times. The 4th time, after the impregnation in the slurry, foams were not squeezed (excess of slurry was not removed). In both cases of foam 1 and foam 2, the slurry-coated foams were left to dry for 1.5-2 h, turning them periodically for even drying. After drying, the heat treatments shown in Table 3.3 were performed to obtain scaffolds (Figure 3.2). It should be noted that foam 1 was used to obtain BG 1, BG 2 and BG 3 scaffolds using the heat treatments HT 1, HT 2 and HT 3, respectively. Later, in order to get mechanically stronger scaffolds, the foam 2 was used with the HT 3, chosen as an optimal heat treatment (according to discussion in the Section 6.1) to obtain BGS scaffold. Carbolite Gero furnace CFW-B 1200 was used for the heat treatments of BG scaffolds.

Figure 3.2: *PU foams coated with the Bioglass slurry (left) and obtained BG scaffolds after the heat treatment (right)*

For synthesis of AWS scaffolds, AW powder (Section 3.1.2) was used in place of BG powder, in otherwise same procedure as described above. The PU foams 2 were coated with an AW slurry

and they were left to dry. The heat treatment used for AWS scaffolds is shown in Table 3.3. Carbolite Gero furnaces CFW-B 1200 and HTF 1800 were used for the heat treatment for preparation of AWS scaffolds. The former was used for burning out processes and it had a maximum temperature 1100 °C. The latter furnace was used for the final step of the heat treatment as it was stable at higher temperatures.

Table 3.3: Heat treatments for BG and AW scaffolds

Scaffolds	Heat treatment (HT)	PU foam	Rate (°C/min)	First step	Intermediate step	Final step
BG 1	HT 1	1	5	550 °C, 1 h	/	1000 °C, 2 h
BG 2	HT 2	1			/	1100 °C, 2 h
BG 3	HT 3	1			800 °C/min, 2 h	
BGS	HT 3	2				
AWS	HT 4	2			900 °C/min, 2 h	1250 °C, 1 h

3.1.5 Coating of Bioglass and apatite-wollastonite scaffolds with the hydrogel

The hydrogel solution was made by adding 0.9 ml of chitosan and 0.1 ml of genipin solutions as in Section 3.1.3 and mixing for 5-10 min. The BGS or AWS scaffolds prepared by HT 3 and HT 4, respectively (Table 3.3, Section 3.1.4) were immersed in the hydrogel solutions for certain amount of time (15 min, 30 min or 1 h) [118, 167]. They were removed from the hydrogel solution, transferred to clean vials, placed in the oven at 37 °C and left for 24 h for the hydrogel to polymerize. An AWS scaffold immersed in the hydrogel solution and after polymerization is shown in Figure 3.3. It was noticed that the coated AWS scaffolds had a dark blue colour at the end of polymerisation.

Table 3.4 contains hydrogel coated BGS and AWS scaffolds with different times of immersion in the hydrogel solution.

Figure 3.3: AWS scaffold immersed in the hydrogel solution (left) and after polymerization of the hydrogel coating (right)

Table 3.4: Hydrogel coated BGS and AWS scaffolds

Coated scaffold	Time of immersion in the hydrogel solution
Hydrogel coated BGS	15 min
	30 min
	1 h
Hydrogel coated AWS	15 min
	30 min
	1 h

3.2 Scanning electron microscopy

Scanning electron microscopy (SEM) has been used to examine the morphology and the surface of hydrogels and glass-ceramic scaffolds, as well as the particle size of glass and glass-ceramic powders [104, 167, 236]. Tescan Vega 3 LMU scanning electron microscope with accelerating voltage of 8 kV and working distance of 6-13 mm was used to observe the structure of hydrogels with and without BG powder (Table 3.2). Prior to imaging, hydrogels were frozen in liquid nitrogen and freeze-dried for 48 h using Labconco, FreeZone 1 L freeze-dryer with the collector temperature of - 50 °C. Samples were then coated with gold, 5-10 nm, using a Polaron SEM Coating Unit. Hitachi TM3030 Tabletop SEM with accelerating voltage of 15 kV and working distance of 6-13 mm was used to examine the Bioglass and AW powders

and Bioglass, BG 1, BG 2, BG 3 and BGS scaffolds, and AWS scaffolds (Table 3.3). In case of hydrogel-coated scaffolds (BGS and AWS hydrogel coated scaffolds with different times of immersion in the hydrogel solution, Table 3.4), samples were freeze-dried for 12 h prior to imaging. As SEM can operate at low vacuum, no prior sample preparation (e.g. gold coating) was needed. ImageJ software was used for measuring the size of particles in case of BG and AW powders or pores in case of hydrogels and scaffolds.

Principles:

SEM uses the property of the material that backscattered and secondary electrons are emitted from the sample upon exposure to electron beam (primary electrons). When primary electrons interact with the sample, two types of interactions can occur which are used for imaging (even though other types of electrons, photons and irradiation occur): elastic scattering (backscattered electrons) and inelastic scattering (secondary electrons) (Figure 3.4) [237]. Backscattered electrons (BE) originate from the primary electrons which are elastically scattered back after interaction with the sample. Since they still contain most of their (high) energy, they can reach the detector from longer distance from the surface. Secondary electrons (SE) are emitted (they escape from the sample) in case of inelastic interaction between the primary electrons and the sample. Secondary electrons have been given a low energy so they only reach the detector from close to the surface. After an electron is promoted to higher energy state, the atom is in excited state. When the vacancy is filled, the atom will go to the relaxation state. The relaxation can happen in three ways: 1) when the vacancy filled is in the valence band (outer shell) so small energy is given and photon in the visible range is emitted (cathodoluminescence, CL), 2) when the vacancy in an inner shell is filled (X-ray emission), and 3) when an electron from the outer shell fills in a vacancy in an inner shell and the other outer electron escapes the sample (Auger emission).
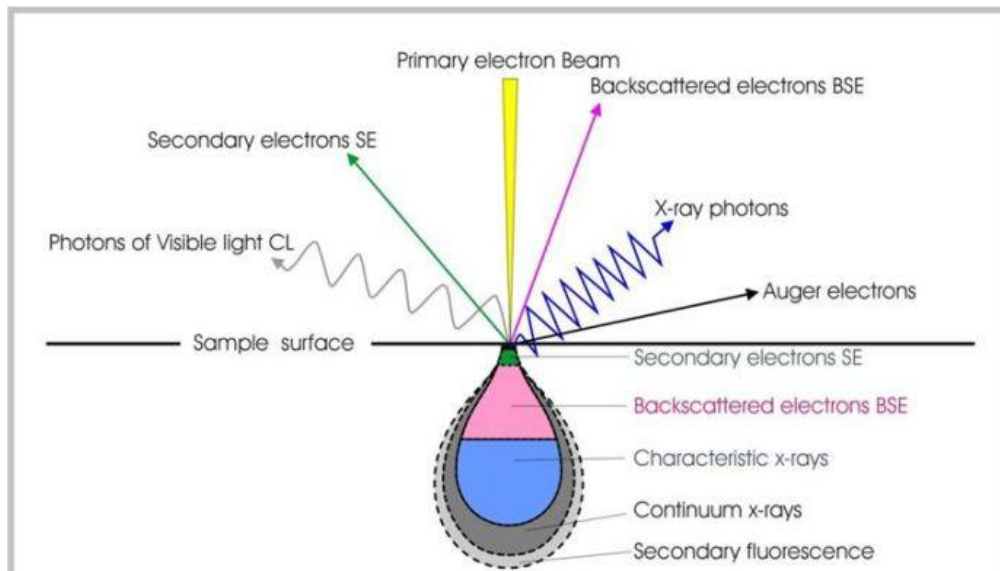
Figure 3.4: *Schematic representation of the interaction between the primary beam and the sample and its effects* [238]

Instrumentation:

SEM typically consists of an electron source, condenser and objective lenses, specimen stage, detectors (Figure 3.5) [237]. It usually operates in high vacuum (other molecules are not present and they do not interfere with the electron beam and electrons collected from the sample) to improve the image quality. The source of electron is called electron gun which acts as a cathode. It can be thermionic (emits electrons by heating a wolfram or LaB_6 filament) or field-emission (FEG) (if electrons are emitted by electric field). From the cathode electrons are accelerated to the anode by an electric field and lenses are used to guide the beam to the sample. Lenses in SEM are electromagnetic-they consist of coils of wires and electric current passes through them generating an electromagnetic field. Electrons are sensitive to the electromagnetic field. Two types of electromagnetic lenses are used. By changing the current through the coils, electromagnetic field changes which in turn affects the electrons-the size of the electron beam can be changed (condenser lenses). Objective lenses are used to focus the beam to the sample. Scanning coils are used for raster scanning -the beam covers a rectangular area on the sample. After interaction with the sample the detectors catch backscattered and secondary electrons. The signal from secondary electrons are most widely used and detected with Everhart-Thornley detector which is a scintillator-photomultiplier

system placed on the side of the sample. For detection of backscattered electrons, usually solid state (semiconductor) detector is used.
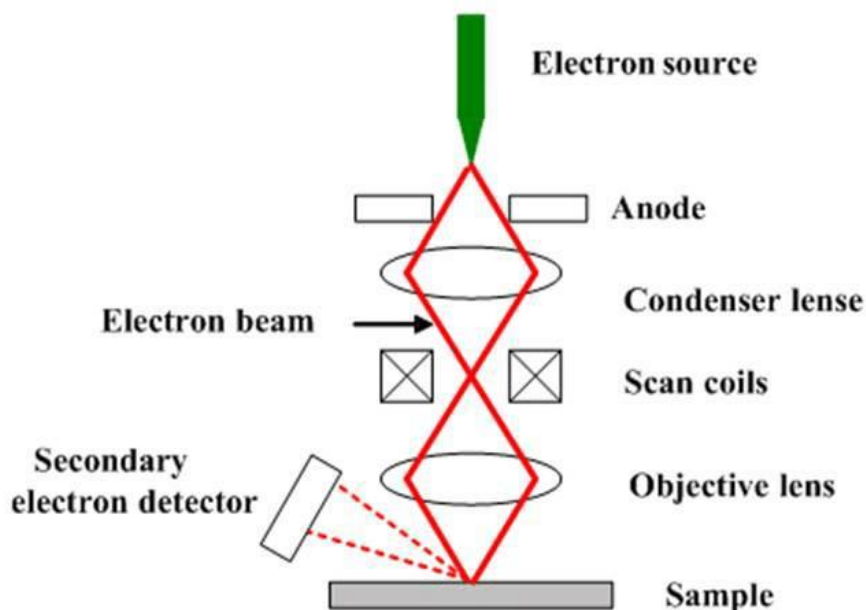
Figure 3.5: *SEM equipment* [239]

Sample preparation:

For SEM imaging, it is important that samples are electrically conductive. In case of non-conductive materials (ceramics or polymers), there can be an aggregation of negative charge on the surface and the primary electrons will be reflected which in turn will affect the imaging. A way to avoid surface charging of non-conductive materials is to operate at low vacuum because the charge will be dissipated by the gas molecules in the chamber. Gas molecules can collide with the electron beam and produce positive ions, which can react with the negative ions adsorbed on the surface of the sample and neutralize the charge. It could be noted that, alternatively, if operating at high vacuum, using a low accelerating voltage (in the range of 1-5 kV) for non-conductive samples can also prevent surface charging. Alternatively, non-conductive samples need to be coated with a thin layer (around 10 nm) of a conductive material (usually gold or carbon) [237].

3.3 Fluorescence spectroscopy

It has been reported that fluorescence measurement can be used for measuring the amount of cross-linking in genipin cross-linked polymers, such as chitosan [136, 140]. In this

work, a UV-VIS spectrophotometer (BMG LABTECH, FLUOstar Omega Microplate Reader) was used to measure fluorescence intensity of hydrogels with and without BG powder (Table 3.2). The spectrophotometer was connected to a PC with BMG LABTECH's Omega software. Vision Plate™ 24 microplate was used to hold the samples. Transparent plastic cover was used to seal the microplate in order to prevent evaporation of the samples and change in concentration during measurement. The measurement was carried out for 24 h using well scan mode (one well scan per sample per hour). For each well scan a matrix of 25 x 25 data points were scanned with 100 flashes per scan point, which were averaged to get a single value for each scan point, and 0.1 s settling time between scan points, which is time before the measurement begins after the well comes to the measurement position. For each well, an average value of all scan points was used for further plotting of the fluorescence intensity against sample. 24-hour-long FI measurement was performed in order to follow the cross-linking reaction in the hydrogels. Excitation and emission wavelength were 550 nm and 650 nm, respectively, as these wavelengths were reported as most appropriate for chitosan-genipin hydrogels according to literature making sure that excitation and emission wavelengths are well separated to avoid capturing excitation light [136, 140]. Additionally, by using appropriate wavelengths for excitation and emission, the fluorescence of the cross-linked gel can be measured without the interference of the individual constituents of the gel. The excitation energy used for the fluorescence measurement of ~ 217 kJ/mol (according to wavelength 550 nm) is lower than the energy of the covalent bonds present in the hydrogels, which allows the stability of the samples during fluorescence measurement [240]. A bottom–up measurement was used, where both the excitation source and the detector were located beneath the microplate. A bottom-up measurement (rather than top-down) was chosen because it avoids the problems of condensation on the covering foil which affects the measurement from the top of the sample. The temperature was set at 37 °C to follow the polymerization of the gels and each well contained 500 µl of the solution/gel.

Principles:

Luminescence is the emission of light by a substance caused by various factors, such as chemical reaction, electric current, crystallization process, absorption of photons. Photoluminescence is the emission of light which is caused by absorption of photons

(electromagnetic radiation). Fluorescence is a type of photoluminescence. Molecules which are able to give fluorescence are called fluorophores. The process consists of three phases: excitation, excited state and emission (Figure 3.6). When a photon from an external source (lamp or laser) is absorbed, an electron from the lowest ground state, S_0, will be transferred to higher vibrational levels in the excited state, S_1. Following, a relaxation to the lowest vibrational level of the excited state will occur (internal conversion). The electron will then return to higher vibrational levels of the ground state, emitting the energy [241, 242]. Considering that some energy is used for the relaxation within the excited state, the energy emitted from the molecule is lower, having a longer wavelength than that of the original source.
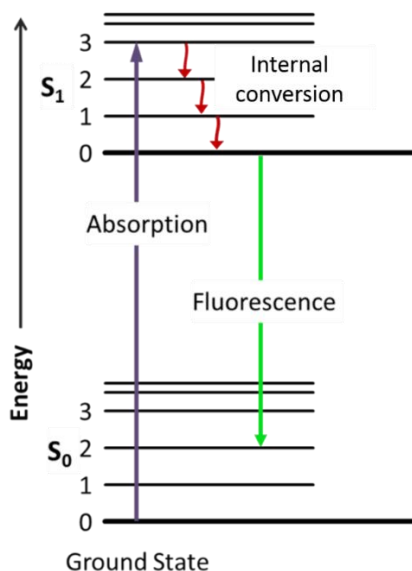
Figure 3.6: Jablonski diagram, where S_0 and S_1 are ground and excited states, respectively, and 0-3 are vibrational levels within ground and excited states [243]

Absorption and emission spectra are typically a mirror image as shown in Figure 3.7. Stokes shift is the difference in position between most intense bands of absorbance and emission (fluorescence) spectra-this occurs because photon energy of emission is lower than of the absorption (Figure 3.8) [241].

61
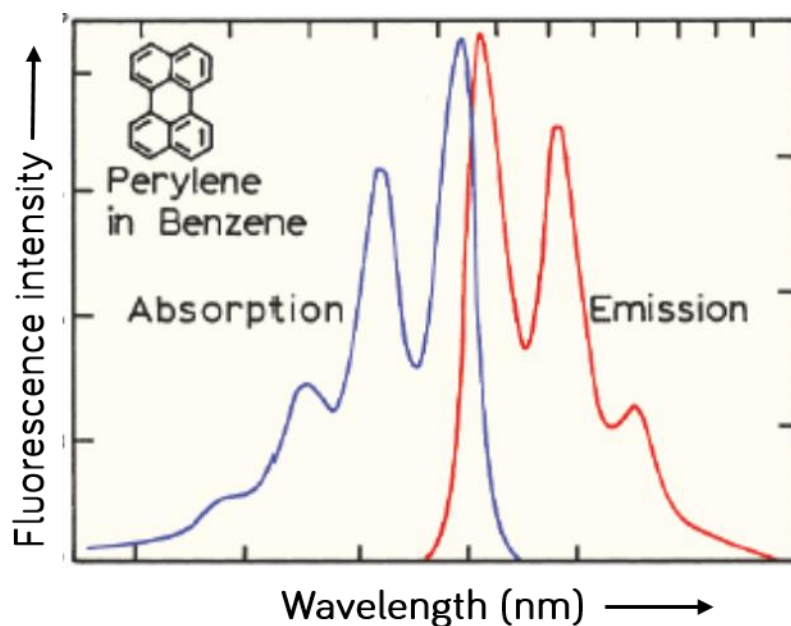
Figure 3.7: *Example of absorption and emission spectra [241]*
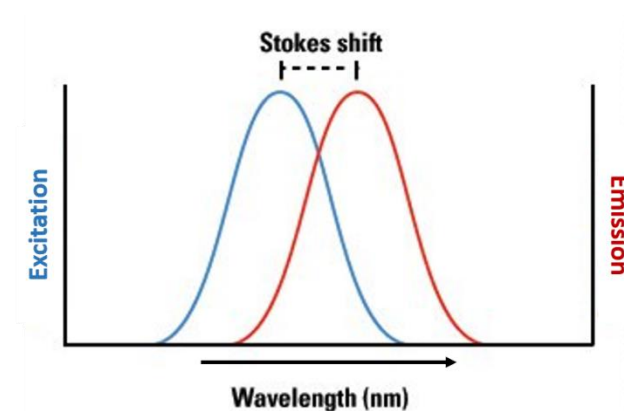
Figure 3.8: *Stokes shift [244]*

Instrumentation:

Figure 3.9 shows the scheme of a fluorescence measurement. Light from a light source (xenon flash-lamp) passes through an excitation filter allowing a fixed wavelength to reach the sample. The photons emitted from the sample go through an emission filter (with fixed wavelength) and reach the detector (photomultiplier tube, PMT). It should be noted that the measurement can be taken from the bottom side when both the excitation source and the detector are located on the bottom side of the sample.
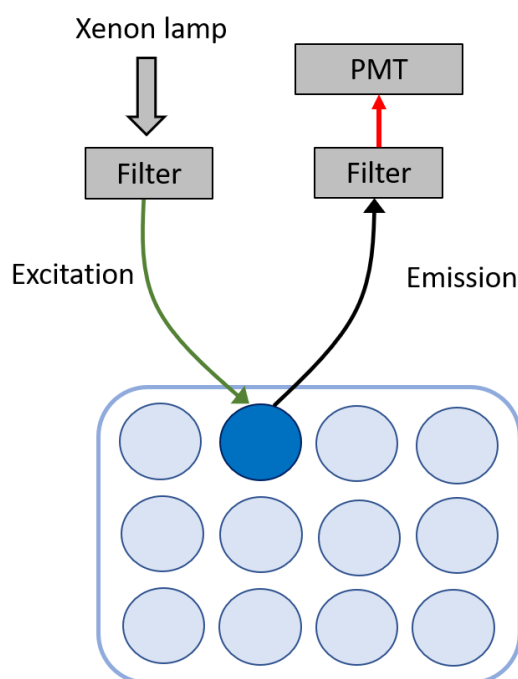
Figure 3.9: *Fluorescence intensity measurement set up*

3.4 Fourier transform infrared spectroscopy

In this work, Fourier transform infrared spectroscopy (FTIR) was used to confirm the presence of characteristic groups and chemical structure of genipin-cross-linked chitosan-based hydrogels, as well as to evaluate the effect of the addition of BG powder on the structure of hydrogels [236, 245, 246]. Agilent Technologies, Cary 630 FTIR spectrometer with diamond attenuated total reflectance (ATR) was used to obtain the FTIR spectra for chitosan and genipin powders, Bioglass powder and freeze-dried hydrogels with and without BG powder (Table 3.2) between 4000-650 cm^{-1} in transmittance mode, with 50 scans per sample and a resolution of 2 cm^{-1}.

Principles:

Infrared spectra originates from transitions between vibrational states within molecules. The machine measures adsorption of infrared radiation which is directed to the sample, and raw data is transformed to absorption/transmission spectrum over a range of wavelengths by using Fourier transformations. This method is based on vibrations that occur in molecules- molecules can only adsorb radiation with frequencies that matches the molecule vibration and it is unique for every structure [247].

Instrumentation:

Figure 3.10 shows typical set up of FTIR apparatus (with ATR feature). In a Michelson interferometer, light from polychromatic infrared source (typically from silicon carbide source which is heated) passes through the beamsplitter. 50 % of the light passes through to the moving mirror and 50 % is refracted to the fixed mirror. Light is then reflected from the both mirrors to the beamsplitter and recombined light passes to the sample area. The beams travel different path to the fixed and moving mirror and this is called retardation or optical path difference (OPD). For zero path difference (ZPD) the beams are perfectly in phase and they recombine constructively (Figure 3.11). If the beams are out of phase they recombine destructively. Interferogram is obtained by varying the retardation and measuring the signal at these different retardations. The maximum signal is recorded at constructive interference and the minimum when destructive interference occurs (intensity of the signal is between these maximum and minimum as interference is between constructive and destructive) [247].
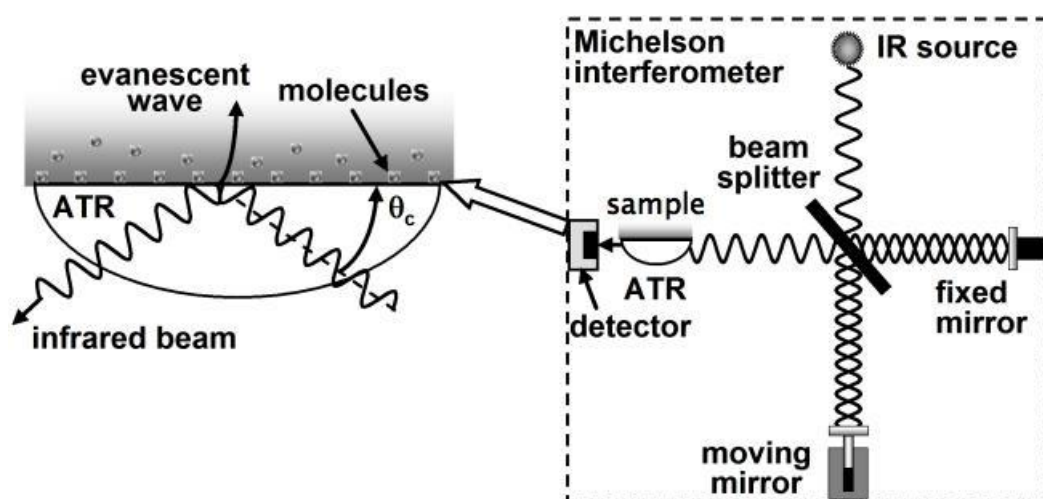
Figure 3.10: *FTIR apparatus with ATR* [248]
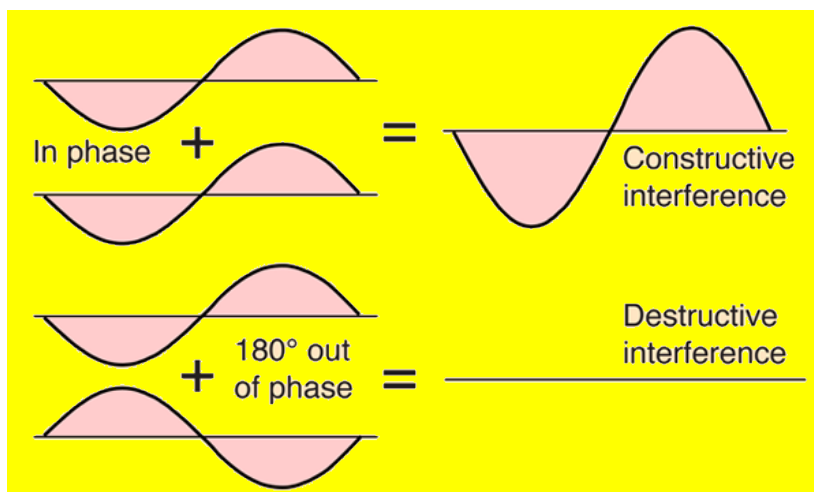
Figure 3.11: *Constructive and destructive interference* [249]

In case of attenuated total reflectance ATR-FTIR, samples can be measured directly without prior preparation, and solid samples are pressed against the crystal (Figure 3.10 and Figure 3.12). ATR-penetration depth is 1-2 microns and it measures surface rather than bulk. The light reaches the crystal with the high reflective index. This index need to be higher than of the sampling material (for most of the crystal is 2-4, and for most polymers 1.2-1.5). The beam is then reflected to the sample in the form of evanescent wave (wave generated when light is totally reflected without breaking at the interface) which continues through the sample. Total internal reflection occurs when reflected angle, Θ is > than critical, Θ_c (Figure 3.13 c). The evanescent wave is attenuated (altered) in regions of the infrared spectrum where sample absorbs the light [250]. The attenuated beam goes back to the crystal and reaches the detector-most commonly deuterated triglycine sulfate (DTGS). It is a pyroelectric detector with the ability to generate voltage upon change of temperature. The attenuated beam is recorded as the interferogram and by using Fourier transform, FTIR (absorbance or transmittance) spectrum can be obtained [251].

Figure 3.12: *ATR* [252]

65
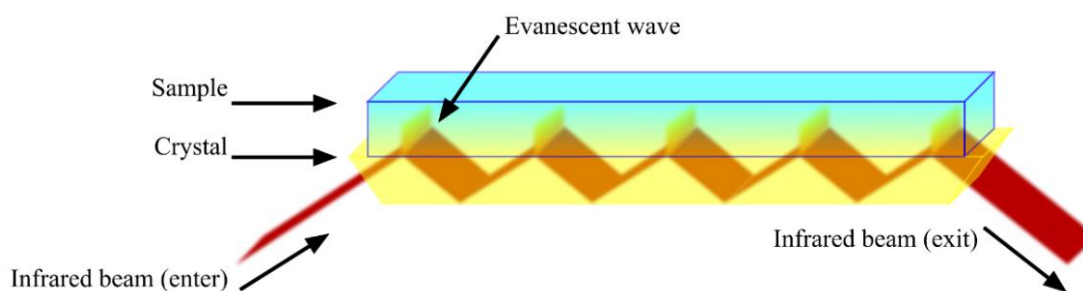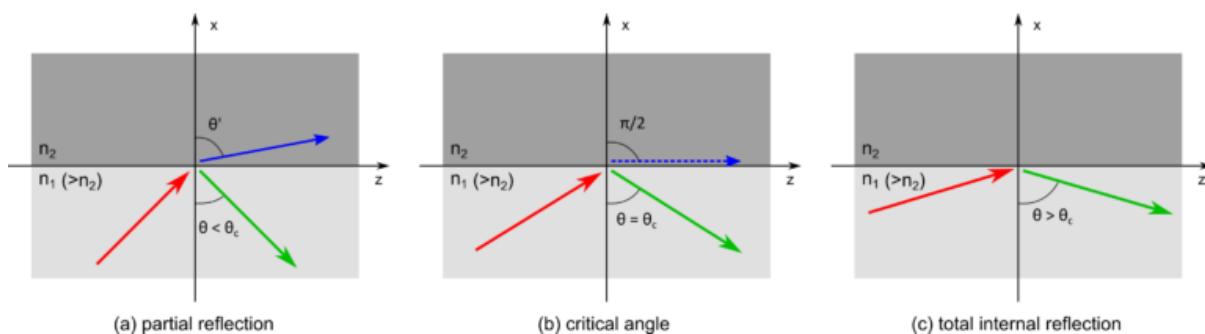
Figure 3.13: *a) partial reflection, b) critical angle, and c) total reflection (evanescent wave)*

[253]

3.5 Synthesis of SBF

SBF was synthesised using a well-known method first developed by Kokubo [27]. Firstly, 700 ml of deionised water was poured in a plastic beaker and heated to ~ 36.5 °C while stirring. The reagents 1-8 (Table 3.5) were added one by one, leaving enough time (~ 10 min) for each reagent to be completely dissolved before adding the next one. When all of the 8 reagents were dissolved, another 200 ml of deionized water was added. The pH and the temperature was ~ 2.0 and 36.5 °C, respectively. Next, 6.118 g of TRIS and ~ 5 ml of HCl were added in turns keeping the pH values between 7.42 and 7.45, keeping in mind that TRIS increases the pH, while HCl decreases it. When all of the TRIS was dissolved, pH was adjusted by adding HCl up to 7.40 exactly at 36.5 °C. Deionized water was then added bringing the total volume to 1000 ml; the solution was cooled down to room temperature and kept in the fridge before use.

Table 3.5: *Reagents used for making SBF [27]*

Order of addition	Reagent	Amount
1	NaCl	8.035 g
2	$NaHCO_3$	0.355 g
3	KCl	0.225 g
4	$K_2HPO_4\ 3H_2O$	0.231 g
5	$MgCl_2\ 6H_2O$	0.311 g
6	HCl	35 ml
7	$CaCl_2$	0.292 g
8	Na_2SO_4	0.072 g

3.6 Volume-change experiments in SBF

The volume-change experiments were used to determine initial volume and volume after immersing gels (with and without BG, Table 3.2) in SBF for certain amount of time (24 h, 3 days and 7 days) [236]. The gels were kept in 25 ml vials that contained 15 ml of SBF in a water bath at 37 °C.

A caliper was used to measure the dimensions (height and diameter) of the gel before and after immersion in SBF. The initial and the final volumes were calculated using the following formulas (Equations 1 and 2):

$$V_i = B_i \times H_i = r_i^2 \times \pi \times H_i = \frac{d_i^2}{4} \times \pi \times H_i \qquad (1)$$

$$V_f = B_f \times H_f = r_f^2 \times \pi \times H_f = \frac{d_f^2}{4} \times \pi \times H_f \qquad (2)$$

where V_i and V_f are the initial and the final volume of the gel, respectively;

r_i and r_f are the initial and the final radius of the gel, respectively;

d_i and d_f are the initial and the final diameter of the gel, respectively;

H_i and H_f are the initial and the final height of the gel, respectively and

B_i and B_f are the initial and the final base of the gel, respectively.

The volume variation of the gel after immersion in SBF was expressed as the volume related to the initial volume (Equation 3):

$$volume\ (related\ to\ inital\ volume)\ (\%) = \frac{V_f}{V_i} \times 100 \qquad (3)$$

The gels shape was approximated to a cylinder.

In addition, pH of the SBF solutions samples were in was measured after 2 h, 24 h, 3 days and 7 days of immersion.

3.7 Compression test

A compression test was performed in order to assess the mechanical properties of the hydrogels (with and without BG powder) and BG and AW scaffolds (with and without hydrogel

coating), as well as to study the effect of addition of BG powder in the hydrogel or the hydrogel coating on scaffolds [126, 167, 254].

Hydrogels, with and without BG powder, Table 3.2, were compressed using a Tinius Olsen H25KS testing machine. A preload force of 0.01 N was applied, and a rate of 1.5 mm/min and 5 N load cell were used. A caliper was used to measure the dimensions of the samples prior to the test. The setup for the compression test for the hydrogels is shown in Figure 3.14. Hydrogels were tested in two ways:

1) as synthesised (without SBF) - prepared gels were pushed out of vials, placed on Petri dish when the measures were taken and compressed; and

2) after immersing hydrogels in SBF for certain amount of time (24 h, 3 days or 7 days). Gels were transferred to a Petri dish together with the fluid, and compressed.

Bioglass and glass-ceramic scaffolds (BGS and AWS scaffolds, Table 3.3, and hydrogel coated BGS and AWS scaffolds with time of immersion of 30 min, Table 3.4) were compressed using a Shimadzu AGS-X testing machine with a rate of 1 mm/min and 1000 N load cell. A preload 10 N in case of BG scaffolds and 20 N in case of AW scaffolds were used. Dimensions of the scaffolds were measured prior to the compression test using a caliper. Figure 3.15 shows the instrumentation for compression test of the scaffolds. The scaffolds were tested as synthesised.

Figure 3.16 shows an example of a stress-strain curve for hydrogels. Compressive stress at 20 % strain (0.2 strain) and compressive modulus at 5-15 % strain (0.05-0.15 strain) are determined from the stress-strain graph. Compressive modulus was calculated as the slope of the strain-stress curve at 5-15 % strain in OriginPro. A typical stress-stress curve for Bioglass and glass-ceramic scaffolds is given in Figure 3.17. In case of scaffolds, maximum stress up to 10 % strain was calculated for each sample (as shown in Figure 3.17).
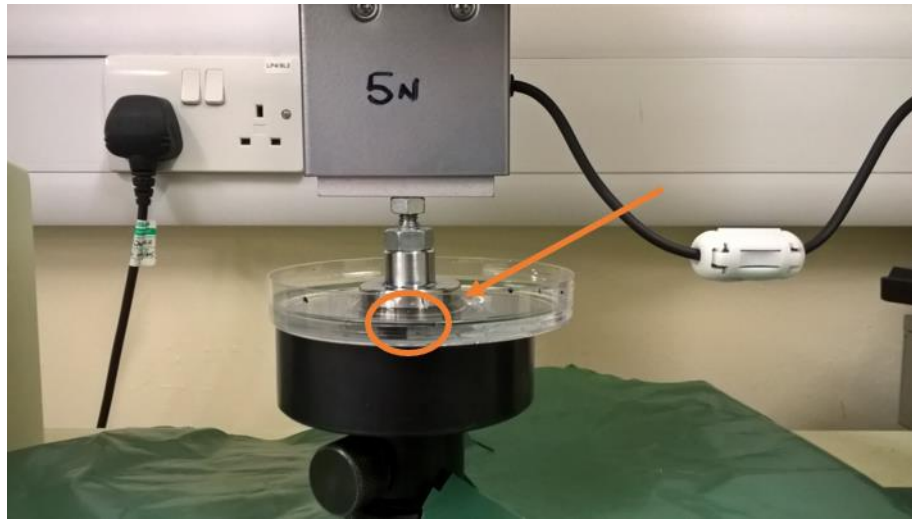
Figure 3.14: *Compression test setup for hydrogels (arrow pointing at the hydrogel)*
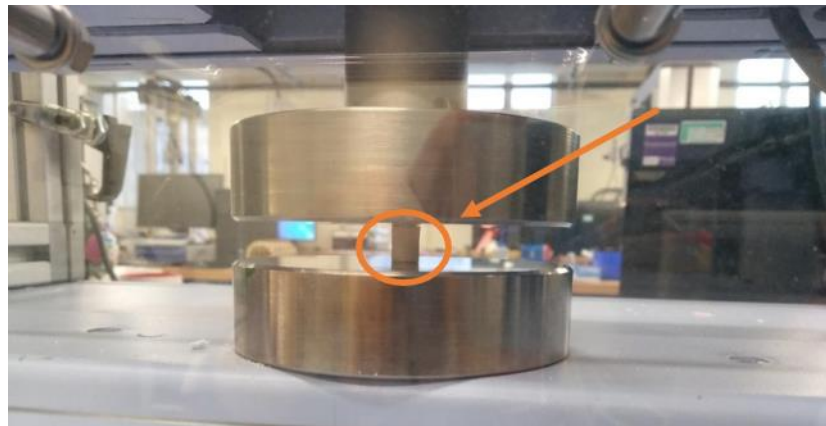
Figure 3.15: *Compression test setup for scaffolds (arrow pointing at the scaffold)*
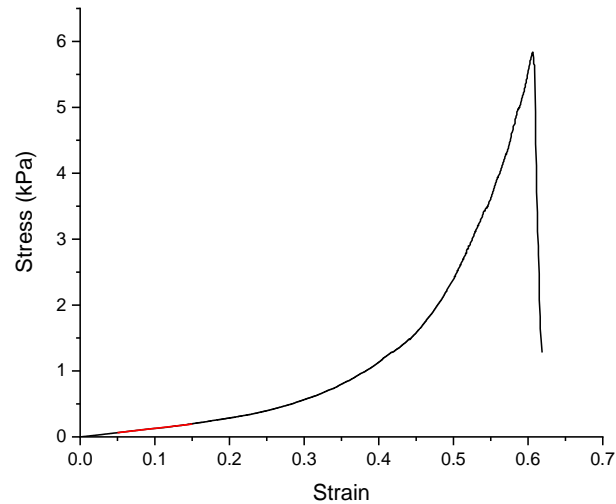
Figure 3.16: *Example of stress-strain curve for hydrogel samples with a slope at 5-15 % (0.05-0.15) strain for determining the compressive modulus (Cht-Gen, without SBF)*
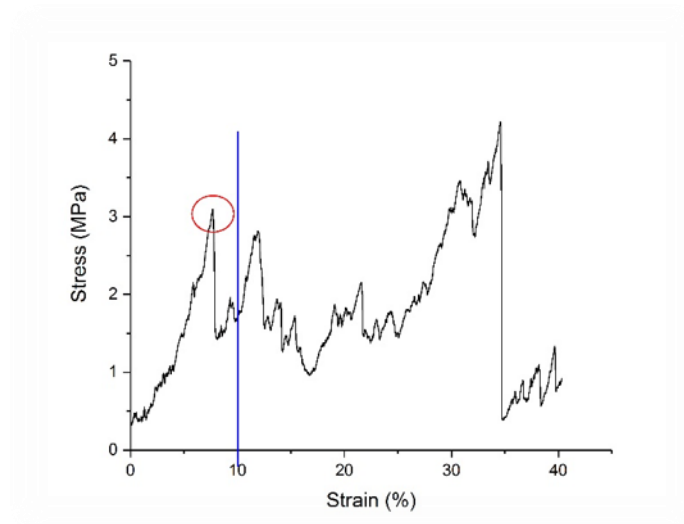
Figure 3.17: *Example of stress-strain curve for scaffolds with a maximum stress up to 10 % strain (AWS)*

Principles:

During the test, the sample is compressed under the constant rate and applied load and contraction measured (Figure 3.18) [255]. As the stress depends of the dimensions of the sample, stress (or engineered stress) (Pa) is calculate by equation (4). Engineering strain (strain) can be calculated by equation (6) [255].

70

$$Stress = \frac{F}{A_0} \tag{4}$$

where F (N) is the applied force, and A_0 (mm^2) is cross-sectional area of the specimen; in case of gels and scaffolds which are approximately cylinder-shaped:

$$A_0 = \pi \times r^2 = \frac{\pi \times d^2}{4} \tag{5}$$

where r and d are radius and diameter, respectively.

$$Strain = \frac{\Delta l}{l_0} = \frac{l_0 - l_i}{l_0} \tag{6}$$

where l_0 (mm) is initial height of the sample, l_i (mm) is the height of the sample after deformation and Δl (mm) is the deformation of the sample during the mechanical test. Dimension are usually expressed in mm, and the strain is unitless (could also be expressed in percentage by multiplying by 100).
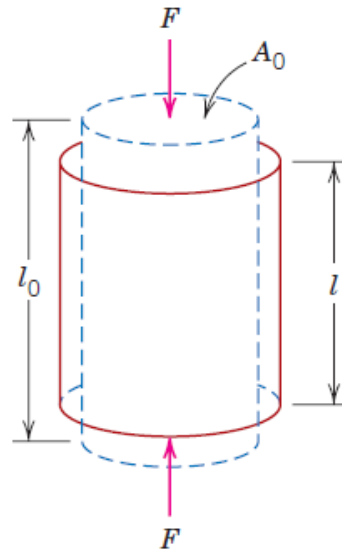
Figure 3.18: Schematic representation of compressive forces and sample contraction during compression test (for cylinder samples) [255]

For some materials, elastic modulus (Young's modulus)/compressive modulus can be calculated as the slope of the linear segment of the stress-strain curve (Figure 3.19). It should be noted that elastic modulus and compressive modulus are calculated in a similar manner from stress-strain curves tested in tensile and compression mode, respectively. However, for

some materials (cast iron, concrete and many polymers) this part of the curve is not linear; hence, the modulus needs to be determined as the slope from the beginning of the curve to a given point (Figure 3.20) [255].
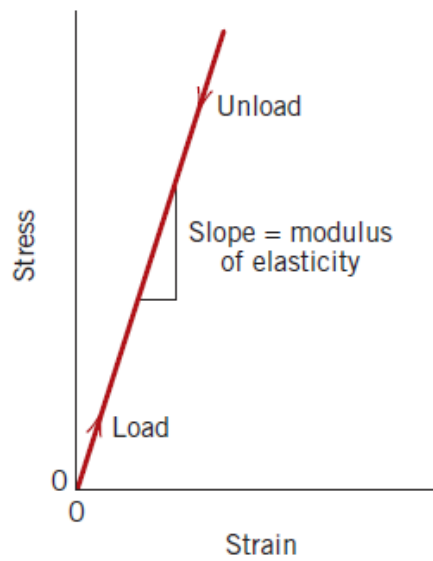
Figure 3.19: *Determining elastic modulus from stress-strain graph (linear deformation)* [255]
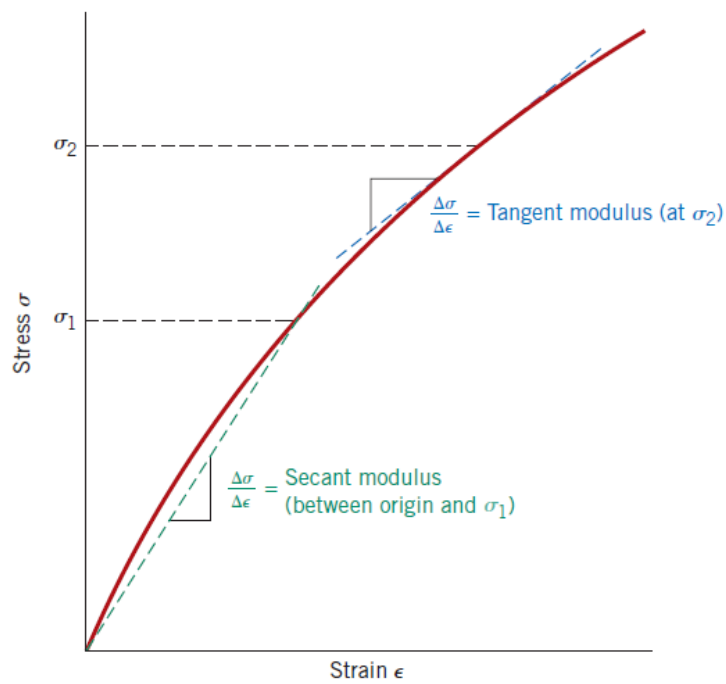
Figure 3.20: *Determining elastic modulus from stress-strain graph (unlinear deformation)*

[255]

3.8 X-ray diffraction

X-ray diffraction (XRD) has been used to identify the structure of Bioglass and glass-ceramic powders, as well as the scaffolds [234, 256]. In this work, the Philips PW3710 diffractometer (current 30 mA, voltage 40 kV, range 2θ: 20–70 °, step size: 0.05 °, time per step 1 s/step) was used for recording XRD spectra. Synthesized and sieved Bioglass powder (Section 3.1.2), received and sieved AW powder (Section 3.1.2) and BG 3 and AWS scaffolds (Table 3.3) crushed to powder using mortar and pestle were placed on a holder and measured. The software HighScore Plus was used for identification of phases.

Principles:

X-rays are electromagnetic radiation of wavelength of around 1 Å and they arise when high-energy electrons hit the material (the energy of these electrons is around 30 kV). When a beam of electrons hits a target, for instance, Cu, an electron from 1s shell is ionised and an electron from 2p shell can fill the vacancy so that the energy is released (Figure 3.21 a) giving an X-ray emission spectrum (Figure 3.21 b). This X-ray spectra is composed of a broad white radiation and fixed wavelengths, such as K_α and K_β.
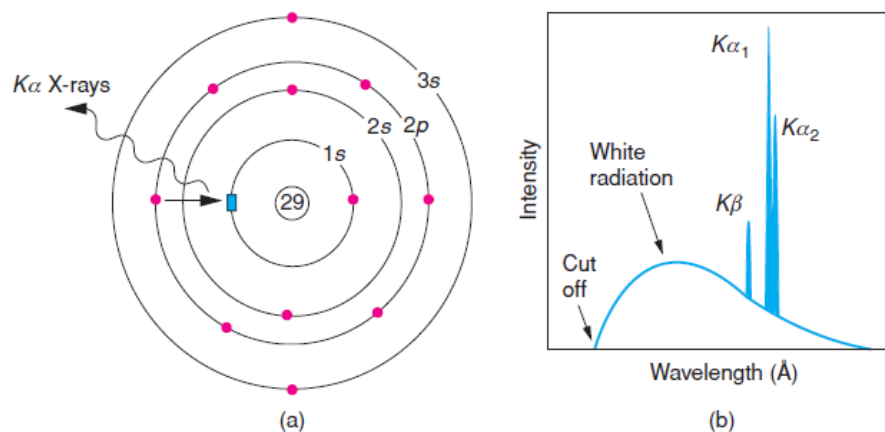
Figure 3.21: a) formation of X-rays and b) X-ray emission spectrum [257]

For X-ray samples analysis, only K_α is used to interact with the examined material. In the X-ray tube (Figure 3.22), tungsten filament (cathode) is heated and electrons are accelerated to the Cu target (anode) to produce X-ray radiation. They are emitted through Be windows towards the sample. Additionally, Ni filter is used to transmit only Cu K_α to the sample, while Cu K_β is absorbed. Once the X-rays reach the sample, some portion of them are

scattered without loss of energy and either a constructive (beams in-phase) or a destructive (beams out of phase) interference takes place (Figure 3.11, Section 3.4). When refracted beams are in-phase, a signal (peak) is recorded on a XRD spectrum of a specimen [257].
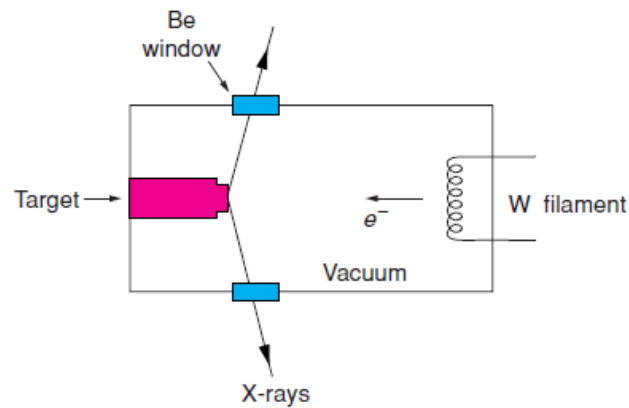
Figure 3.22: X-ray tube [257]

Figure 3.23 is a schematic representation of planes A and B within a crystal where incident beams 1 and 2 scatter at angle Θ. d is distance between the planes and n is a whole number of wavelengths.
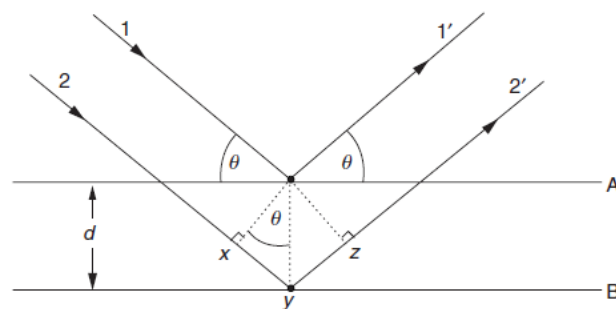
Figure 3.23: Bragg's law [257]

Reflected beams are in-phase and a constructive interference occurs, when Bragg's law (7) is satisfied [257]:

$$n\,\lambda = 2\,d\,\sin\Theta \tag{7}$$

Instrumentation:

Figure 3.24 shows a source of the X-rays, a sample and a detector [257]. The source and a detector lie on the same circle and a detector moves and records the intensity of diffracted X-rays at the angle of 2Θ.
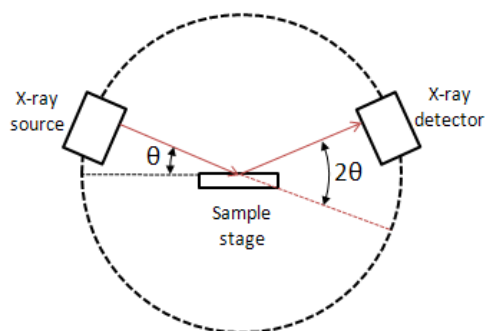
Figure 3.24: *Schematic image of instrumentation for XRD [258]*

3.9 Differential thermal analysis

Differential thermal analysis has been used for determining the thermal behaviour of ceramic materials upon heating, which is used for determining the heat treatment for preparation of scaffolds [113, 234, 256]. In this work, the measurement was carried out using Setaram Labsys Evo STA (simultaneous thermal analysis). 45 mg of BG and 43.6 mg of AW powders (Section 3.1.2) were placed in platinum crucibles for testing. Pure alumina was used as reference material and for the baseline. The samples were heated up with the rate of 20 °C/min from the room temperature to 1500 °C. The measurement was done in air.

Principles

Differential thermal analysis is a method that measures a difference in temperature between the sample and a reference material while a thermal programme is set (heating). The reference material is inert within the temperature range studied. DTA graphs which are plots of heat flow against temperature are obtained. They show exothermic or endothermic changes which are in turn indicators of the changes that occur in the sample upon heating or cooling, for example glass transition, crystallization, melting [259].

Instrumentation

Figure 3.25 shows a DTA instrument that consists of a furnace, a sample, a reference material and a thermocouple [260]. The sample and the reference material are placed inside

the furnace. The temperature inside the furnace is controlled. Upon heating, the temperature difference between the sample and the reference, as well as the sample temperature are measured by the thermocouple.
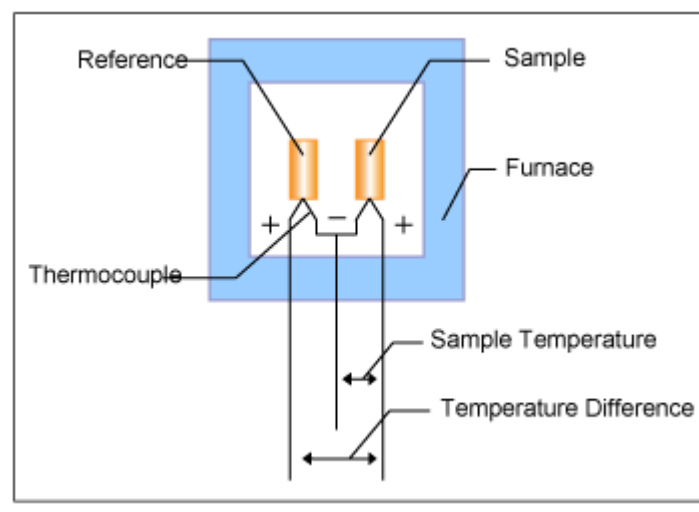
Figure 3.25: *DTA instrumentation [261]*

3.10 Heating microscopy

Heating microscopy has been reported in the literature as a method used to assess a thermal behaviour of a material upon heating, including sintering, softening and melting [234]. This method, together with DTA, has been utilized for setting the heat treatment for synthesis of scaffolds. Both temperature and silhouette (area) of the samples are measured during the analysis. For this study, samples were prepared by manually compressing the BG or AW powder using a rectangular die. The Misura® HSML-ODL Expert System Solution (Heating Microscope and Horizontal Optical Dilatometer), was used. Samples were heated in air atmosphere with the rate of 10 °C/min to 1200 °C for BG and 20 °C/min to 1300 °C for AW. Area (%) vs temperature curves were calculated by the software.

Principles

Upon heating, when a material goes through changes such as sintering, softening and melting, the shape of the initial sample changes. A video camera takes images of the sample at different temperatures during heating. All these images with the changes in sample's silhouette/area are recorded by a software (Figure 3.26) [262]. Initially, the sample has a rectangular shape with sharp edges (Figure 3.26 a). With the increase of temperature, the

76

sample starts to shrink (Figure 3.26 b) and its edges become rounded (Figure 3.26 c). This shrinkage occurs due to sintering. With the further increase of temperature, the sample starts to melt, passing through the hemisphere shape (Figure 3.26 d). Melting is completed when the height of the sample shrinks more than 1/3 of the initial height (Figure 3.26 e).
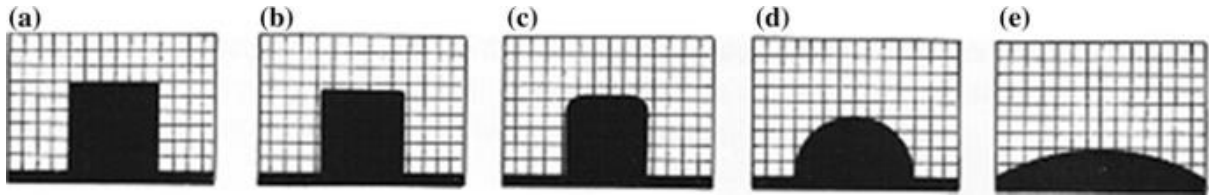
Figure 3.26: Examples of heating microscope images: a) initial shape at room temperature; b) start of sintering; c) softening; d) hemisphere and e) end of melting [262]

Instrumentation

The main parts of an instrument are a light source, a reaction tube with a stage/sample holder, a video camera, a thermocouple, a heater and a gas tube (Figure 3.27) [263, 264].
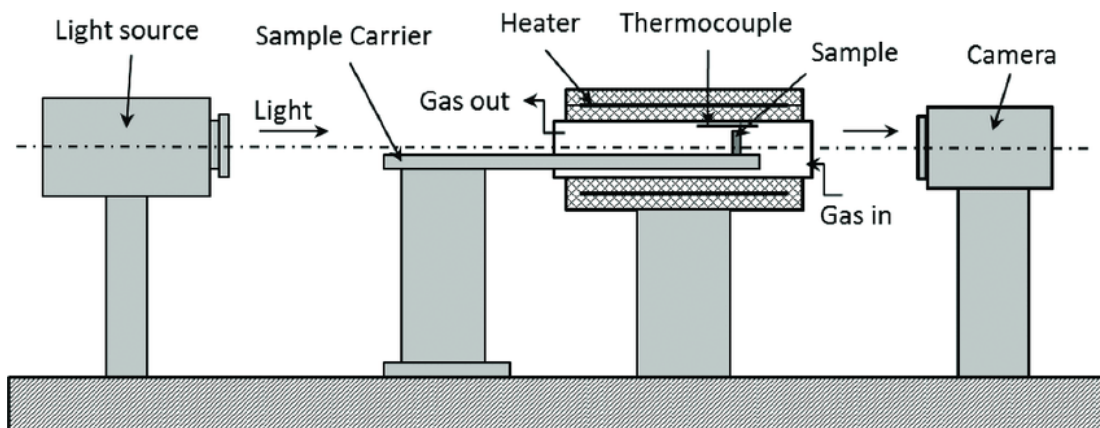
Figure 3.27: Heating microscope apparatus [264]

3.11 Tests in simulated body fluid

Simulated body fluid (SBF) has been used for *in vitro* testing of Bioglass and glass-ceramic scaffolds [171, 265]. In this work, the scaffolds (uncoated BGS and AWS, Table 3.3, and hydrogel coated BGS and AWS with 30 min of immersion in the hydrogel solution, Table 3.4) were placed in 25 ml vials containing 15 ml of SBF, and kept in the oven at 37 °C for up to 2 weeks. The SBF solution was changed (refreshed) every 3-4 days. The samples after SBF

immersion were analysed using scanning electron microscopy (SEM), compression test and pH measurement. SEM was done similarly as in the Section 3.2 using Hitachi TM3030 Tabletop SEM for the samples immersed in the SBF for 1 and 2 weeks. A part of hydrogel-coated BGS and AWS were freeze-dried prior to imaging for 12 h using Labconco, FreeZone 1 L freeze-dryer. A subset of hydrogel-coated BGS and AWS samples were air-dried and nominated non-freeze-dried. Compression test was performed similarly as in the Section 3.7 for scaffolds immersed in the SBF for 1 and 2 weeks using a Shimadzu AGS-X testing machine with a rate of 1 mm/min and 1000 N load cell. A preload of 10 N and 20 N were used for BGS and AWS scaffolds, respectively. Samples were gently wiped with a tissue to remove the excess of the solution and the dimensions were measured with a calliper prior to the test. Maximum stress up to 10 % strain was determined from the stress-strain curve. pH of SBF was measured after 3, 7, 10 and 14 days of immersion. At each time point the pH was measured before the solution was refreshed.

Chapter 4 Bioglass powder

Bioglass (BG) powder synthesized according to the procedure described in Section 3.1.2 was characterized using scanning electron microscopy (SEM) to assess the size of BG particles. Furthermore, information obtained from differential thermal analysis (DTA) and heating microscopy (HM) was used for determining the properties of the powder upon heating, which was relevant for the selection of a heat treatment of the BG powder during the preparation of scaffolds. X-ray diffraction (XRD) was utilised in order to confirm the presence of amorphous BG powder.

4.1 Scanning electron microscopy (SEM) of Bioglass powder

An SEM image of sieved BG powder is shown in Figure 4.1. Sieving was performed in order to get all the particles below 53 μm. SEM confirmed that the particle size is less than 53 μm, which is favourable for the next steps of the work that involve addition of these particles to the chitosan-genipin hydrogels, as well as the synthesis of BG scaffolds. Therefore, sieving of the powder was performed in order to remove big particles and get more homogeneous particle range, which would enable better distribution within the hydrogel. Also, sieving was done to ensure that the BG particles would be well dispersed in the BG slurry, which would lead to an even coating of the PU foams with the slurry during the impregnation process of the synthesis of the scaffolds. Due to unavailability of a particles size analyser, the size of the particles was determined by manually measuring the particles with ImageJ software.
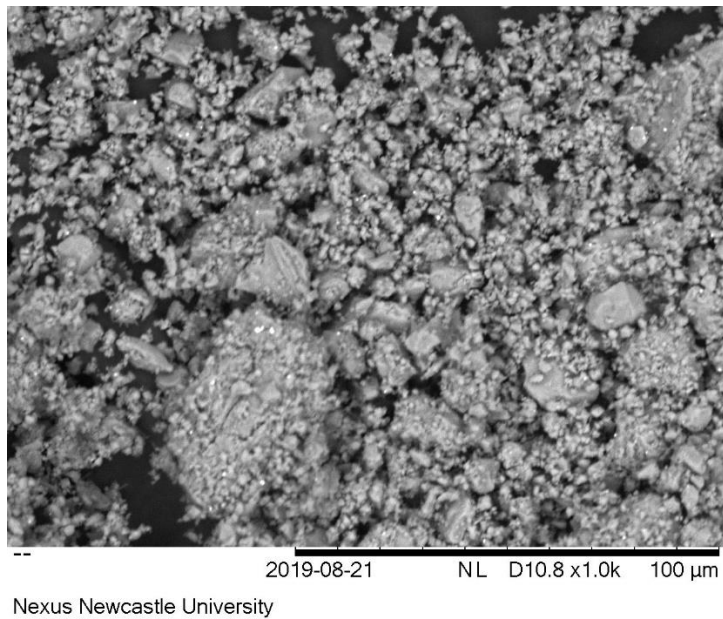
Figure 4.1: SEM image of sieved BG powder

4.2 X-ray diffraction (XRD) of Bioglass powder

Figure 4.2 shows an XRD pattern of the BG powder, carried out using the method described in Section 3.8. The broad peak at ~ 32° is characteristic of amorphous BG structure [234, 265]. The amorphous structure is expected for the BG powder before the heat treatment. After the heat treatment used to prepare scaffolds (Section 3.1.4), crystallization is expected to occur [4].
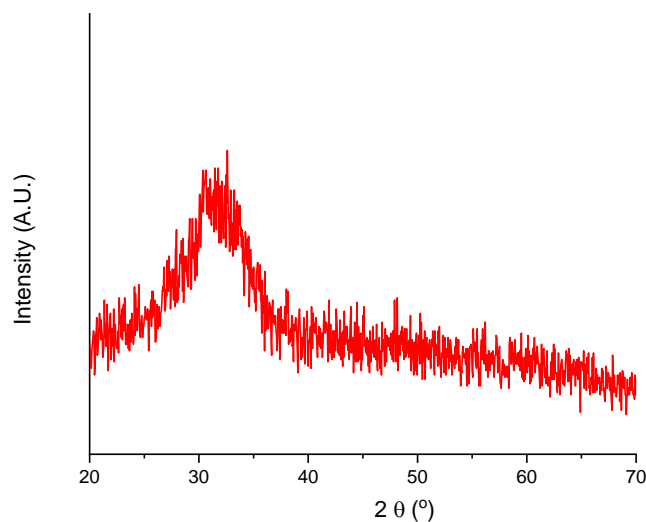
Figure 4.2: XRD of BG powder

4.3 Differential thermal analysis (DTA) of Bioglass powder

Figure 4.3 shows the DTA graph for BG powder. The glass transition temperature, T_g, known as the transition point from brittle/glassy state to viscous/rubbery state, is at 550 °C, which is in agreement with the literature [113, 234]. The exothermic peak between 600-725 °C with a maximum at 650 °C corresponds to glass crystallization. The endothermic peak at ~ 1230 °C corresponds to the melting point. Although the literature reports existence of two melting peaks (for two crystalline phases later discussed in Section 6.2), this is not clear from Figure 4.3 [113, 234]. A large endothermic peak at 1230 °C is observed, and a shoulder at 1200 °C is seen as well, which might correspond to the second melting peak. The reason that the melting peak at 1200 °C cannot be clearly distinguished might be the overlapping of the two peaks. It should be noted that the peaks at approximately 200 °C are due to an error of the instrument as shown in the Appendix A.
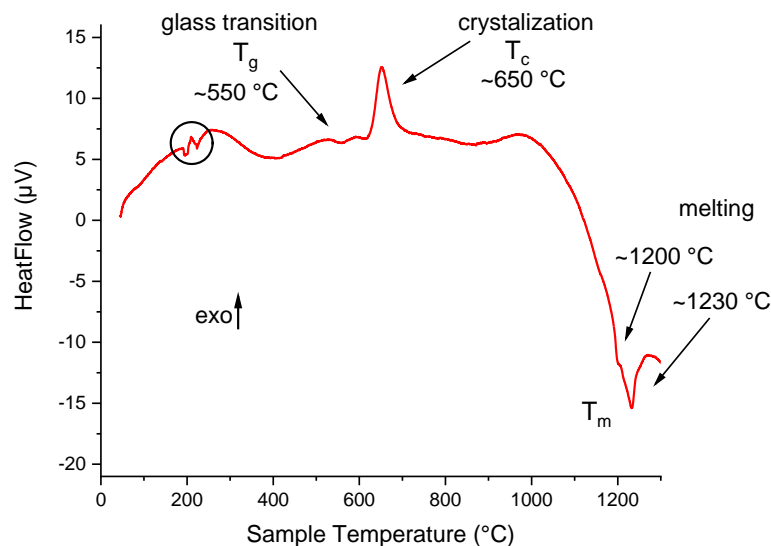
Figure 4.3: DTA for BG powder (heating rate 20 °C/min)

4.4 Heating microscopy of Bioglass powder

The heating curve of the BG sample recorded using the heating microscope (HM), as described in Section 3.10, is shown in Figure 4.4. During the heat treatment the pressed particles bond together, yielding a compact structure with reduced dimensions in comparison to the initial sample (shrinkage ~ 55 %). This process is called sintering or densification. The

81

sample shows shrinkage at ~ 545-610 °C, which indicates a first densification/sintering process, align with a literature [234]. In this first sintering step, a shrinkage of 15 % is recorded. The second densification occurs at ~ 900 °C, yielding a shrinkage of 39 %, followed by melting at approximately 1200 °C, as also seen in [234]. It is suggested that temperatures in the interval 1000-1100 °C (below the melting point), when high densification is reached, are to be used in fabrication of scaffolds in order to obtain highly sintered and mechanically stable scaffolds [234].
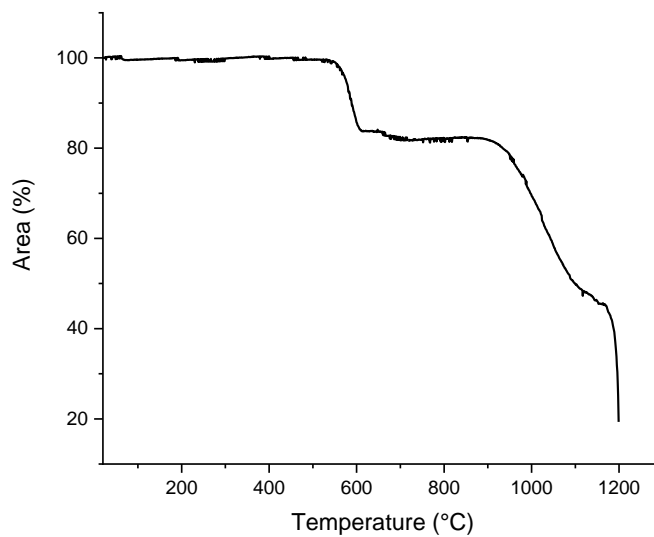
Figure 4.4: Shrinkage of the BG sample upon heating recorded by the heating microscope (heating rate 10 °C/min)

Figure 4.5 shows the silhouettes of the BG sample whose heating profile was shown in Figure 4.4, (see Section 3.10) at representative temperatures during the heating. Comparing the sample at 50 °C (Figure 4.5 a) and at 1195 °C (Figure 4.5 f), significant shrinkage occurs due to sintering. After this point, the sample started melting.
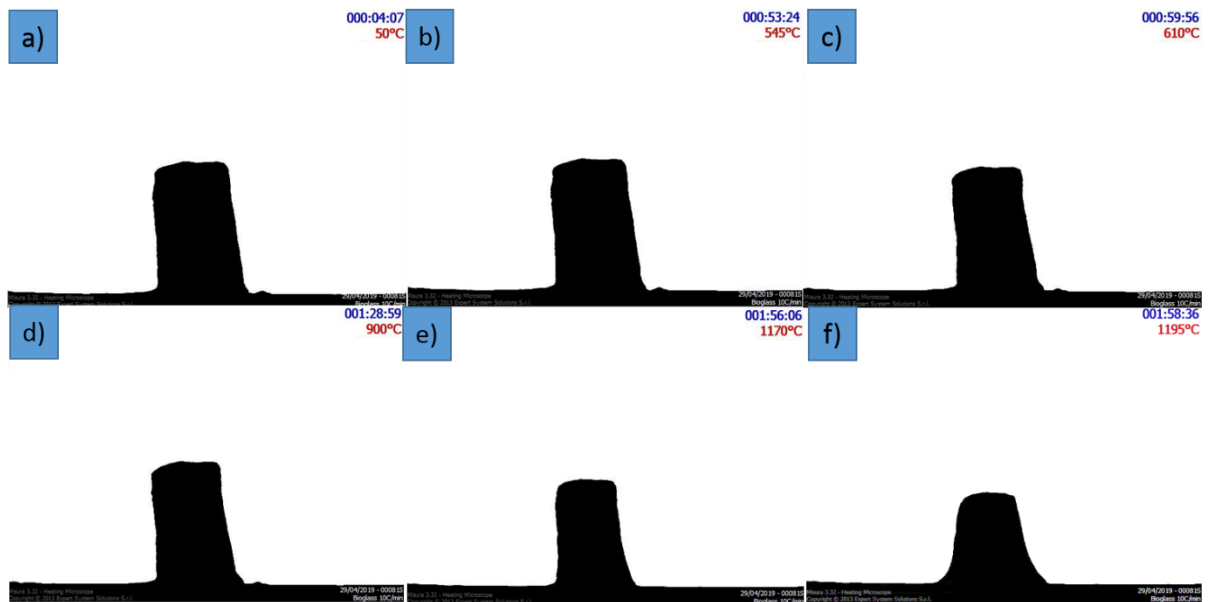
Figure 4.5: *BG sample on HM at different temperatures: a) 50 °C, b) 545 °C, c) 610 °C, d) 900 °C, e) 1170 °C and f) 1195 °C*

Bretcanu et al. reported that characteristic temperatures (sintering, glass transition T_g, crystallization, T_c and melting T_m) recorded using DTA and HM differ, where DTA has characteristic temperatures slightly higher than those observed using HM [234]. The reason behind this could be the sample preparation (see Sections 3.9 and 3.10). Powder is used for DTA and compacted powder for HM. When the powder is compressed (the porosity between the particles is lower), the sintering process is accelerated, and hence the characteristic temperatures of HM are slightly lower than those of DTA. Furthermore, the characteristic temperatures slightly differ for different heating rates, as reported by Bretcanu et al., with the increase in the heating rate, T_g and T_c increase, but T_m decreases [234]. The rate during the sintering of the scaffolds was 5 °C/min, while it was 10 and 20 °C/min for DTA and HM analysis, respectively, due to equipment constrains.

The information gathered from DTA and HM is used for the optimisation of the heat treatment applied in the formation of BG scaffolds. Both sintering intervals and the melting point are taken into consideration, so that the temperatures for the heat treatment should be after the densification process (in this case second densification process) but below the melting point.

Final comments

In this chapter BG powder was synthesized and characterised using SEM, XRD, DTA and HM analysis. BG powder exhibited similar properties, namely amorphous structure, morphology and thermal behaviour, to those found in the literature for BG 45S5 synthesised by melt-quenching method [113, 234, 265]. BG powder will be added to hydrogels and will be used to prepare BG scaffolds which will be subsequently coated with the chitosan-genipin hydrogel. The properties of the hydrogels and the scaffolds will be discussed in Chapters 5 and 6, respectively.

Chapter 5 Hydrogels with and without Bioglass powder

Chitosan-genipin gels with and without Bioglass (BG) powder, synthesized using the method defined in Section 3.1.3 (Table 3.2), were characterised using scanning electron microscopy (SEM), fluorescence intensity (FI), FTIR and compression test, in order to assess the hydrogel structure and the effect of addition of BG powder on the chitosan-genipin gels. The variation in volume, before and after immersion of gels (with and without BG powder) in SBF, as well as the pH of the SBF with gels in, was recorded.

5.1 Scanning electron microscopy of chitosan-genipin hydrogels with and without Bioglass

Scanning electron microscopy (SEM) images (methodology described in Section 3.2) of chitosan-genipin gel at different magnifications are given in Figure 5.1. It can be noted that the hydrogel is highly porous, with pore sizes 10-15 μm in length and 25-35 μm in width. Such pore sizes are reported to be favourable for cells and nutrients flow [266]. Further imaging was conducted for chitosan-genipin-BG hydrogels (Cht-Gen with 1, 3 and 5 mg BG) as shown in Figure 5.2. The addition of BG, in all cases studied (1-5 mg BG), did not noticeably affect the porous structure. It should be mentioned that agglomeration of the particles for higher amounts of BG added to the gels was observed during the synthesis by the naked eye.

It can be observed that the pores in Figure 5.1 and Figure 5.2 are rather elliptical (regardless of a presence of BG). This may be due to the freeze-drying process, as lamellar ice crystals grow during freezing in liquid nitrogen prior to freeze-drying the samples, but also due to cutting of the hydrogels prior to SEM imaging [267, 268].
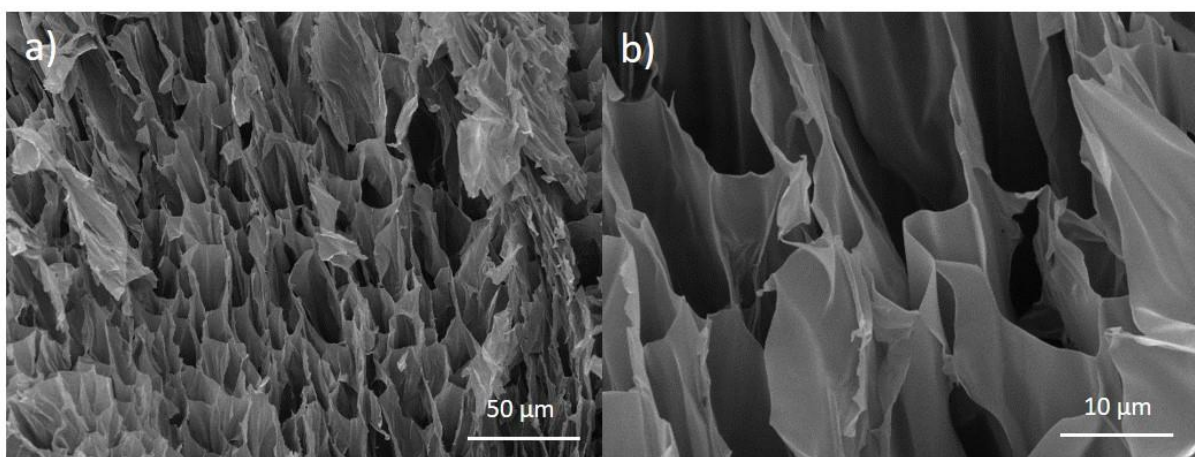
Figure 5.1: SEM images of Cht-Gen hydrogel at different magnification: a) x1000 and b) x5000
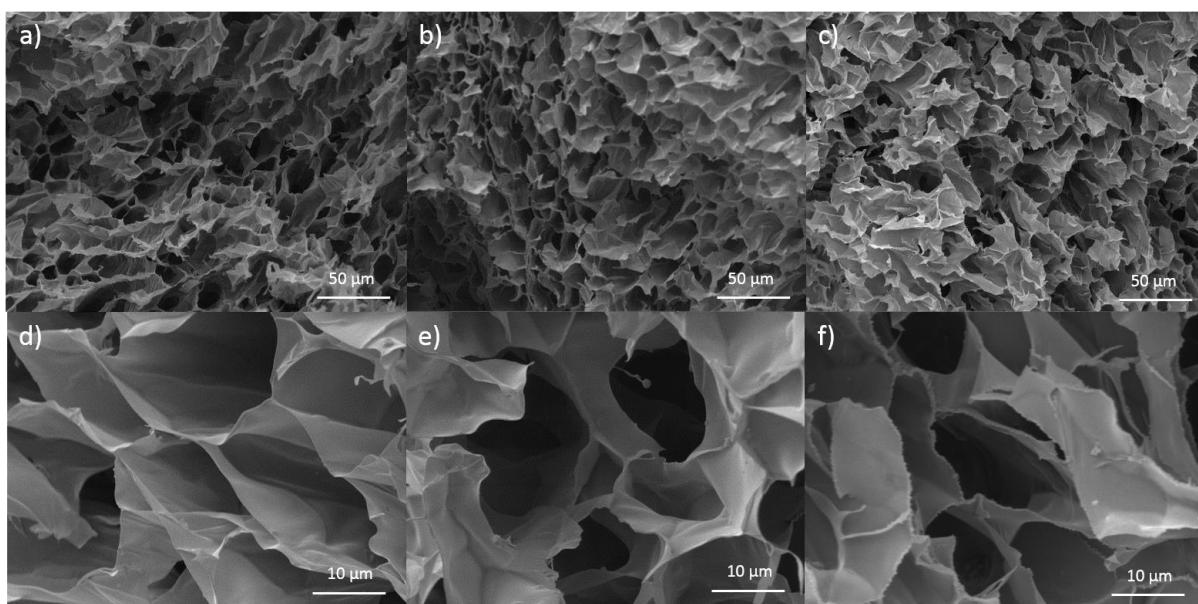
Figure 5.2: SEM images of chitosan-genipin hydrogels with BG: Cht-Gen 1mg BG a) and d); Cht-Gen 3mg BG b) and e); and Cht-Gen 5mg BG c) and f)

5.2 Fluorescence intensity measurement of chitosan-genipin gels with and without Bioglass powder

Figure 5.3 shows fluorescence intensity (FI) of chitosan-genipin hydrogels with and without BG powder (Section 3.1.3, Table 3.2) over the 24 h period. FI was recorded using the procedure detailed in Section 3.3. Since the cross-links which genipin forms with NH_2 groups in polymers, such as chitosan, appear blue by the naked eye and fluoresce in the red region, fluorescence measurements have been used to follow the cross-linking in the hydrogel

samples [136, 140]. Here, FI is measured *in-situ* from the moment all constituents are mixed together so that both gelation process and the final fully formed gels were assessed. As can be denoted from Figure 5.3, there is an initial steep increase in FI (0-4 h), which is considered to correspond to the increase in cross-linking density. Within the first 4 hours, increase in FI is proportional to the amount of BG added, fastest for the highest amount of BG added and slowest for the lowest amount of BG added. After 3-6 h the FI increase slows down and flattens out, likely due to either slowing down (or possible ending) of the cross-linking reaction, or fluorescence quenching effect. The decrease of FI started earlier for Cht-Gen 5 mg BG samples, containing the highest amount of BG (5 mg). As can be seen in Figure 5.3, the FI started to decrease after around 3 h (from the beginning of the reaction) for the gel with 5 mg BG, while for the gel with 1 mg BG or without BG, this process started after 6 h. All curves flattened after 12-15 h from the beginning of the polymerisation. Fully polymerised gels had the FI inverse proportional with the BG amount. Thus, after 24 h (fully polymerised gels) the gel with the highest amount of BG (Cht-Gen 5 mg BG) has the lowest FI values.

The presence of BG powder in the hydrogels is expected to increase the pH. As the hydrogels are considered acidic (pH up to around 5), deprotonisation of some NH_3^+ groups could allow cross-linking [146]. It should be noted that only non-protonated free amino groups can be cross-linked with genipin. The literature reports that at higher pH values of the solutions self-polymerization of genipin can occur in addition to the cross-linking of chitosan and genipin [142]. Therefore, it was possible that samples with a higher amount of BG had higher pH and more cross-linking, together with genipin self-crosslinking, which contributed to the higher FI values measured at the beginning. The pH of the hydrogels was not measured but the pH of the SBF solution with hydrogels showed that addition of BG increases the pH, which will be later discussed in Section 5.4.

In case of the hydrogel without BG, it is possible that the cross-linking density becomes very high (high concentration of fluorophores) so that the penetration depth of the excitation light is reduced leading to a decrease/stagnation in fluorescence intensity [147]. It may be postulated that this is the reason Cht-Gen gel shows a plateau of fluorescence intensity after 15 h. On the other hand, recorded results for gels with BG may be interpreted as the BG particles disrupting the cross-linking process (physically or by inducing genipin self-cross-

linking), yielding a lower amount of cross-links and lower FI after 3-6 h. Equally, BG could react with fluorescent species within the gel to form a non-fluorescent entity, which is known as quenching of fluorescence [147]. Furthermore, it has been reported that the pH can have a significant effect on the fluorescence [147]. Fluorescence intensity can increase or decrease, and a shift of the emission wavelength can occur due to the change of pH. In this way, it is possible that the number of cross-links is similar to that of a Cht-Gen gel and the BG particles serve as reinforcement, but hinder the FI.

Therefore, it is unclear why BG addition decreases the FI values after 3-6 h from the beginning of polymerisation. This was further investigated with compression tests in Section 5.5 to confirm how addition of BG affects mechanical stability of the final hydrogels and if the FI values represent the true amount of the cross-linking in the hydrogels.
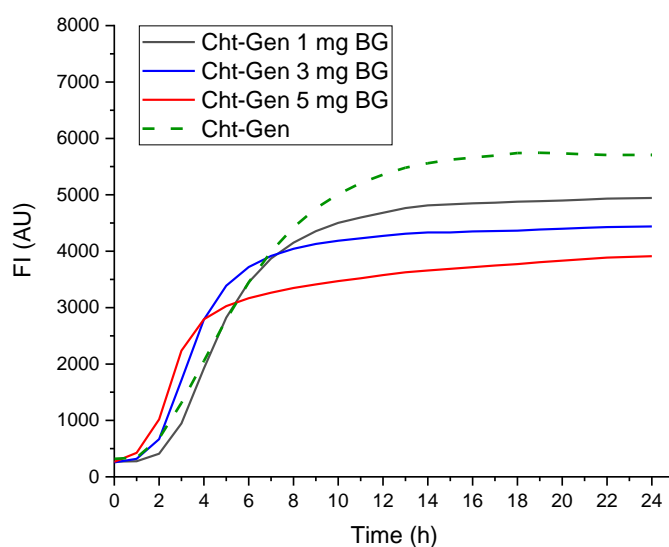
Figure 5.3: *Fluorescence intensity during polymerisation over 24 h for chitosan-genipin and chitosan-genipin-BG gels*

5.3 FTIR of chitosan-genipin hydrogels with and without Bioglass powder

FTIR was performed by the method described in Section 3.4, to gain more insight into the crosslinking mechanism and bonds that are formed in the hydrogels [245, 269]. Figure 5.4 shows the spectra for chitosan and genipin powders, and cross-linked chitosan-genipin hydrogel (Cht-Gen gel, Table 3.2, Section 3.1.3). The summary of the FTIR bands observed in

all three spectra is presented in Table 5.1 with band assignments using the literature [140, 236, 269-273]. A wide band at 3500-3200 cm^{-1} is attributed to overlapping of O-H and N-H stretching vibrations in the spectra of chitosan and hydrogel. Furthermore, FTIR spectra of all samples show a medium band at around 2870 cm^{-1} for C-H stretching. The band around 2100 cm^{-1}, seen on all three spectra, originates from C-C of diamond used in ATR measurement. In the genipin spectrum, bands at 3390 cm^{-1} and 3212 cm^{-1} are assigned to O-H and C=C-H stretching.
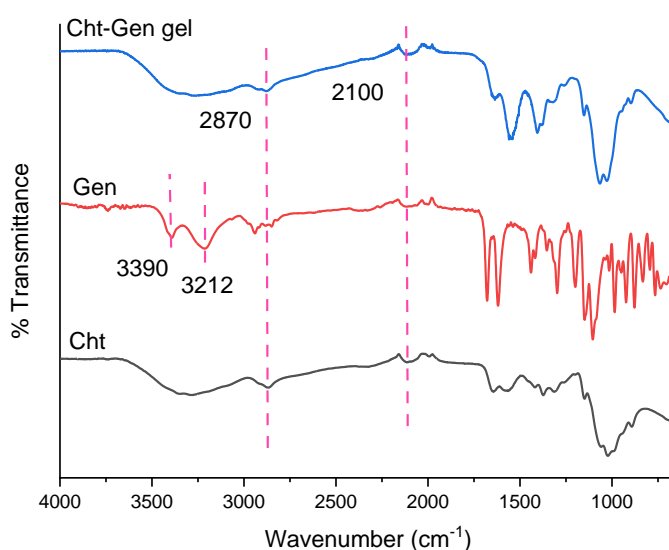
Figure 5.4: FTIR spectra of chitosan powder, genipin powder and Cht-Gen hydrogel- full spectrum 4000 cm^{-1}- 650 cm^{-1}

Below 2000 cm^{-1} a number of bands occur for all samples (Figure 5.5). In the genipin spectrum, bands at 1678 cm^{-1} and 1619 cm^{-1} are due to C=O stretching in carboxymethyl group and C=C aromatic stretching in genipin molecule, respectively. In the chitosan spectrum, the bands at 1649 cm^{-1} and 1560 cm^{-1} belong to the carbonyl (C=O) stretching of the secondary amide (amide I band) in acetylated amine residues and the bending vibration of N-H bond in acetylated amine residues (amide II band), respectively. In the spectra of the cross-linked hydrogel, the band for C=O stretching is shifted to lower frequency (1642 cm^{-1}) and the band at 1560 cm^{-1} increases due to cross-linking reaction and formation of N-H bonds (see Figure 2.14 Section 2.5.2.2). In chitosan and hydrogel spectra, the bands at around 1150, 1060, 1030

and 893 cm^{-1} are for stretching of C-O-C in the cyclic ether. Also, the band at 1150 cm^{-1} is present in the genipin spectrum.

FTIR method confirmed the chemical structure of synthesized hydrogels and cross-linking reaction between chitosan and genipin.
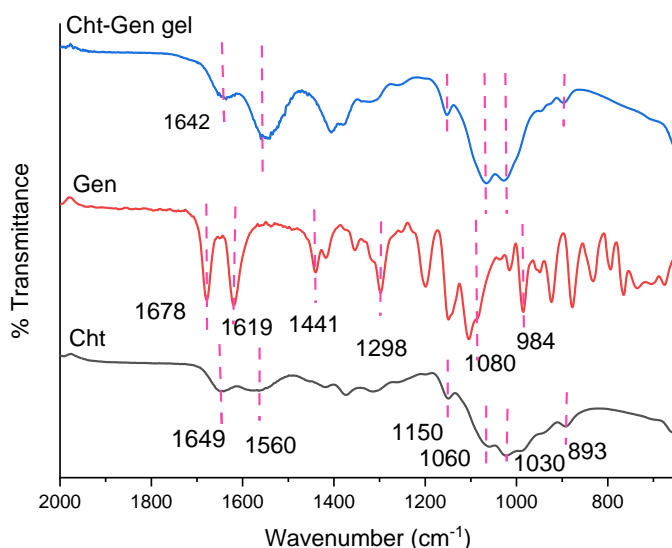
Figure 5.5: *FTIR spectra of chitosan powder, genipin powder and Cht-Gen hydrogel zoomed in from 2000 cm^{-1}- 650 cm^{-1}*

Table 5.1: *FTIR bands for chitosan, genipin and Cht-Gen hydrogel*

Assignments	Bands (cm^{-1})		
	Chitosan	Genipin	Cht-Gen gel
O-H and N-H stretching	3200-3500		3200-3500
O-H stretching		3390	
C=C-H stretching		3212	
C-H stretching	2870		
C=O stretching in carboxymethyl group		1678	
C=O stretching (amide I)	1649		1642
C=C aromatic stretching		1619	
N-H bending (amide II)	1560		1560
CH$_3$ bending of methyl ester		1441	
C-O-C asymmetric stretching of methyl ester		1298	

90

C-O-C (cyclic ether)	1150	1104	1150
Aromatic C-H bending in plane *and* C-O stretching in primary alcohol		1080	
C-O-C (cyclic ether)	1060		1060
C-O-C (cyclic ether)	1030		1030
Aromatic C-H bending out of plane		984	
C-O-C (cyclic ether)	893		893

Figure 5.6 shows FTIR spectra of BG powder (as prepared in the Section 3.1.2), and hydrogels with and without BG powder for comparison (Cht-Gen and Cht-Gen 5 mg BG, Table 3.2, Section 3.1.3). Table 5.2 gives an overview of FTIR bands, which are assigned according to the literature [246, 274, 275]. In the spectrum of BG powder, the bands at 1480 and 1440 cm^{-1} are associated with C-O stretching of CO_3^{2-} adsorbed from the atmosphere. Additionally, the bands at 1010 and 900 cm^{-1} are due to asymmetric Si-O-Si stretching of silanol groups with the presence of network modifiers (Na^+ and Ca^{2+} ions) in the glass structure. The bands at 1010 and 900 cm^{-1} in the spectrum of the hydrogel with BG, could be related to both the presence of silanol groups of BG and the stretching of C-O-C in cyclic ether present in Cht-Gen gel, as they overlap. The bands at 1642 cm^{-1} and 1560 cm^{-1} are also present in the spectrum of Cht-Gen 5 mg BG gel and assigned to C=O stretching (amide I) and N-H bending (amide II), respectively. Furthermore, lower intensity of C=O at 1642 cm^{-1} relative to N-H at 1560 cm^{-1} in the Cht-Gen 5 mg BG gel in comparison to Cht-Gen gel suggests hydrogen bonding between C=O groups in chitosan and hydroxyl groups of BG.
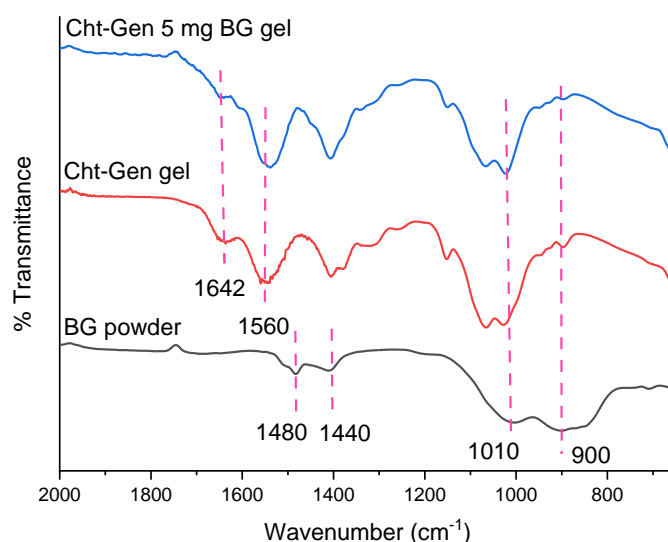
Figure 5.6: FTIR spectra of BG powder, chitosan-genipin hydrogel and chitosan-genipin hydrogel with BG

Table 5.2: FTIR bands for BG powder, Cht-Gen gel and Cht-Gen 5 mg BG gel

Assignments	Bands (cm^{-1})		
	BG powder	Cht-Gen gel	Cht-Gen 5 mg BG gel
C=O stretching (amide I)		1642	1642
N-H bending (amide II)		1560	1560
C-O stretching of CO_3^{2-} (from air)	1480		
	1440		
asymmetric Si-O-Si stretching of silanol groups	1010		
	900		

5.4 Volume-change experiments of chitosan-genipin hydrogels with and without Bioglass powder

Chitosan-genipin hydrogels with and without BG powder, synthesised following procedure described in Section 3.1.3 (Table 3.2), were further evaluated upon immersion in simulated body fluid (SBF) using the method described in Section 3.6. SBF solution represents an environment (composition and pH=7.4) similar to human body plasma, and it has been used for *in vitro* testing of biomaterials [276-278]. As the chitosan-genipin gels are pH

92

responsive, the tests in SBF were performed in order to examine their behaviour in terms of the conformational (volume) change and their effect on the pH when they are immersed in the solution for prolonged time. The effect of the addition of BG was also investigated. The samples were held in SBF solution for up to 7 days at 37.0 °C (to simulate the human body temperature), followed by pH measurements and calculations of volume. Three samples of each composition of the gel were tested. Information from this study could help in predicting the hydrogels behaviour *in vivo*. For tissue engineering applications, biodegradable implants degrade over a period ranging from a few weeks up to a few months; therefore it is necessary to investigate their behaviour over time. Due to equipment and lab availability, the tests in SBF were carried out for 7 days. It should be noted that upon the preparation, the pH of the SBF solution was 7.40 at 36.5 °C. Even though the samples were kept at 37 °C, the pH of the samples, as well as the SBF before the immersion of the samples, was measured at 36.7 ± 0.2 °C, due to equipment restrictions and temperature of the lab. The pH of the SBF was ~ 7.35 before addition of samples.

For all samples studied it can be noted that after 24 h of immersion pH values decreased from the initially measured value of ~ 7.35, but the more BG powder in the gel, the higher the pH (Figure 5.7). For example, the pH values for the hydrogel with 5 mg BG was 7.17, for the hydrogel with 3 mg BG 7.04, while pH for the chitosan-genipin hydrogel without BG was 6.78. The reason for the higher pH values for samples containing BG is an intensive ion exchange between cations present in BG, such as Ca^{2+} and Na^+, and H^+ ions from the SBF solution (Figure 2.5, Section 2.4.1), which leads to an increase in pH [4]. Furthermore, the change in volume of the hydrogels followed an opposite trend - the more BG in the sample, higher the volume decrease. The chitosan-genipin gels shrank to 84 % and the hydrogel with 5 mg BG to 49 % of their initial volume. Chitosan-based hydrogels are reported to shrink in the basic environment due to deprotonation of NH_3^+ groups [236]. In case of the gels containing BG powder, it can be suggested that BG increases the pH which in turn leads to increase in deprotonation of chitosan chains and greater shrinkage. Therefore, increasing the amount of the BG in the hydrogel, the values of pH and the shrinkage of the hydrogels increase.
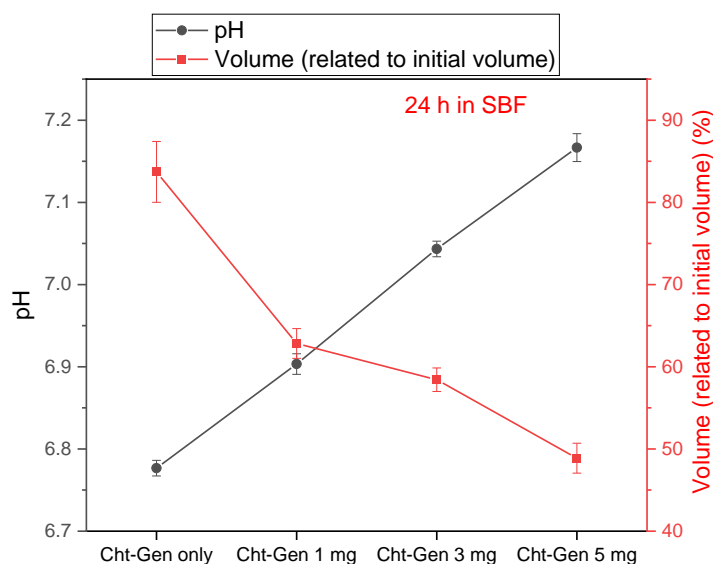
Figure 5.7: *pH and volume variation after 24 h in SBF observed in chitosan-genipin and chitosan-genipin-BG hydrogels*

Figure 5.8 shows the volume variations of samples after 24 h, 3 days and 7 days of immersion in SBF (Section 3.6). In comparison to 24 h, longer time of immersion (3 and 7 days) allowed all hydrogels to shrink below 40 % of their initial volume. While the trend noted at day 3 shows that Cht-Gen gels with BG had a slightly higher volume than Cht-Gen, after 7 days the Cht-Gen gel shrank to around 35 % of its volume, while the hydrogels with BG had even lower volume around 30 %, independent of the amount of BG. Results suggest that when the hydrogels are kept in SBF for 24 h large variations of volume are observed, while there are only minor variations after 3 days.
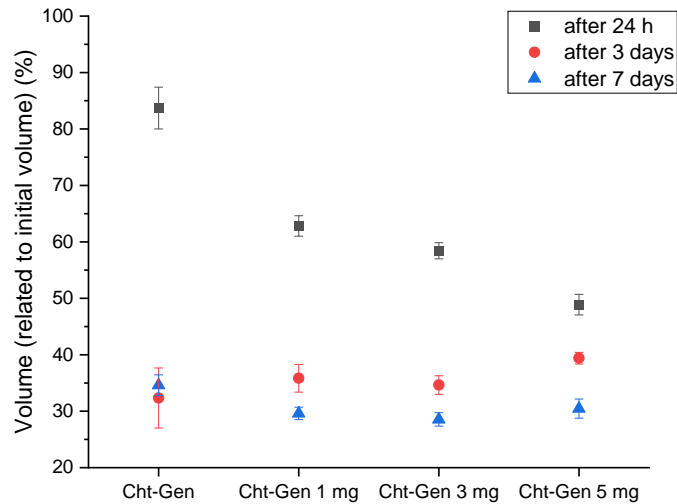
Figure 5.8: *Volume variation after 24 h, 3 days and 7 days in SBF observed in chitosan-genipin and chitosan-genipin-BG hydrogels*

The pH values for the samples measured at different time points for 7 days are shown in Figure 5.9. The largest change in pH is observed at 2 h, when the pH values for all samples decrease from the initial 7.35 for SBF solution, being higher for higher amount of BG. It could be observed that pH does not change significantly after 24 h of immersion for all samples. Also, the same trend remains - more BG in the samples, the higher the pH. Leaching of BG powder is considered to lead to higher pH and greater shrinking within the first 24 h of immersion (Figure 5.7). However, after 3 days, the hydrogels had enough time to shrink, so all the compositions had similar volume at days 3 and 7, independent on pH (Figure 5.8).
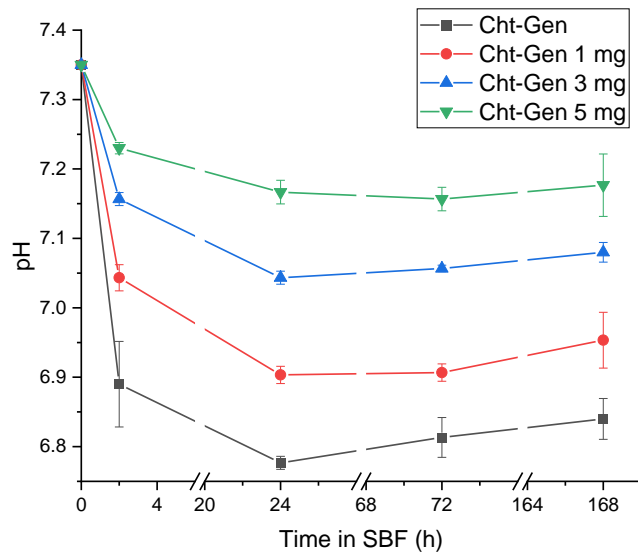
Figure 5.9: *pH measured for gels after 7 days in SBF observed in chitosan-genipin and chitosan-genipin-BG hydrogels*

Figure 5.10 shows correlation between pH and variation in volume measured after 7 days of immersion in SBF for hydrogels with and without BG powder. It can be seen that pH and volumes for the samples have opposite trends. The more BG in the samples, pH is higher, while the volume is smaller, in comparison to the sample without BG. In terms of volume, there is no significant difference with different amounts of BG.
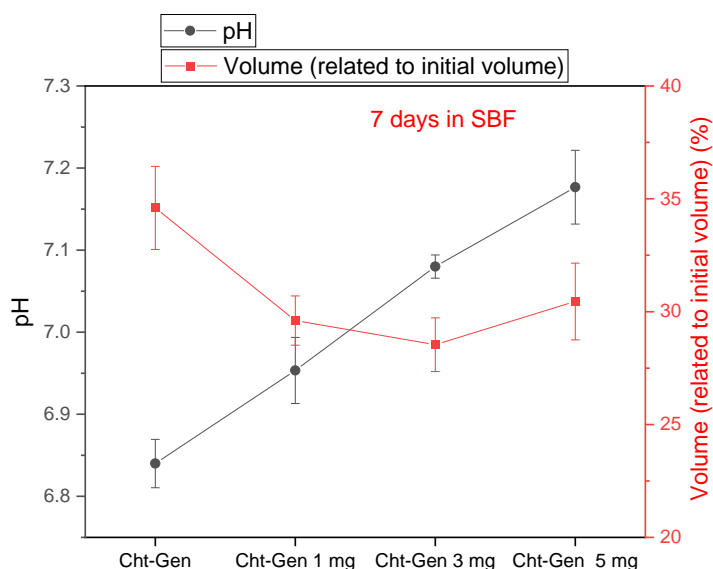
Figure 5.10: *pH and volume variation after 7 days in SBF observed in chitosan-genipin and chitosan-genipin-BG hydrogels*

5.5 Compression test of chitosan-genipin hydrogels with and without Bioglass powder

Compression test was performed for hydrogels with and without BG powder (Section 3.1.3, Table 3.2) in order to investigate if BG improves mechanical properties of the hydrogels and link these findings to FI measurements (Section 5.2). Previously, the fluorescence intensity measurements showed that the increase of FI slows down after 3-6 h and the values of FI after 24 h decrease with the increase of the amount of BG. It was reported that higher amount of cross-linking yields stronger genipin-cross-linked gels that exhibit higher fluorescence intensity [140]. The mechanical tests were used to confirm if FI values correspond to the amount of the cross-linking in the samples, e.g. if the decrease in FI occurs because BG hinders the cross-linking reaction or obstructs the FI measurement. Also, the influence of immersion of the samples in SBF on mechanical properties is also investigated. It should be noted that 3 samples per each gel composition were tested.

For samples tested upon synthesis without SBF (following the method described in Section 3.7), compressive stress increases when BG is added to the hydrogels (Figure 5.11). The average compressive stress is 0.69 kPa for chitosan-genipin gel, 0.82 kPa for the gel with 1 mg BG, 1.06 kPa for gel with 3 mg BG and 1.07 kPa for the gel with 5 mg BG. In terms of the average compressive modulus, it also increases from 3.41 kPa for the gel without BG, to

4.15 kPa for the gel with 1 mg BG and to about 5.22 kPa for the gels with 3 and 5 mg BG. It can be observed that the addition of up to 5 mg BG to the chitosan-genipin gels increases both compressive stress and modulus, while these values are higher for a higher amount of BG (3 and 5 mg) in comparison to the gel with 1 mg BG. It can also be seen that the standard deviations seem significant for the compressive modulus. The reason is the irregular shape of the samples, as well as the uneven surfaces, that affect the mechanical test. Testing larger number of samples would reduce the standard deviation.

These results showed that BG particles do not greatly disrupt the cross-linking reaction in the hydrogels and that the FI recorded for fully polymerized hydrogels does not correspond to the actual amount of cross-linking. There might be a slight decrease in the cross-linking due to BG particles but this is compensated by the effect of BG reinforcement. It can be concluded that under conditions studied addition of BG powder improves the mechanical properties of the hydrogels and that the FI measurement is obstructed by the BG particles which lower the FI.

In the case of Cht-Gen hydrogel, it cannot be concluded if the cross-linking reactions stops after 15 h, or if it continues, but FI reaches a high value which leads to self-quenching of fluorescence keeping the FI constant after 15 h. In order to determine if the cross-linking reaction terminates after 15 h additional compression tests could be done for hydrogels which are not fully polymerized (24 h) but for a shorter time (15 h).
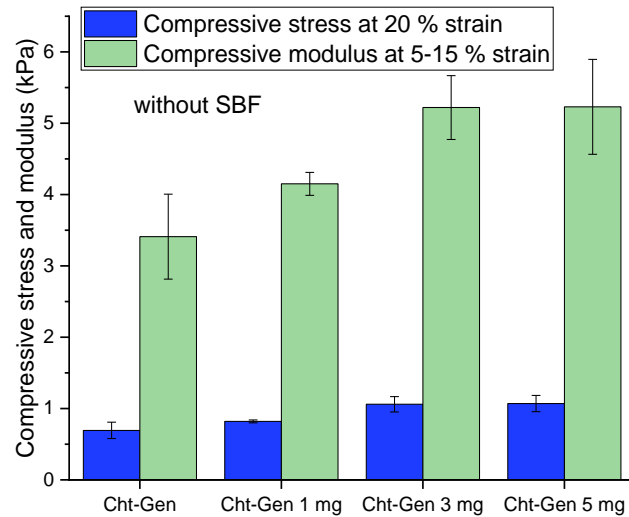
Figure 5.11: *Compressive stress at 20 % strain and compressive modulus at 5-15 % strain for chitosan-genipin hydrogels with and without BG tested without SBF*

Similar trends are observed when the gels were tested after immersion in SBF for 24 h (method detailed in Section 3.7) (Figure 5.12). Both stress and modulus increase with the addition of BG in the hydrogels. These values are higher for a higher content of BG (3 and 5 mg) in comparison to Cht-Gen 1 mg BG. Again, large standard deviations are due to the irregular shape of the hydrogels.
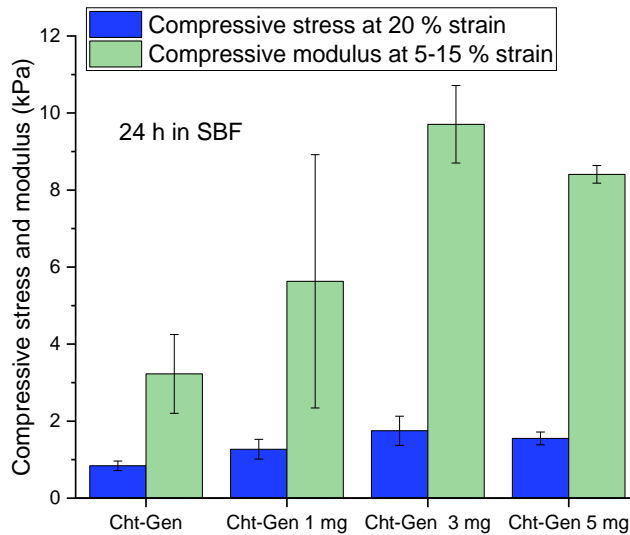
Figure 5.12: *Compressive stress at 20 % strain and compressive modulus at 5-15 % strain for chitosan-genipin hydrogels with and without BG tested after immersion in SBF for 24 h*

Figure 5.13 shows a comparison of compressive stress for the samples tested before and after immersion in SBF for 24 h. In both cases addition of BG increases the compressive stress, with higher values obtained for 3 and 5 mg of BG. Also, after immersion in the SBF solution, all hydrogel compositions have higher stress. The main reason is that samples shrink upon immersion in SBF (Figure 5.7) and exhibit higher stress. Similarly, the modulus shows this trend (Figure 5.14). Chitosan-genipin gel with 5 mg BG has equal or lower stress than sample with 3 mg BG. Likewise, values of compressive modulus are also equal or lower for Cht-Gen 5 mg BG than for Cht-Gen 3 mg BG. The reason might be agglomeration of BG particles. It has been reported that homogenous dispersion of bioglass particles in the polymer matrix is important for mechanical properties and that the agglomeration of the particles leads to a decrease in these properties [199].
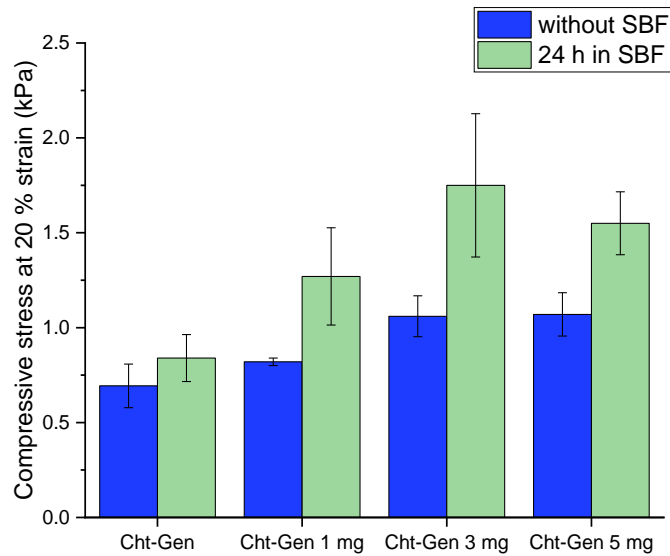
Figure 5.13: Comparison of compressive stress at 20 % strain for chitosan-genipin gels with and without BG tested without SBF and after immersion in SBF for 24 h
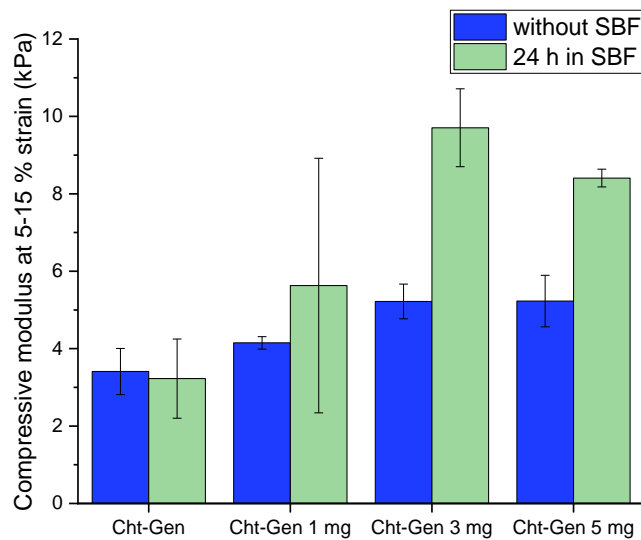
Figure 5.14: Comparison of compressive modulus at 5-15 % strain for chitosan-genipin gels with and without BG tested without media and after immersion in SBF for 24 h

Compressive stress and modulus for the hydrogels immersed in the SBF for 3 days are shown in Figure 5.15. In this case, no clear trend is observed. The addition of 1 mg and 5 mg of BG does not improve the mechanical properties of the chitosan-genipin gels, as Cht-

Gen 1 mg BG and Cht-Gen 5 mg BG show equal or lower both stress and modulus in comparison to the gel without BG. However, the addition of 3 mg of BG shows the highest values for both stress and modulus, which was also observed for 24 h of immersion in SBF.
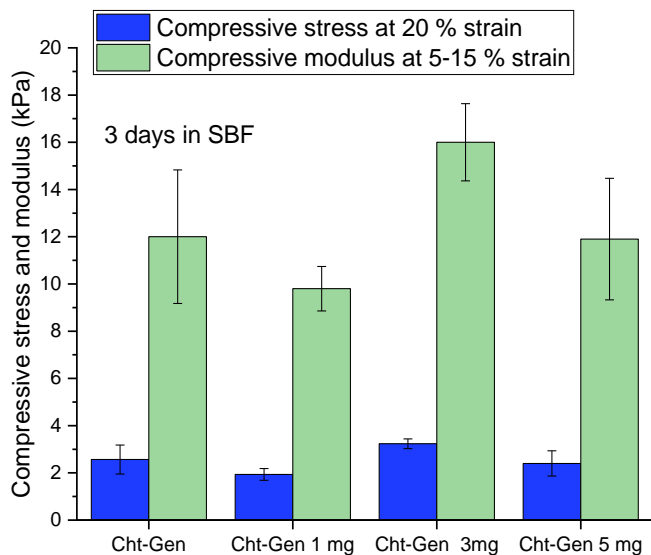
Figure 5.15: *Compressive stress at 20 % strain and compressive modulus at 5-15 % strain for chitosan-genipin hydrogels with and without BG tested after immersion in SBF for 3 days*

Figure 5.16 shows compressive stress and modulus for the hydrogels immersed in the SBF for 7 days. It seems that with the increase in BG content, values for both stress and modulus increase.
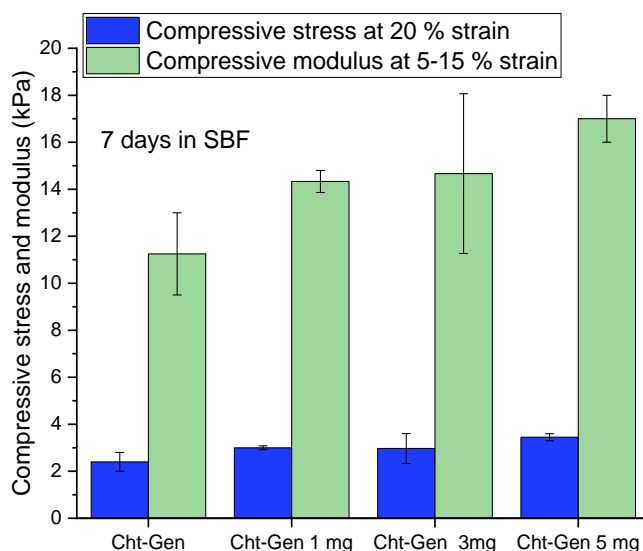
Figure 5.16: *Compressive stress at 20 % strain and compressive modulus at 5-15 % strain for chitosan-genipin hydrogels with and without BG tested after immersion in SBF for 7 days*

In order to compare compressive characteristics for the hydrogels tested before and after different times of SBF post-treatment, average values of compressive stress are shown in Table 5.3 and the compressive stress (Figure 5.17) is plotted together for hydrogels tested without SBF, and after immersion in the SBF for 24 h, 3 days and 7 days. Likewise, the average compressive modulus for hydrogels tested without SBF, and after 24 h, 3 days and 7 days of immersion in SBF is presented in Table 5.4, while the graph is shown in Figure 5.18. The general trend is that compressive stress and modulus values increase with the increase of BG content and after immersion in SBF. The average values for stress for Cht-Gen gel range from 0.69 kPa without media to 2.40 kPa after 7 days of immersion in SBF. When 5 mg of BG was added to the chitosan-genipin hydrogel, an increase in stress from 1.07 kPa to 3.45 kPa is observed for samples without media and after 7 days of immersion, respectively. Similarly, while average modulus for Cht-Gen hydrogel is 3.41 kPa when no media is added, 7 days of immersion in SBF yields a higher stress of 11.24 kPa. The average compressive modulus for the hydrogel Cht-Gen 5 mg BG is 5.23 kPa and 17.00 kPa for the samples tested without media and after immersion for 7 days in SBF, respectively.

Table 5.3: Average compressive stress at 20 % strain for chitosan-genipin gels with and without BG tested without SBF and after immersion in SBF for 24 h, 3 days and 7 days

Hydrogel	Average compressive stress at 20 % strain (kPa)			
	Without SBF	24 h in SBF	3 days in SBF	7 days in SBF
Cht-Gen	0.69 ± 0.11	0.84 ± 0.12	2.56 ± 0.61	2.40 ± 0.40
Cht-Gen 1 mg BG	0.82 ± 0.02	1.27 ± 0.26	1.93 ± 0.25	3.00 ± 0.08
Cht-Gen 3 mg BG	1.06 ± 0.11	1.75 ± 0.38	3.23 ± 0.20	2.97 ± 0.63
Cht-Gen 5 mg BG	1.07 ± 0.11	1.55 ± 0.17	2.40 ± 0.53	3.45 ± 0.15
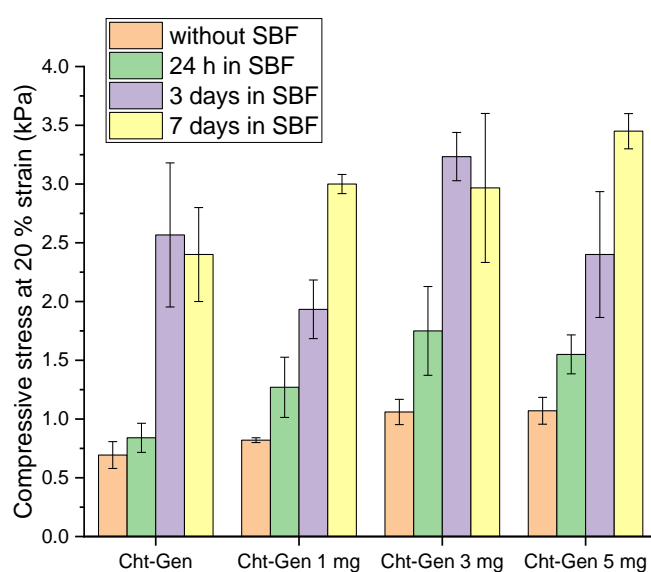
Figure 5.17: Comparison of compressive stress at 20 % strain for chitosan-genipin gels with and without BG tested without SBF, and after immersion in SBF for 24 h, 3 days and 7 days

Table 5.4: *Average compressive modulus at 5-15 % strain for chitosan-genipin gels with and without BG tested without SBF and after immersion in SBF for 24 h, 3 days and 7 days*

	Average compressive modulus at 5-15 % strain (kPa)			
Hydrogel	**Without SBF**	**24 h in SBF**	**3 days in SBF**	**7 days in SBF**
Cht-Gen	3.41 ± 0.59	3.23 ± 1.02	12.00 ± 2.83	11.24 ± 1.75
Cht-Gen 1 mg BG	4.15 ± 0.16	5.63 ± 3.29	9.80 ± 0.94	14.33 ± 0.47
Cht-Gen 3 mg BG	5.22 ± 0.45	9.70 ± 1.00	16.00 ± 1.63	14.67 ± 3.40
Cht-Gen 5 mg BG	5.23 ± 0.66	8.40 ± 0.23	11.90 ± 2.57	17.00 ± 1.00
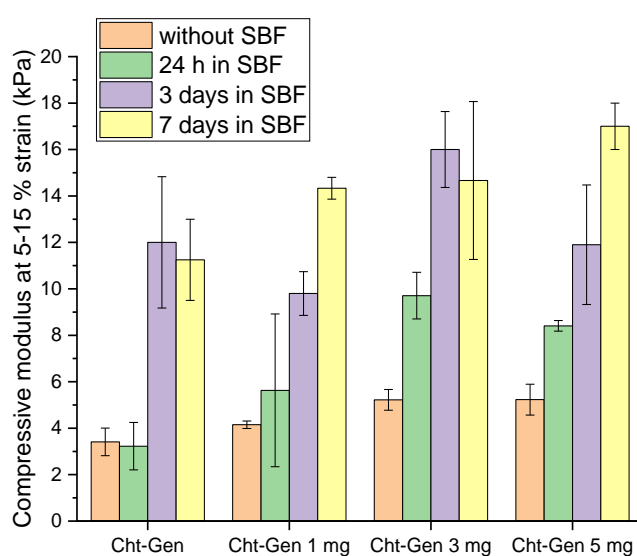
Figure 5.18: *Comparison of compressive modulus at 5-15 % strain for chitosan-genipin gels with and without BG tested without SBF, and after immersion in SBF for 24 h, 3 days and 7 days*

A relationship between volume and mechanical properties of hydrogels after immersion in SBF could be observed. Plots showing the correlation between the volume variation and compressive stress (Figure 5.19), as well as the volume variation and compressive modulus (Figure 5.20) after 24 h of immersion in SBF are presented. It can be noticed that with the addition of 1 and 3 mg BG both stress and modulus increase linearly, while the volume decreases. Exception was Cht-Gen 5 mg BG, which had the lowest volume but stress and modulus lower than for Cht-Gen 3 mg BG. However, for the time of immersion

in SBF of 3 days, no such trends can be observed (Figure 5.21 and Figure 5.22). The volume seems similar for all compositions (Cht-Gen and Cht-Gen with 1-5 mg BG), while stress varies between 1.6 kPa and 3.6 kPa with no obvious trend (Figure 5.21). Similarly, no trend between volume and modulus were observed for samples which were immersed in SBF for 3 days (Figure 5.22). Furthermore, trends are again visible for samples which were immersed in SBF for 7 days, when both stress and modulus seem to increase with the increase of BG in the hydrogels, followed by the decrease of volume (Figure 5.23 and Figure 5.24). Cht-Gen 5 mg BG had the highest average stress and modulus but higher volume than Cht-Gen 3 mg.
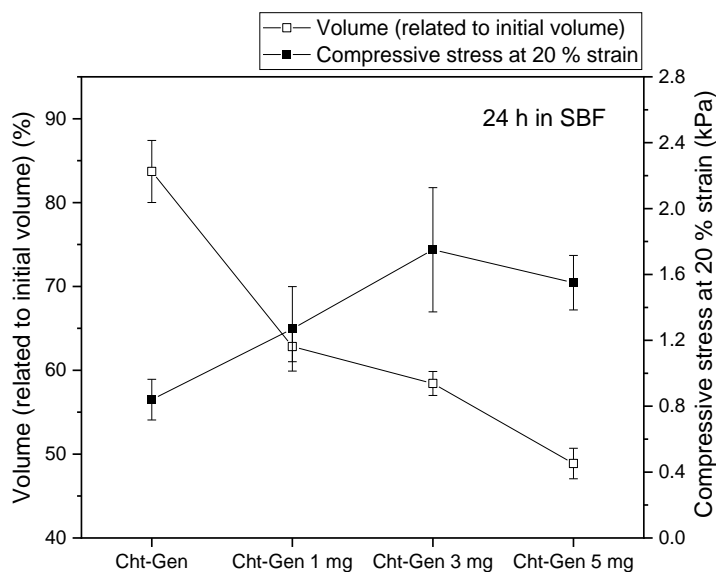
Figure 5.19: *Volume and compressive stress at 20 % strain after 24 h in SBF strain for chitosan-genipin gels with and without BG*
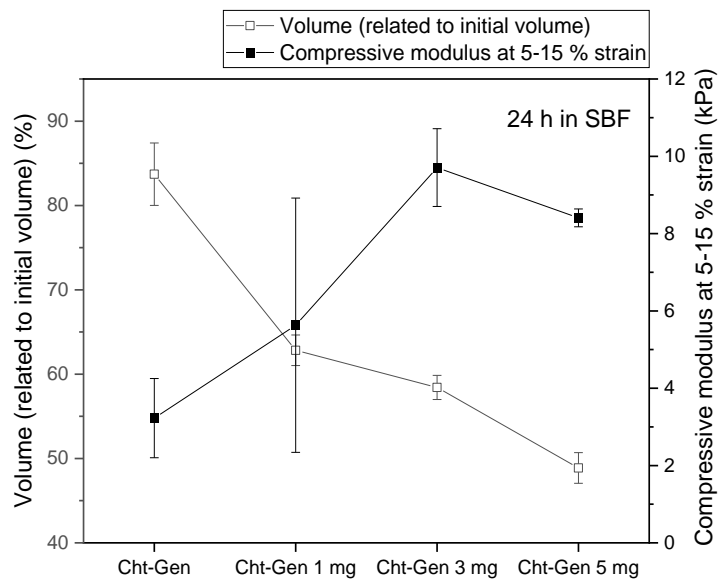
Figure 5.20: *Volume against compressive modulus at 5-15 % strain after 24 h in SBF strain for chitosan-genipin gels with and without BG*
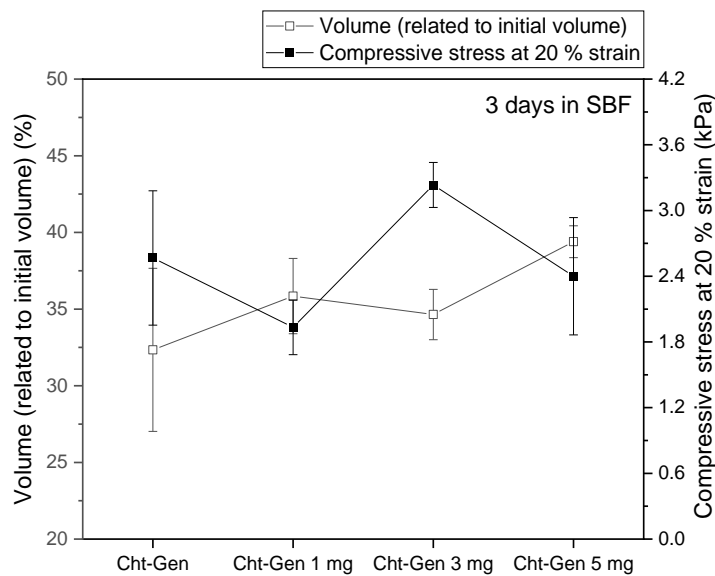
Figure 5.21: *Volume against compressive stress at 20 % strain after 3 days in SBF strain for chitosan-genipin gels with and without BG*
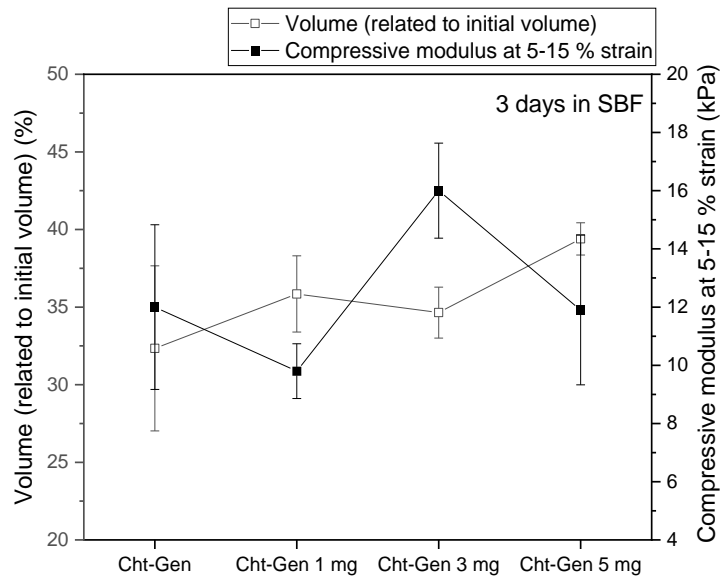
Figure 5.22: *Volume against compressive modulus at 5-15 % strain after 3 days in SBF strain for chitosan-genipin gels with and without BG*
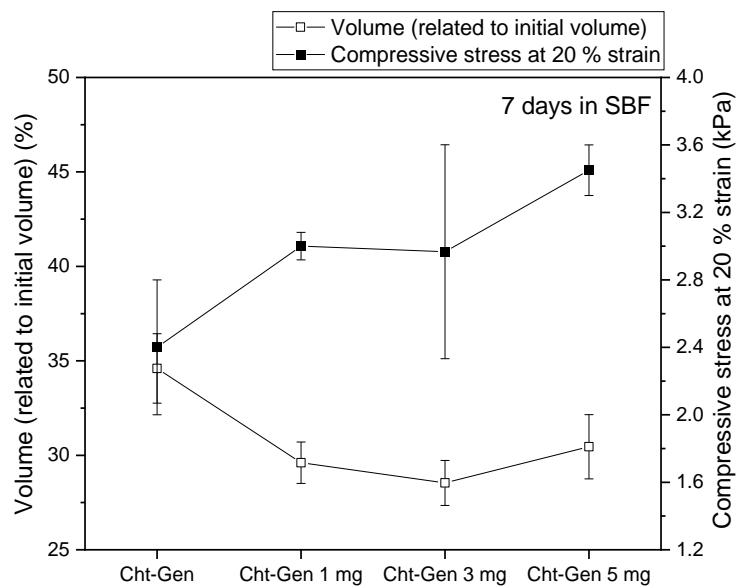
Figure 5.23: *Volume against compressive stress at 20 % strain after 7 days in SBF strain for chitosan-genipin gels with and without BG*
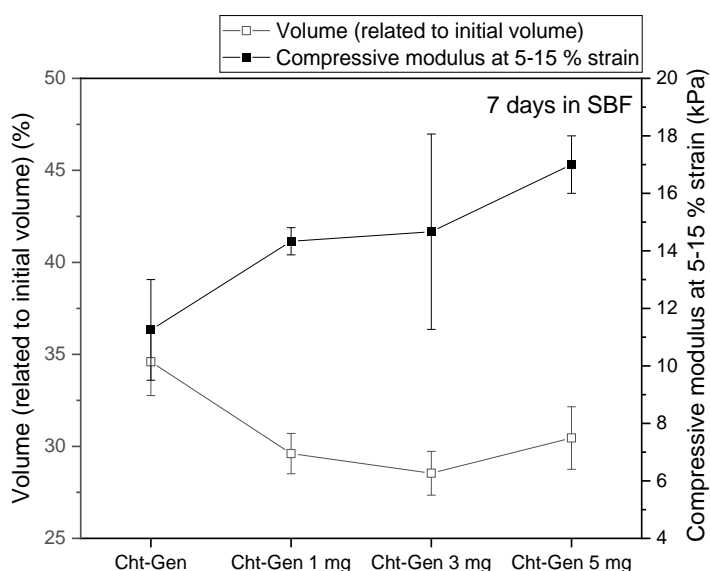
Figure 5.24: *Volume against compressive modulus at 5-15 % strain after 7 days in SBF strain for chitosan-genipin gels with and without BG*

Final comments

In this chapter, chitosan-genipin hydrogels were synthesized and characterised using SEM, fluorescence intensity measurement, FTIR and compression test. The variation in volume and the pH after immersion in SBF were recorded. The influence of BG powder on their properties was also investigated. It should be noted that other authors rarely reported use of genipin as a cross-linker, especially in combination with chitosan as an organic part of the composite (Table 2.4). According to the data for chitosan-genipin hydrogels with BG powder, it can be concluded that addition of BG does not affect the microstructure and gelation of the hydrogels. Fluorescent intensity measurement was previously reported for other genipin cross-linked gels (without BG) [136, 140, 151]; however, this method does not seem adequate to assess the cross-linking process with the presence of BG. Mechanical properties of the hydrogels were enhanced by the addition of BG even though still showing low values for bone tissue requirements. In the literature, freeze-drying is frequently reported as a method to prepare hydrogel scaffolds; however, this method alters the properties of the hydrogels. Hence, in this work, hydrogels were cross-linked at physiological temperature (37° C) and kept in a wet state. Studying hydrogels in this form and under these conditions gives an opportunity for their applications via injection of the hydrogels *in vivo* and *in situ* gelation. Furthermore,

chitosan hydrogels can exhibit smart behaviour of swelling-deswelling in different pH environments. Here, gels shrank in the basic SBF, while BG showed a significant effect on the percentage of shrinking. Mechanical properties of the hydrogels have rarely been assessed upon immersion in SBF in the literature. Here, the shrinkage of the hydrogels can be linked to the increase in mechanical stability. Furthermore, BG improves the mechanical properties not only by inducing more shrinkage, but also serves as a reinforcement on its own. However, chitosan-based hydrogels with BG are not adequate for bone tissue engineering applications due to low mechanical properties. It is suggested that a cross-linking agent, such as GPTMS, could be used to further improve the mechanical properties.

In the following section, the second method, coating of the glass-ceramic scaffolds with the hydrogel, was used in order to obtain mechanically stronger composites.

Chapter 6 Uncoated and coated Bioglass scaffolds

Herein, the selection of the heat treatments used to produce Bioglass (BG) scaffold is discussed. BG scaffolds were characterized using scanning electron microscopy (SEM) in order to observe the porous structure and assess the size of the pores, as well as to observe the influence of the different PU foams used for the preparation of scaffolds on the final structure. Also, the subsequent hydrogel coating, and its effect on the porosity was examined. XRD was performed in order to identify crystalline phases in the prepared scaffolds.

6.1 Selection of the heat treatment for the preparation of Bioglass scaffolds and scanning electron microscopy (SEM) of uncoated Bioglass scaffolds

The characteristic temperatures in the BG powder during heating were captured on DTA and HM graphs (Figure 4.3 and Figure 4.4). According to that information, a three-step heat treatment for the synthesis of BG scaffolds was chosen. The first step of the heating was at 550 °C and it was used to burn the PU foam and to form a porous replicate structure made of BG, similarly as reported in the literature [113, 214, 279]. As detailed in the Section 4.4, the maximum temperature of the heating treatment should be below the melting point (1200 °C), and preferably between 1000 and 1100 °C, in order to accomplish good sintering [234]. Hence, maximum temperatures of 1000 °C (HT 1, BG 1) and 1100 °C (HT 2, BG 2 and HT 3, BG 3 and BGS) were used. Additionally, an intermediate step at 800 °C was also used (HT 3, BG 3 and BGS) to allow crystallization, in order to improve mechanical stability of the scaffolds.

Figure 6.1 shows the PU foam 1 used for the preparation of BG 1, BG 2 and BG 3 scaffolds under SEM. SEM images in Figure 6.2 show porous structures of BG scaffolds (BG 1, BG 2 and BG 3) prepared using different heat treatments. Factors, such as mechanical stability, assessed by handling/hand grip, and sinterability, assessed by SEM (neck formation), were taken into account to choose the optimal heat treatment. Samples which can be handled without crumbling or breaking, and with SEM images showing neck formation and dense struts, were considered well sintered. It can be seen that when the final temperature is 1000 °C (HT 1), the particles are not well sintered and despite the formation of necks between particles, particles shape and edges are still visible (Figure 6.2 a and d). Mechanically, these samples were weak and broke down easily when handled. When the temperature is increased to 1100 °C (HT 2), the BG particles are better sintered and are mechanically stronger (Figure

6.2 b and e). For the HT 3, the structure remained similar as for the HT 2 in terms of sinterability and samples seemed the most stable by the visual assessment and hand grip, and therefore, this heat treatment was chosen for further testing (Figure 6.2 c and f).
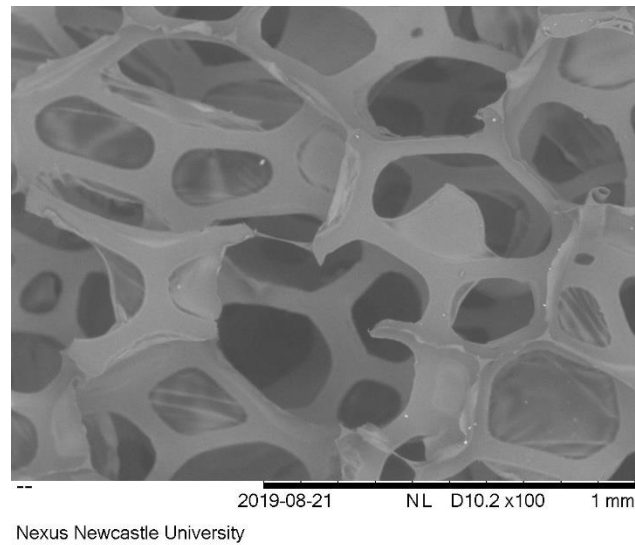
Figure 6.1: PU foam 1 used for the preparation of BG 1, BG 2 and BG 3
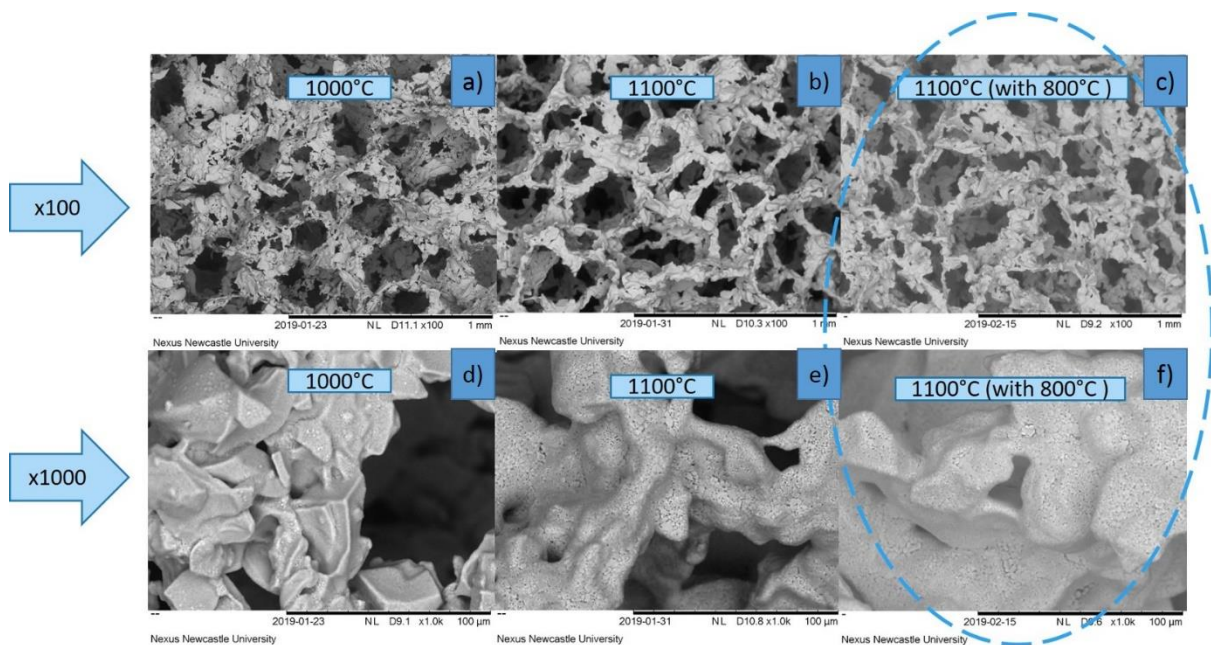
Figure 6.2: BG scaffolds made using different heat treatments at magnification x100: a) BG 1 (HT 1), b) BG 2 (HT 2) and c) BG 3 (HT 3) and at x1000 d) BG 1 (HT 1), e) BG 2 (HT 2) and f) BG 3 (HT 3)

After initial optimisation studies and the heat treatment selection (HT 3), PU foam 2 with a different impregnation method has been employed in order to improve the mechanical

stability of the BG scaffolds. The PU foam 2 used for the preparation of BGS and AWS scaffolds is shown in Figure 6.3. According to the SEM images, PU foam 2 (Figure 6.3) has a similar structure to PU foam 1 (Figure 6.1) and it is therefore presumed that the porosity of the PU foam 2 is also approximately 60 ppi, as it is not provided by the manufacturer. Figure 6.4 shows the structure of BGS scaffolds using SEM, resembling the structure of the PU foam 2. An open porosity with pores ranging from 100 μm to 300 μm can be observed, with the average of 200 μm assessed by measuring the pores using ImageJ software. This open porous structure and these pore sizes are considered suitable for bone ingrowth, as literature reports that open porosity and pores with at least 100 μm are necessary [35].
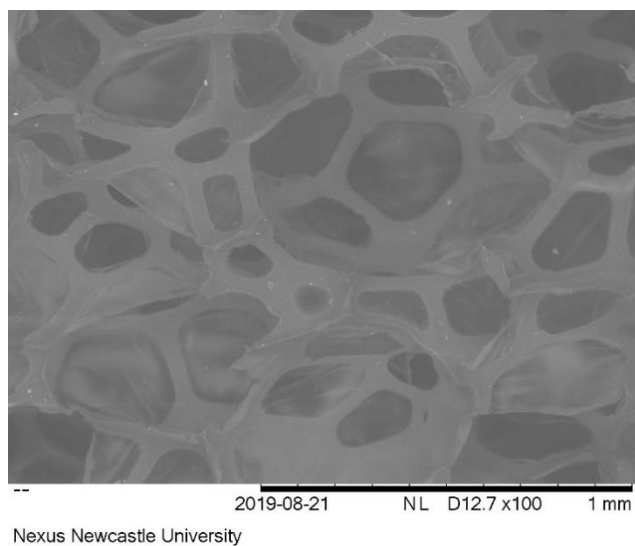
Figure 6.3: *PU foam 2 used for preparation of the BGS and AWS (Section 7.2.1)*
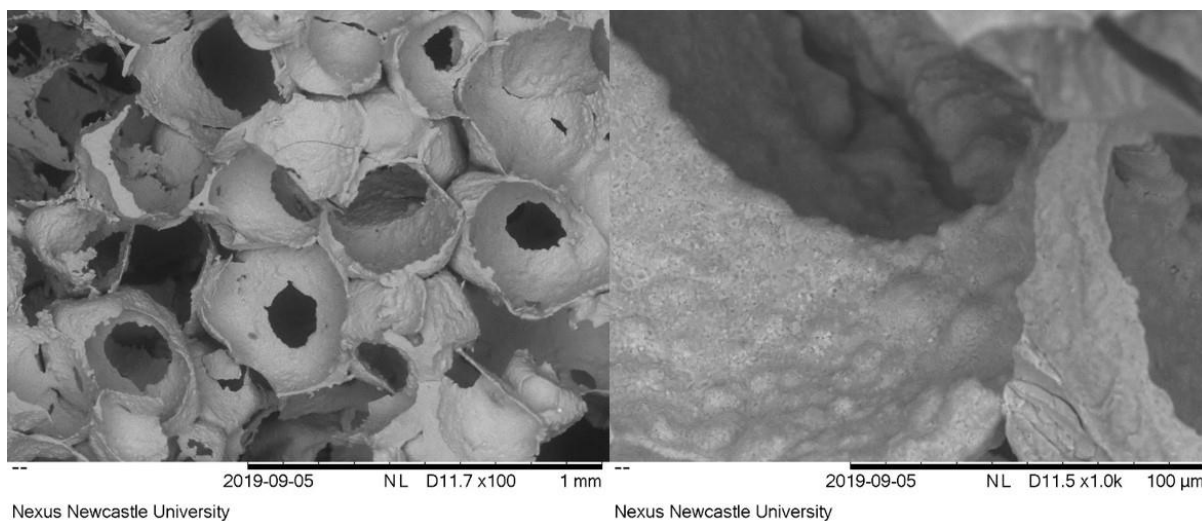
Figure 6.4: *SEM image of BGS using PU foam 2 and HT 3 at x100 (left) and x1000 (right)*

113

6.2 X-ray diffraction (XRD) of uncoated Bioglass scaffolds

After the heat treatment, the XRD patterns show a crystalline structure of the BG scaffolds (BG 3) in comparison to the amorphous BG powder (Figure 6.5). Sharp, distinctive peaks for the two crystalline phases have been registered: $Na_4Ca_4Si_6O_{18}$ (COD 96-901-5838) and $Na_2Ca_4(PO_4)_2SiO_4$, as anticipated for the BG after heat treatment [214, 234, 265]. Crystallization in scaffolds synthesised by this method cannot be avoided because the temperatures used for the heat treatment exceed the crystallization temperature of the BG. Although crystallization hinders degradation and bioactivity, it increases mechanical strength of the scaffolds [4, 113].
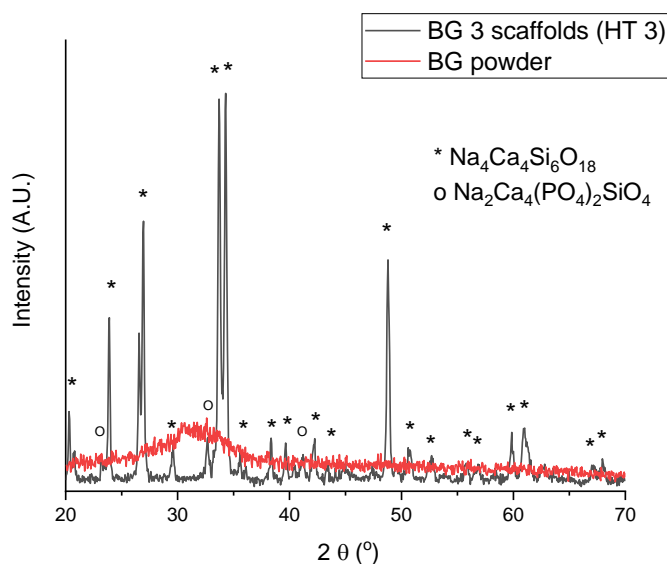
Figure 6.5: *XRD of BG powder and crystalized BG 3 scaffolds after the heat treatment 3*

6.3 Scanning electron microscopy of Bioglass scaffolds coated with the hydrogel

BGS were further coated with the hydrogel, as described in the Section 3.1.5. Figure 6.6 shows SEM images of BGS immersed in the hydrogel solution for different times (15 min, 30 min and 1h) followed by polymerization for 24 h in the oven at 37°C. As can be seen in the Figure 6.6, the porosity was altered by the hydrogel coating, as the pores seem blocked by the hydrogel. These blockages may have been induced by the freeze-drying prior to SEM imaging, which will be further discussed in Section 8.2. Visually, there was no obvious difference between the composite scaffolds prepared using different immersion times (Figure 6.6). It

seems that the hydrogel fills the pores and surfaces of the scaffolds after 15 min of immersion. Further immersion times do not seem to significantly affect the structure of the coated BGS. However the coverage of the BGS surface with a gel is slightly higher for 30 min (Figure 6.6 e) and 1 h immersion (Figure 6.6 f) compared to 15 min immersion time (Figure 6.6 d). Since the coverage of the surface by the gel is similar for 30 min and 1 h immersion, 30 min was selected for the subsequent sample preparation.
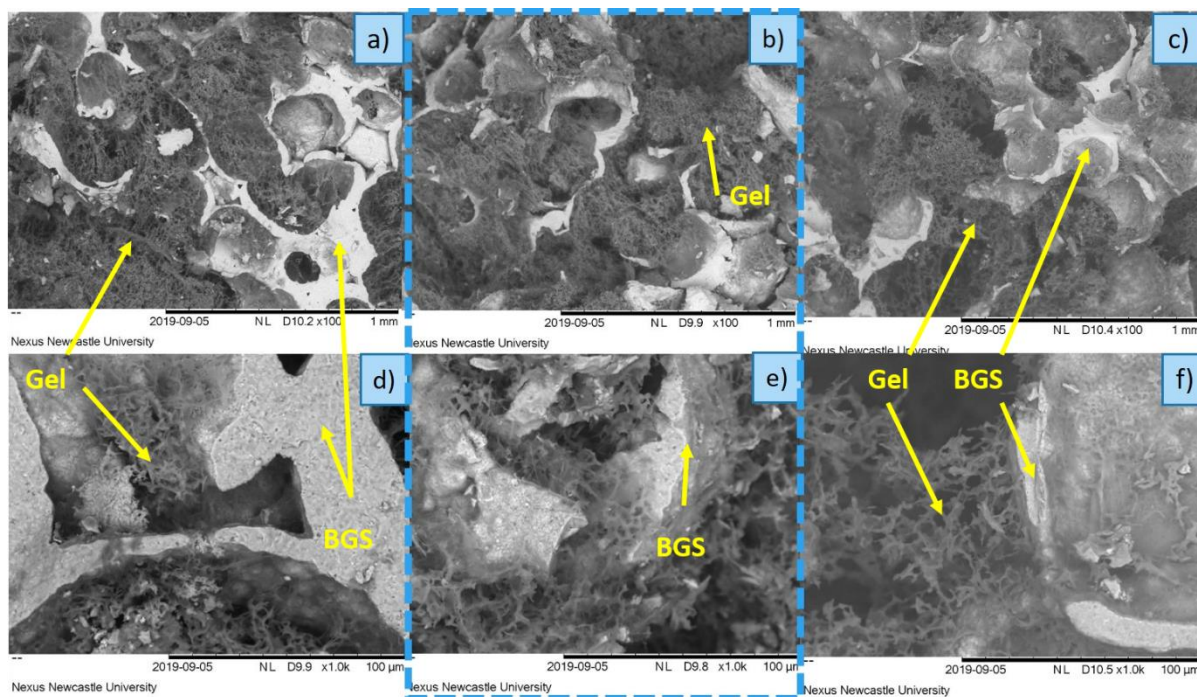
Figure 6.6: SEM images of BGS scaffolds immersed in the hydrogel solution for different times, at magnification x100: a) 15 min, b) 30 min and c) 1 h, and x1000 d) 15 min, e) 30 min and f) 1 h (30 min chosen as the optimal time)

Final comments

In this section, BG scaffolds coated with the hydrogel were synthesized and characterized. It should be noted that although chitosan was used in some cases (Table 2.4), the use of genipin or other cross-linkers [118, 216-218] has not been reported. In order to improve the mechanical stability of the composites, AW scaffolds coated with the hydrogel will be prepared similarly and compared. While BG scaffolds in combination with natural polymers were explored in the papers by some authors, compositions of AW glass-ceramic with the polymers are rare, even though AW glass-ceramic is stronger than other glasses and glass-ceramics, including BG, according to the literature.

Chapter 7 Apatite-wollastonite powder and scaffolds (uncoated and coated with the hydrogel)

In this section, characterization of the apatite-wollastonite (AW) powder (prepared as described in Section 3.1.2), and AW scaffolds (prepared as described in Section 3.1.4) is discussed. Additionally, the effect of the hydrogel coating on the AW scaffolds (prepared as detailed in Section 3.1.5) is evaluated.

7.1 Apatite-wollastonite powder characterization

AW powder was characterized using scanning electron microscopy (SEM) to assess the particle size. Similarly to BG powder, differential thermal analysis (DTA) and heating microscopy (HM) were performed in order to examine the behaviour of the AW powder upon heating and subsequently select the heat treatment for the preparation of the scaffolds. X-ray diffraction (XRD) was used to investigate the structure of AW powder before the heat treatment.

7.1.1 Scanning electron microscopy of apatite-wollastonite powder

AW powder with particle size below 50 µm provided by the manufacturer, was sieved using 53 µm sieve for verification. The SEM image in Figure 7.1 confirms that the particles are below 53 µm. As no particle size analyser was available for determining both the size and the size range of the particles, particles were manually measured using ImageJ software. The size of 53 µm was chosen similarly to the BG powder.

2019-08-21   N L   D10.3 x500   200 μm

Nexus Newcastle University
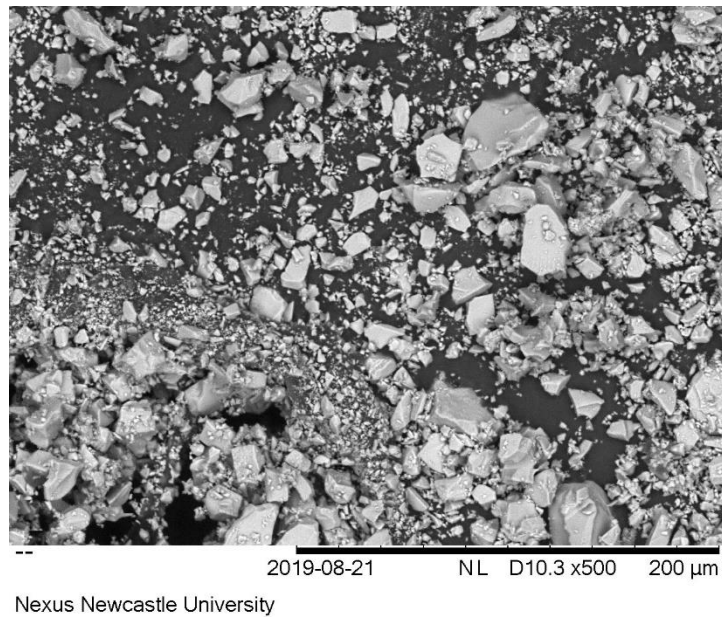
Figure 7.1: *SEM image of sieved AW powder*

7.1.2 X-ray diffraction of apatite-wollastonite powder

XRD of the AW powder is shown in Figure 7.2. The structure of AW powder is mostly amorphous as indicated by the broad peak at ~ 30°, typical for glass. The peaks were identified as wollasonite ($CaSiO_3$) (COD 96-901-1914) and apatite ($Ca_{10}(PO_4)_6(OH,F)_2$) (COD 96-900-1390) crystalline phases by using HighScore Plus software, also shown by Mancuso et al. [103, 108, 280]. Due to the high background and low signal to noise ratio, some peaks could have been omitted by the software. Nevertheless, XRD analysis was used for AW powder in order to confirm the highly amorphous structure of the glass-ceramic powder (with some crystalline peaks), which is expected to crystallise after the heat treatment, as seen later in Figure 5.43. As mentioned before, crystallization improves the mechanical stability of the scaffolds.
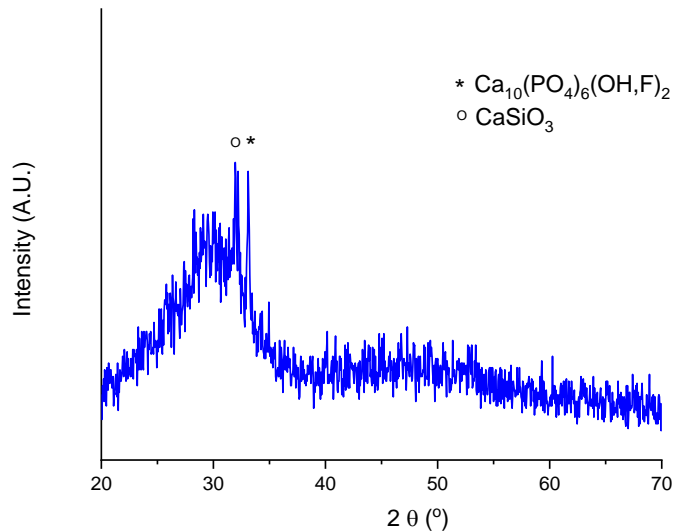
Figure 7.2: *XRD of AW powder*

7.1.3 Differential thermal analysis of apatite-wollastonite powder

DTA graph of the AW powder is shown in Figure 7.3. The glass transition temperature is at approx. 750 °C, while two exothermic peaks for crystallization appear at approx. 890 °C and 945 °C, that correspond to apatite and β-wollastonite phases, respectively [256]. Two endothermic peaks are reported for the melting of the two phases at approx. 1285 °C and 1300 °C by Cannillo et al. [256]; however, in Figure 7.3, one sharp, distinctive melting peak can be observed at approx. 1300 °C, that could be an overlap of two peaks. It should be noted that the peaks at ~ 200 °C are due to an instrument error, as shown in the Appendix A.
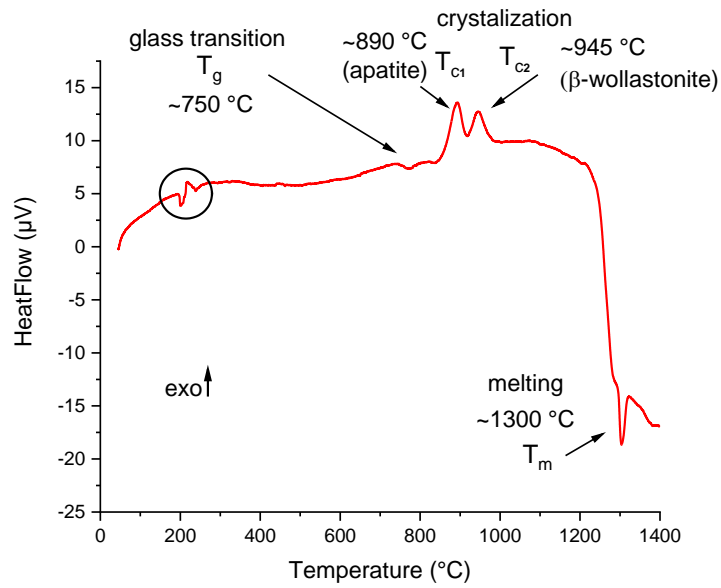
Figure 7.3: *DTA for AW powder (heating rate 20 °C/min)*

7.1.4 Heating microscopy of apatite-wollastonite powder

The AW powder was further tested using the HM. Figure 7.4 shows the curve of AW sample during heating on the heating microscope. It can be noted that the sintering step starts at approx. 780 °C which corresponds to approx. 15 % of reduction in the area. Similar behaviour was reported by Kokubo et al. [106]. The melting starts at around 1250 °C indicated by the sharp drop in the curve.
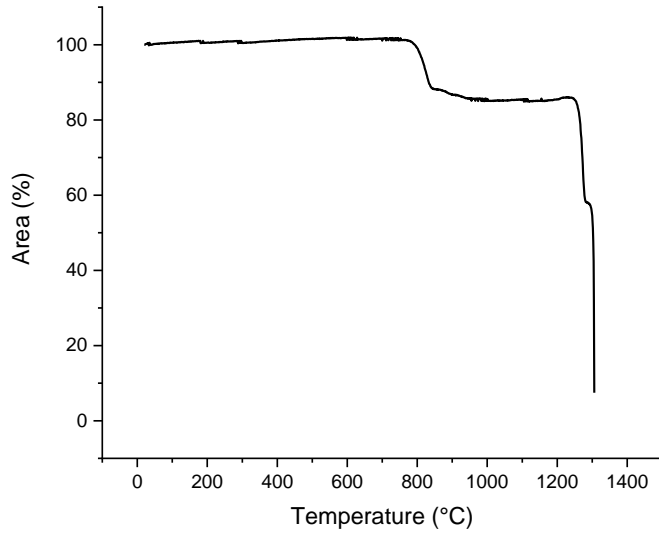
Figure 7.4: *Shrinkage of the AW sample upon heating recorded by the heating microscope (heating rate 20 °C/min)*

Figure 7.5 shows the silhouettes of the AW sample captured by the heating microscope at relevant temperatures. Figure 7.5 a shows the sample at 50 °C. Between 780 °C (Figure 7.5 b), when the sintering starts, and 900 °C (Figure 7.5 c), when the sintering is finished, sample visibly shrinks. At 1303 °C (Figure 7.5 e) the sample starts to melt.
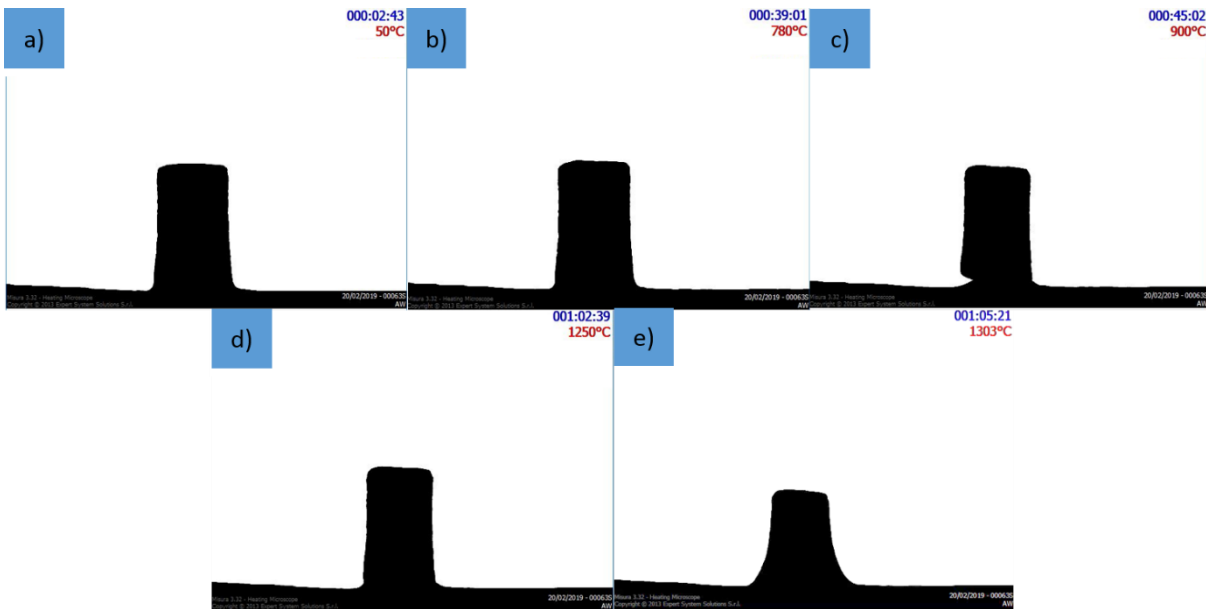
Figure 7.5: *AW sample on HM at different temperatures: a) 50 °C, b) 780 °C, c) 1250 °C, d) 900 °C and e) 1303 °C*

120

7.2 Uncoated and coated apatite-wollastonite scaffolds

Using the AW powder, scaffolds are prepared following the procedure described in Section 3.1.4. They were analysed using scanning electron microscopy (SEM) and X-ray diffraction (XRD) in order to observe the morphology and identify crystalline phases after the heat treatment, respectively. Furthermore, the scaffolds were coated with the Cht-Gen hydrogel (as described in Section 3.1.5) and observed on SEM.

7.2.1 Selection of the heat treatment for apatite-wollastonite scaffolds (AWS)

The heat treatment for the preparation of AW scaffolds (AWS) was chosen with the help of DTA and HM studies of AW powder, which showed sintering interval and melting point (Figure 7.3 and Figure 7.4). Similarly to the BG scaffolds (Section 6.1), a three-step heat treatment was selected. The first step at 550 °C was chosen to burn the PU foams, while the intermediate step at 900°C was chosen to increase the stability of the samples by allowing crystallization. The final step for the heat treatment at 1250 °C (just before the melting point of around 1300 °C), was selected to increase the densification and mechanical stability.

The PU foam 2, used for the synthesis of BGS and AWS, BGS and AWS are shown in Figure 7.6. A non-uniform sintering of AWS can be observed (Figure 7.6 c). The AWS scaffolds had an irregular shape of the deformed cylinder with different diameters on the top and on the base surface. In particular, the base was partially melted. During the last sintering step AWS samples appear to have been exposed to a slightly different temperatures between the top and the bottom sides. Change in final step temperatures to lower than 1250 °C led to a poorly sintered samples. Constrained with a furnaces available, it was not possible to further optimise the heat treatment. As can be seen in Figure 7.6 b, BGS scaffolds had a regular shape.
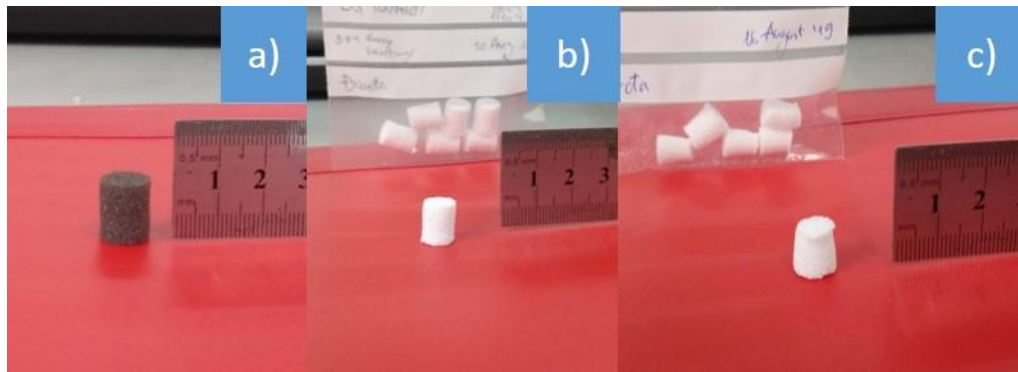
Figure 7.6: *a) PU foam 2 used for preparation of scaffolds, b) BGS and c) AWS*

7.2.2 Scanning electron microscopy (SEM) of uncoated apatite-wollastonite scaffolds

SEM images of AWS scaffolds are presented in Figure 7.7. The scaffolds have pore sizes ranging from 80 µm to 300 µm, with the average of approx. 180 µm. For comparison, BGS scaffolds had the average pore diameter of approx. 100 µm (Section 6.1, Figure 6.4). The pore sizes were measured manually using the ImageJ software. While open porosity was observed with pores > 100 µm, some smaller pores, as well as some closed/blocked pores can be noted.
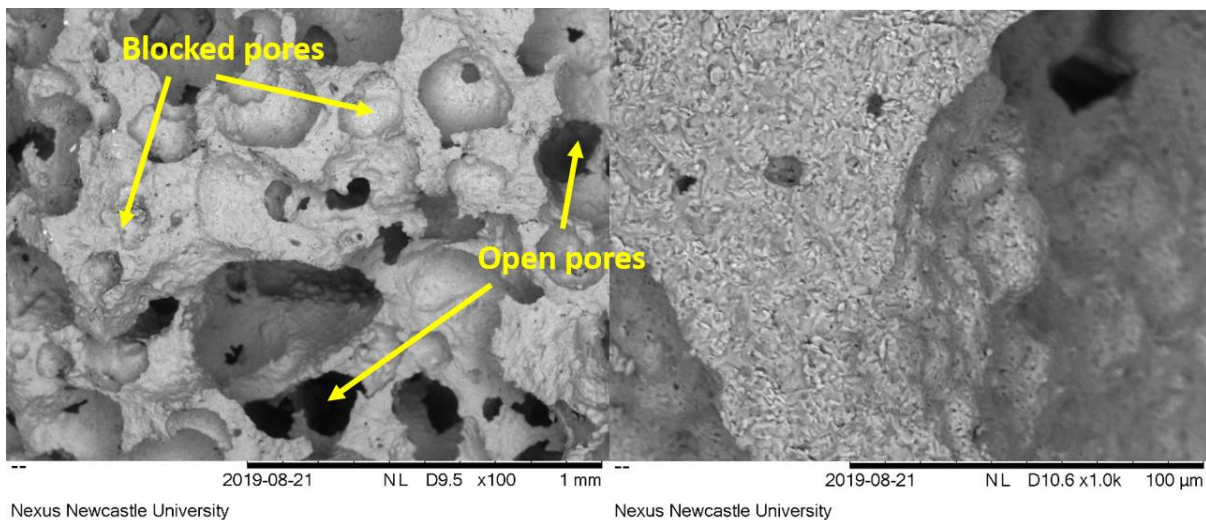
Figure 7.7: *SEM images of the AWS at magnification x100 (left) and x1000 (right)*

7.2.3 X-ray diffraction of uncoated apatite-wollastonite scaffolds

XRD for AWS scaffolds was carried out using the procedure described in the Section 3.8. Figure 7.8 shows the XRD patterns of the AW powder and AWS scaffolds after the heat treatment. AW powder is mainly amorphous, and it has small peaks corresponding to wollastonite and apatite. After the heat treatment, AWS is completely crystalline. The main

peaks were identified as wollastonite, $CaSiO_3$ (COD 96-901-1914) and whitlockite, $Ca_9Mg(PO_4)_6PO_3OH$ (COD 96-901-2137), similar to previously reported [281]. Additionally, some peaks corresponding to apatite (COD 96-900-1390) can be observed, as also reported by other authors [102, 108].

DTA (Figure 7.3) shows two crystallisation peaks, probably corresponding to apatite and wollastonite, as reported by [256]. The differences between DTA and XRD are a result of different heat treatments. The DTA was performed using a heating rate of 20 °C/min, while the heat treatment of the scaffolds was carried out at 5 °C/min with a step of 1 h at 1250 °C. It was reported that apatite phase converts to whitlockite above 1100 °C [106]. Therefore, it was assumed that the two crystallisation peaks observed on the DTA could correspond to apatite and wollastonite.
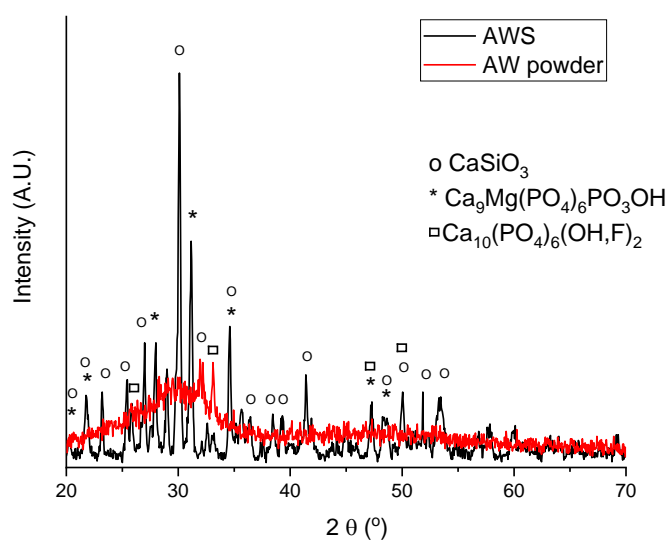
Figure 7.8: *XRD of semi-crystalline AW powder and crystalized AWS after the heat treatment*

7.2.4 Scanning electron microscopy of apatite-wollastonite scaffolds coated with the hydrogel

The AWS scaffolds were coated with the hydrogel as described in the Section 3.1.5. Figure 7.9 shows SEM images of AWS scaffolds with different times of immersion in the hydrogel solution (15 min, 30 min and 1 h), followed by polymerisation. The samples were freeze-dried prior to SEM imaging. It seems that the hydrogel penetrates the scaffolds, covering the pores. Freeze-drying is considered to have an effect on the hydrogel coating and

blockage of the pores, and will be discussed in Section 8.2. According to the SEM images, time did not have a significant role on the final structure of the composite scaffolds. Since the time of immersion in the hydrogel solution was not crucial for the final structure of the hydrogel coated scaffolds, 30 min was considered sufficient for the AWS, likewise for BGS (see Section 6.3, Figure 6.6).
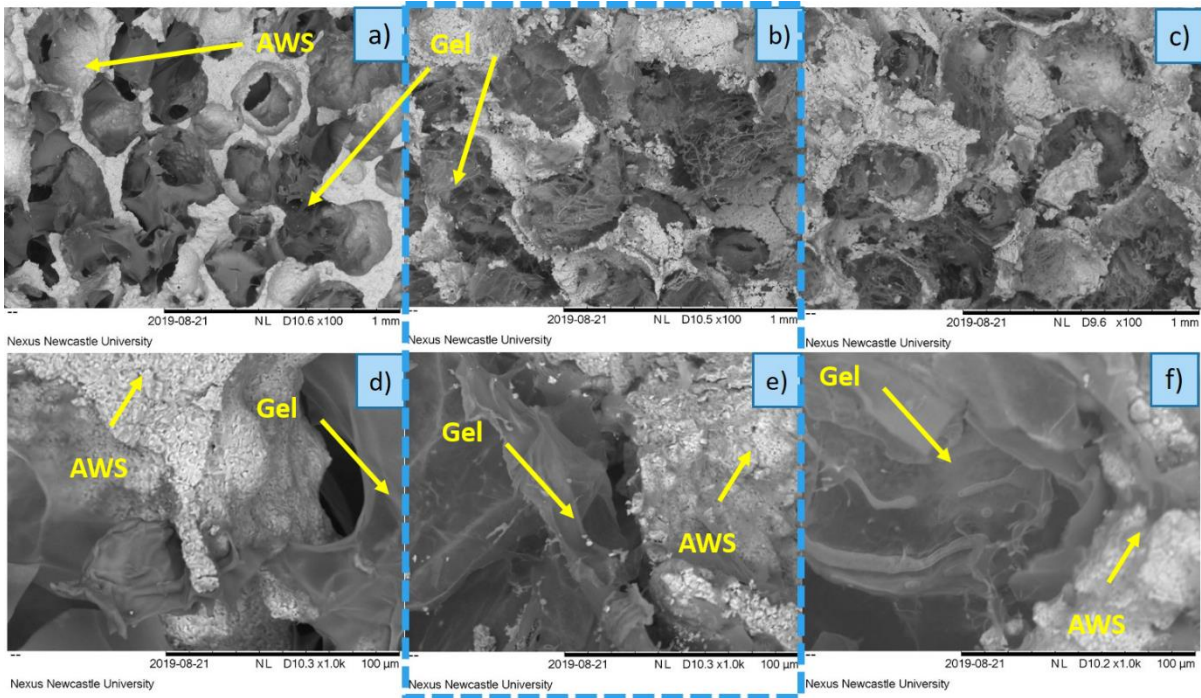
Figure 7.9: *SEM images of AWS immersed in the hydrogel solution for different times, at magnification x100: a) 15 min, b) 30 min and c) 1 h, and x1000 d) 15 min, e) 30 min and f) 1 h (30 min chosen as the optimal time)*

In comparison to the BGS scaffolds, the hydrogel coating on the AWS scaffolds looks different. While the hydrogel in case of BGS scaffolds seems to be in a form of threads/fibres (Figure 6.6), the hydrogel in the structure of AWS scaffolds is firmer, thicker and denser. Furthermore, these different gel structures are not dependant on the time of immersion in the Cht-Gen hydrogel, but only on the type of the scaffold (BGS or AWS). There could be a few reasons for this behaviour. Firstly, as observed in the Figure 6.4 and Figure 7.7, the surface roughness seemed greater for AWS scaffolds (possibly due to poor sintering), and that could allow more hydrogel to adhere on the surface and subsequently form a thicker layer. Secondly, the hydrophilicity of the BG scaffolds is reported to be greater than for AW scaffolds [282, 283]. That could lead to the reaction of BGS scaffolds and the hydrogel, possibly dissolving the

scaffold and making a thinner, fibre-looking layer, while the hydrogel would form a separate layer on AWS scaffolds. Finally, BG is more reactive and raises the pH of the surrounding solution more than AW (experimental study, Section 8.2). Hence, it could be considered that the hydrogel is formed at basic pH conditions (above 8) in case of BGS, and at neutral pH (around 7) conditions in case of AWS. It was previously reported that the cross-linking of chitosan and genipin greatly depends on the pH conditions [142]. At neutral pH, more chitosan and genipin cross-links will be formed to make a stronger hydrogel. When the pH is basic, more genipin self-crosslinking will take place, reducing number of chitosan-genipin bonds, which would then lead to a less cross-linked and weaker gel.

Furthermore, the colour of the hydrogel coated BGS and AWS scaffolds is different (Figure 7.10). BGS and AWS scaffolds were cut in half (transversely) for the purposes of imaging. As it can be seen in the Figure 7.10, both coatings on the BGS and AWS scaffolds look homogenous judging by the uniform colours. After the polymerization of the coating is complete (24 h) BGS scaffold has a pale blue colour, while AWS scaffold has a darker blue colour. It was observed that, after 3-4 h of polymerization of the hydrogel coating, BGS scaffolds had a darker blue colour. This might be due to fast genipin self-crosslinking together with the deprotonisation of NH_3^+ groups of chitosan at higher pH, allowing cross-linking; as a result, BGS scaffolds had a darker blue colour, at the beginning of hydrogel polymerisation. As seen in the Section 5.2, FI measurements showed that increasing the amount of BG in the hydrogel (higher pH), the FI values were higher in the first few hours of polymerization (3-6 h), but lower at the end of polymerisation (24 h). The hydrogel coating on AWS had a higher amount of final cross-linking (after 24 h) and therefore a darker colour. Mi et al. reported that a darker colour is connected to a higher cross-linking degree [142]. As mentioned before in Section 2.5.2.2, the blue colour is a result of forming both genipin self-crosslinks and chitosan-genipin bonds. In addition, the darker colour is an indicator of a more cross-linked and stronger/stiffer gel [143, 146]. Although the hydrogel composition (concentration of genipin) and time of polymerization were the same for BG and AW scaffolds, the colour of the coatings was different (Figure 7.10). As previous studies showed that darker colour means more cross-linked gel, it was concluded that the gel on the AW scaffold was more cross-linked and thus stronger, which was also observed on SEM images.

In summary, the hydrogel coating differs on BG and AW scaffolds by colour, observed by the naked eye, and microstructure, as shown on SEM, likely due to different pH conditions. The darker colour on synthesised AW scaffolds corresponds to more cross-linked and stronger hydrogel. Although it is difficult to predict the exact pH values at the hydrogel-scaffolds interface, it is suggested that the gel is formed at more basic conditions (above 8) in case of BG scaffold. At higher pH genipin self-cross-links, which in turn leads to formation of less cross-linked, weaker and more porous hydrogel.
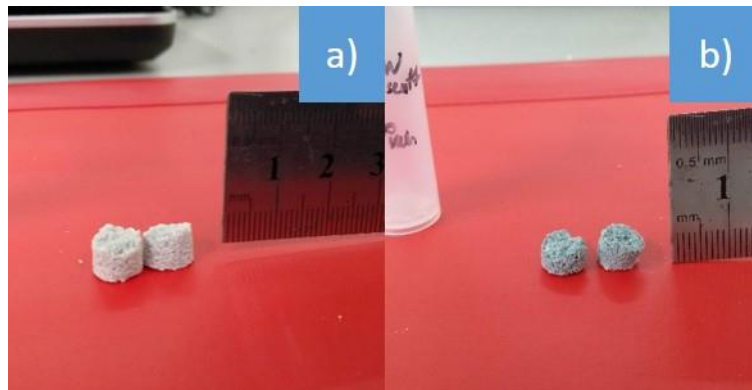
Figure 7.10: Hydrogel coated a) BGS and b) AWS scaffolds showing different colours of the coating after polymerization

Final comments

To sum up, AW scaffolds have been synthesized and coated with the chitosan hydrogel cross-linked with genipin for the first time, to the best of our knowledge. Only few AW/polymer compositions have been reported in the literature, and only without the use of a cross-linker (Table 2.4). It should be noted that AW has the advantage over BG and other glasses and glass-ceramic as it is considered stronger, due to wollastonite crystalline phase. Here, a stable composite of AW scaffold coated with the chitosan-genipin hydrogel was obtained and will be further assessed using the compression test and studies in SBF. It should be mentioned that the hydrogel coating looks different on BG and AW due to different pH conditions, which affect the cross-linking and the microstructure of the hydrogel. Moreover, the sintering of AW in this work needs to be improved in order to obtain regular-shaped samples. This could be achieved by using a single burning-out furnace which is stable at high temperatures (instead of two furnaces, as mention in Section 3.1.4) and platinum moulds during sintering that could preserve the shape of the samples.

Chapter 8 Mechanical properties and *in vitro* bioactivity in SBF of Bioglass and apatite-wollastonite scaffolds

8.1 Compression test of uncoated and coated Bioglass and apatite-wollastonite scaffolds

BGS and AWS scaffolds, uncoated as well as coated with the hydrogel (time of immersion 30 min) were compressed as described in Section 3.7. An example of a stress-strain curve for the uncoated AWS is shown in Figure 8.1. The serrated curve is typical for brittle and porous glass-ceramic scaffolds, as the breaking of the scaffolds' struts is gradual [171, 254, 265]. A maximum stress up to 10 % strain was determined and average values for the samples were plotted (3 samples per composition were tested).
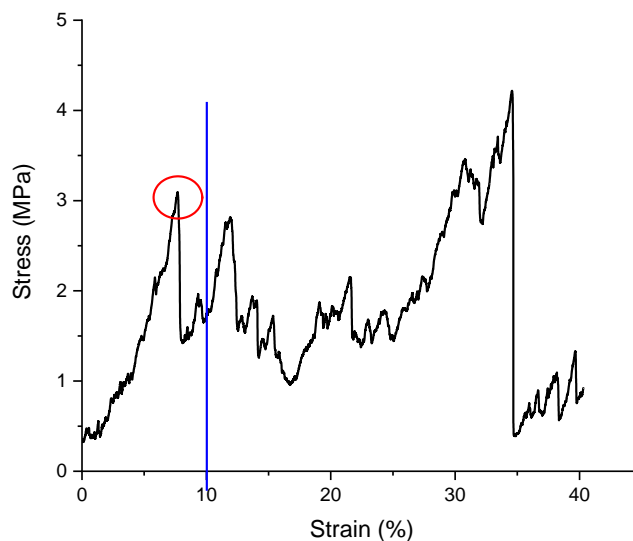
Figure 8.1: *Example of the stress-strain curve of uncoated AWS and determination of maximum stress up to 10 % strain*

As seen in Figure 8.2, AWS scaffolds are stronger than BGS scaffolds. This is in agreement with the literature stating that wollastonite phase within the glassy matrix in AW glass-ceramics increases the mechanical properties [104, 108]. For BGS scaffolds, compressive stress is higher before the coating with the hydrogel, and the average compressive stress decreases from 1.10 to 0.64 MPa (42 %) after the coating. This might be due to the reactivity of the BG and partial dissolution and weakening of the BG scaffolds. In case of AWS scaffolds, there were no significant differences between coated and uncoated samples. The values for

compressive stress varied from 1.19 to 4.09 MPa, with the average of approx. 2.6 MPa. Larger error bars seen for AWS scaffolds are due to irregular shape of the AWS scaffolds, caused by poor sintering elaborated in Section 7.2.1 (Figure 7.6). As the AWS samples were melted on the bottom, the diameter of the samples differed from the bottom to the top. The top surface was not flat, which greatly affected the measurement. However, as expected [104], both coated and uncoated AWS scaffolds were on average stronger than BGS scaffolds.
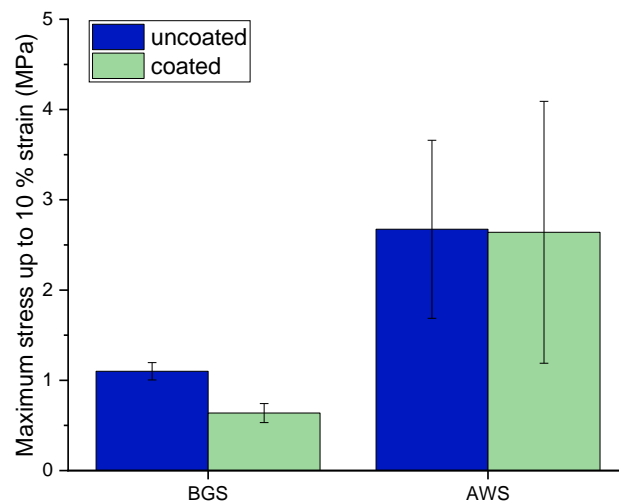
Figure 8.2: *Maximum stress up to 10 % strain for BGS and AWS uncoated and coated (30 min) scaffolds*

8.2 Studies of Bioglass and apatite-wollastonite uncoated and coated scaffolds in SBF - pH, SEM and compression test

As the final application of these scaffolds is intended for bone regeration, the behaviour in the body-like fluid is important. Hence, the scaffolds (BGS and AWS scaffolds, uncoated and coated) were further tested in SBF for their behaviour in terms of pH of the SBF, apatite formation and mechanical properties. Both BG and AW are considered bioactive and the formation of an apatite layer on their surface was expected, which could further affect the pH, their morphology and compressive stress values [102, 103, 108, 171, 214, 254, 265]. As aforementioned, SBF can be used for *in vitro* testing of bioactivity, as it has a similar composition to human body plasma. Figure 8.3 and Figure 8.4 show SEM images of the scaffolds after immersion in SBF for 1 week, at lower and higher magnification, respectively.

The samples were freeze-dried prior to SEM imaging. The SEM images of the samples after the immersion in SBF look similar to those prior to immersion (Figure 6.4, Figure 6.6, Figure 7.7 and Figure 7.9). In some cases, in Figure 8.3 a, Figure 8.3 b and Figure 8.4 a, for uncoated scaffolds, a structure similar to the gel coating in the form of fibres and threads can be noticed. This is believed to be due to freeze-drying which is further discussed later in this section. No layer or deposition of apatite crystals could be clearly observed on any of the samples. Both BG and AW scaffolds have been reported to form an apatite layer within less than 1 week of immersion in SBF [102, 108, 214, 265]. Therefore, the reasons that an apatite layer was not detected might be that it was difficult to distinguish it on the scaffolds surface, as it looks similar as glass-ceramic structures. High-resolution SEM could be used in the future in order to get better images. Also, energy dispersive X-ray spectroscopy (EDS) could be utilized for elemental analysis that would show increase in amount of calcium and phosphate for apatite deposits.
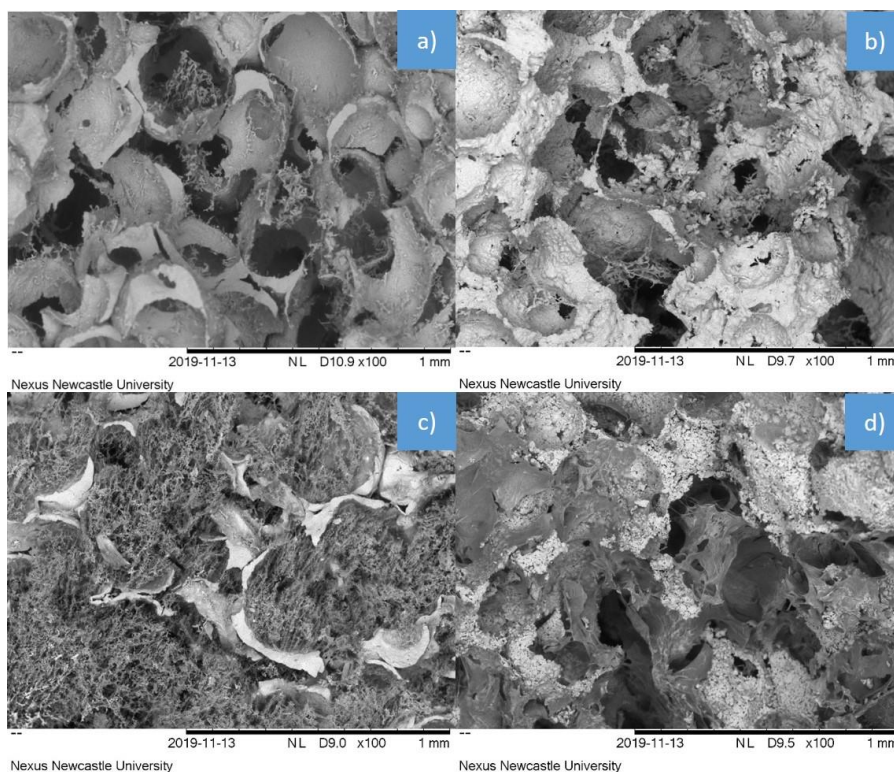
Figure 8.3: SEM images of freeze-dried samples after 1 week in SBF at lower magnification (x100): a) BGS uncoated, b) AWS uncoated, c) BGS coated (30 min) and d) AWS coated (30 min) scaffold
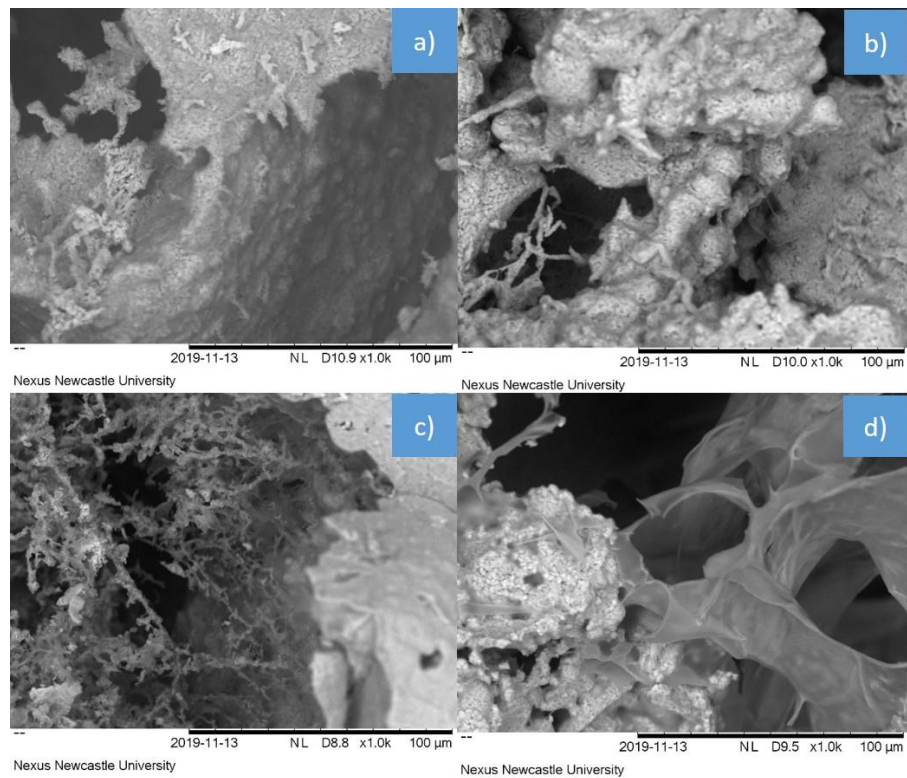
Figure 8.4: *SEM images of freeze-dried samples after 1 week in SBF at higher magnification (x1000): a) BGS uncoated, b) AWS uncoated, c) BGS coated (30 min) and d) AWS coated (30 min) scaffold*

Similarly, SEM images of BGS and AWS uncoated and coated scaffolds after 2 weeks in SBF are shown in Figure 8.5. The samples look similar as after 1 week in SBF (Figure 8.3). The fibre-like structures on the uncoated samples are suggested to be due to freeze-drying. However, at higher magnifications (x1000 in Figure 8.6, and x2000 and x5000 in Figure 8.7) some deposits could be observed on uncoated BGS samples (Figure 8.6 a, Figure 8.7 a and Figure 8.7 b), that look similar to hydroxyapatite crystals previously reported for BG scaffolds [214]. In comparison, no deposits are detected on AWS scaffolds (Figure 8.7 c and Figure 8.7 d). BG is reported to be more bioactive so it is expected that more apatite layer is formed on its surface [113].
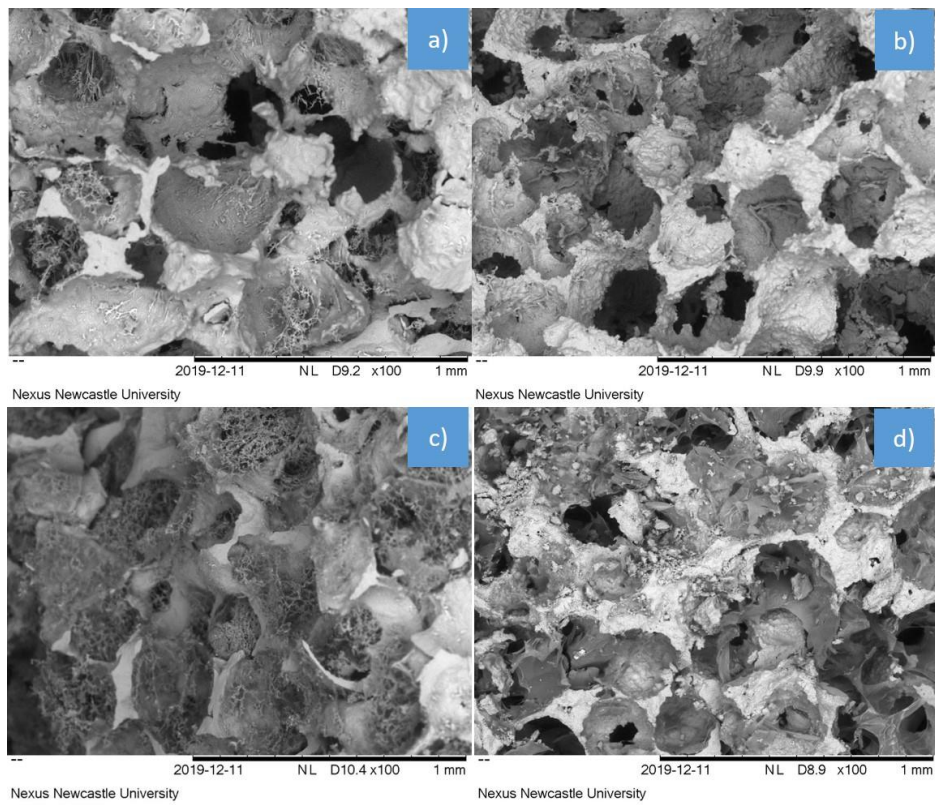
Figure 8.5: *SEM images of freeze-dried samples after 2 weeks in SBF at lower magnification (x100): a) BGS uncoated, b) AWS uncoated, c) BGS coated (30 min) and d) AWS coated (30 min) scaffold*
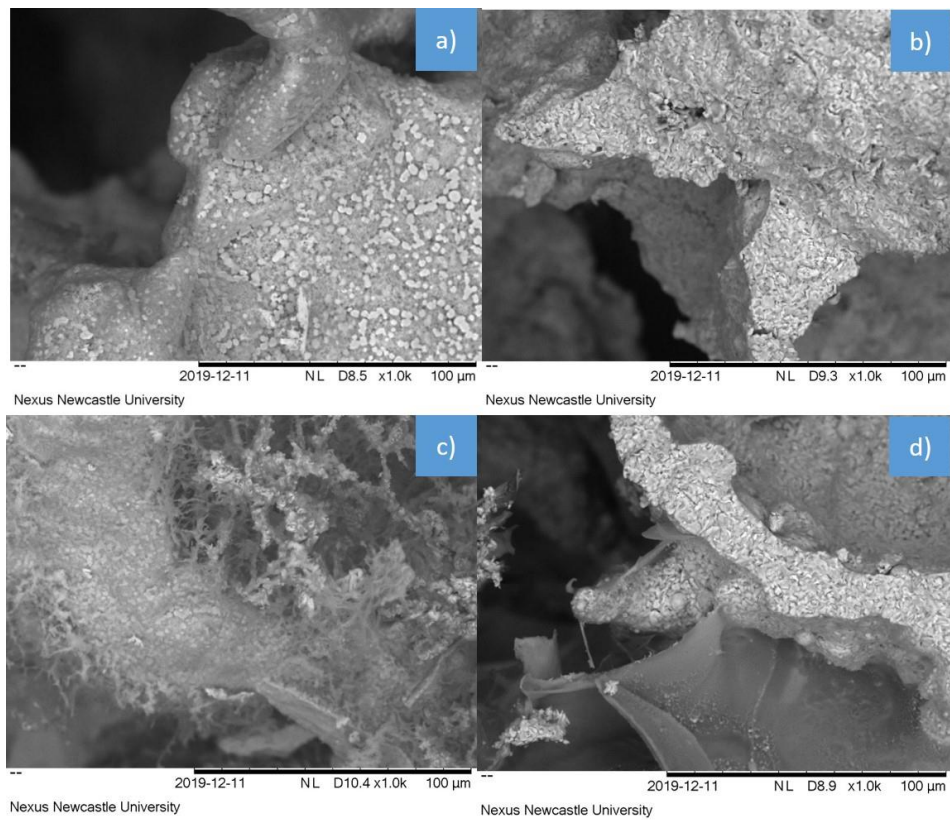
Figure 8.6: SEM images of freeze-dried samples after 2 weeks in SBF at higher magnification (x1000): a) BGS uncoated, b) AWS uncoated, c) BGS coated (30 min) and d) AWS coated (30 min) scaffold
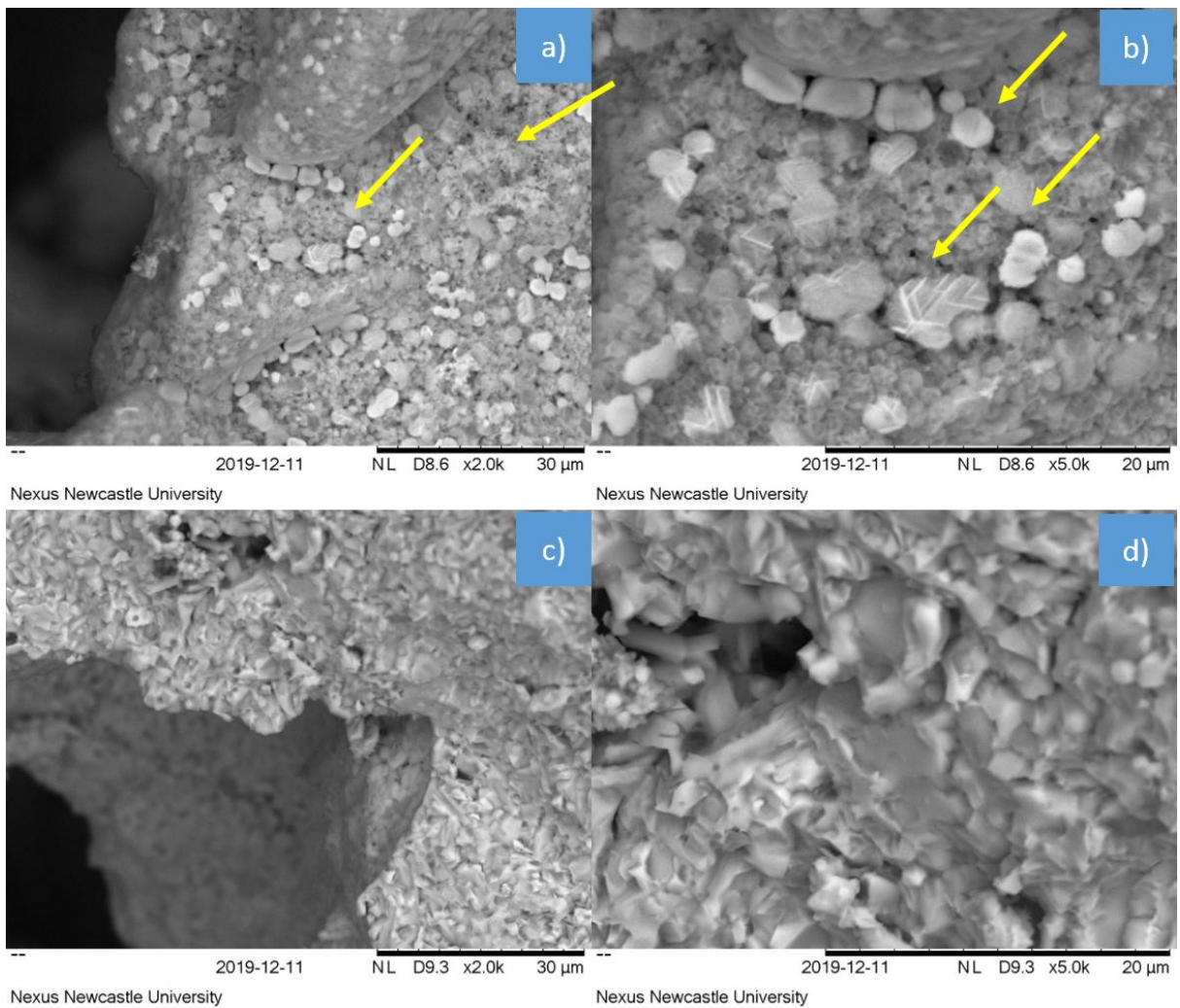
Figure 8.7: Arrows pointing at deposited apatite on BGS uncoated scaffolds after 2 weeks of SBF at a) x2000 and b) x5000, in comparison to no visible apatite crystals on AWS uncoated scaffolds at c) x2000 and d) x5000

As unusual fibre-like structures were observed on uncoated BGS and AWS scaffolds after immersion in SBF, it might be suggested that it is due to freeze-drying, when an apatite layer which could be deposited during immersion in SBF, was peeled off the scaffolds surface (Figure 8.3 a and b, Figure 8.4 a and b; Figure 8.5 a and b). Therefore, a set of samples kept in SBF for 2 weeks was only air-dried and imaged using SEM (Figure 8.8 and Figure 8.9). For these non-freeze-dried samples no fibres could be seen on uncoated scaffolds (Figure 8.8 a and b, and Figure 8.9 a and b). However, no apatite deposition could be observed either. For the coated samples, it could be noticed that as the hydrogel coating on scaffolds collapsed, we can no longer see pores which were visible on SEM images for the hydrogels (Section 5.1, Figure 5.1 and Figure 5.2). The hydrogel coating was attached to the scaffolds surface (Figure

8.8 c and d, Figure 8.9 c and d), unlike for freeze-dried samples (Figure 8.5/Figure 8.6 c and d). In case of the non-freeze-dried samples, as well as the freeze-dried, firmer/thicker coating on AWS scaffolds could be seen than in the case of BGS scaffold. Therefore, it can be suggested that the loose structure of the hydrogel coating on BGS (Section 6.3, Figure 6.6) and AWS (Section 7.2.4, Figure 7.9) scaffolds was due to freeze-drying and that the hydrogel coating firmly adheres to the scaffolds surface and does not block the pores.
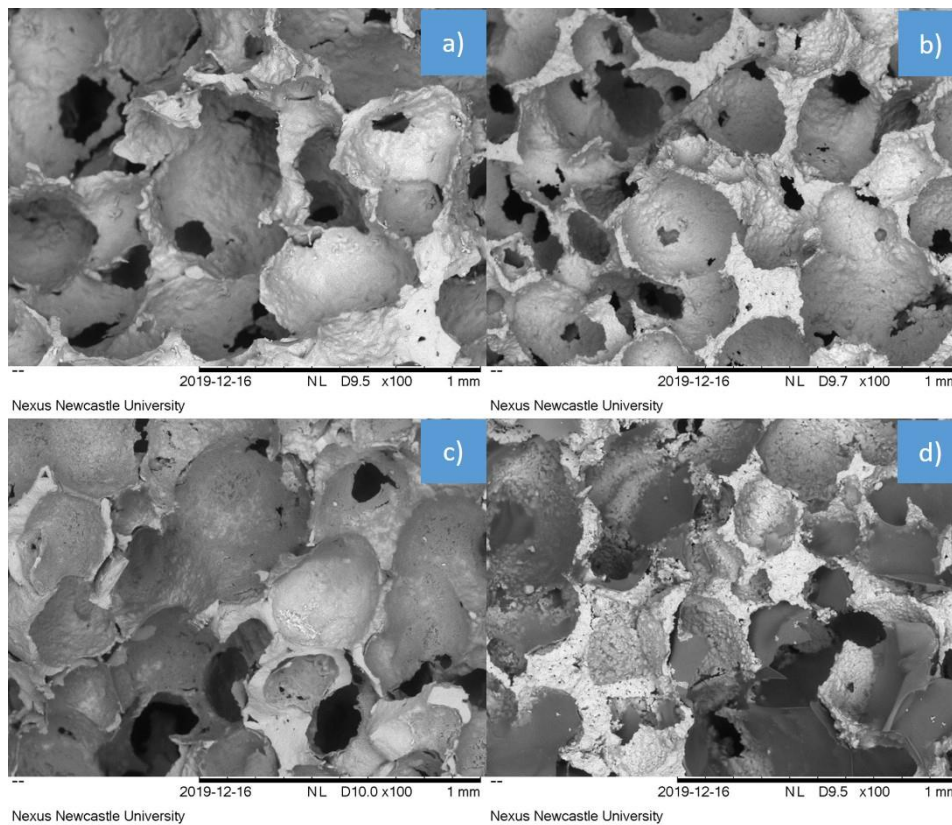
Figure 8.8: *Non-freeze-dried samples after 2 weeks in SBF at lower magnification (x100): a) BGS uncoated, b) AWS uncoated, c) BGS coated (30 min) and d) AWS coated (30 min) scaffold*
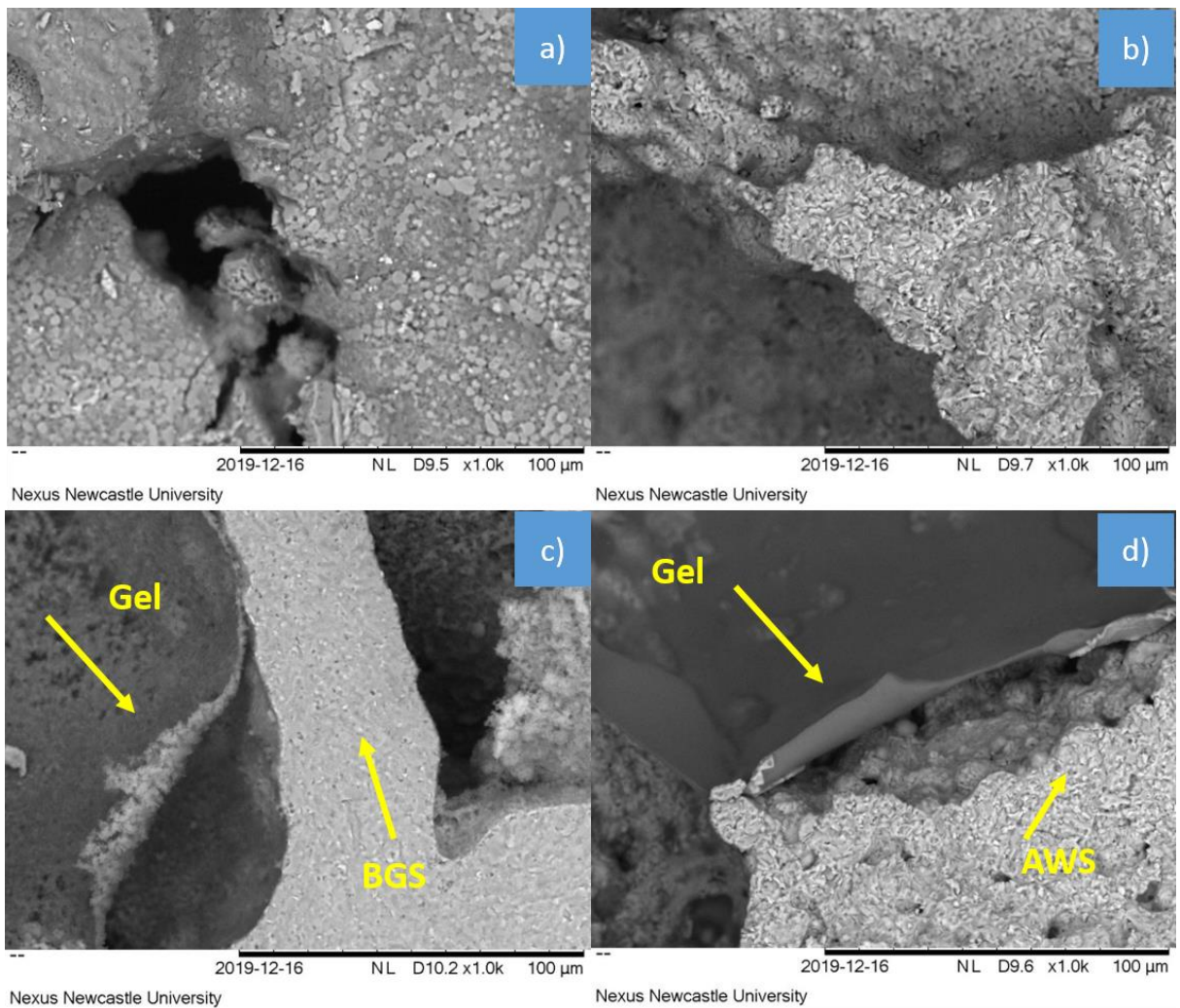
Figure 8.9: *Non-freeze-dried samples after 2 weeks in SBF at higher magnification (x1000): a)*
BGS uncoated, b) AWS uncoated, c) BGS coated (30 min) and d) AWS coated (30 min) scaffold

Next, pH measurements were performed using the procedure described in Section
3.11. pH values of the SBF soultions with uncoated and coated BGS and AWS scaffolds after 1
and 2 weeks of immersion are shown in Figure 8.10 and Figure 8.11, respectively. Three
samples per composition were tested. It should be noted that although samples were kept at
37 °C in the oven during the tests and removed only to refresh the soultion, pH was measured
at 34 °C. The reason is the low outside temperature and the fact that the temperature of the
samples dropped as soon as they were taken out of the oven to take a pH reading. The pH of
the SBF solution was ~ 7.5 before adding the samples.

It could be observed that BGS scaffolds raised the pH from neutral ~ 7.5 to ~ 8.3, for
both uncoated and coated samples during 1 week of immersion in SBF. AWS scaffolds raised

the pH up to ~ 7.7. However, there was not a significant difference between uncoated and coated samples, for both BGS and AWS scaffolds.
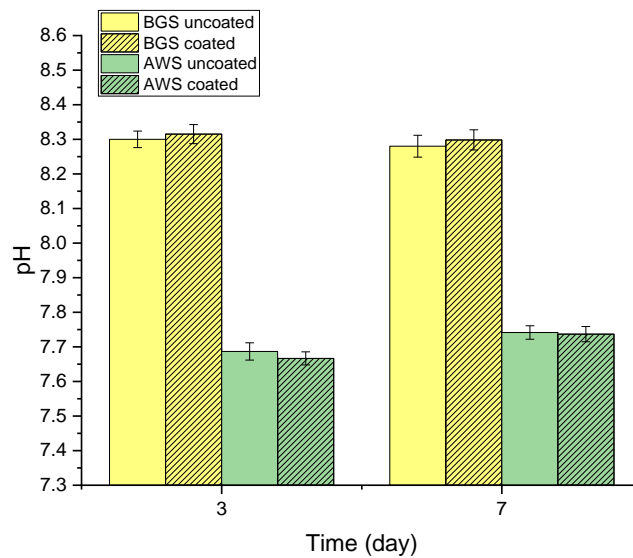
Figure 8.10: pH values for uncoated and coated (30 min) BGS and AWS scaffolds immersed in SBF for 1 week, as well as for the SBF before immersion of the samples

During 2 weeks of immersion in SBF (Figure 8.11), the pH for BGS both uncoated and coated scaffolds was ~ 8.3 on days 3 and 7. On both day 10 and day 14, the average pH values slightly dropped to 8.25 for uncoated BGS scaffolds and to 8.19 (day 10) and 8.16 (day 14) for coated BGS scaffolds. Coated and uncoated AWS scaffolds during 2 weeks of immersion in SBF had pH values in the range between 7.56 and 7.77. There was no a significant difference between coated and uncoated AWS.
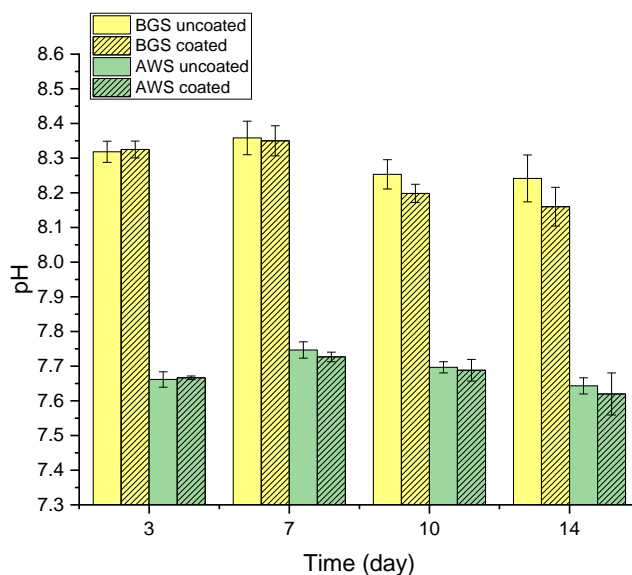
Figure 8.11: *pH values for uncoated and coated (30 min) BGS and AWS scaffolds immersed in SBF for 2 weeks, as well as for the SBF before adding the samples*

Figure 8.12 shows calculated maximum stress up to 10 % strain for uncoated and coated BGS and AWS scaffolds after immersion in SBF for 1 week. Three samples were tested for each composition. Independent of the coating, BGS scaffolds have shown lower stress (up to ~ 1.05 MPa) in comparison to AWS scaffolds (ranging from ~ 1.35 to ~ 5.68 MPa). The coated BGS scaffolds had slightly higher stress after 1 week in SBF than uncoated samples. Similarly, the average value of maximum stress increases after coating of AWS with hydrogel, from 2.08 to 3.89 MPa. The big error bars observed on AWS scaffolds are due to irregular shape of the samples.
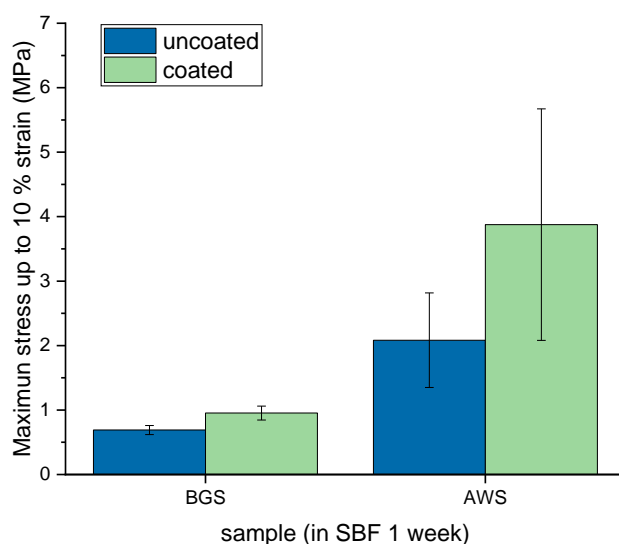
Figure 8.12: *Maximum stress up to 10 % strain for BGS and AWS uncoated and coated scaffolds after 1 week of immersion in SBF*

Figure 8.13 shows maximum stress up to 10 % strain for BGS and AWS uncoated and coated scaffolds, as synthesised (without SBF) and after 1 week of immersion in SBF for comparison. When compared to the samples without SBF, BGS scaffolds show an interesting feature: while average stress decreases after immersion in SBF for uncoated BGS scaffolds (from 1.10 to 0.69 MPa), in case of coated BGS scaffolds, average stress increases after being kept in SBF (from 0.64 to 0.95 MPa). Therefore, coated BGS scaffolds have higher stress of 0.95 MPa after immersion in SBF for 1 week than uncoated BGS scaffolds with 0.69 MPa. It appears that the hydrogel coating hinders the dissolution of the BGS scaffold which leads to a higher stress for coated BGS; however, pH values are almost identical for both samples with or without the coating (Figure 8.10). It is also possible that the coating acts like a glue holding the structure firmer. When it comes to AWS scaffolds, due to the large fluctuations between analysed samples, no firm comparison could be drawn but it seems that the trend is similar to BGS. The average stress for uncoated AWS decreases, while the stress for coated AWS increases after immersion in SBF. The average stress after 1 week in SBF is higher for the coated AWS than for the uncoated AWS. In general, BGS scaffolds have lower stress than AWS scaffolds without SBF and after 1 week in SBF.
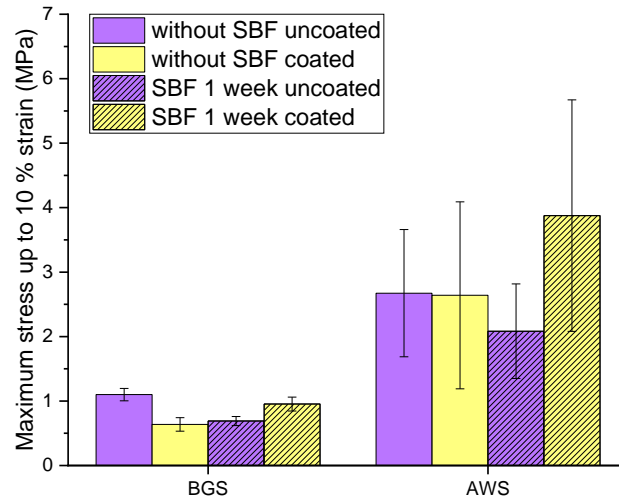
Figure 8.13: *Maximum stress up to 10 % strain for BGS and AWS uncoated and coated (30 min) scaffolds, as synthesised (without SBF) and after 1 week of immersion in SBF*

Comparison of BGS and AWS compression tests after immersion in SBF for 2 weeks is given in Figure 8.14. The coated BGS scaffolds have higher average stress than the uncoated samples (0.95 MPa compared to 0.61 MPa). BGS scaffolds have lower stress (ranging from 0.46 to 1.12 MPa) than AWS scaffolds altogether (ranging from 1.39 to 3.65 MPa). While the results for AWS scaffolds have a wide error bars, the average values show that the coating on AWS scaffolds decreases the stress from approx. 2.52 MPa (uncoated AWS) to 1.83 MPa (coated AWS).
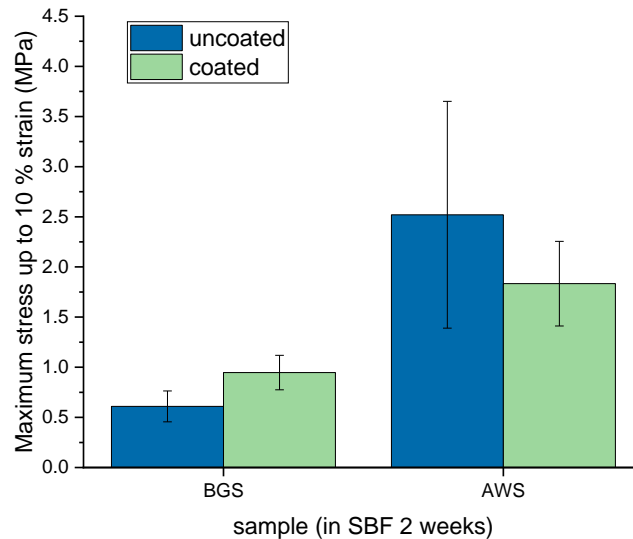
Figure 8.14: *Maximum stress up to 10 % strain for BGS and AWS uncoated and coated*
(30 min) scaffolds after 2 weeks of immersion in SBF

Average values of the maximum compressive stress up to 10 % strain for BGS and AWS uncoated and coated scaffolds without SBF and after immersion in SBF for 1 and 2 weeks are recapped in Table 8.1. Figure 8.15 presents the maximum stress values for BGS and AWS uncoated and coated scaffolds tested without SBF, after immersion in SBF for 1 week and after immersion in SBF for 2 weeks. It could be concluded that BGS scaffolds have lower stress (ranging from 0.46 to 1.20 MPa) than AWS scaffolds (ranging from 1.19 to 5.68 MPa), independent of the coating or testing conditions (without SBF and after being kept in SBF). The stress for uncoated BGS scaffolds decreased after immersion in SBF, while the stress for coated BGS scaffolds increased after immersion in SBF. There are no solid conclusions for AWS scaffolds as the values vary extremely because of their irregular shape and uneven surface. Looking at the average values, the stress for uncoated AWS decreases after immersion in SBF while for the coated AWS the stress increases after 1 week in SBF, reaching the highest value overall for all tested samples. However, after 2 weeks in SBF the stress decreases to a value below that of the coated AWS before immersion in SBF.

140

Table 8.1: Average values of maximum stress up to 10 % strain for BGS and AWS uncoated and coated scaffolds before SBF and after immersion in SBF for 1 and 2 weeks

Scaffold	Maximum stress up to 10 % strain (MPa)		
	Without SBF	1 week in SBF	2 weeks in SBF
Uncoated BGS	1.10 ± 0.10	0.69 ± 0.07	0.61 ± 0.15
Coated BGS	0.64 ± 0.10	0.95 ± 0.11	0.95 ± 0.17
Uncoated AWS	2.68 ± 0.99	2.08 ± 0.73	2.52 ± 1.13
Coated AWS	2.64 ± 1.45	3.89 ± 1.79	1.83 ± 0.42
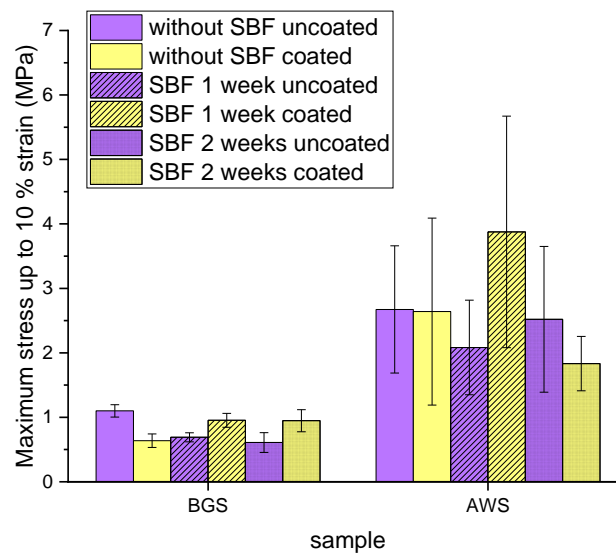
Figure 8.15: Maximum stress up to 10 % strain for BGS and AWS uncoated and coated scaffolds, as synthesised (without SBF), and after 1 week and 2 weeks of immersion in SBF

Final comments

From the compression tests in SBF, it can be concluded that the coating of the BGS increases the stress, while inconclusive results are obtained for AWS. However, all AWS showed average stress values above 2 MPa, which is reported to be the lower limit for the human cancellous bone [24, 30]. The values of compression stress obtained here are comparable to the values from the literature for similar scaffolds (Table 2.4). In order to increase the mechanical properties of AWS scaffolds, sintering process needs to be improved to yield uniform and well-sintered samples. Using platinum moulds during sintering could

preserve the shape of the samples. Since the coated BGS scaffolds have higher stress after immersion in SBF for 1 or 2 weeks than uncoated BGS scaffolds, additional tests in SBF for longer periods of time (up to 6 months) would show if the coating has lasting impact on the mechanical properties during prolonged time. Possible outcome is that the coating slows down the degradation of the scaffolds and thus maintain their mechanical stability for longer. According to the literature, it is important that the implanted scaffold maintains its mechanical properties for longer time conferring enough support for the new bone to form [4, 24]. Even though the obtained BG and AW scaffolds could be considered for the low load-bearing bone tissue applications, their mechanical properties could still be improved. It is suggested that better mechanical properties for the composite scaffolds could be achieved by using novel methods, such as 3D printing or formation of multi-layered composites, such as type 4 described in Section 2.6.1. Another option could be seeding the cells on the scaffolds, which would lead to the formation of the ECM, before implantation in the body (type 5, Section 2.6.1). Also, the addition of a cross-linking agent and formation of a hybrid (similar to Section 2.6.2) could improve the bonding between the glass-ceramic and the polymer and therefore, enhance the mechanical properties.

Chapter 9 Conclusions and recommendations for future work

The aim of this PhD research was to develop and analyse chitosan-Bioglass 45S5 (BG) and chitosan-apatite-wollastonite (AW) composites for applications in bone tissue engineering. Two methods were used for the fabrication of these composites. In the first method BG particles were added to the chitosan hydrogels. For the second method BG and AW glass-ceramic scaffolds were fabricated using the replication method and then coated with the chitosan hydrogel. Genipin was used as a natural, low toxicity cross-linker, in order to improve stability of the chitosan hydrogels. The microstructure and mechanical properties of these composites were investigated. The effect of the BG particles on the hydrogels, as well as the effect of the hydrogel coating on BG and AW scaffolds, were examined.

Genipin-cross-linked chitosan hydrogels with and without BG particles were synthesised. The BG particles were used to reinforce the hydrogels. According to scanning electron microscopy (SEM) images, BG particles did not affect the porous structure and gelation, since the pore size seemed similar before and after addition of BG (10-35 μm) and the hydrogel structure remains uniform. FTIR confirmed the cross-linking reaction between chitosan and genipin, and indicated a hydrogen bonding between the gels and BG. BG particles improved the mechanical properties of the hydrogels, as expected, but affected the fluorescence intensity (FI) measurements. The average compressive stress and modulus increased from 0.69 ± 0.11 kPa and 3.41 ± 0.59 kPa, respectively, for the hydrogels without BG, to 1.07 ± 0.11 kPa and 5.23 ± 0.66 kPa, respectively, for the hydrogels with 5 mg/ml BG. Similar average values for compressive stress and modulus were achieved for the hydrogel with 3 mg/ml BG- 1.06 ± 0.11 kPa and 5.22 ± 0.45 kPa, respectively. Even if the addition of BG lowered the final FI values, the samples were mechanically more stable. Thus, it is considered that FI values to do not correspond to the actual cross-linking in the hydrogels. Therefore, FI does not seem to be a suitable method for following the cross-linking reaction of the hydrogels containing BG.

The hydrogels were consequently immersed in simulated body fluid (SBF) for 1 week with the goal to investigate their properties in the body-like environment for bone engineering applications. It was observed that the hydrogels shrank to 30-40 % of their initial volume after 1 week of immersion in SBF, which should be considered for their applications *in vivo*.

However, the BG hydrogels were mechanically stronger after immersion in SBF. Their mechanical properties improved with the increase of BG content- the average compressive stress increased from 2.40 ± 0.40 kPa for the hydrogel without BG to 3.45 ± 0.15 kPa for the hydrogel with 5 mg/ml BG, while the average compressive modulus increased form 11.24 ± 1.75 kPa for chitosan-genipin gel to 17.00 ± 1.00 kPa for the hydrogel with 5 mg/ml BG after 1 week in SBF. Even though BG particles reinforced the hydrogels both before and after immersion in SBF, their compressive stress and modulus were up to ~ 3.60 kPa and ~ 18.0 kPa respectively for hydrogels containing 5 mg/ml BG, well below the range of mechanical properties of the human bone.

To sum up, the addition of BG powder to the hydrogels improves the mechanical properties of the chitosan-genipin to some extent, as hypothesized. Fluorescence intensity measurement is not suitable for the investigation of the cross-linking process as the end of the cross-linking and the effect of BG cannot be clearly distinguished. The hydrogels with BG powder did not disintegrate in the SBF for the time measured (1 week), while exhibiting shrinkage as the reaction to the basic pH and subsequent increase in mechanical properties, dependent on the BG content. It is recommended that a cross-linking agent between inorganic and organic parts is used, such as GPTMS, in order to further improve the mechanical properties of the composites.

BG and AW scaffolds were coated with genipin-cross-linked chitosan hydrogels in order to improve their mechanical properties and slow down their degradation in SBF. The results showed that both freeze-drying and air-drying prior to SEM affected the hydrogel coating on the scaffolds. However, since the images of air-dried samples showed collapsed but uniform and adherent coating, it is believed that the hydrogel coating did not significantly hinder the open porosity of the scaffolds (pore range of 100-300 μm before the coating). Furthermore, the morphology and colour of hydrogel coating differed on BG and AW scaffolds mainly because the gelation of the coating was affected by different pH conditions. After immersion in SBF some apatite deposition on uncoated BG scaffolds was detected.

As expected, AW scaffolds had a higher compressive stress than BG scaffolds, independent of the coating or testing conditions, with the compressive stress ranging from 0.46 to 1.20 MPa for BG and from 1.19 to 5.68 MPa for AW scaffolds, reaching the lower limit

of the cancellous bone (2-20 MPa). Inconclusive results were obtained for AW samples due to non-homogeneous sintering. The hydrogel coating did not improve the mechanical properties of either BG or AW scaffolds before SBF immersion. Uncoated BG scaffolds had an average compressive stress of 1.10 ± 0.10 MPa in comparison to 0.64 ± 0.10 MPa for coated BG scaffolds, while uncoated AW scaffolds had an average compressive stress of 2.68 ± 0.99 MPa, compared to 2.64 ± 1.45 MPa for coated AW scaffolds. Nevertheless, coating of BG scaffolds improved the compressive stress after immersion in SBF. After 2 weeks in SBF, the average compressive stress of coated BG scaffolds increased from 0.64 ± 0.10 MPa to 0.95 ± 0.17 MPa, while the average compressive stress of uncoated BG scaffolds decreased from 1.10 ± 0.10 MPa to 0.61 ± 0.15 MPa. Furthermore, the highest average value recorded for AW scaffolds was 3.89 ± 1.79 MPa for coated AW scaffold after 1 week in SBF. It would be interesting to assess the mechanical properties of coated BG and AW scaffolds after longer immersion time in SBF (up to 6 months).

In case of BG and AW scaffolds coated with the hydrogel, it can be concluded that the samples showed similar microstructural and mechanical properties as reported in the literature. Interestingly, gelation of the hydrogel coating was influenced by the pH conditions on the BG and AW contact surfaces and therefore the morphology and the colour of the hydrogel coating were different on these two types of scaffolds. In accordance with the initial research hypothesis, AW scaffolds demonstrated higher compressive strength than BG scaffolds and the coating with the hydrogel has shown significant influence on mechanical properties of the samples after immersion in SBF, suggesting that it can hinder the dissolution of the BG and maintain mechanical stability over time.

Ultimately, chitosan-genipin hydrogels with the BG particles do not seem adequate for the applications in bone tissue engineering due to low mechanical properties, rejecting the research hypothesis. BG and AW scaffolds show potential as their compressive stress was close to/within the range of that of the cancellous bone, confirming our hypothesis. Although chitosan- BG and AW scaffolds are not appropriate for high load-bearing applications, they could be applied for low load-bearing sites as alternative materials to hydroxyapatite and collagen, which are commonly used for commercially available inorganic-organic composites.

Novel methods for synthesis of scaffolds, such as 3D printing to control the pore size and distribution, and fabrication of bi- or multi-layered composites, could significantly improve mechanical properties. Additionally, formation of hybrids by using a cross-linking agent, such as GPTMS or APS, could enhance the bonding between the phases which would enhance the mechanical properties. Further investigation of AW composites is recommended as AW scaffolds are rarely explored in the literature even though they show improved mechanical properties compared to other glasses and glass-ceramics, such as Bioglass.

Immediate future work should involve several experiments that were not carried out due to the laboratory closure, such as SEM imaging of hydrogels after SBF and energy dispersive X-ray spectroscopy (EDS), as well as the improvement of the sintering of AW scaffolds and long-term SBF tests (up to 6 months) for BG and AW scaffolds, which would give additional information about the materials and contribute to the results gathered so far in this thesis.

SEM imaging of hydrogels after immersion in SBF should be conducted to observe their structure in a simulated physiological environment. As the gels shrink in this basic environment, smaller pores are expected. However, it is important that the hydrogels remain highly porous, which enables the blood and nutrient flow, necessary for the formation of the new tissue. It is expected that apatite will form on the hydrogels containing BG particles over time, which can enhance the bone formation *in vivo*.

Both AW and BG are reported to be highly bioactive materials, able to form an apatite layer within 1 week of immersion in SBF, which is vital for the cell attachment and subsequent bone formation. Using the scanning electron microscope available in this thesis, an apatite layer was observed on uncoated BG scaffolds after 2 weeks in SBF. As apatite has a similar appearance as the glass-ceramic scaffolds, it was difficult to distinguish it. It is proposed that high-resolution SEM and energy dispersive X-ray spectroscopy (EDS) are used for detection of apatite formation on BG and AW scaffolds.

Due to non-homogeneous sintering, AW scaffolds had irregular shape and microstructure, which affected their mechanical properties and reproducibility of the results, yielding large standard deviations. A better sintering of AW scaffolds is needed in the future which can be achieved by using a single furnace, stable at high temperatures (1300-1400 °C).

Also, cylindrical moulds made of platinum can be used to preserve the shape of the scaffolds inside the furnace, during the sintering process.

As the hydrogel coated BG scaffolds showed improved mechanical properties in comparison to the uncoated BG scaffolds after immersion in SBF for up to 2 weeks, a longer period of immersion (up to 6 months) is recommended to understand if the hydrogel coating hinders the dissolution of scaffolds and maintain their mechanical stability for prolonged time. Additionally, studies involving different hydrogel compositions with different concentrations of the cross-linker, and thicker coatings of the scaffolds, obtained by coating the scaffolds with the hydrogel 2 or 3 times, can be performed to investigate their effect on the dissolution and mechanical properties of the coated scaffolds. The time of the degradation of the implants usually varies between 3 to 12 months and it is crucial to understand how the degradation time can be controlled by varying hydrogel composition and the thickness of the coating.

Since the current study shows that the chitosan- BG and AW scaffolds have potential for use in tissue engineering, further experiments are recommended to enable progression towards *in vitro* and *in vivo* studies.

As antibacterial properties have been previously reported for both BG and chitosan, future tests should be conducted in order to explore this antibacterial effect. Additionally, both BG and AW showed to increase the pH of SBF, which is reported to be beneficial for the antibacterial activity of the glasses and glass-ceramics.

Further on, *in vitro* biocompatibility tests are recommended to investigate the potential of these composites for bone engineering applications.

References

1. Kumar, M.N.V.R., R.A.A. Muzzarelli, C. Muzzarelli, H. Sashiwa, and A.J. Domb, *Chitosan chemistry and pharmaceutical perspectives.* Chem Rev, 2004. **104**(12): p. 6017-6084.

2. researchandmarkets.coom. *Biomaterials market research report by type, by application - global forecast to 2025 - cumulative impact of COVID-19*. 2020 [cited 2020 1 July]; Available from: https://www.researchandmarkets.com/reports/4807794/biomaterials-market-research-report-by-type-by.

3. Wu, S., X. Liu, K.W.K. Yeung, C. Liu, and X. Yang, *Biomimetic porous scaffolds for bone tissue engineering.* Mater Sci Eng R Rep, 2014. **80**: p. 1-36.

4. Jones, J.R., *Review of bioactive glass: From Hench to hybrids.* Acta Biomater, 2013. **9**(1): p. 4457-4486.

5. Yunus Basha, R., T.S. Sampath Kumar, and M. Doble, *Design of biocomposite materials for bone tissue regeneration.* Mater Sci Eng C, 2015. **57**: p. 452-463.

6. Mallick, K.K. and J. Winnett, *Preparation and characterization of porous Bioglass® and PLLA scaffolds for tissue engineering applications.* J Am Ceram Soc, 2012. **95**(9): p. 2680-2686.

7. Ramakrishna, S., J. Mayer, E. Wintermantel, and K.W. Leong, *Biomedical applications of polymer-composite materials: a review.* Composites Science and Technology, 2001. **61**(9): p. 1189-1224.

8. Griffin, K.S., K.M. Davis, T.O. McKinley, J.O. Anglen, T.-M.G. Chu, J.D. Boerckel, and M.A. Kacena, *Evolution of bone grafting: Bone grafts and tissue engineering strategies for vascularized bone regeneration.* Clin Rev Bone Miner Metab, 2015. **13**(4): p. 232-244.

9. Berthiaume, F., T.J. Maguire, and M.L. Yarmush, *Tissue engineering and regenerative medicine: history, progress, and challenges.* Annual Review of Chemical and Biomolecular Engineering, 2011. **2**(1): p. 403-430.

10. Asa'ad, F., G. Pagni, S.P. Pilipchuk, A.B. Gianni, W.V. Giannobile, and G. Rasperini, *3D-printed scaffolds and biomaterials: Review of alveolar bone augmentation and periodontal regeneration applications.* Int J Dent, 2016. **2016**(4): p. 1-15.

11. Kumar, P., B. Vinitha, and G. Fathima, *Bone grafts in dentistry.* J Pharm Bioallied Sci, 2013. **5**(Suppl 1): p. S125-S127.

12. van Vugt, T.A., J. Geurts, and J.J. Arts, *Clinical application of antimicrobial bone graft substitute in osteomyelitis treatment: A systematic review of different bone graft substitutes available in clinical treatment of osteomyelitis.* Biomed Res Int, 2016. **2016**: p. 1-9.

13. Lopa, S. and H. Madry, *Bioinspired scaffolds for osteochondral regeneration.* Tissue Eng A, 2014. **20**(15-16): p. 2052-2076.

14. Kurien, T., R.G. Pearson, and B.E. Scammell, *Bone graft substitutes currently available in orthopaedic practice. The evidence for their use.* Bone Joint J, 2013. **95-B**(5): p. 583-597.

15. Mishra, R., T. Bishop, I.L. Valerio, J.P. Fisher, and D. Dean, *The potential impact of bone tissue engineering in the clinic.* Regen Med, 2016. **11**(6): p. 571-587.

16. Garcia-Gareta, E., M.J. Coathup, and G.W. Blunn, *Osteoinduction of bone grafting materials for bone repair and regeneration.* Bone, 2015. **81**: p. 112-121.

17. Villa, M.M., L. Wang, J. Huang, D.W. Rowe, and M. Wei, *Bone tissue engineering with a collagen-hydroxyapatite scaffold and culture expanded bone marrow stromal cells.* Journal of biomedical materials research. Part B, Applied biomaterials, 2015. **103**(2): p. 243-253.

18. Murugan, R., S. Ramakrishna, and K. Panduranga Rao, *Nanoporous hydroxy-carbonate apatite scaffold made of natural bone.* Materials Letters, 2006. **60**(23): p. 2844-2847.

19. Lee, S., M. Porter, S. Wasko, G. Lau, P.-Y. Chen, E.E. Novitskaya, A.P. Tomsia, A. Almutairi, M.A. Meyers, and J. McKittrick, *Potential bone replacement materials prepared by two methods.* MRS Proceedings, 2012. **1418**: p. mrsf11-1418-mm06-02.

20. Freeeducationforall. *Bone tissue metabolism*. 2015 [cited 2017 25 May]; Available from: https://www.slideshare.net/Ouniyeh/bone-tissue-metabolism.

21. OpenStax, *Anatomy & Physiology*. 2013, OpenStax.

22. Owen, H., *The cellular and molecular mechanisms of glucocorticoid-induced growth retardation*. 2007, The University of Glasgow Faculty of Medicine.

23. Velasco, M.A., C.A. Narváez-Tovar, and D.A. Garzón-Alvarado, *Design, Materials, and Mechanobiology of Biodegradable Scaffolds for Bone Tissue Engineering.* BioMed Research International, 2015. **2015**: p. 1-21.

24. Bose, S., M. Roy, and A. Bandyopadhyay, *Recent advances in bone tissue engineering scaffolds.* Trends Biotechnol, 2012. **30**(10): p. 546-554.

25. Deepthi, S., J. Venkatesan, S.-K. Kim, J.D. Bumgardner, and R. Jayakumar, *An overview of chitin or chitosan/nano ceramic composite scaffolds for bone tissue engineering.* Int J Biol Macromol, 2016. **93**: p. 1338-1353.

26. Albrektsson, T. and C. Johansson, *Osteoinduction, osteoconduction and osseointegration.* Eur Spine J, 2001. **10**(2): p. S96-S101.

27. Kokubo, T. and H. Takadama, *How useful is SBF in predicting in vivo bone bioactivity?* Biomaterials, 2006. **27**(15): p. 2907-2915.

28. Thompson, I.D. and L.L. Hench, *Mechanical properties of bioactive glasses, glass-ceramics and composites.* Proc Inst Mech Eng H, 1998. **212**(2): p. 127-136.

29. Yang, J., T. Long, N.-F. He, Y.-P. Guo, Z.-A. Zhu, and Q.-F. Ke, *Fabrication of a chitosan/bioglass three-dimensional porous scaffold for bone tissue engineering applications.* J Mater Chem B, 2014. **2**(38): p. 6611-6618.

30. Gerhardt, L.C. and A.R. Boccaccini, *Bioactive glass and glass-ceramic scaffolds for bone tissue engineering.* Materials (Basel), 2010. **3**(7): p. 3867-3910.

31. A. Kraitzer. *Bone grafts engineering*. 2012 [cited 2017 25 May]; Available from: https://www.slideshare.net/amirkraitzer/bone-grafts-enineering.

32. Cao, B., D. Zhou, M. Xue, G. Li, W. Yang, Q. Long, and L. Ji, *Study on surface modification of porous apatite-wollastonite bioactive glass ceramic scaffold.* Applied Surface Science, 2008. **255**(2): p. 505-508.

33. Murphy, C.M., M.G. Haugh, and F.J. O'Brien, *The effect of mean pore size on cell attachment, proliferation and migration in collagen–glycosaminoglycan scaffolds for bone tissue engineering.* Biomaterials, 2010. **31**(3): p. 461-466.

34. Woodard, J.R., A.J. Hilldore, S.K. Lan, C.J. Park, A.W. Morgan, J.A.C. Eurell, S.G. Clark, M.B. Wheeler, R.D. Jamison, and A.J. Wagoner Johnson, *The mechanical properties and osteoconductivity of hydroxyapatite bone scaffolds with multi-scale porosity.* Biomaterials, 2007. **28**(1): p. 45-54.

35. Karageorgiou, V. and D. Kaplan, *Porosity of 3D biomaterial scaffolds and osteogenesis.* Biomaterials, 2005. **26**(27): p. 5474-5491.

36. Rezwan, K., Q.Z. Chen, J.J. Blaker, and A.R. Boccaccini, *Biodegradable and bioactive porous polymer/inorganic composite scaffolds for bone tissue engineering.* Biomaterials, 2006. **27**(18): p. 3413-3431.

37. Yuan, H., K. Kurashina, J.D. de Bruijn, Y. Li, K. de Groot, and X. Zhang, *A preliminary study on osteoinduction of two kinds of calcium phosphate ceramics.* Biomaterials, 1999. **20**(19): p. 1799-1806.

38. Habibovic, P., H. Yuan, C.M. van der Valk, G. Meijer, C.A. van Blitterswijk, and K. de Groot, *3D microenvironment as essential element for osteoinduction by biomaterials.* Biomaterials, 2005. **26**(17): p. 3565-3575.

39. Thavornyutikarn, B., P. Tesavibul, K. Sitthiseripratip, N. Chatarapanich, B. Feltis, P.F.A. Wright, and T.W. Turney, *Porous 45S5 Bioglass(R)-based scaffolds using stereolithography: Effect of partial pre-sintering on structural and mechanical properties of scaffolds.* Mater Sci Eng C Mater Biol Appl, 2017. **75**: p. 1281-1288.

40. Simon, J.L., T.D. Roy, J.R. Parsons, E.D. Rekow, V.P. Thompson, J. Kemnitzer, and J.L. Ricci, *Engineered cellular response to scaffold architecture in a rabbit trephine defect.* J Biomed Mater Res A, 2003. **66A**(2): p. 275-282.

41. Ochoa, I., J.A. Sanz-Herrera, J.M. García-Aznar, M. Doblaré, D.M. Yunos, and A.R. Boccaccini, *Permeability evaluation of 45S5 Bioglass®-based scaffolds for bone tissue engineering.* J Biomech, 2009. **42**(3): p. 257-260.

42. Hum, J. and A.R. Boccaccini, *Bioactive glasses as carriers for bioactive molecules and therapeutic drugs: A review.* J Mater Sci Mater Med, 2012. **23**(10): p. 2317-2333.

43. Soundrapandian, C., A. Mahato, B. Kundu, S. Datta, B. Sa, and D. Basu, *Development and effect of different bioactive silicate glass scaffolds: In vitro evaluation for use as a bone drug delivery system.* J Mech Behav Biomed Mater, 2014. **40**: p. 1-12.

44. Wers, E., H. Oudadesse, B. Lefeuvre, O. Merdrignac-Conanec, and A. Barroug, *Evaluation of the kinetic and relaxation time of gentamicin sulfate released from hybrid biomaterial bioglass-chitosan scaffolds.* Appl Surf Sci, 2015. **353**: p. 200-208.

45. Nazemi, K., P. Azadpour, F. Moztarzadeh, A.M. Urbanska, and M. Mozafari, *Tissue-engineered chitosan/bioactive glass bone scaffolds integrated with PLGA*

nanoparticles: A therapeutic design for on-demand drug delivery. Mater Lett, 2015. **138**: p. 16-20.

46.   Mostafa, A.A., M.M.H. El-Sayed, A.A. Mahmoud, and A.M. Gamal-Eldeen, *Bioactive/natural polymeric scaffolds loaded with ciprofloxacin for treatment of osteomyelitis.* AAPS PharmSciTech, 2016. **18**(4): p. 1056-1069.

47.   Abdelfattah, M.I., S.A. Nasry, and A.A. Mostafa, *Characterization and cytotoxicity analysis of a ciprofloxacin loaded chitosan/bioglass scaffold on cultured human periodontal ligament stem cells: A preliminary report.* Open Access Maced J Med Sci, 2016. **4**(3): p. 461-467.

48.   Soundrapandian, C., S. Datta, B. Kundu, D. Basu, and B. Sa, *Porous bioactive glass scaffolds for local drug delivery in osteomyelitis: Development and in vitro characterization.* AAPS PharmSciTech, 2010. **11**(4): p. 1675-1683.

49.   Shamosi, A., D. Mehrabani, M. Azami, S. Ebrahimi-Barough, V. Siavashi, H. Ghanbari, E. Sharifi, R. Roozafzoon, and J. Ai, *Differentiation of human endometrial stem cells into endothelial-like cells on gelatin/chitosan/bioglass nanofibrous scaffolds.* Artif Cells Nanomed Biotechnol, 2017. **45**(1): p. 163-173.

50.   Habraken, W.J., J.G. Wolke, and J.A. Jansen, *Ceramic composites as matrices and scaffolds for drug delivery in tissue engineering.* Adv Drug Deliv Rev, 2007. **59**(4-5): p. 234-248.

51.   Leach, J.K., D. Kaigler, Z. Wang, P.H. Krebsbach, and D.J. Mooney, *Coating of VEGF-releasing scaffolds with bioactive glass for angiogenesis and bone regeneration.* Biomaterials, 2006. **27**(17): p. 3249-3255.

52.   Wu, J., K. Xue, H. Li, J. Sun, and K. Liu, *Improvement of PHBV scaffolds with bioglass for cartilage tissue engineering.* PLoS ONE, 2013. **8**(8): p. e71563.

53.   Alvarez, K. and H. Nakajima, *Metallic scaffolds for bone regeneration.* Materials, 2009. **2**(3): p. 790-832.

54.   Bianchi, A., G. Dolci, M. Sberna, and S. Sanfilippo, *Factors affecting bone response around loaded titanium dental implants: A literature review.* Journal of applied biomaterials & biomechanics : JABB, 2005. **3**: p. 135-40.

55.   Shuai, C., W. Yang, Y. Yang, H. Pan, C. He, F. Qi, D. Xie, and H. Liang, *Selective laser melted Fe-Mn bone scaffold: microstructure, corrosion behavior and cell response.* Materials Research Express, 2020. **7**(1).

56.   Zheng, Y.F., X.N. Gu, and F. Witte, *Biodegradable metals.* Materials Science and Engineering: R: Reports, 2014. **77**: p. 1-34.

57.   Li, H., Y. Zheng, and L. Qin, *Progress of biodegradable metals.* Progress in Natural Science: Materials International, 2014. **24**(5): p. 414-422.

58.   Yusop, A.H., A.A. Bakir, N.A. Shaharom, M.R. Abdul Kadir, and H. Hermawan, *Porous biodegradable metals for hard tissue scaffolds: a review.* Int J Biomater, 2012. **2012**: p. 641430.

59.   Malladi, L., A. Mahapatro, and A.S. Gomes, *Fabrication of magnesium-based metallic scaffolds for bone tissue engineering.* Materials Technology, 2018. **33**(2): p. 173-182.

60.   Baino, F., G. Novajra, and C. Vitale-Brovarone, *Bioceramics and scaffolds: A Winning combination for tissue engineering.* Frontiers in Bioengineering and Biotechnology, 2015. **3**(202).

61.   Dorozhkin, S.V., *Calcium orthophosphates as bioceramics: state of the art.* Journal of functional biomaterials, 2010. **1**(1): p. 22-107.

62.   Dhandayuthapani, B., Y. Yoshida, T. Maekawa, and D.S. Kumar, *Polymeric scaffolds in tissue engineering application: A Review.* International Journal of Polymer Science, 2011. **2011**: p. 1-19.

63.   Dai, Z., J. Ronholm, Y. Tian, B. Sethi, and X. Cao, *Sterilization techniques for biodegradable scaffolds in tissue engineering applications.* Journal of Tissue Engineering, 2016. **7**: p. 1-13.

64.   Westhauser, F., C. Weis, M. Prokscha, L.A. Bittrich, W. Li, K. Xiao, U. Kneser, H.-U. Kauczor, G. Schmidmaier, A.R. Boccaccini, and A. Moghaddam, *Three-dimensional polymer coated 45S5-type bioactive glass scaffolds seeded with human mesenchymal stem cells show bone formation in vivo.* J Mater Sci Mater Med, 2016. **27**(7): p. 119-125.

65.   Chen, C., H. Li, J. Pan, Z. Yan, Z. Yao, W. Fan, and C. Guo, *Biodegradable composite scaffolds of bioactive glass/chitosan/carboxymethyl cellulose for hemostatic and bone regeneration.* Biotechnol Lett, 2015. **37**(2): p. 457-465.

66. Yang, X.B., D. Webb, J. Blaker, A.R. Boccaccini, V. Maquet, C. Cooper, and R.O.C. Oreffo, *Evaluation of human bone marrow stromal cell growth on biodegradable polymer/Bioglass® composites.* Biochem Biophys Res Commun, 2006. **342**(4): p. 1098-1107.

67. Filipowska, J., K. Cholewa-Kowalska, J. Wieczorek, D. Semik, Z. Dabrowski, M. Laczka, and A.M. Osyczka, *Ectopic bone formation by gel-derived bioactive glass-poly-L-lactide-co-glycolide composites in a rabbit muscle model.* Biomed Mater, 2017. **12**(1): p. 015015.

68. Ardeshirylajimi, A., S. Farhadian, F.J. Adegani, S. Mirzaei, M.S. Zomorrod, L. Langroudi, A. Doostmohammadi, E. Seyedjafari, and M. Soleimani, *Enhanced osteoconductivity of polyethersulphone nanofibres loaded with bioactive glass nanoparticles in in vitro and in vivo models.* Cell Prolif, 2015. **48**(4): p. 455-464.

69. Boccaccini, A.R., M. Erol, W.J. Stark, D. Mohn, Z. Hong, and J.F. Mano, *Polymer/bioactive glass nanocomposites for biomedical applications: A review.* Compos Sci Technol, 2010. **70**(13): p. 1764-1776.

70. Day, R.M., V. Maquet, A.R. Boccaccini, R. Jerome, and A. Forbes, *In vitro and in vivo analysis of macroporous biodegradable poly(D,L-lactide-co-glycolide) scaffolds containing bioactive glass.* J Biomed Mater Res A, 2005. **75**(4): p. 778-787.

71. Renth, A.N. and M.S. Detamore, *Leveraging "raw materials" as building blocks and bioactive signals in regenerative medicine.* Tissue Eng Part B Rev, 2012. **18**(5): p. 341-362.

72. Lu, W., K. Ji, J. Kirkham, Y. Yan, A.R. Boccaccini, M. Kellett, Y. Jin, and X.B. Yang, *Bone tissue engineering by using a combination of polymer/bioglass composites with human adipose-derived stem cells.* Cell Tissue Res, 2014. **356**(1): p. 97-107.

73. Shakya, A.K., R. Holmdahl, K.S. Nandakumar, and A. Kumar, *Polymeric cryogels are biocompatible, and their biodegradation is independent of oxidative radicals.* J Biomed Mater Res A, 2014. **102**(10): p. 3409-3418.

74. Raina, D.B., H. Isaksson, A.K. Teotia, L. Lidgren, M. Tagil, and A. Kumar, *Biocomposite macroporous cryogels as potential carrier scaffolds for bone active agents augmenting bone regeneration.* J Control Release, 2016. **235**: p. 365-378.

75. Getgood, A.M., S.J. Kew, R. Brooks, H. Aberman, T. Simon, A.K. Lynn, and N. Rushton, *Evaluation of early-stage osteochondral defect repair using a biphasic scaffold based on a collagen-glycosaminoglycan biopolymer in a caprine model.* Knee, 2012. **19**(4): p. 422-430.

76. Albano, D., N. Martinelli, A. Bianchi, C. Messina, F. Malerba, and L.M. Sconfienza, *Clinical and imaging outcome of osteochondral lesions of the talus treated using autologous matrix-induced chondrogenesis technique with a biomimetic scaffold.* BMC Musculoskelet Disord, 2017. **18**: p. 306-312.

77. Kon, E., G. Filardo, F. Perdisa, G. Venieri, and M. Marcacci, *Clinical results of multilayered biomaterials for osteochondral regeneration.* J Exp Orthop, 2014. **1**: p. 10-17.

78. Collagen solutions. *Positive eight-year results of ChondroMimetic® cartilage repair clinical study*. 2018 [cited 2018 9 July]; Available from: http://ir.collagensolutions.com/content/news/2018/210218.asp.

79. Perdisa, F., G. Filardo, B. Di Matteo, A. Di Martino, and M. Marcacci, *Biological knee reconstruction: a case report of an Olympic athlete.* Eur Rev Med Pharmaco, 2014. **18**(1 Suppl): p. 76-80.

80. Cornell, C.N., J.M. Lane, M. Chapman, R. Merkow, D. Seligson, S. Henry, R. Gustilo, and K. Vincent, *Multicenter trial of Collagraft as bone graft substitute.* J Orthop Trauma, 1991. **5**(1): p. 1-8.

81. Lerner, T., V. Bullmann, T.L. Schulte, M. Schneider, and U. Liljenqvist, *A level-1 pilot study to evaluate of ultraporous β-tricalcium phosphate as a graft extender in the posterior correction of adolescent idiopathic scoliosis.* Eur Spine J, 2009. **18**(2): p. 170-179.

82. Neen, D., D. Noyes, M. Shaw, S. Gwilym, N. Fairlie, and N. Birch, *Healos and bone marrow aspirate used for lumbar spine fusion: a case controlled study comparing healos with autograft.* Spine, 2006. **31**(18): p. E636-640.

83. McCoy Jr, J.P., W. Schade, R.J. Siegle, E.E. Vanderveen, C.B. Zachary, T.P. Waldinger, and N.A. Swanson, *Immune responses to bovine collagen implants. Significance of pretreatment serology.* J Am Acad Dermatol, 1987. **16**(5 Pt 1): p. 955-960.

84. Roberts, T.T. and A.J. Rosenbaum, *Bone grafts, bone substitutes and orthobiologics: The bridge between basic science and clinical advancements in fracture healing.* Organogenesis, 2012. **8**(4): p. 114-124.

85. Baino, F., S. Fiorilli, and C. Vitale-Brovarone, *Bioactive glass-based materials with hierarchical porosity for medical applications: Review of recent advances.* Acta Biomater, 2016. **42**: p. 18-32.

86. Alksne, M., M. Kalvaityte, E. Simoliunas, I. Rinkunaite, I. Gendviliene, J. Locs, V. Rutkunas, and V. Bukelskiene, *In vitro comparison of 3D printed polylactic acid/hydroxyapatite and polylactic acid/bioglass composite scaffolds: Insights into materials for bone regeneration.* Journal of the Mechanical Behavior of Biomedical Materials, 2020. **104**: p. 103641.

87. Brauer, D.S. and D. Möncke, *Chapter 3 Introduction to the structure of silicate, phosphate and borate glasses*, in *Bioactive Glasses: Fundamentals, Technology and Applications*. 2017, The Royal Society of Chemistry. p. 61-88.

88. PhysicsOpenLab. *Crystalline and amorphous solids*. 2018 [cited 2020 2 June]; Available from: http://physicsopenlab.org/2018/02/13/crystalline-and-amorphous-solids/.

89. Cacciotti, I., *Bivalent cationic ions doped bioactive glasses: the influence of magnesium, zinc, strontium and copper on the physical and biological properties.* Journal of Materials Science, 2017. **52**: p. 1-20.

90. Rahaman, M.N., D.E. Day, B.S. Bal, Q. Fu, S.B. Jung, L.F. Bonewald, and A.P. Tomsia, *Bioactive glass in tissue engineering.* Acta Biomater, 2011. **7**(6): p. 2355-73.

91. Islam, M.T., R.M. Felfel, E.A. Abou Neel, D.M. Grant, I. Ahmed, and K.M.Z. Hossain, *Bioactive calcium phosphate–based glasses and ceramics and their biomedical applications: A review.* Journal of Tissue Engineering, 2017. **8**: p. 2041731417719170.

92. Hench, L.L. *Bioceramics: From concept to clinic*. 1991.

93. Renno, A., P. Bossini, M. Crovace, A.C.M. Rodrigues, E. Zanotto, and N. Parizotto, *Characterization and in vivo biological performance of biosilicate.* BioMed Research International, 2013. **2013**: p. 141427.

94. The QUARTZ Corp. *The mechanism of bioactive glass*. 2019 [cited 2020 2 June]; Available from: https://www.thequartzcorp.com/2019/09/23/the-mechanism-of-bioactive-glass/.

156

95. Hampshire, S. *Bioglasses and bioglass-ceramics*. 2015 [cited 2017 25 October]; Available from: http://www.cost-newgen.org/wp-content/uploads/2016/06/3B-Bioglasses-and-glass-ceramics-S-Hampshire.pdf.

96. Pilia, M., T. Guda, and M. Appleford, *Development of composite scaffolds for load-bearing segmental bone defects.* Biomed Res Int, 2013. **2013**: p. 1-15.

97. Allan, I., H. Newman, and M. Wilson, *Antibacterial activity of particulate Bioglass® against supra- and subgingival bacteria.* Biomaterials, 2001. **22**(12): p. 1683-1687.

98. Leppäranta, O., M. Vaahtio, T. Peltola, D. Zhang, L. Hupa, M. Hupa, H. Ylänen, J.I. Salonen, M.K. Viljanen, and E. Eerola, *Antibacterial effect of bioactive glasses on clinically important anaerobic bacteria in vitro.* J Mater Sci Mater Med, 2008. **19**(2): p. 547-551.

99. Zhang, D., O. Leppäranta, E. Munukka, H. Ylänen, M.K. Viljanen, E. Eerola, M. Hupa, and L. Hupa, *Antibacterial effects and dissolution behavior of six bioactive glasses.* J Biomed Mater Res A, 2010. **93A**(2): p. 475-483.

100. Munukka, E., O. Leppäranta, M. Korkeamäki, M. Vaahtio, T. Peltola, D. Zhang, L. Hupa, H. Ylänen, J.I. Salonen, M.K. Viljanen, and E. Eerola, *Bactericidal effects of bioactive glasses on clinically important aerobic bacteria.* J Mater Sci Mater Med, 2008. **19**(1): p. 27-32.

101. Hu, S., J. Chang, M. Liu, and C. Ning, *Study on antibacterial effect of 45S5 Bioglass®.* J Mater Sci Mater Med, 2009. **20**(1): p. 281-286.

102. Xue, M., J. Ou, D.L. Zhou, D. Feng, W.Z. Yang, G. Li, D.P. Liu, and Y.S. Wang, *Preparation and properties of porous apatite-wollastonite bioactive glass-ceramic.* Key Engineering Materials, 2007. **330-332**: p. 169-172.

103. Sooksaen, P., K. Chaithep, T. Saliwong, and T. Duangart, *Apatite-wollastonite bioactive glass-ceramic scaffolds for hard tissue engineering.* Advanced Materials Research, 2012. **506**: p. 146-149.

104. Suwanprateeb, J., R. Sanngam, W. Suvannapruk, and T. Panyathanmaporn, *Mechanical and in vitro performance of apatite-wollastonite glass ceramic reinforced hydroxyapatite composite fabricated by 3D-printing.* J Mater Sci Mater Med, 2009. **20**(6): p. 1281-9.

105. Duminis, T., S. Shahid, and R.G. Hill, *Apatite glass-ceramics: A review.* Frontiers in Materials, 2017. **3**(59).

106. Kokubo, T., M. Shigematsu, Y. Nagashima, M. Tashiro, T. Nakamura, T. Yamamuro, and S. Higashi, *Apatite- and wollastonite-containg glass-ceramics for prosthetic application.* Bull. Inst. Chem. Res. Kyoto Univ., 1982. **60**.

107. Juhasz, J.A., S.M. Best, W. Bonfield, M. Kawashita, N. Miyata, T. Kokubo, and T. Nakamura, *Apatite-forming ability of glass-ceramic apatite–wollastonite – polyethylene composites: effect of filler content.* Journal of Materials Science: Materials in Medicine, 2003. **14**(6): p. 489-495.

108. Sooksaen, P., N. Pengsuwan, S. Karawatthanaworrakul, and S. Pianpraditkul, *Formation of porous apatite layer during in vitro study of hydroxyapatite-AW based glass composites.* Advances in Condensed Matter Physics, 2015. **2015**: p. 1-9.

109. Kokubo, T., H. Kushitani, C. Ohtsuki, S. Sakka, and T. Yamamuro, *Chemical reaction of bioactive glass and glass-ceramics with a simulated body fluid.* Journal of Materials Science: Materials in Medicine, 1992. **3**(2): p. 79-83.

110. Zanotto, E., *A bright future for glass-ceramic.* American Ceramic Society Bulletin, 2010. **89**: p. 19-27.

111. Fang, Z.Z., *1.1 Introduction*, in *Sintering of Advanced Materials - Fundamentals and Processes*. 2010, Woodhead Publishing.

112. Nguyen Van, C., S. Sistla, and S. van Kempen, *A comparative study of different sintering models for Al2O3.* Journal of the Ceramic Society of Japan, 2016. **124**: p. 301-312.

113. Boccaccini, A.R., Q. Chen, L. Lefebvre, L. Gremillard, and J. Chevalier, *Sintering, crystallisation and biodegradation behaviour of Bioglass®-derived glass–ceramics.* Faraday Discussions, 2007. **136**(0): p. 27-44.

114. Poologasundarampillai, G., P.D. Lee, C. Lam, A.-M. Kourkouta, and J.R. Jones, *Compressive strength of bioactive sol–gel glass foam scaffolds.* Int J Appl Glass Sci, 2016. **7**(2): p. 229-237.

115. Boccardi, E., V. Melli, G. Catignoli, L. Altomare, M.T. Jahromi, M. Cerruti, L.-P. Lefebvre, and L.D. Nardo, *Study of the mechanical stability and bioactivity of Bioglass ® based glass-ceramic scaffolds produced via powder metallurgy-inspired technology.* Biomed Mater, 2016. **11**(1): p. 015005.

116.   Fu, Q., E. Saiz, M.N. Rahaman, and A.P. Tomsia, *Toward strong and tough glass and ceramic scaffolds for bone repair.* Adv Funct Mater, 2013. **23**(44): p. 5461-5476.

117.   Tajbakhsh, S. and F. Hajiali, *A comprehensive study on the fabrication and properties of biocomposites of poly(lactic acid)/ceramics for bone tissue engineering.* Mater Sci Eng C, 2017. **70**: p. 897-912.

118.   Motealleh, A., S. Eqtesadi, A. Pajares, and P. Miranda, *Enhancing the mechanical and in vitro performance of robocast bioglass scaffolds by polymeric coatings: Effect of polymer composition.* Journal of the Mechanical Behavior of Biomedical Materials, 2018. **84**: p. 35-45.

119.   Hench, L.L., *Bioactive glasses and glass-ceramics.* Mater Sci Forum, 1999. **293**: p. 37-64.

120.   Nandi, S., B. Kundu, and S. Datta. *Development and applications of varieties of bioactive glass compositions in dental surgery, third generation tissue engineering, orthopaedic surgery and as drug delivery system*. 2011 [cited 2018 10th July]; Available from: https://www.intechopen.com/books/biomaterials-applications-for-nanomedicine/development-and-applications-of-varieties-of-bioactive-glass-compositions-in-dental-surgery-third-ge.

121.   Ahmadi, F., Z. Oveisi, S.M. Samani, and Z. Amoozgar, *Chitosan based hydrogels: Characteristics and pharmaceutical applications.* Res Pharm Sci, 2015. **10**(1): p. 1-16.

122.   Cheung, R.C.F., T.B. Ng, J.H. Wong, and W.Y. Chan, *Chitosan: An update on potential biomedical and pharmaceutical applications.* Mar Drugs, 2015. **13**(8): p. 5156-5186.

123.   Kuttappan, S., D. Mathew, and M.B. Nair, *Biomimetic composite scaffolds containing bioceramics and collagen/gelatin for bone tissue engineering - A mini review.* International Journal of Biological Macromolecules, 2016. **93**: p. 1390-1401.

124.   Ravi Kumar, M.N.V., *A review of chitin and chitosan applications.* React Funct Polym, 2000. **46**(1): p. 1-27.

125.   Croisier, F. and C. Jérôme, *Chitosan-based biomaterials for tissue engineering.* Eur Polym J, 2013. **49**(4): p. 780-792.

126.   Nwosu, C.J., G.A. Hurst, and K. Novakovic, *Genipin cross-linked chitosan-polyvinylpyrrolidone hydrogels: Influence of composition and postsynthesis treatment on pH responsive behaviour.* Adv Mater Sci Eng, 2015. **2015**: p. 1-10.

127. Hurst, G.A. and K. Novakovic, *A facile in situ morphological characterization of smart genipin-crosslinked chitosan–poly(vinyl pyrrolidone) hydrogels.* J Mater Res, 2013. **28**(17): p. 2401-2408.

128. Dash, M., F. Chiellini, R.M. Ottenbrite, and E. Chiellini, *Chitosan—A versatile semi-synthetic polymer in biomedical applications.* Prog Polym Sci, 2011. **36**(8): p. 981-1014.

129. LogithKumar, R., A. KeshavNarayan, S. Dhivya, A. Chawla, S. Saravanan, and N. Selvamurugan, *A review of chitosan and its derivatives in bone tissue engineering.* Carbohydr Polym, 2016. **151**: p. 172-188.

130. Liu, L., Q. Gao, X. Lu, and H. Zhou, *In situ forming hydrogels based on chitosan for drug delivery and tissue regeneration.* AJPS, 2016. **11**(6): p. 673-683.

131. Bhattarai, N., J. Gunn, and M. Zhang, *Chitosan-based hydrogels for controlled, localized drug delivery.* Adv Drug Deliv Rev, 2010. **62**(1): p. 83-99.

132. Hennink, W.E. and C.F. van Nostrum, *Novel crosslinking methods to design hydrogels.* Adv Drug Deliv Rev, 2012. **64**(SUPPL.): p. 223-236.

133. Ahmed, E.M., *Hydrogel: Preparation, characterization, and applications: A review.* J Adv Res, 2015. **6**(2): p. 105-121.

134. Croisier, F. and C. Jérôme, *Chitosan-based biomaterials for tissue engineering.* European Polymer Journal, 2013. **49**: p. 780–792.

135. Irimia, T., C.-E. Dinu-Pîrvu, M. Ghica, D. Lupuleasa, D.-L. Muntean, D. Udeanu, and L. Popa, *Chitosan-based in situ gels for ocular delivery of therapeutics: A State-of-the-art review.* Marine Drugs, 2018. **16**: p. 373.

136. Hwang, Y.J., J. Larsen, T.B. Krasieva, and J.G. Lyubovitsky, *Effect of genipin crosslinking on the optical spectral properties and structures of collagen hydrogels.* ACS Appl Mater Interfaces, 2011. **3**(7): p. 2579-2584.

137. Matcham, S. and K. Novakovic, *Fluorescence imaging in genipin crosslinked chitosan–poly(vinyl pyrrolidone) hydrogels.* Polymers, 2016. **8**(12): p. 385-394.

138. Gao, L., H. Gan, Z. Meng, R. Gu, Z. Wu, L. Zhang, X. Zhu, W. Sun, J. Li, Y. Zheng, and G. Dou, *Effects of genipin cross-linking of chitosan hydrogels on cellular adhesion and viability.* Colloids Surf B Biointerfaces, 2014. **117**: p. 398-405.

139. Oryan, A., A. Kamali, A. Moshiri, H. Baharvand, and H. Daemi, *Chemical crosslinking of biopolymeric scaffolds: Current knowledge and future directions of crosslinked engineered bone scaffolds.* Int J Biol Macromol, 2018. **107**(Pt A): p. 678-688.

140. Sundararaghavan, H.G., G.A. Monteiro, N.A. Lapin, Y.J. Chabal, J.R. Miksan, and D.I. Shreiber, *Genipin-induced changes in collagen gels: Correlation of mechanical properties to fluorescence.* J Biomed Mater Res A, 2008. **87A**(2): p. 308-320.

141. Muzzarelli, R.A., M. El Mehtedi, C. Bottegoni, A. Aquili, and A. Gigante, *Genipin-crosslinked chitosan gels and scaffolds for tissue engineering and regeneration of cartilage and bone.* Mar Drugs, 2015. **13**(12): p. 7314-38.

142. Mi, F.L., S.S. Shyu, and C.K. Peng, *Characterization of ring-opening polymerization of genipin and pH-dependent cross-linking reactions between chitosan and genipin.* Journal of Polymer Science Part A: Polymer Chemistry, 2005. **43**(10): p. 1985-2000.

143. Dimida, S., C. Demitri, V.M. De Benedictis, F. Scalera, F. Gervaso, and A. Sannino, *Genipin-cross-linked chitosan-based hydrogels: Reaction kinetics and structure-related characteristics.* J Appl Polym Sci, 2015. **132**(28): p. 42256-42263.

144. Muzzarelli, R.A.A., *Genipin-crosslinked chitosan hydrogels as biomedical and pharmaceutical aids.* Carbohydr Polym, 2009. **77**(1): p. 1-9.

145. Mi, F.L., H.W. Sung, and S.S. Shyu, *Synthesis and characterization of a novel chitosan-based network prepared using naturally occurring crosslinker.* Polym Sci A Polym Chem, 2000. **38**: p. 2804-2814.

146. Delmar, K. and H. Bianco-Peled, *The dramatic effect of small pH changes on the properties of chitosan hydrogels crosslinked with genipin.* Carbohydr Polym, 2015. **127**: p. 28-37.

147. Reynolds, D.M., *The principles of fluorescence*, in *Aquatic Organic Matter Fluorescence*, A. Baker, et al., Editors. 2014, Cambridge University Press: Cambridge. p. 3-34.

148. Mi, F.L., *Synthesis and characterization of a novel chitosan-gelatin bioconjugate with fluorescence emission.* Biomacromolecules, 2005. **6**(2): p. 975-87.

149. Lee, H.M., M.H. Kim, Y.I. Yoon, and W.H. Park, *Fluorescent property of chitosan oligomer and its application as a metal ion sensor.* Mar Drugs, 2017. **15**(4).

150. Ninh, C., A. Iftikhar, M. Cramer, and C.J. Bettinger, *Diffusion-reaction models of genipin incorporation into fibrin networks.* J Mater Chem B, 2015. **3**(22): p. 4607-4615.

151. Liu, S.-T., H.-Y. Tuan-Mu, J.-J. Hu, and J.-S. Jan, *Genipin cross-linked PEG-block-poly(l-lysine)/disulfide-based polymer complex micelles as fluorescent probes and pH-/redox-responsive drug vehicles.* RSC Advances, 2015. **5**(106): p. 87098-87107.

152. Zhang, W., G. Ren, H. Xu, J. Zhang, H. Liu, S. Mu, X. Cai, and T. Wu, *Genipin cross-linked chitosan hydrogel for the controlled release of tetracycline with controlled release property, lower cytotoxicity, and long-term bioactivity.* Journal of Polym Res, 2016. **23**(8): p. 156-164.

153. Chen, H., W. Ouyang, B. Lawuyi, and S. Prakash, *Genipin cross-linked alginate-chitosan microcapsules: membrane characterization and optimization of cross-linking reaction.* Biomacromolecules, 2006. **7**(7): p. 2091-2098.

154. Mi, F.L., H.W. Sung, and S.S. Shyu, *Release of indomethacin from a novel chitosan microsphere prepared by a naturally occurring crosslinker: Examination of crosslinking and polycation–anionic drug interaction.* J Appl Polym Sci, 2001. **81**(7): p. 1700-1711.

155. Nie, J., Z. Wang, and Q. Hu, *Difference between chitosan hydrogels via alkaline and acidic solvent systems.* Sci Rep, 2016. **6**: p. 36053-36060.

156. Kumar B, N.P., M. S, and S. S, *Chitosan in medicine-A mini review.* Journal of Molecular Pharmaceutics & Organic Process Research, 2017. **05**(01).

157. Cicciu, M., L. Fiorillo, and G. Cervino, *Chitosan use in dentistry: A systematic review of recent clinical studies.* Mar Drugs, 2019. **17**(7).

158. Jones, M., M. Kujundzic, S. John, and A. Bismarck, *Crab vs. mushroom: A review of crustacean and fungal chitin in wound treatment.* Mar Drugs, 2020. **18**(1).

159. Kitozyme. *Healthcare solutions*. 2020 [cited 2020 4 April]; Available from: https://www.kitozyme.com/en/.

160. Chen, Q.Z. and A.R. Boccaccini, *Poly(D,L-lactic acid) coated 45S5 Bioglass-based scaffolds: Processing and characterization.* J Biomed Mater Res A, 2006. **77**(3): p. 445-57.

161. Durgalakshmi, D. and S. Balakumar, *Analysis of solvent induced porous PMMA-bioglass monoliths by the phase separation method-mechanical and in vitro biocompatible studies.* Phys Chem Chem Phys, 2015. **17**(2): p. 1247-1256.

162.   Zeimaran, E., S. Pourshahrestani, I. Djordjevic, B. Pingguan-Murphy, N.A. Kadri, and M.R. Towler, *Bioactive glass reinforced elastomer composites for skeletal regeneration: A review.* Mater Sci Eng C Mater Biol Appl, 2015. **53**: p. 175-188.

163.   Motealleh, A., S. Eqtesadi, F.H. Perera, A. Pajares, F. Guiberteau, and P. Miranda, *Understanding the role of dip-coating process parameters in the mechanical performance of polymer-coated bioglass robocast scaffolds.* J Mech Behav Biomed Mater, 2016. **64**: p. 253-261.

164.   Dziadek, M., J. Pawlik, E. Menaszek, E. Stodolak-Zych, and K. Cholewa-Kowalska, *Effect of the preparation methods on architecture, crystallinity, hydrolytic degradation, bioactivity, and biocompatibility of PCL/bioglass composite scaffolds.* J Biomed Mater Res B, 2015. **103**(8): p. 1580-1593.

165.   Larranaga, A., E. Diamanti, E. Rubio, T. Palomares, A. Alonso-Varona, P. Aldazabal, F.J. Martin, and J.R. Sarasua, *A study of the mechanical properties and cytocompatibility of lactide and caprolactone based scaffolds filled with inorganic bioactive particles.* Mater Sci Eng C Mater Biol Appl, 2014. **42**: p. 451-460.

166.   Maquet, V., A.R. Boccaccini, L. Pravata, I. Notingher, and R. Jerome, *Porous poly(alpha-hydroxyacid)/bioglass composite scaffolds for bone tissue engineering. I: Preparation and in vitro characterisation.* Biomaterials, 2004. **25**(18): p. 4185-4194.

167.   Bretcanu, O., A.R. Boccaccini, and V. Salih, *Poly-dl-lactic acid coated Bioglass® scaffolds: Toughening effects and osteosarcoma cell proliferation.* J Mater Sci, 2012. **47**(15): p. 5661-5672.

168.   Venkatesan, J., I. Bhatnagar, P. Manivasagan, K.H. Kang, and S.K. Kim, *Alginate composites for bone tissue engineering: A review.* Int J Biol Macromol, 2015. **72**: p. 269-281.

169.   Yao, Q., W. Li, S. Yu, L. Ma, D. Jin, A.R. Boccaccini, and Y. Liu, *Multifunctional chitosan/polyvinyl pyrrolidone/45S5 Bioglass® scaffolds for MC3T3-E1 cell stimulation and drug release.* Mater Sci Eng C Mater Biol Appl, 2015. **56**: p. 473-480.

170.   Moreira, C.D., S.M. Carvalho, H.S. Mansur, and M.M. Pereira, *Thermogelling chitosan-collagen-bioactive glass nanoparticle hybrids as potential injectable systems for tissue engineering.* Mater Sci Eng C Mater Biol Appl, 2016. **58**: p. 1207-1216.

171. Gentile, P., M. Mattioli-Belmonte, V. Chiono, C. Ferretti, F. Baino, C. Tonda-Turo, C. Vitale-Brovarone, I. Pashkuleva, R.L. Reis, and G. Ciardelli, *Bioactive glass/polymer composite scaffolds mimicking bone tissue.* J Biomed Mater Res A, 2012. **100**(10): p. 2654-2667.

172. Pourhaghgouy, M., A. Zamanian, M. Shahrezaee, and M.P. Masouleh, *Physicochemical properties and bioactivity of freeze-cast chitosan nanocomposite scaffolds reinforced with bioactive glass.* Mater Sci Eng C, 2016. **58**: p. 180-186.

173. Correia, C.O., Á.J. Leite, and J.F. Mano, *Chitosan/bioactive glass nanoparticles scaffolds with shape memory properties.* Carbohydr Polym, 2015. **123**: p. 39-45.

174. Martins, T., A.A.R. Oliveira, A.C. Oliveira, T.P. Boaventura, B.R. Barrioni, E.S. Costa-Júnior, and M.M. Pereira, *Novel 3D composites with highly flexible behavior based on chitosan and bioactive glass for biomedical applications.* Mater Chem Phys, 2017. **189**: p. 1-11.

175. Peter, M., N.S. Binulal, S. Soumya, S.V. Nair, T. Furuike, H. Tamura, and R. Jayakumar, *Nanocomposite scaffolds of bioactive glass ceramic nanoparticles disseminated chitosan matrix for tissue engineering applications.* Carbohydr Polym, 2010. **79**(2): p. 284-289.

176. Lemos, E.M.F., P.S.O. Patrício, and M.M. Pereira, *3D nanocomposite chitosan/bioactive glass scaffolds obtained using two different routes: An evaluation of the porous structure and mechanical properties.* Quím Nova, 2016. **39**(4): p. 462-466.

177. Melo, P., A.-M. Ferreira, K. Waldron, T. Swift, P. Gentile, M. Magallanes, M. Marshall, and K. Dalgarno, *Osteoinduction of 3D printed particulate and short-fibre reinforced composites produced using PLLA and apatite-wollastonite.* Composites Science and Technology, 2019. **184**: p. 107834.

178. Tcacencu, I., N. Rodrigues, N. Alharbi, M. Benning, S. Toumpaniari, E. Mancuso, M. Marshall, O. Bretcanu, M. Birch, A. McCaskie, and K. Dalgarno, *Osseointegration of porous apatite-wollastonite and poly(lactic acid) composite structures created using 3D printing techniques.* Mater Sci Eng C Mater Biol Appl, 2018. **90**: p. 1-7.

179. Roether, J.A., J.E. Gough, A.R. Boccaccini, L.L. Hench, V. Maquet, and R. Jérôme, *Novel bioresorbable and bioactive composites based on bioactive glass and polylactide foams for bone tissue engineering.* J Mater Sci Mater Med, 2002. **13**(12): p. 1207-1214.

180. Valliant, E.M. and J.R. Jones, *Softening bioactive glass for bone regeneration: sol–gel hybrid materials.* Soft Matter, 2011. **7**(11): p. 5083-5095.

181. Hild, N., P.N. Tawakoli, J.G. Halter, B. Sauer, W. Buchalla, W.J. Stark, and D. Mohn, *pH-dependent antibacterial effects on oral microorganisms through pure PLGA implants and composites with nanosized bioactive glass.* Acta Biomater, 2013. **9**(11): p. 9118-9125.

182. Wang, D., H. Lin, J. Jiang, Q. Jin, L. Li, Y. Dong, and F. Qu, *Fabrication of long-acting drug release property of hierarchical porous bioglasses/polylactic acid fibre scaffolds for bone tissue engineering.* IET Nanobiotechnol, 2015. **9**(2): p. 58-65.

183. Ren, J., K.A. Blackwood, A. Doustgani, P.P. Poh, R. Steck, M.M. Stevens, and M.A. Woodruff, *Melt-electrospun polycaprolactone strontium-substituted bioactive glass scaffolds for bone regeneration.* J Biomed Mater Res A, 2014. **102**(9): p. 3140-3153.

184. Ahtiainen, K., L. Sippola, M. Nurminen, B. Mannerstrom, S. Haimi, R. Suuronen, J. Hyttinen, T. Ylikomi, M. Kellomaki, and S. Miettinen, *Effects of chitosan and bioactive glass modifications of knitted and rolled polylactide-based 96/4 L/D scaffolds on chondrogenic differentiation of adipose stem cells.* J Tissue Eng Regen Med, 2015. **9**(1): p. 55-65.

185. Santocildes-Romero, M.E., R.L. Goodchild, P.V. Hatton, A. Crawford, I.M. Reaney, and C.A. Miller, *Preparation of composite electrospun membranes containing strontium-substituted bioactive glasses for bone tissue regeneration.* Macromol Mater Eng, 2016. **301**(8): p. 972-981.

186. Ding, Y., W. Li, T. Muller, D.W. Schubert, A.R. Boccaccini, Q. Yao, and J.A. Roether, *Electrospun polyhydroxybutyrate/poly(epsilon-caprolactone)/58S sol-gel bioactive glass hybrid scaffolds with highly improved osteogenic potential for bone tissue engineering.* ACS Appl Mater Interfaces, 2016. **8**(27): p. 17098-17108.

187. Foroughi, M.R., S. Karbasi, M. Khoroushi, and A.A. Khademi, *Polyhydroxybutyrate/chitosan/bioglass nanocomposite as a novel electrospun scaffold: Fabrication and characterization.* J Porous Mater, 2017. **24**(6): p. 1447-1460.

188. Shahabi, S., Y. Rezaei, F. Moztarzadeh, and F. Najafi, *In vitro degradation and bioactivity of poly(propylene fumarate)/bioactive glass sintered microsphere scaffolds for bone tissue engineering.* Sci Eng Compos Mater, 2016. **23**(3): p. 245-256.

189. Huang, W., X. Li, X. Shi, and C. Lai, *Microsphere based scaffolds for bone regenerative applications.* Biomater Sci, 2014. **2**(9): p. 1145-1153.

190. Alaribe, F.N., S.L. Manoto, and S.C.K.M. Motaung, *Scaffolds from biomaterials: Advantages and limitations in bone and tissue engineering.* Biologia, 2016. **71**(4): p. 353-366.

191. Shi, X., K. Su, R.R. Varshney, Y. Wang, and D.A. Wang, *Sintered microsphere scaffolds for controlled release and tissue engineering.* Pharm Res, 2011. **28**(5): p. 1224-1228.

192. Liverani, L., J.A. Roether, P. Nooeaid, M. Trombetta, D.W. Schubert, and A.R. Boccaccini, *Simple fabrication technique for multilayered stratified composite scaffolds suitable for interface tissue engineering.* Mater Sci Eng C, 2012. **557**: p. 54-58.

193. Yao, Q., P. Nooeaid, R. Detsch, J.A. Roether, Y. Dong, O.M. Goudouri, D.W. Schubert, and A.R. Boccaccini, *Bioglass®/chitosan-polycaprolactone bilayered composite scaffolds intended for osteochondral tissue engineering.* J Biomed Mater Res A, 2014. **102**(12): p. 4510-4518.

194. Balasubramanian, P. and A.R. Boccaccini, *Bilayered bioactive glass scaffolds incorporating fibrous morphology by flock technology.* Mater Lett, 2015. **158**: p. 313-316.

195. Piard, C.M., Y. Chen, and J.P. Fisher, *Cell-laden 3D printed scaffolds for bone tissue engineering.* Clin Rev Bone Miner Metab, 2015. **13**(4): p. 245-255.

196. Helen, W. and J.E. Gough, *Cell viability, proliferation and extracellular matrix production of human annulus fibrosus cells cultured within PDLLA/bioglass composite foam scaffolds in vitro.* Acta Biomater, 2008. **4**(2): p. 230-243.

197. Florczyk, S.J., M. Leung, S. Jana, Z. Li, N. Bhattarai, J.I. Huang, R.A. Hopper, and M. Zhang, *Enhanced bone tissue formation by alginate gel-assisted cell seeding in porous ceramic scaffolds and sustained release of growth factor.* J Biomed Mater Res A, 2012. **100A**(12): p. 3408-3415.

198. Eqtesadi, S., A. Motealleh, A. Pajares, F. Guiberteau, and P. Miranda, *Improving mechanical properties of 13–93 bioactive glass robocast scaffold by poly (lactic acid) and poly (ε-caprolactone) melt infiltration.* J Non-Cryst Solids, 2016. **432**: p. 111-119.

199. Vichery, C. and J.-M. Nedelec, *Bioactive glass nanoparticles: From synthesis to materials design for biomedical applications.* Materials, 2016. **9**(4): p. 288-305.

200. Jones, J. and A. Clare, *Bio-Glasses : An Introduction*. 2012, John Wiley & Sons, Incorporated.

201. Chung, J.J., S. Li, M.M. Stevens, T.K. Georgiou, and J.R. Jones, *Tailoring mechanical properties of sol–gel hybrids for bone regeneration through polymer structure.* Chemistry of Materials, 2016. **28**(17): p. 6127-6135.

202. Ravarian, R., M. Craft, and F. Dehghani, *Enhancing the biological activity of chitosan and controlling the degradation by nanoscale interaction with bioglass.* J Biomed Mater Res A, 2015. **103**(9): p. 2898-2908.

203. Shirosaki, Y., *Preparation of organic-inorganic hybrids with silicate network for the medical applications.* J Ceram Soc Jpn, 2012. **120**(1408): p. 555-559.

204. Lao, J., X. Dieudonné, F. Fayon, V. Montouillout, and E. Jallot, *Bioactive glass–gelatin hybrids: Building scaffolds with enhanced calcium incorporation and controlled porosity for bone regeneration.* J Mater Chem B, 2016. **4**(14): p. 2486-2497.

205. Liu, A., Z. Hong, X. Zhuang, X. Chen, Y. Cui, Y. Liu, and X. Jing, *Surface modification of bioactive glass nanoparticles and the mechanical and biological properties of poly(L-lactide) composites.* Acta Biomater, 2008. **4**(4): p. 1005-1015.

206. Zhang, K., Y. Wang, M.A. Hillmyer, and L.F. Francis, *Processing and properties of porous poly(l-lactide)/bioactive glass composites.* Biomaterials, 2004. **25**(13): p. 2489-2500.

207. Costa, V.C., H.S. Costa, W.L. Vasconcelos, M.d.M. Pereira, R.L. Oréfice, and H.S. Mansur, *Preparation of hybrid biomaterials for bone tissue engineering.* Mat Res, 2007. **10**(1): p. 21-26.

208. Silva, A.R.P.d., T.L. Macedo, D.J. Coletta, S. Feldman, and M.d.M. Pereira, *Synthesis, characterization and cytotoxicity of chitosan/polyvinyl alcohol/bioactive glass hybrid scaffolds obtained by lyophilization.* Materia Brazil, 2016. **21**(4): p. 964-973.

209. Mansur, H.S. and H.S. Costa, *Nanostructured poly(vinyl alcohol)/bioactive glass and poly(vinyl alcohol)/chitosan/bioactive glass hybrid scaffolds for biomedical applications.* Chem Eng J, 2008. **137**(1): p. 72-83.

210. Mondal, D., A.S. Rizkalla, and K. Mequanint, *Bioactive borophosphosilicate-polycaprolactone hybrid biomaterials via a non-aqueous sol gel process.* RSC Advances, 2016. **6**(95): p. 92824-92832.

211. Mahony, O., O. Tsigkou, C. Ionescu, C. Minelli, L. Ling, R. Hanly, M.E. Smith, M.M. Stevens, and J.R. Jones, *Silica-Gelatin Hybrids with Tailorable Degradation and Mechanical Properties for Tissue Regeneration.* Advanced Functional Materials, 2010. **20**(22): p. 3835-3845.

212. Hum, J. and A. Boccaccini, *Collagen as coating material for 45S5 Bioactive glass-based scaffolds for bone tissue engineering.* International Journal of Molecular Sciences, 2018. **19**: p. 1807.

213. Tallia, F., L. Russo, S. Li, A.L.H. Orrin, X. Shi, S. Chen, J.A.M. Steele, S. Meille, J. Chevalier, P.D. Lee, M.M. Stevens, L. Cipolla, and J.R. Jones, *Bouncing and 3D printable hybrids with self-healing properties.* Materials Horizons, 2018. **5**(5): p. 849-860.

214. Li, W., H. Wang, Y. Ding, E.C. Scheithauer, O.-M. Goudouri, A. Grünewald, R. Detsch, S. Agarwal, and A.R. Boccaccini, *Antibacterial 45S5 Bioglass®-based scaffolds reinforced with genipin cross-linked gelatin for bone tissue engineering.* Journal of Materials Chemistry B, 2015. **3**(16): p. 3367-3378.

215. Li, W., M.-I. Pastrama, Y. Ding, K. Zheng, C. Hellmich, and A.R. Boccaccini, *Ultrasonic elasticity determination of 45S5 Bioglass®-based scaffolds: Influence of polymer coating and crosslinking treatment.* Journal of the Mechanical Behavior of Biomedical Materials, 2014. **40**: p. 85-94.

216. Yao, Q., P. Nooeaid, J.A. Roether, Y. Dong, Q. Zhang, and A.R. Boccaccini, *Bioglass®-based scaffolds incorporating polycaprolactone and chitosan coatings for controlled vancomycin delivery.* Ceramics International, 2013. **39**(7): p. 7517-7522.

217. Zhou, P., Y. Xia, L. Jiang, Y. Zhang, C. Qiu, Y. Xie, and S. Xu, *O-Acrylamidomethyl-2-hydroxypropyltrimethyl ammonium chloride chitosan and silk modified mesoporous bioactive glass scaffolds with excellent mechanical properties, bioactivity and long-lasting antibacterial activity.* RSC Advances, 2016. **6**(71): p. 66938-66948.

218. Zhou, P., Y. Xia, J. Wang, C. Liang, L. Yu, W. Tang, S. Gu, and S. Xu, *Antibacterial properties and bioactivity of HACC- and HACC–Zein-modified mesoporous bioactive glass scaffolds.* J. Mater. Chem. B, 2013. **1**: p. 685-692.

219. Lao, J., X. Dieudonné, M. Benbakkar, and É. Jallot, *Bioactive glass coating on gelatin scaffolds at ambient temperature: easy route to make polymer scaffolds become bioactive.* Journal of Materials Science, 2017. **52**(15): p. 9129-9139.

220. Pon-On, W., N. Charoenphandhu, J. Teerapornpuntakit, J. Thongbunchoo, N. Krishnamra, and I.M. Tang, *Mechanical properties, biological activity and protein controlled release by poly(vinyl alcohol)–bioglass/chitosan–collagen composite scaffolds: A bone tissue engineering applications.* Materials Science and Engineering: C, 2014. **38**: p. 63–72.

221. Maji, K., S. Dasgupta, K. Pramanik, and A. Bissoyi, *Preparation and Evaluation of Gelatin-Chitosan-Nanobioglass 3D Porous Scaffold for Bone Tissue Engineering.* Int J Biomater, 2016. **2016**: p. 9825659.

222. Nazemi, K., F. Moztarzadeh, N. Jalali, S. Asgari, and M. Mozafari, *Synthesis and characterization of poly(lactic-co-glycolic) acid nanoparticles-loaded chitosan/bioactive glass scaffolds as a localized delivery system in the bone defects.* BioMed research international, 2014. **2014**: p. 898930-898930.

223. Sehgal, R., E. Carvalho, and R. Banerjee, *Mechanically stiff, zinc cross-linked nanocomposite scaffolds with improved osteostimulation and antibacterial properties.* ACS applied materials & interfaces, 2016. **8**.

224. Mishra, R., B. Basu, and A. Kumar, *Physical and cytocompatibility properties of bioactive glass–polyvinyl alcohol–sodium alginate biocomposite foams prepared via sol–gel processing for trabecular bone regeneration.* Journal of Materials Science: Materials in Medicine, 2009. **20**(12): p. 2493.

225. Luo, Y., C. Wu, A. Lode, and M. Gelinsky, *Hierarchical mesoporous bioactive glass/alginate composite scaffolds fabricated by three-dimensional plotting for bone tissue engineering.* Biofabrication, 2013. **5**(1): p. 015005.

226. Sowjanya, J.A., J. Singh, T. Mohita, S. Sarvanan, A. Moorthi, N. Srinivasan, and N. Selvamurugan, *Biocomposite scaffolds containing chitosan/alginate/nano-silica for bone tissue engineering.* Colloids Surf B Biointerfaces, 2013. **109**: p. 294-300.

227. Kumar, P., M. Saini, B.S. Dehiya, A. Umar, A. Sindhu, H. Mohammed, Y. Al-Hadeethi, and Z. Guo, *Fabrication and in-vitro biocompatibility of freeze-dried CTS-nHA and CTS-nBG scaffolds for bone regeneration applications.* Int J Biol Macromol, 2020. **149**: p. 1-10.

228. Ahmadi, Z. and F. Moztarzadeh, *Synthesizing and characterizing of gelatin-chitosan-bioactive glass (58s) scaffolds for bone tissue engineering.* Silicon, 2018. **10**(4): p. 1393-1402.

229. El-Meliegy, E., M. Mabrouk, S.A.M. El-Sayed, B.M. Abd El- Hady, M.R. Shehata, and W.M. Hosny, *Novel Fe2O3-doped glass /chitosan scaffolds for bone tissue replacement.* Ceramics International, 2018. **44**(8): p. 9140-9151.

230. Foroughi, M.R., S. Karbasi, M. Khoroushi, and A.A. Khademi, *Polyhydroxybutyrate/chitosan/bioglass nanocomposite as a novel electrospun scaffold: fabrication and characterization.* Journal of Porous Materials, 2017. **24**(6): p. 1447-1460.

231. Wang, D., F. Romer, L. Connell, C. Walter, E. Saiz, S. Yue, P.D. Lee, D.S. McPhail, J.V. Hanna, and J.R. Jones, *Highly flexible silica/chitosan hybrid scaffolds with oriented pores for tissue regeneration.* J Mater Chem B, 2015. **3**(38): p. 7560-7576.

232. Connell, L.S., F. Romer, M. Suarez, E.M. Valliant, Z. Zhang, P.D. Lee, M.E. Smith, J.V. Hanna, and J.R. Jones, *Chemical characterisation and fabrication of chitosan-silica hybrid scaffolds with 3-glycidoxypropyl trimethoxysilane.* J Mater Chem B, 2014. **2**(6): p. 668-680.

233. Shirosaki, Y., K. Tsuru, S. Hayakawa, A. Osaka, M.A. Lopes, J.D. Santos, M.A. Costa, and M.H. Fernandes, *Physical, chemical and in vitro biological profile of chitosan hybrid membrane as a function of organosiloxane concentration.* Acta Biomaterialia, 2009. **5**(1): p. 346-355.

234. Bretcanu, O., X. Chatzistavrou, K. Paraskevopoulos, R. Conradt, I. Thompson, and A.R. Boccaccini, *Sintering and crystallisation of 45S5 Bioglass® powder.* Journal of the European Ceramic Society, 2009. **29**(16): p. 3299-3306.

235. Marin, D., M. Fairlie, P. Bunton, C.J. Nwosu, J. Parker, F. Franklin, and K. Novakovic, *Design and validation study of a laboratory scale chemical reactor for non-invasive imaging of macro objects in situ.* Chem Eng J, 2017. **327**: p. 889-897.

236. Vo, N.T.N., L. Huang, H. Lemos, A. Mellor, and K. Novakovic, *Poly(ethylene glycol)-interpenetrated genipin-crosslinked chitosan hydrogels: Structure, pH responsiveness, gelation kinetics, and rheology.* Journal of Applied Polymer Science, 2020.

237. Goodhew, P.J., J. Humphreys, and R. Beanland, *Electron microscopy and analyisis*. 3rd ed. 2001: Taylor & Francis.

238. University of Glasgow. *ISAAC : Imaging spectroscopy and analysis centre*. [cited 2020 29 May]; Available from: https://www.gla.ac.uk/schools/ges/research/researchfacilities/isaac/services/scanningelectronmicroscopy/.

239. Thermo Fisher Scientific. *What is SEM? Scanning electron microscope technology explained*. 2019 [cited 2020 29 May]; Available from: https://blog.phenom-world.com/what-is-sem.

240. Clayden, J., N. Greeves, and S. Warren, *Organic chemistry*. 2nd ed. 2012: Oxford University Press.

241. Lakowicz, J.R., *Principles of fluorescence spectroscopy*. 3rd ed. 2006: Springer, Boston, MA.

242. Protein Biology Resource Library. *Fluorescent probes*. 2017 [cited 2017 1 June]; Available from: https://www.thermofisher.com/uk/en/home/life-science/protein-biology/protein-biology-learning-center/protein-biology-resource-library/pierce-protein-methods/fluorescent-probes.html#.

243. BiteSize Bio. *How fluorescent molecules work: Shine bright like a diamond*. 2017 [cited 2020 1 July]; Available from: https://bitesizebio.com/32973/fluorescent-molecules/.

244. Thermo Fisher Scientific. *Fluorescent Probes*. [cited 2020 29 May]; Available from: https://www.thermofisher.com/uk/en/home/life-science/protein-biology/protein-biology-learning-center/protein-biology-resource-library/pierce-protein-methods/fluorescent-probes.html.

245. Nawrotek, K., Z. Modrzejewska, D. Paluch, R. Zarzycki, and A. Rusak, *Cytotoxicity of chitosan based thermo-sensitive hydrogels intended for nervous tissue engineering.* Prog Chem Appl Chitin Deriv, 2015. **XX**: p. 222-235.

246. Pishbin, F., A. Simchi, M.P. Ryan, and A.R. Boccaccini, *Electrophoretic deposition of chitosan/45S5 Bioglass® composite coatings for orthopaedic applications.* Surf Coat Technol, 2011. **205**(23–24): p. 5260-5268.

247. Griffiths, P., J.A.D. Haseth, P.R. Griffiths, and J.A. De Haseth, *Fourier transform infrared spectrometry*. 2007, Hoboken, United States: John Wiley & Sons, Incorporated.

248. Rossman, G.R. *Ge 116 - Analytical techniques in geochemistry*. 2013 [cited 2020 29 May]; Available from: http://minerals.gps.caltech.edu/ge116/.

249. Nave, R. *Interference and Phase*. [cited 2020 29 May]; Available from: http://hyperphysics.phy-astr.gsu.edu/hbase/Sound/interf.html.

250. Beasley, M.M., E.J. Bartelink, L. Taylor, and R.M. Miller, *Comparison of transmission FTIR, ATR, and DRIFT spectra: implications for assessment of bone bioapatite diagenesis.* Journal of Archaeological Science, 2014. **46**: p. 16-22.

251. Kazarian, S.G. and K.L.A. Chan, *FTIR Imaging of polymeric materials*, in *Polymer Morphology*. 2016, John Wiley & Sons, Inc. p. 118-130.

252. Oregon State University. *CH362: Experimental Chemistry I*. 2017 [cited 2020 29 May]; Available from: http://sites.science.oregonstate.edu/chemistry/courses/ch361-464/ch362/IR_NMRuse/ATR.htm.

253. FiberLabes Inc. *Total Internal Reflection (TIR)*. [cited 2020 29 May]; Available from: https://www.fiberlabs.com/glossary/total-internal-reflection/.

254. Bretcanu, O., S. Misra, I. Roy, C. Renghini, F. Fiori, A.R. Boccaccini, and V. Salih, *In vitro biocompatibility of 45S5 Bioglass-derived glass-ceramic scaffolds coated with poly(3-hydroxybutyrate).* J Tissue Eng Regen Med, 2009. **3**(2): p. 139-48.

255. Callister, W.D.J., *Materials science and engineering: An introduction*. 7th ed. 2007: John Wiley & Sons, Inc.

256. Cannillo, V., F. Pierli, S. Sampath, and C. Siligardi, *Thermal and physical characterisation of apatite/wollastonite bioactive glass–ceramics.* Journal of the European Ceramic Society, 2009. **29**(4): p. 611-619.

257. West, A.R., *Solid state chemistry and its applications*. 2nd ed. 2014: John Wiley & Sons, Ltd.

258. Modern Studio Pro on Genesis Framework. *Component parts of an X-ray diffractometer*. 2020 [cited 2020 29 May]; Available from: http://xrd.co/component-parts-x-ray-diffractometer/.

259. Haines, P.J., *Thermal methods of analysis: Principles, applications and problems*. 1995: Chapman & Hall 1995.

260. Corporation, H.H.-T. *Principle of differential thermal analysis (DTA)*. 2001 [cited 2020 28 April]; Available from: https://www.hitachi-hightech.com/global/products/science/tech/ana/thermal/descriptions/dta.html.

261. Hitachi High-Tech Corporation. *Principle of differential thermal analysis (DTA)*. 2020 [cited 2020 29 May]; Available from: https://www.hitachi-hightech.com/global/products/science/tech/ana/thermal/descriptions/dta.html.

262. Panna, W., P. Wyszomirski, and P. Kohut, *Application of hot-stage microscopy to evaluating sample morphology changes on heating.* Journal of Thermal Analysis and Calorimetry, 2016. **125**(3): p. 1053-1059.

263. Ahmed, H., A. Persson, L. Okvist, and B. Bjorkman, *Reduction behaviour of self-reducing blends of in-plant fines in inert atmosphere.* ISIJ International, 2015. **55**.

264. Jiang, L., Y.W. Bao, Y. Chen, G. Liu, X. Zhang, F. Han, and Q. Yang, *Structural characteristics and hydration kinetics of oxidized steel slag in a CaO-FeO-SiO2-MgO system.* High Temperature Materials and Processes, 2018. **38**.

265. Aguilar-Reyes, E.A., C.A. León-Patiño, E. Villicaña-Molina, V.I. Macías-Andrés, and L.-P. Lefebvre, *Processing and in vitro bioactivity of high-strength 45S5 glass-ceramic scaffolds for bone regeneration.* Ceramics International, 2017. **43**(9): p. 6868-6875.

266. Cascone, M., L. Lazzeri, E. Sparvoli, M. Scatena, L. Pio Serino, and S. Danti, *Morphological evaluation of bioartificial hydrogels as potential tissue engineering scaffolds*. Vol. 15. 2005. 1309-13.

267. Schugens, C., V. Maquet, C. Grandfils, R. Jerome, and P. Teyssie, *Biodegradable and macroporous polylactide implants for cell transplantation: 1. Preparation of macroporous polylactide supports by solid-liquid phase separation.* Polymer, 1996. **37**(6): p. 1027-1038.

268. Kazarian, S.G., K.L. Chan, V. Maquet, and A.R. Boccaccini, *Characterisation of bioactive and resorbable polylactide/Bioglass composites by FTIR spectroscopic imaging.* Biomaterials, 2004. **25**(18): p. 3931-8.

269. Sankalia, M.G., R.C. Mashru, J.M. Sankalia, and V.B. Sutariya, *Reversed chitosan–alginate polyelectrolyte complex for stability improvement of alpha-amylase: Optimization and physicochemical characterization.* Eur J Pharm Biopharm, 2007. **65**(2): p. 215-232.

270. Zu, Y., X. Yu, X. Zhao, W. Wang, and K. Wang, *Nanocrystallization of the pharmaceutically active agent genipin by an emulsion solvent evaporation method.* Journal of Nanomaterials, 2014. **2014**: p. 1-13.

271. Li, Q., X. Wang, X. Lou, H. Yuan, H. Tu, B. Li, and Y. Zhang, *Genipin-crosslinked electrospun chitosan nanofibers: Determination of crosslinking conditions and evaluation of cytocompatibility.* Carbohydr Polym, 2015. **130**: p. 166-74.

272. Dimida, S., A. Barca, N. Cancelli, V. De Benedictis, M.G. Raucci, and C. Demitri, *Effects of Genipin Concentration on Cross-Linked Chitosan Scaffolds for Bone Tissue Engineering: Structural Characterization and Evidence of Biocompatibility Features.* International Journal of Polymer Science, 2017. **2017**: p. 1-8.

273. Xu, J., S. Strandman, J.X. Zhu, J. Barralet, and M. Cerruti, *Genipin-crosslinked catechol-chitosan mucoadhesive hydrogels for buccal drug delivery.* Biomaterials, 2015. **37**: p. 395-404.

274. Essien, E.R., L.A. Adams, R.O. Shaibu, and A. Oki, *Sol-gel bioceramic material from bentonite clay.* Journal of Biomedical Science and Engineering, 2013. **06**(03): p. 258-264.

275. Muthusamy, P., S. Priscilla, K. Kandiah, P. Manivasakan, R. Venkatachalam, and P. Kulandaivelu, *In vitro bioactivity and antimicrobial tuning of bioactive glass nanoparticles added with Neem (Azadirachta indica) leaf powder.* BioMed research international, 2014. **2014**: p. 950691.

276. Jang, J.H., M.G. Lee, J.L. Ferracane, H. Davis, H.E. Bae, D. Choi, and D.S. Kim, *Effect of bioactive glass-containing resin composite on dentin remineralization.* J Dent, 2018. **75**: p. 58-64.

277. Aziz A, A.E., A.E. Maghraby, and S.H. Kandil, *Study of In vitro bioactivity and biodegradability of the hydrothermally prepared carbon nanofibrous/hydroxyapatite (Cnf/Ha) membranes.* Journal of Bone Research, 2017. **05**(02).

278. Susanne, H., R.S. Philipp, T.T. Tobias, J.S. Wendelin, Z. Matthias, and M. Dirk, *Incorporation of particulate bioactive glasses into a dental root canal sealer.* Biomedical Glasses, 2016(1).

279. Fariza, A.R., Z. Ahmad, and I. Sopyan, *Application of Low Cost Polyurethane (PU) Foam for Fabricating Porous Tri-Calcium Phosphate (TCP).* Journal of Biomimetics Biomaterials and Tissue Engineering, 2010. **8**: p. 1-7.

280. Mancuso, E., O. Bretcanu, M. Marshall, and K.W. Dalgarno, *Sensitivity of novel silicate and borate-based glass structures on in vitro bioactivity and degradation behaviour.* Ceramics International, 2017. **43**(15): p. 12651-12657.

281. Chang, C.K., D.L. Mao, and J.S. Wu, *Characteristics of crystals precipitated in sintered apatite/wollastonite glass ceramics.* Ceramics International, 2000. **26**(7): p. 779-785.

282. Li, W., N. Garmendia, U. Pérez de Larraya, Y. Ding, R. Detsch, A. Grünewald, J.A. Roether, D.W. Schubert, and A.R. Boccaccini, *45S5 bioactive glass-based scaffolds coated with cellulose nanowhiskers for bone tissue engineering.* RSC Adv., 2014. **4**(99): p. 56156-56164.

283. Loty, C., J.M. Sautier, H. Boulekbache, T. Kokubo, H.M. Kim, and N. Forest, *In vitro bone formation on a bone-like apatite layer prepared by biomimetic process on a bioactive glass-ceramic.* Journal of biomedical materials research, 2000. **49**: p. 423-34.

Appendix A

Differential thermal analysis

Differential thermal analysis was done for BG (Section 4.3) and AW (Section 7.1.3) powders. A test without a crucible (Figure A1) was performed in order to show that the peak at ~ 250 °C occurs due to an error of the instrument and not the samples.
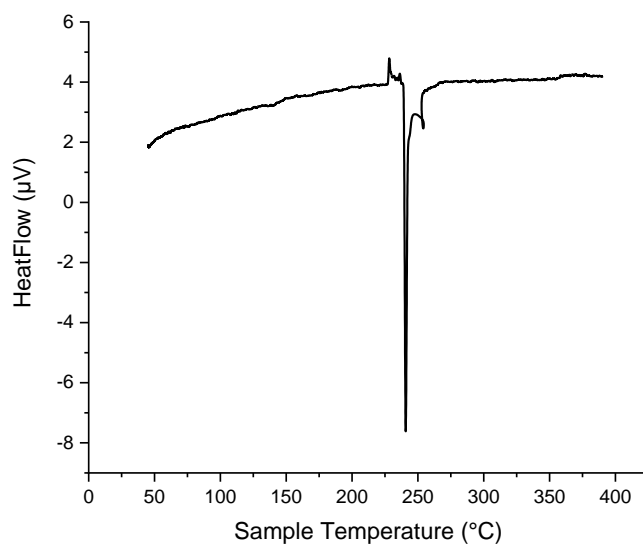

Figure A1: Measurement without a crucible (heating rate 20 °C/min)

Appendix B

Fluorescence intensity measurement

Average values of fluorescence intensity are shown in Section 5.2. Figures B1-B3 show fluorescence intensity values over 24 h for chitosan-genipin and chitosan-genipin-BG gels, recorded for 3 individual tests.
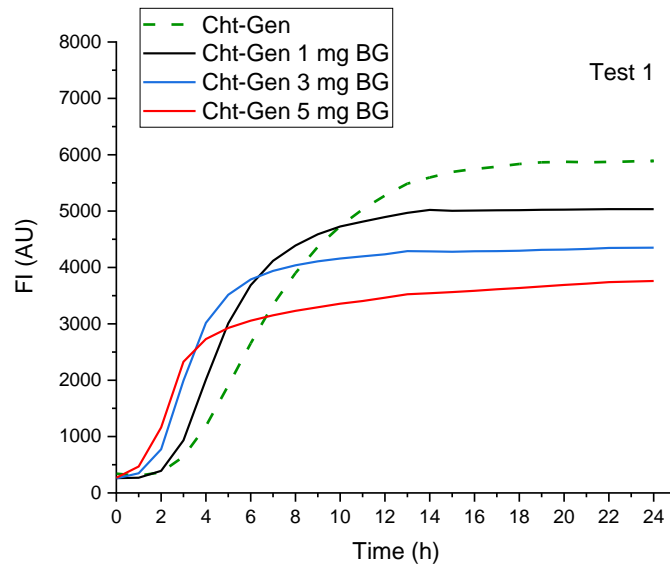

Figure B1: Fluorescence intensity during polymerisation over 24 h for chitosan-genipin and chitosan-genipin-BG gels (test 1)
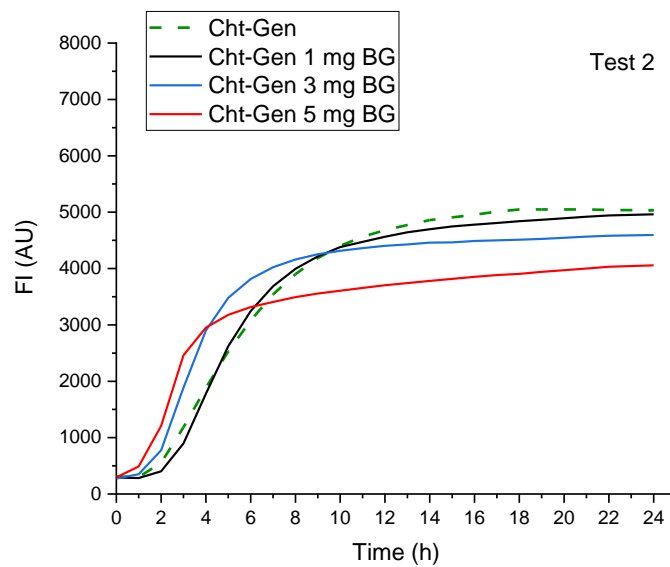
Figure B2: Fluorescence intensity during polymerisation over 24 h for chitosan-genipin and chitosan-genipin-BG gels (test 2)
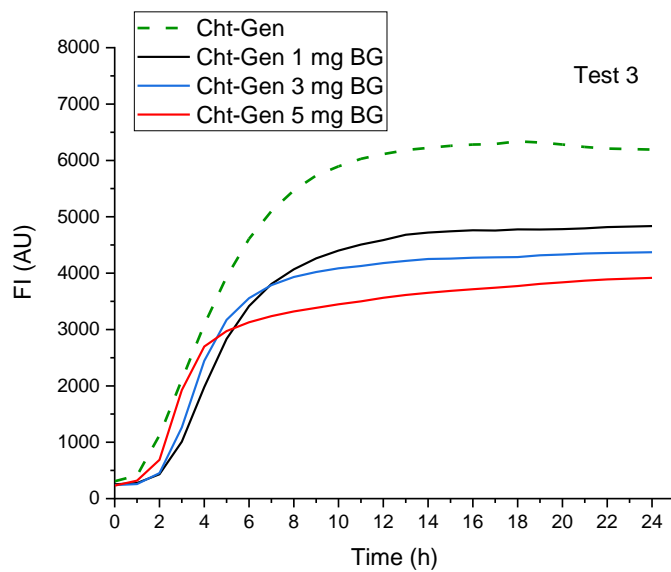

Figure B3: Fluorescence intensity during polymerisation over 24 h for chitosan-genipin and chitosan-genipin-BG gels (test 3)